SYNTHESIS AND PHOTOLUMINESCENCE PROPERTIES OF Eu^{3+} BASED RED PHOSPHORS FOR WHITE LIGHT EMITTING DIODE (WLED) APPLICATIONS

Thesis submitted to
The University of Kerala for the award of
The Degree of

DOCTOR OF PHILOSOPHY
IN PHYSICS
UNDER THE FACULTY OF SCIENCE

BY

SREENA T. S.

MATERIALS SCIENCE & TECHNOLOGY DIVISION
CSIR- NATIONAL INSTITUTE FOR INTERDISCIPLINARY SCIENCE AND TECHNOLOGY (NIIST), THIRUVANANTHAPURAM 695 019, KERALA

SEPTEMBER 2018

To my parents...

DECLARATION

I hereby declare that the PhD thesis entitled **"Synthesis and Photoluminescence Properties of Eu^{3+} based Red Phosphors for White Light Emitting Diode (WLED) Applications"** is an independent work carried out by me and it has not been submitted anywhere else for any other degree, diploma, or title.

Sreena T. S

THIRUVANANTHAPURAM

Date: 31.08.2018

राष्ट्रीय अंतर्विषयी विज्ञान तथा प्रौद्योगिकी संस्थान
NATIONAL INSTITUTE FOR INTERDISCIPLINARY SCIENCE AND TECHNOLOGY
वैज्ञानिक तथा औद्योगिक अनुसंधान परिषद् | Council of Scientific and Industrial Research
इंडस्ट्रियल इस्टेट पी. ओ, पाप्पनंकोड, तिरुवनंतपुरम, भारत - 695 019 | Industrial Estate P.O., Pappanamcode, Thiruvananthapuram, India-695 019

30.08.2018

CERTIFICATE

This is to certify that the work embodied in the thesis entitled **"Synthesis and Photoluminescence Properties of Eu^{3+} based Red Phosphors for White Light Emitting Diode (WLED) Applications"** has been carried out by Ms. Sreena T. S under my supervision and guidance at the Materials Science and Technology Division of National Institute for Interdisciplinary Science and Technology (CSIR-NIIST), Thiruvananthapuram and the same has not been submitted elsewhere for any other degree.

THIRUVANANTHAPURAM

Date: Aug. 30, 2018

Dr. P. Prabhakar Rao

(Thesis Supervisor)

Dr. P. PRABHAKAR RAO M.Sc., Tech, Ph.D
Chief Scientist
Materials Science & Technology Division
CSIR-National Institute for Interdisciplinary
Science and Technology, (CSIR-NIIST)
Industrial Estate P.O.
Thiruvananthapuram-695 019, Kerala, India

Tel: 91 471 2515239 Fax: 91 471 2491895, 2490389, (D) 2515239/510/511/256/384 E-mail: spo@niist.res.in. Website: http//www.niist.res.in

ACKNOWLEDGEMENTS

Undertaking this PhD has been a truly life-changing experience for me and it would not have been possible to do without the support and guidance that I received from many people. I take this opportunity to extend my sincere gratitude and appreciation to all those who made this PhD thesis possible.

Firstly, I would like to express my sincere gratitude to my research supervisor, Dr. P. Prabhakar Rao for introducing me to this exciting field of science and for his dedicated help, advice, inspiration, encouragement and continuous support, throughout my Ph.D. His positive outlook and confidence in my research inspired me and gave me confidence. I have been extremely lucky to have a supervisor who cared so much about my work, and who responded to my questions and queries so promptly.

I am grateful to Dr. A. Ajayghosh, Director CSIR-NIIST, and former director, Dr. Suresh Das for allowing me to carry out my research in this esteemed laboratory. I owe a great deal to Dr. Harikrishna Bhat, Dr. P. Prabhakar Rao, Dr. M. L. P. Reddy and Dr. M. T. Sebastian, present and former Head of Materials Science and Technology Division, for extending the research facilities. Also, I sincerely thank all scientists and staffs of MSTD for all the help and support extended to me.

I am privileged to thank Department of Science and Technology, INSPIRE Program for the financial support granted to me to undertake this research work and also for giving me the opportunity to attend conferences and meet so many interesting people. Also I am thankful to Council for Scientific and Industrial Research (CSIR) for providing me all the facilities and infrastructure to perform my research work.

Special thanks to Mr. M. R. Chandran, Mrs. Luci Paul, Mrs. Soumya Valsalam and Mr. Harish Raj for SEM imaging. I wish to thank Mr. Pruthiviraj, Mr. M. P. Varkey and Mr. Shanoj for the technical support. I also thank Department of Optoelectronics, Kerala University for the help with Raman analysis.

I am most grateful to the senior colleagues Dr. Mariyam Thomas, Dr. Linda Francis, Dr. Sameera S, Dr. Divya S, Dr. Vaisakhan Thampi, Mr. Mahesh, Dr. Sumi S, Mrs. Vineetha James and Mrs. Reshmi V R, for lending me their expertise to my

scientific and technical problems. Special thanks to my colleagues and friends of Energy Materials Lab in the Materials Science and Technology Division particularly Mrs. Athira K. V Raj, Mrs. Renju U A, Mrs. Parvathi S Babu, Ms. Suchithra V. G, Mrs. Aswathi B A and Ms. Aju Thara T. R. To the greatest friends I've ever had, Athira K V Raj and Aju Thara. Thank you so much for everything. Completing this work would have been all the more difficult were it not for the support and friendship provided by Mrs. Athira K. V Raj and Ms. Aju Thara T. R. I am extremely indebted to them for their help.

I am thankful to library staff and administrative staff for their help and services.

My special regards to my teachers because of whose teaching at different stages of education has made it possible for me to see this day. Because of their kindness I feel, was able to reach a stage where I could write this thesis.

I feel a deep sense of gratitude for my parents, Thankam and Sreedharan who formed part of my vision and taught me good things that really matter in life. Their selfless love, care, pain and sacrifice will remain my inspiration throughout my life. Also I express my thanks to my sisters Sreeja and Sreeji and brother Sreejith, for their constant inspiration and encouragement.

Above all, I praise God, the almighty, whose blessings have made me who I am today.

Sreena T. S

CONTENTS

LIST OF TABLES

LIST OF FIGURES

ABBREVIATIONS

CCT	:	Correlated Color Temperature
CF	:	Crystal Field
CIE	:	Commission Internationale de I' Eclairage
CN	:	Coordination Number
CRI	:	Color Rendering Index
CT	:	Charge Transfer
CTB	:	Charge Transfer Band
CTS	:	Charge Transfer State
ED	:	Electric Dipole
EDS	:	Energy Dispersive Spectroscopy
FWHM	:	Full Width at Half Maximum
FT- IR	:	Fourier Transform Infrared
InGaN	:	Indium Gallium Nitride
JCPDS	:	Joint Committee on Powder Diffraction Standards
J-O	:	Judd-Ofelt
LED	:	Light Emitting Diode
Ln	:	Lanthanide
MD	:	Magnetic Dipole
NTSC	:	National Television Standards Committee
NUV	:	Near Ultraviolet
pc-WLED	:	Phosphor Converted White Light Emitting Diode
PL	:	Photoluminescence
QE	:	Quantum Efficiency
RE	:	Rare Earth
SEM	:	Scanning Electron Microscopy
SSL	:	Solid State Lighting
SSR	:	Solid State Reaction
TEM	:	Transmission Electron Microscopy
XPS	:	X-ray Photoelectron Spectroscopy
XRD	:	X-ray Diffraction

PREFACE

White light-emitting diodes, as an emerging solid state lighting (SSL) source, offers benefits in terms of reliability, energy saving, maintenance and positive environment effects and stands a real chance of replacing the traditional light sources such as incandescent and fluorescent lamps. Until now, major challenges in pc-WLEDs have been to achieve high luminous efficacy, high chromatic stability, brilliant color-rendering properties, and price competitiveness against fluorescent lamps, which rely critically on the phosphor properties. The first white LED commercialized by Nichia Corporation, Japan consists of InGaN blue LED and a yellow YAG: Ce^{3+} phosphor. The white created by the blue LED + yellow phosphor differs from that of natural white light due to halo effect of blue/yellow colour separation and poor color rendering index caused by the lack of red emission. Finding novel families of red phosphor materials with high absorption in the NUV to blue region and the reduced degradation by UV radiation are important challenges to overcome. Eu^{3+} doped phosphors are of immense interest for applications in near UV LEDs, since they exhibit a high lumen equivalent, quantum efficiency and photo stability. Generally, Eu^{3+} activated phosphors possess high CRI values but exhibit low absorption in blue or near UV region because of the dynamics of rare earth ion, which depends on the interaction between the rare earth ion and the host, such as local environment around the dopants, the doping concentration, the distribution of activator ions in the host lattice and the energy transfer from the host lattice to the activator ions. The absorption of Eu^{3+} ions can be increased by selecting a suitable host lattice where absorption is increased due to the increased optical pathway of the incident photons. So our intimidating task is to find a suitable host materials that have broad and intense charge transfer (CT) absorption bands in the near UV and are therefore capable of efficiently absorbing the emission from InGaN based LEDs. Among the existing materials of interest, pyrochlores scores over the other due to their inherent properties such as high chemical stability, lattice stiffness, thermal stability, ability to incorporate a diverse range of elements at the A and B sites and to tolerate both cation and anion disorder etc. A recently adopted strategy is to convert near UV or blue light via the 4f-4f transitions of Eu^{3+} located at 394 ($^7F_0$- $^5L_6$) and 465 run ($^7F_0$- $^5D_2$), which are rather intense in pyrochlores. Keeping all these facts in

mind, in the current research work an attempt has been made to develop novel red phosphors based on pyrochlore host lattice and also manipulating the Eu^{3+} environment for enhanced luminescence.

The present research work is organized into seven chapters. Introduction chapter discusses about solid state lighting technology and different methods for white light generation with their advantages and practical challenges. The mechanism of luminescence in Eu^{3+} activated phosphors is also emphasized. Major objectives of the present work are highlighted and the motivation and importance of choosing pyrochlore based host lattice is also emphasized. In addition to this, the importance of narrow band red emitting phosphors is discussed in detail. A brief literature review of Eu^{3+} luminescence in various pyrochlore host lattices and different narrow band red emitting phosphors are discussed in the second chapter.

Third chapter details the structural and photoluminescence properties of stannate based displaced pyrochlore-type red phosphors: $Ca_{3-x}Sn_3Nb_2O_{14}:xEu^{3+}$. The influence of partial occupancy of Sn in both A and B sites of the pyrochlore-type oxides on the photoluminescence properties is studied in this chapter. These phosphors exhibit strong absorptions at near UV and blue wavelength regions and emit intense multiband emissions due to Eu^{3+} $^5D_0$–$^7F_{0,\ 1,\ 2}$ transitions. The influence of partial occupation of Ti in both A and B sites of the pyrochlore structure is also highlighted in the second part of the third chapter.

Influence of structural disorder on the photoluminescence properties of Eu^{3+} doped red phosphors:$Ca_2Y_{3-x}Nb_3O_{14}:xEu^{3+}$ is discussed in the fourth chapter. The Eu^{3+} incorporation induces structural disorder in the lattice reducing the pyrochlore D_{3d} symmetry. These phosphors emit intense red light due to forbidden electric dipole transition with more Stark splitting indicating the low symmetry of Eu^{3+} ions in the host. Substitution of calcium ions by bigger strontium ions is found to have enhanced the luminescence properties. The influence of effective positive charge of the central Eu^{3+} ions when it replaces a metal ion having lower oxidation state is discussed in the second part of the fourth chapter.

Exploitation of Eu^{3+} red luminescence through order-disorder structural transition in lanthanide stannate pyrochlore for warm white LED

applications details the fifth chapter. Eu^{3+} ion epitomize as an excellent structural probe for the detection of disorder induced by the structural variation in stannate pyrochlores due to its relatively simple energy level structure. The substitution of Ln^{3+} ions (Ln = La, Gd, Y and Lu) in the A site of the pyrochlore $Ln_3YSnNbO_{10.5}$ system induces a structural transition from an ordered pyrochlore to a disordered fluorite structure with decreasing ionic radius. These phosphors exhibit strong absorption in the near UV region and emit red luminescence under 392nm excitation which is also correlated with their crystal structures. Their luminescence properties got enhanced with increased ordering of cations from Lu to La. In the second part of the fifth chapter, we have discussed the manipulation of Eu^{3+} luminescence through phase evolution in $Ln_4YSn_2NbO_{14}$ (Ln = La, Gd, Y and Lu) host lattice in correlation with their crystal structures.

Commercially applied red phosphors exhibit a broad emission band with a large portion of emitted light lie outside the human eye sensitivity wasting energy in the infrared region. Therefore, narrow band red-emitting materials are necessary. In this regard, we have synthesized a series of Eu^{3+} doped narrow band red emitting phosphors $Gd_3Zn_2Nb_3O_{14}$ and investigate the evolution of emission spectra with partial occupation of Zn^{2+} ions on both A and B site of the fergusonite type structure. The developed phosphor exhibits a strong red emission peaking at 613 nm with a fwhm of merely ~3.50 nm under the 392 nm excitation. Chapter six details these results. In the second part of the sixth chapter, we have highlighted the evolution of emission spectra with partial occupation of Mg^{2+} ions on both A and B site of the fergusonite type structure $Y_3Mg_2Nb_3O_{14}$. The developed phosphors exhibited higher emission intensities than the standard Y_2O_3:Eu^{3+} red phosphors.

Chapter seven summarizes the major findings and conclusions drawn from the work and gives the scope for further studies.

Chapter 1

IMPERATIVE ASPECTS OF PHOSPHORS

Advances in solid state lighting technologies witness the explosive development of phosphor materials for general lighting applications in the last few decades. A large amount of evidence has demonstrated the revolutionary role of the emerging lanthanide-activated phosphors in producing superior white light-emitting diodes for lighting and display applications. In this chapter, the state-of-art progress on the various lighting techniques and a basic understanding of the solid state lighting are discussed. This chapter also highlights the electronic and luminescence properties of Eu^{3+} ions as a component for red phosphors and focuses the correlation between host crystal structures with the f-f luminescence characteristics of Eu^{3+} ions. Finally, the challenges and outlooks in this type of promising down-conversion luminescent materials are highlighted.

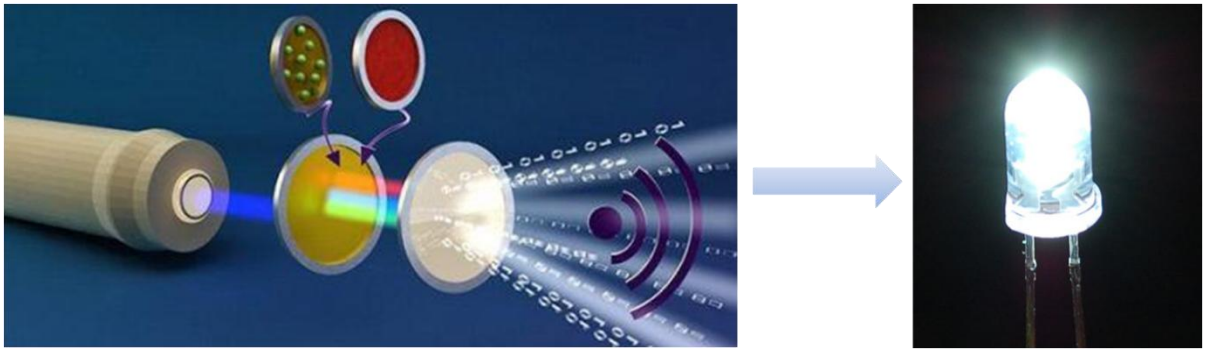

1.1 Introduction

Global population growth and urbanization increases the overall demand for lighting products and the corresponding energy consumption by lighting. According to recent studies by US Department of Energy (DOE), lighting requires ~22 % of global electricity consumption. A new era in lighting and display applications has emerged with the development of white light-emitting diodes (WLEDs), which outperform the more traditional light sources such as incandescent or fluorescent lamps because of their superior properties such as high efficiency, prolonged lifetime, compactness, reliability and environment friendliness (Qin *et al*. 2017). LEDs are projected to reduce total lighting electricity consumption by 15% in the year 2020 and by 40% in 2030. These energy savings would reduce green house gas emission by approximately 180 million metric tons of carbon dioxide. Considering the global population growth, resource scarcity and climate change concerns, the development and implementation of LED technology is strategically important for a sustainable society.

The high brightness blue LEDs based on InGaN are the most substantial innovation in the development of WLEDs and were developed by Isamu Akasaki, Hiroshi Amano, Shuji Nakakmura, who won 2014 Noble Prize for this achievement. InGaN-based white LEDs (WLEDs) were therefore debuted and appeared as a new generation and a possible substitute of solid state lighting (SSL), which are now ushering in the next lighting revolution and offering many opportunities not only to give people much visual and aesthetic enjoyment but also to make substantial energy savings and a significant reduction in environmental impact over conventional power generation. Since the invention of efficient blue LEDs, much progress has been made in the search for suitable down-conversion materials, bringing phosphor-converted LEDs (pc-LEDs) into widespread applications. However, there is still need for luminescent materials (phosphors) with improved luminescence properties to improve pc-LEDs for general lighting and other special applications.

1.2 Solid state lighting

Along with the progress of human civilization, the lighting technology has gone through a diversified course of development. The current lighting technology in the public realm is dominated by conventional incandescent filament bulbs or fluorescent lamps, and this lighting technology lasts for more than 100 years. In the case of incandescent lamps, majority of the energy is converted into heat, which does not make this source suitable for an efficient lighting application. Fluorescent lighting is more efficient than filament lamp, but the hazardous waste mercury used in them renders a disposal problem and imposes threat to the environment. Although most people are comfortable with them, the cost, efficiency and environmental concern of traditional lighting is now being questioned more broadly. Following an increasing awareness of climate change and environmental issues, people are looking for new technologies to reduce energy consumption and provide eco-friendly illumination and displays. Solid state lighting based on light emitting diodes (LEDs) offers an alternative method of illumination (Xie *et al*. 2007). In recent years, the ever-growing impact of solid state lighting technology on household usage in the form of white-light emitting diodes (WLEDs) and high-resolution displays has initiated a pan-global hunt for the improvement and optimization of brightness and color purity. WLEDs, the fourth-generation lighting source have attracted much attention due to their high luminescence and brightness, compactness, longer lifetime, and resultant energy saving and are gradually replacing conventional light sources,

The history of solid state lighting technology goes back more than a century. The evolution in the lighting technology is shown in Fig. 1.1 (Pawade *et al*. 2015). In 1907, H. J. Round published light emission from a silicon carbide (SiC) junction diode and effectively created the first LED. Independently, Losev also observed similar emission from ZnO and SiC diodes. However, potential of this technology was not realized and this major invention remained largely unnoticed for the next 50 years until research on semiconductors started. In 1962, Hall announced the first semiconductor diode laser at General Electric Research Labs in Schenectady, New York, but there was almost no application besides used in numeric displays or signaling applications (Henini *et al*.

2001, Kovac *et al*. 2003). However, the situation almost completely changed with Shuji Nakamura's invention, who successfully fabricated double-heterostructure high brightness InGaN/GaN based blue LED chips for the first time in 1993 (Nakamura *et al*. 1993). The first commercial white light-emitting diode (LED) was produced by Nichia Corporation in 1996. After that, tremendous progress has been achieved in development of solid-state lighting based on InGaN semiconductors.

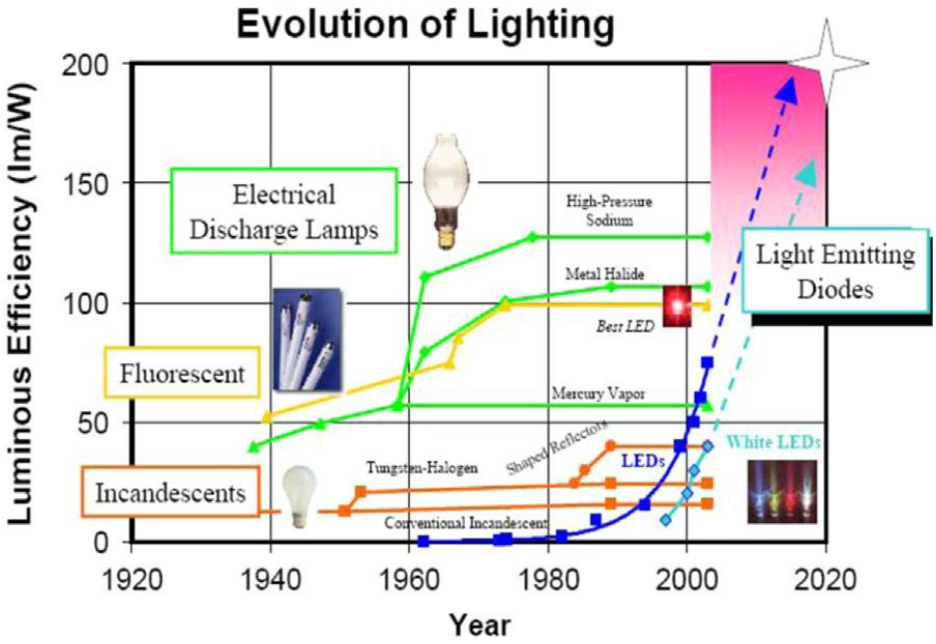

Fig. 1.1 Evolution in the lighting technology

The maximum efficiency of a commercial high-power white LED is currently about 30% (100 lmW^{-1} efficacy), which is six times greater than that of a filament light bulb and 50% better than that of a compact fluorescent lamp. Currently, the most popular WLED in the market is manufactured using an InGaN based blue LED chip with the well-known yellow emitting YAG: Ce^{3+} phosphor (Lee *et al*. 2015; Jiang *et al*. 2014). However, because of the innate absence of red light, this type of WLED suffers from a high correlated color temperature (CCT>4500 K) and a low color-rendering index (CRI<80), which limits their widespread commercialization for indoor lighting purposes. To circumvent these problems, a red phosphor must be incorporated into the WLED package, which is a feasible approach to accomplish a warm white emission with low correlated color temperature and high color rendering index (CRI>80). For this

purpose, extensive efforts have been made in developing novel red-emitting materials for WLED applications. Nevertheless, we are on the bridges of solid state lighting. The competition from WLEDs is however increasing and will change the future of lighting.

1.3 Basic photometric quantities

For indoors and outdoors lighting applications, it is theoretically possible to use any visible spectrum, or even monochromatic light. However, we are generally looking for white light only, as this type of light source can be used as a replacement of incandescent or compact fluorescent lamps. In order to determine whether the spectrum of a light source is suitable for general lighting, there are several criteria that have to be considered for practical applications in lighting and displays. This includes:

1.3.1 Luminous flux (lm)

It is the photometric equivalent of the radiant flux in radiometry. It measures the total light energy emitted by a light source per unit time as perceived by the human eye. The unit for the luminous flux is lumen (lm).

1.3.2 Luminous efficacy (lm/W)

Every color in the visible spectrum can be described in terms of its wavelength. The actual perception of a color depends on the reflection properties of the object, but is possible only if the object is illuminated by a source possessing the correspondent wavelength. The luminous efficacy of radiation measures how well a given quantity of electromagnetic radiation from a source produces visible light. It is defined as the ratio of the total luminous flux (lm) to radiant flux (W) and is also determined by the human eye sensitivity over the spectral distribution of light (Ye *et al*. 2010). This specifies the overall luminous efficacy of a source and express how well it converts energy to electromagnetic radiation, and how well the emitted radiation is detected by the human eye. The light sensitivity of the human eye depends on the wavelength of the light and in a lighted environment it enables color around 555nm (green light) to be appreciated brighter than in the red ones. The human eye's peak perception at 555 nm is shown in Fig. 1.2 (http://www.brite-led.com/HumanEyeResponse.htm). The theoretically

attainable maximum luminous efficacy corresponding to green light at a frequency of 540×10^{12} Hz is 683lm/W. The luminous efficacies that can be actually attained vary depending on the lamps, but always remain far below this ideal value. Luminous efficacy values of different lighting sources are given in Table 1.1.

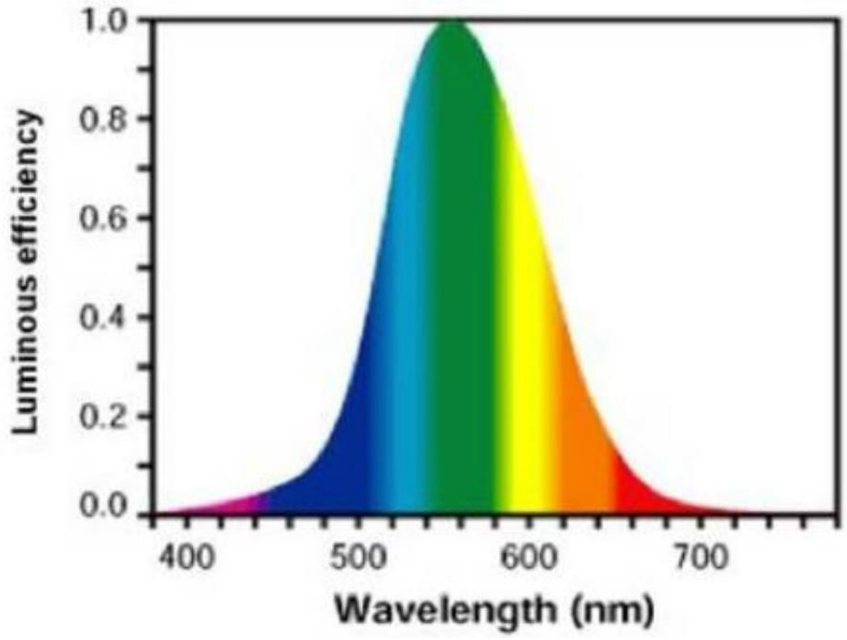

Fig. 1.2 The response of a typical human eye to light, as standardized by the CIE in 1924.

1.3.3 Lifetime (hrs)

The lifetime of a lighting source indicate how long it takes for a certain percentage of light bulbs to fail and is measured in hours. There are numerous factors that determine the life of any bulb. It depends on the application as well as the environment in which it is used. Incandescent bulbs or florescent lights burn out over time. LEDs are the longest-lasting light bulbs. In LED lighting lumen depreciation (slowly dimming overtime due to the heating at the junction) occurs. The lifetime of LEDs is defined as the time it takes until its light output reaches 70% of its initial output. The lifetimes of various lighting sources are given in Table 1.1 (Khan *et al*. 2011).

Table 1.1 Efficacy, efficiency and lifetime of various light sources.

Light Source	Incandescent	Halogen	Fluorescent	Metal halide	White LED
Efficacy (lm/W)	7-20	15-20	50-100	80-110	90-120
Efficiency (%)	1.9-2.6	8-11	9-15	9-14	20-22
Lifetime (hrs)	750-2000	2000-4000	9000-20000	5000-20000	50000+

1.3.4 Correlated color temperature (CCT)

The color of light can be calculated theoretically, but light can also have a certain feel. Light can feel warm or cool and is quantified with correlated color temperature (CCT). The CCT is the temperature of an ideal black body radiator that has the same color as that of the light source (Kaufman *et al*. 1972). Materials which are heated to temperatures of ~1500 K may appear "warm". When the temperature increases to ~6000 K, the material has less color hue and appears white. These materials appear "cool" or blue at temperatures of ~9000 K, The CCT scale is shown in Fig. 1.3 (http://www.smartenergy.company). The cooler light appears blue is beneficial for studying or working, but warmer light seems more relaxing making them preferred in many homes. Typical CCT of the white region range between 2500 and 10000 K and lamps with a CCT rating below 3200 K are considered as "warm" sources, while those with a CCT above 4000 K are considered "cool" in appearance as shown in Fig. 1.3. CCT for warm white-emitting LEDs is in between 3500-4000 K and for cool white-emitting LED, near 6000-6500K. CCT of various light sources are listed in Table 1.2 (http://en.wikipedia.org/wiki/Color_temperature).

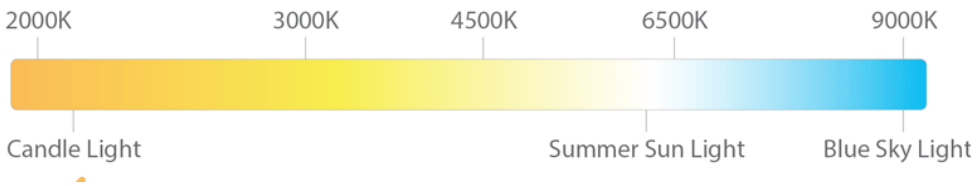

Fig. 1.3 Correlated color temperature scale.

Table 1.2 CCT of various light sources

Source	Temperature
Match flame	1,700 K
Candle flame, sunset/sunrise	1,850 K
Incandescent lamps	2,700-3,300 K
Soft White compact fluorescent lamps	3,000 K
Studio lamps, photofloods,	3,200 K
Moonlight, Xenon arc lamp	4,100-4,150 K
Horizon daylight	5,000 K
Compact fluorescent lamps (CFL)	5,000 K
Vertical daylight, electronic flash	5,500-6,000 K
Daylight, overcast	6,500 K
Liquid crystal display (LCD) screen	5,500-10,500 K
Clear blue pole ward sky	15,000-27,000 K

1.3.5 Colour Rendering Index (CRI)

The colour rendering index (CRI) is introduced to quantitatively measure the ability of a light source to reproduce the colors of various objects faithfully in comparison with an ideal or natural light source and has been in wide use in the lighting industry for many years. It is defined by the CIE as 'effect of an illuminant on the colour appearance of various objects by conscious or subconscious comparison with their colour appearance under a standard illuminant'. CRI is scored on a scale of 0-100, where 100 is equivalent to natural light. It is calculated by comparing the colour difference between the reflection spectra of the selected test colors attained by the irradiation of the given light source and the reflection spectra when irradiated by a black-body radiator. The smaller the difference in chromaticities, the better will be the CRI. A light source with CRI greater than 90 can be considered good in color rendering. So a line emitter with single emission line has a CRI of 0 since not all colors could be displayed under such a light source. It is worth noting that the perceived colors under reference light sources vary for different colour temperatures (Table 1.3) (Jones, 2001).

Table 1.3 Color rendering index of various light sources

Light Source	CRI
Daylight	100
Incandescent/halogen bulb	100
Cool White fluorescent	57
Warm White fluorescent	51
Cool White Deluxe	89
Warm White Deluxe	73
Metal Halide	85
Clear Mercury Vapor	18
Coated Mercury Vapor	49
High Pressure Sodium	24

1.3.6 CIE Colour Coordinates

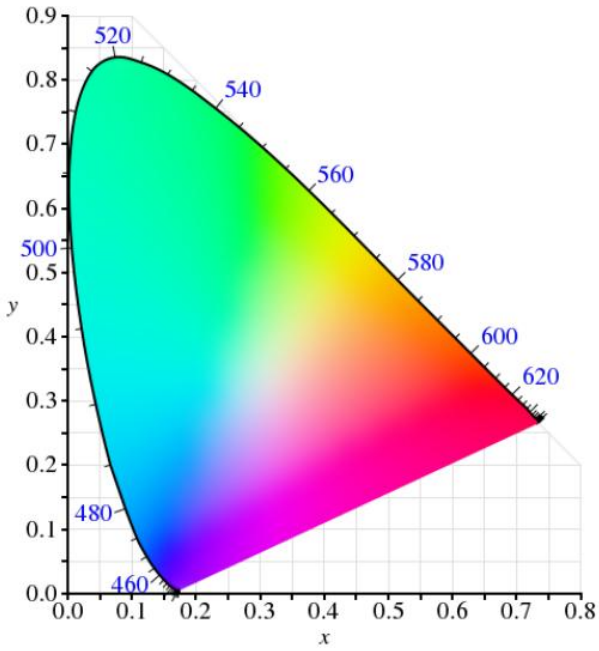

Fig. 1.4 1931 CIE chromaticity coordinate diagram

To study color perception, one of the first mathematically defined color spaces is the International Commission on Illumination (CIE) 1931 *XYZ* color space, created by the CIE in 1931. CIE XYZ color space was derived by William David Wright and John Guild. A color space is a three dimensional space; color is specified by a set of three

numbers (the CIE coordinates *X*, *Y*, and *Z* or hue, colorfulness, and luminance) which specify the color and brightness of a particular homogeneous visual stimulus (Stevens *et al*. 1969). Artificial colors, denoted by X, Y, Z, are called tristimulus values, can be added to produce real spectral colors. By a piece of mathematic legerdemain, it is necessary only to quote the quantity of two of the reference stimuli to define a color since the three quantities (x, y, z) are made always to sum to 1. The x, y, z, i.e. the ratios of X, Y, Z of the light to the sum of the three tristimulus values, are the so-called chromaticity coordinates. The standard CIE *XYZ* color space projects directly to the corresponding chromaticity space specified by the two chromaticity coordinates known as x and y, called chromaticity coordinates creating the familiar chromaticity diagram shown in the Fig. 1.4 (Smith *et al*. 1931). According to the chromaticity diagram, the CIE color coordinates of primary colors red, blue and green are represented as (0.67, 0.33), (0.14, 0.08), (0.21, 0.71) respectively. The CIE color coordinate of pure white is (0.33, 0.33).

1.4 Strategies for solid-state white lighting

For LEDs to be used for white light generation, excellent color rendering and luminous efficacy must be taken into account. However, there is a trade-off between the two criteria for white light since color rendering is best achieved by a broadband spectra distributed throughout the visible region, while the efficacy is best achieved by a monochromatic radiation at 555 nm (green) where the human eye sensitivity is maximum. Generally, there are three principal strategies used for generating white light based on LEDs for high quality lighting application. Fig. 1.5 shows the schematics of three kinds of approaches for white light generation (Moreno *et al*. 2007).

RGB LED approach:

The most common method used to generate white light is by mixing differently colored lights red, green, and blue (RGB). The luminous efficacy of white-light generated by this approach, using currently available LEDs is around 120lm/W but has very low color rendering. Despite of the great advantages such as excellent versatility and larger efficacies, there are potential problems with this approach. LED chips that

emit at different wavelengths have a different light intensity response to changes in voltage and hence the task of color-tuning of individual diodes is likely to be difficult. Moreover, since these LEDs are subject to significant changes in color and intensity with variations in temperature, which have detrimental effects on the quality of white light. However, the color temperature of a multi-LED device is tunable by varying the power of individual LED components, which needs additional circuitry, adding cost and complexity. Another problem is the variation in operating life of different color LEDs. This effect becomes a serious challenge for this approach where the white-light color rendering is critically dependent on the relative intensities of the separate red, green, and blue colors. Finally, these white light sources are relatively expensive since multiple LED chips are necessary to produce a single source of white light.

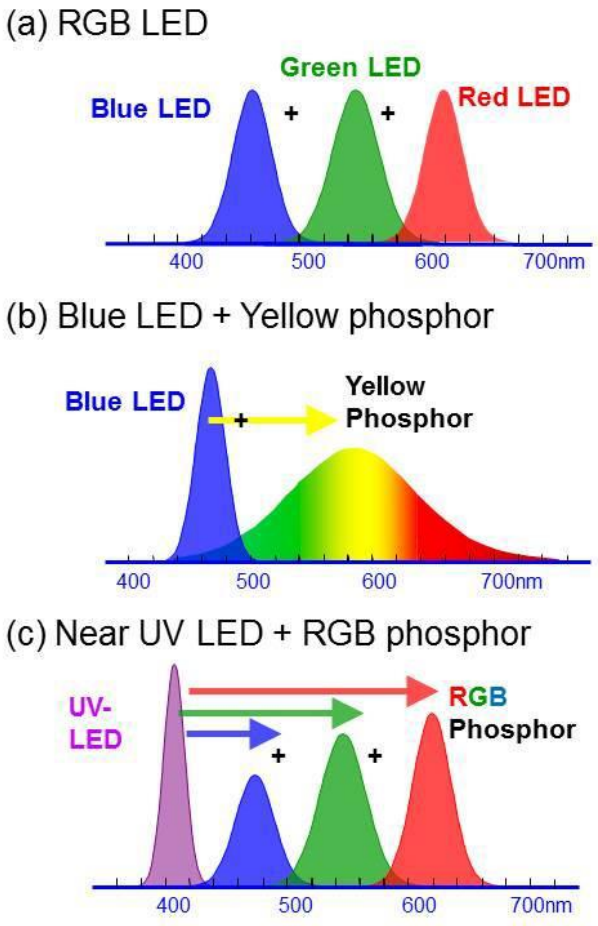

Fig. 1.5 Three types of white LED approaches

Blue LED chip and Yellow Phosphor:

An alternative and commercialized method for generating white-light involves the use of a blue LED chip and a yellow emitting phosphor. Commercially available white LEDs consist of a blue InGaN LED chip covered with a YAG:Ce^{3+} yellow phosphor. The InGaN LED emits blue light at a peak wavelength of about 460 nm, which excites the YAG:Ce^{3+} phosphor to emit yellow light. The combination of the blue light emitted by the LED and the yellow light from the phosphor results in white light. However, there are several significant problems with this approach. The light output is not uniform as blue light escapes and observed at the edges of the diode. Also, there is a significant gap between 450-550 nm where emission intensity is considerably lower than that in other spectral region, the CRI value is low. The deterioration of the chip or YAG:Ce phosphors would cause some significant color changes. So, if warm white light is desired, such as for residential applications, this method may not suffice. In addition, the manufacturing steps are complicated as uniformity of the powder mixture is difficult to achieve in the epoxy. However, these white light emitting LEDs are used for a variety of applications such as household lighting, warehouse and factory floor lighting, street lighting, backlights for laptops and cell phones, and automotive lighting. The phosphor converted blue LED device is currently the most common solid-state white lighting device produced today, despite the limitation of relatively poor color rendering (CRI < 80) and high color temperatures (>4,000 K).

UV LED and RGB Phosphor:

Another approach to generate white light uses a near-UV (nUV) LED source to excite a white light emitting single phased phosphor or RGB tricolor phosphor. Here the UV light is absorbed by the phosphor and the output appears white. But, the quantum deficit between UV pump and the phosphor dissipate significant energy, makes this approach inherently less efficient. Also, the reabsorption of emission by the phosphors, adding a loss mechanism and decreases the efficiency of the system. However, this approach has some advantages compared to blue LED method. The UV LED and multiple phosphors can cover a broad range of emission wavelengths, giving good color

rendering and stable light color output at different drive currents. Hence, emission spectrum can be more stable with respect to driving current and temperatures of the LED chip. Also the electrical to optical conversion is more efficient in UV than in blue LEDs, yielding efficient design. In this method, the spectral shifts of pumping LEDs do not change the emission intensity of the phosphors. But in the case of blue LED, the shift in the emission spectrum of the LED will induce a color shift of the white LEDs. Therefore, It is considered that UV LEDs might be the direction of SSL development for their high efficiency and easy fabrication.

In general, phosphors are vital to the development of white LED lighting and backlight display industry. Highly efficient and emission-tunable phosphors can enhance the energy efficiencies of WLEDs due to their potential advantages in color rendering index, correlated color temperature and color gamut. Therefore, novel and efficient fluorescent materials for improving the performance of solid state lighting must be developed.

1.5 Phosphors – an overview

Phosphors are solid luminescent materials that emit photons when excited by an external energy source, such as an electron beam or ultraviolet light or any wavelength of light in the electromagnetic spectrum. The role of phosphor is to convert the radiation energy into visible or infrared light (Feldmann *et al*. 2003). Phosphors usually consist of an inert host lattice, which is transparent to the excitation radiation and an activator, typically a 3d or 4f electron metal, which is excited under energy bombardment. The relevant hosts for phosphors are oxides, nitrides, fluorides, vanadates, silicates, molybdates, tungstates, phosphates and sulphides etc. The absorption of energy, which is used to excite the phosphor material, takes place by either the host lattice or by the activator itself. In most cases, the emission originates from the impurity ions, when they are excited by an external energy source (Nalwa *et al*. 2003). If the activator ions show too weak absorption, another kind of impurity ions known as the sensitizers can be added. The sensitizers absorb the energy and subsequently transfer the excitation energy to the activator. This process involves

transport of energy through the luminescent materials. The most commonly used activators are Eu^{3+}/Eu^{2+}, Ce^{3+}, Tb^{3+}, Gd^{3+}, Yb^{3+}, Dy^{3+}, Sm^{3+}, Tm^{3+}, Er^{3+}, Nd^{3+} etc. The emission color can be adjusted by choosing proper activator ion, without changing the host lattice.

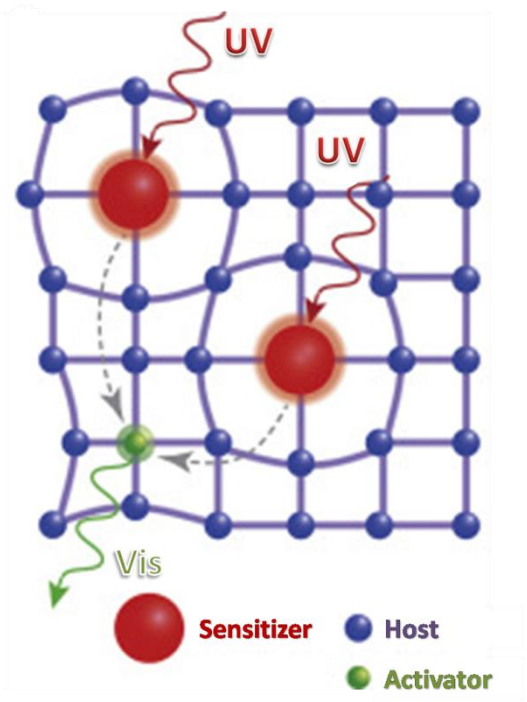

Fig. 1.6 Schematic representation of a typical phosphor material

The sequences of processes that occur within a phosphor material include absorption of energy by the activator ion, relaxation and subsequent emission of a photon and return to the ground state. The efficiency of a phosphor material depends on the amount of relaxation that take place during the excitation and emission. Relaxation is the process in which energy lost to the lattice as heat needs to be minimized in order to extract the highest possible luminous efficiency. The basic processes involved in the phenomenon of characteristic luminescence of a phosphor material are shown in Fig. 1.6.

1.6. Basic Mechanism of Phosphors

1.6.1 Phosphorescence

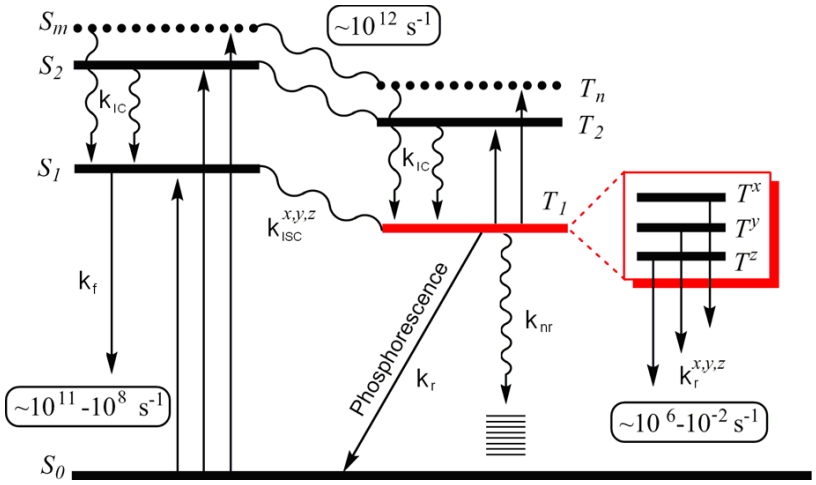

Fig. 1.7 Modified Jablonski diagram for the main photophysical processes in molecular systems

Phosphors work on the principle of phosphorescence which is a form of delayed luminescence that corresponds to the radiative decay of the molecular triplet state. Phosphorescence is the simplest physical process which involves spin-forbidden transformation with a characteristic spin selectivity and magnetic field dependence. It refers to triplet → singlet transitions in stable molecules having longer lifetime >10^{-5} seconds. The electronic states of a molecule and the transitions between them are illustrated in the Jablonski diagram given in Fig. 1.7 (Baryshnikov *et al*. 2017). As can be seen from the figure, the lowest-lying triplet state (T_1) can be populated through the following series of processes: the $S_0 \rightarrow S_m$ absorption induced by the incident UV light and followed by a fast internal conversion; (i) fluorescence occurs from the lowest S_1 state (ii) nonradiative direct $S_1 \sim T_1$ intersystem crossing produces a T_1 state population and (iii) the intersystem crossing between the highest S_m and T_n states with the subsequent T_n-T_1 internal conversion that in some cases also can lead to the phosphorescent state. However, after the population of T_1 state, the nonradiative $T_1 \sim S_0$ relaxation takes place effectively with the T_1-S_0 phosphorescence radiation. But, the $T_1 \rightarrow S_0$ transition is spin forbidden which renders the phosphorescence process to be usually much less intense compared with the spin-allowed fluorescence emission. An important feature of the T_1 state is that it consists of three spin sublevels. Since the triplet-singlet transitions are forbidden, the absorbed radiation may be re-emitted

during several seconds or even minutes after the original excitation by light. At the same time, the nonradiative intersystem crossing ($S_1 \sim T_1$) is usually observed in the nanosecond scale due to the small S_1-T_1 energy gap. So, the kinetics of the spin-forbidden relaxation depends on the T-S band gap (ΔE_{TS}).

Based on the electronic transitions, the principal localized luminescent centers can be classified as follows (Shionoya *et al*. 2006):

(i) $1s \leftrightarrow 2p$ (e.g. F center)

(ii) $ns^2 \leftrightarrow nsnp$ (e.g. Ga^+, In^+, Tl^+, Ge^{2+}, Sn^{2+}, Pb^{2+}, As^{3+}, Sb^{3+}, Bi^{3+}, Cu^-, Ag^-, Au^-)

(iii) $nd^{10} \leftrightarrow nd^9(n + 1)s$ (e.g. Cu^+, Ag^+ and Au^+)

(iv) $3d^n \leftrightarrow 3d^n$, $4d^n \leftrightarrow 4d^n$ (e.g. first and second transition metal ions)

(v) $4f^n \leftrightarrow 4f^n$, $5f^n \leftrightarrow 5f^n$ (e.g. rare-earth and actinide ions)

(vi) $4f^n \leftrightarrow 4f^{n-1}5d$ (e.g. Ce^{3+}, Sm^{2+}, Eu^{2+}, Tm^{2+} and Yb^{2+})

(vii) A charge transfer transition i.e., a transition between an anion p electron and an empty cation orbital (e.g. intramolecular transitions in complexes such as VO_4^{3-}, MoO_4^{2-} and WO_4^{2-})

Rare-earth and transition metal ions are the commonly used activators in phosphors. The 4f-4f transitions of rare-earth ions are line-shaped, while 4f-5d transitions of RE ions and d-d transitions of TM ions are broadband shaped and can be adjusted by varying the coordination environment.

1.6.2 Energy Transfer (ET)

In pc-WLEDs, energy transfer between ions plays an important role. The center which absorbs radiation in a phosphor is called sensitizer (S) and the center to which energy is transferred is called activator (A) which could emit light and terminate the whole process. Energy transfer may occur, if the energy difference between the ground and excited state of the sensitizer is equal to that of the activator and there exists a

suitable interaction between systems. Four basic mechanisms involved in ET processes between ions:

(i) S luminescence itself, thus acting as an activator

(ii) S returns non-radiatively to the ground state dissipating heat to the lattice

(iii) S transfer the excitation energy to A followed by emission from A or radiationless transition to the ground state

(iv) cross-relaxation (S transfers its energy to another center S)

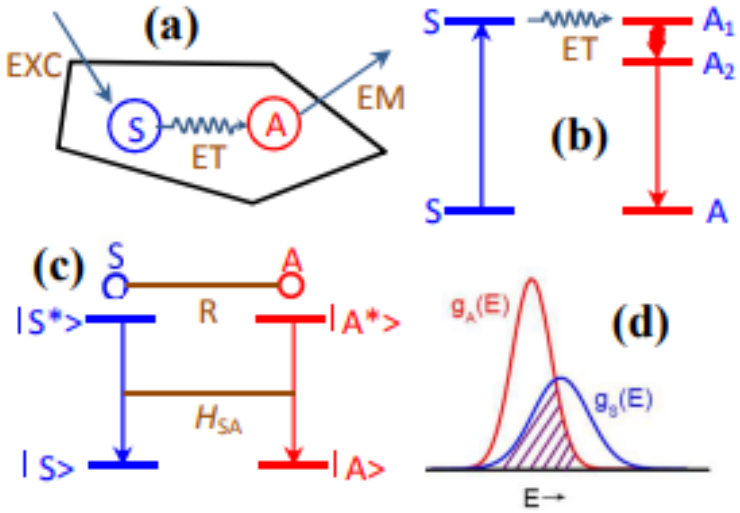

Fig. 1.8 Schematic illustration of different energy transfer processes between sensitizer and activator ions.

The different ET processes between two ions is schematically represented in Fig. 1.8 (Li *et al*. 2016). The efficiency of radiative transfer depends on how efficiently the activator fluorescence is excited by the sensitizer emission. For that, it requires a significant spectral overlap between the emission spectrum of the sensitizer and the absorption spectrum of the activator (Liu *et al*. 2005). If radiative energy transfer takes place predominantly, the decay time of sensitizer fluorescence does not change with the activator concentration. In contrast to the radiative ET, the nonradiative ET accompanies a significant decrease in decay time of sensitizer fluorescence with the

activator concentration. For a considerable absorption capability of activator, the radiative ET can usually be neglected relative to nonradiative ET in most inorganic systems. Only in a few cases, the requirements for radiative ET are satisfied (Nalwa *et al*. 2003). If the difference between the ground and excited state of sensitizer and the activator is large, non-resonant ET can also take place with the assistance of a phonon. For the electrostatic interaction, it appears to be multipole interaction. According to the transition characteristic of sensitizer and the activator, this can be classified as dipole-dipole (d-d) interaction, dipole-quadrupole (d-q) interaction, quadrupole-quadrupole (q-q) interaction.

Cross-relaxation includes all types of down conversion energy between identical ions. The excitation existing in an ion can migrate to another ion of the same species in the ground state by the resonant energy transfer when they are located close to each other. This energy migration processes increases the probability that the optical excitation is trapped at defects or impurity sites, enhancing the nonradiative relaxation. It causes concentration quenching because an increase in the activator concentration encourages such nonradiative processes. Consequently, the excitation energy diffuses from ion to ion before it is trapped and leads to emission.

1.7 Selection criteria of phosphors

As discussed, phosphors play a vital role in determining the optical properties of white LEDs such as spectral distribution, luminous efficacy, color rendering, color temperature and lifetime. To pursue better performance of solid state lighting devices, the down conversion luminescent materials must be carefully chosen to meet the requirements for different applications (Xie *et al*. 2011). The basic requirements of a phosphor material for practical applications are described in the following.

(1) Strong Absorption of the LED Light

Phosphor should have strong absorption of the emissions from UV (350-410 nm) or blue (440-480 nm) LEDs which are the primary light source to excite the phosphors. A stronger absorption means large number of photons can be involved in

the sequential luminescence process, which is beneficial to improve the luminescence efficiency of phosphors. Also, it should not significantly absorb the emission from other down converters in the blend.

(2) Suitable Emission Spectrum

The optical properties of WLEDs depend on the position and shape of the emission spectrum, such as peak and dominant emission wavelengths and full width half maximum (*fwhm*). For general lighting, phosphors with much broader emission spectra are desired to achieve high color rendering indices, whereas for backlighting the phosphors should have narrow emission bands to attain wide color gamut. However, in both cases there are inevitable trade-offs between luminous efficacy and color rendering, making it extremely important to specially tackle the selection of phosphors with suitable emission spectra.

(3) High Quantum Efficiency

The quantum efficiency is a measure of the ability of a phosphor to convert the absorbed photons into luminescence, and higher efficiency indicates less energy loss during the luminescence process. The quantum efficiency is greatly affected by the composition, microstructure, defects, and impurities of luminescent materials.

(4) High Quantum Yield

Phosphors materials possessing 90-95% quantum yield values are ideal for solid state lighting applications.

(5) High Luminous Efficacy of Radiation

The phosphors must produce light to which the human eye is sensitive; even a very high quantum yield is not useful if the eye is insensitive to that radiation.

(6) High Thermal Stability

Thermal stability of phosphor depends on the crystal structure, structural rigidity, chemical composition, and surface state of phosphor materials. The phosphors

should have high thermal stability to maintain the brightness and color coordinates of WLEDs.

(7) High Chemical Stability

The phosphor materials should be stable for handling, storage, and usage under the ambient atmosphere and should not chemically react with CO, CO_2, H_2O, air, etc. Phosphors that are fully oxidized are normally very stable under ambient conditions.

(8) Photostability

The phosphors must retain their quantum yield and other spectral properties under continuous irradiation with high power LEDs which is very important to be used in high power and high-brightness SSL.

(9) High CRI and low CCT

Phosphors should have CRI~85 and CCT~3000K for warm white emission.

(10) Long lifetime

The phosphors must have a suitable lifetime (>30000h) under the high excitation fluences in SSL applications.

1.8 Current status of the red phosphors

Today's commercial pc-WLEDs normally use a 450-470 nm blue GaN LED chip covered by a yellow phosphor, YAG: Ce^{3+}. The $5d^1 \rightarrow 4f^1$ emission of Ce^{3+} in this host exhibits a broad band with maximum intensity at 520 nm. Extensive research in the field of developing novel and stable phosphors for pc-WLEDs was carried out by many research groups concerning the combination of this yellow emission with blue light from an LED in order to produce white light. However, they suffer from some weaknesses, such as poor color rendering index and low stability of color temperature. The color rendering index of white LEDs made by blue LED with yellow emitting phosphor method is low due to the deficiency of red light component. These drawbacks make it inappropriate for applications in indoor lighting and full colour displays.

Therefore, numerous efforts have been made to search for new phosphors that can emit suitable red light for inclusion with the blue LED-YAG: Ce^{3+} combination.

The relevant hosts for red phosphors are fluorides, nitrides, borates, phosphates, oxides, vanadates, silicates, molybdates, tungstates and sulphides. The luminescence centres for red phosphors in WLEDs may be either rare earth activated or non-rare-earth activated ones. The commonly used rare-earth activators which provide red emission are Eu^{2+}, Eu^{3+}, Pr^{3+} and Sm^{3+}. However, the luminescence of these activators is greatly influenced by the host lattice and some exhibits weak absorption in the near-UV region. Therefore, tuning of red emission color has been realized in Bi^{3+}/Eu^{3+}, Tb^{3+}/Eu^{3+} and $Ce^{3+}/Tb^{3+}/Eu^{3+}$ co-doped systems (Wen *et al*. 2015; Zhang *et al*. 2014; Xie *et al*. 2015). In addition to this, non rare-earth activated phosphors are of current interest. Among them, Mn^{2+} /Mn^{4+} doped materials attract recent attention (Zhou *et al*. 2015).

To improve the deficiency of the red emission component in WLEDs, extra red emission is required either from other chips or from co-fabricated phosphors. Zhou et al. reported that the addition of $BaGeF_6$:Mn^{4+} is favorable for improving both the CRI and CCT value of YAG: Ce^{3+}-based WLEDs. Another type of WLED is based upon the co-fabrication with Eu^{2+}-activated phosphors (Xie *et al*. 2013; Pust *et al*. 2014). By incorporating $Sr(LiAl_3N_4):Eu^{2+}$ as a red component, the LED lamp can provide excellent white emission with low CCT (2700 K), high CRI (91%) and satisfactory lumen equivalent (282 lm/W). In near UV LED method, $Y_2O_2S:Eu^{3+}$ for red, ZnS: Cu^{2+}, Al^{3+} for green and $BaMgAl_{10}O_{17}$: Eu^{2+} for blue are used. But the current red phosphor cannot absorb light efficiently in the UV region and its brightness is about eight times less than that of the available green and blue phosphors. Also the sulfide based red phosphors lacks chemical stability and is highly harmful to the environment. Other major red phosphors in today's market also fall in the sulfide family. Thus novel red phosphor materials that could be effectively excited in the near UV and visible region with good optical properties and preferably with low cost should be developed to meet the requirements.

1.9 Rare-earth activated phosphors

Rare-earth elements are a set of 17 chemical elements in the periodic table, the lanthanides along with the transition metals scandium and yttrium, which are highly recognized for their versatile applications (Bunzli *et al*. 2005). Particularly, there has been a steady increase in the theoretical and experimental studies of lanthanide-activated inorganic phosphors over the past decade, mainly due to an ever increasing demand for photoluminescence and related applications, including lighting, electronic display, lasing, anti counterfeiting, biological labeling, and imaging. The rare earth ions are characterized by their deep lying 4f shells which are not entirely filled. The electrons in the 4f orbitals are shielded by the outer electrons shells, so they give rise to discrete energy levels. This feature is in strong contrast with transition metal ions, whose 3d electrons, located in an outer orbit are heavily affected by the environmental or crystal field. The electronic configurations of the lanthanide ions are [Xe] $4f^n5d^0$ and [Xe] $4f^{n-1}5d^1$. As the number of electrons increases, the number of possible states also increases. The possible energy bands fall into two groups. In the first group one of the 4f electrons is raised to the higher 5d level: $4f \rightarrow 4f^{n-1}5d$. This 5d level can be strongly influenced by the host lattice. In the second group one of the electrons of the surrounding anions is promoted to the 4f orbital of the RE^{3+} ion (charge transfer state). Obviously the position of this energy band depends on the surrounding ions. Thus the energy levels of lanthanides may be divided into three categories: 4f-4f transitions, 4f - 5d transitions, and charge-transfer state transitions.

4f - 4f transitions

4f-4f transitions are due to the electronic transitions inside the 4f shell. These transitions are very important in most of the practical phosphors containing rare earth activator ions since they involve movements of electrons between the different energy levels of the 4f orbitals of the same lanthanide ion. They are not accompanied by a change in electronic configuration and are called intra-configurational transitions. However, these 4f-4f electric dipole transitions are forbidden by the selection rule. In practice they are generally observed, but the corresponding emission bands are usually

narrow because the 4f electrons are shielded by filled by the 5s and 5p orbitals, which have a higher energy than the 4f shell. The lifetime of these weak transitions mostly lie in the range of milliseconds.

4f - 5d transitions

In this transition, one of the 4f electrons is raised to the higher 5d orbital denoted as $4f^n$ - $4f^{n-1}5d$ and is typically observed in Ce^{3+} ions ($4f^1$ configuration). Since empty, half filled or completely filled electron shell configurations are the most stable ones, the excess 4f electron of Ce^{3+} is easily transferred to the 5d orbital. Since 4f-5d transitions are parity allowed and spin selection is not appropriate, the emission transition is a fully allowed which results in strong and broad absorption cross-sections. The divalent rare earth ions (Sm^{2+}, Eu^{2+} and Yb^{2+}) also exhibit this transition.

Charge - transfer state (CTS) transitions

The last possible excitation mechanism is the charge-transfer state (CTS) transition, in which 2p electrons from the surrounding anions (e.g. O^{2-} in oxides) are promoted to a 4f shell. This is usually observed in Eu^{3+} ($4f^6$) which need an additional electron to reach the half filled configuration, which is relatively stable compared to the parity filled configurations. These transitions are parity allowed and result in broad and intense absorptions band known as charge transfer band. This band depends on the particle size of the host and environment around the RE ions.

1.9.1 Selection Rules

Selection rules determine whether an electronic transition is allowed or not. The electronic transition occurs through the multipolar interaction of the radiation with the material. The strongest interaction occurs through the electric dipole moment operator of the radiation, but weaker interactions are through the magnetic dipole moment or electric quadrupole moment operators. The ^SL_J selection rules from Judd-Ofelt theory for $4f^N$-$4f^N$ transitions and for $4f^N$-$4f^{N-1}5d$ transitions are listed in Table 1.4 (Tanner 2013). If the transition is allowed according to selection rules it can be strong, but in some cases it may be too weak. If the transition is forbidden by one mechanism it may

still be observed through another weaker mechanism. Judd-Ofelt theory gives rise to less restrictive selection rules to account for the presence of forbidden transitions which may be experimentally weakly observed (e.g. $^5D_0$-$^7F_0$, $^7F_3$, $^7F_5$ transitions of Eu^{3+}), by incorporating higher order mechanisms.

Table 1.4 ^SL_J selection rules for electronic transitions of lanthanide ions

Type of transition	**^SL_J selection rules**	**Approximate order of magnitude of oscillator strength**
Electric dipole (ED) $4f^N$-$4f^{N-1}5d$ (parity change)	$\Delta S = 0$; $\lvert\Delta L\rvert \leq 1$; $\lvert\Delta J\rvert \leq 1$; $J = 0 \leftrightarrow J' = 0$ and $L = 0 \leftrightarrow L' = 0$ are forbidden.	~0.01–1
Judd forced (induced) ED $4f^N$–$4f^N$ (no change in parity)	$\Delta S = 0$; $\lvert\Delta L\rvert \leq 6$; if $L = 0$ or $L' = 0$, $\lvert\Delta L\rvert = 2, 4, 6$; $\lvert\Delta J\rvert \leq 6$; if $J = 0$ or $J' = 0$, $\lvert\Delta J\rvert = 2, 4, 6$. This implies that $J = 0 \leftrightarrow J' = 0$ and $L = 0 \leftrightarrow L' = 0$ are forbidden.	~10^{-4} of ED
Magnetic dipole (MD) $4f^N$-$4f^N$	$\Delta S = 0$; $\Delta L = 0$; $\lvert\Delta J\rvert \leq 1$; $J = 0 \leftrightarrow J' = 0$ is forbidden	~10^{-6} of ED
Electric quadrupole (EQ) $4f^N$–$4f^N$	$\Delta S = 0$; $\lvert\Delta L\rvert \leq 2$; $\lvert\Delta J\rvert \leq 2$; $J = 0 \leftrightarrow J' = 0, 1$ and $L = 0 \leftrightarrow L' = 0, 1$ are forbidden	~10^{-10} of ED
One phonon ED vibronic $4f^N$–$4f^N$	The same as forced (induced) ED.	~10^{-7} - 10^{-11} of ED

1.10 Luminescence properties of Eu^{3+} ions

Eu^{3+} ion has six electrons in the 4f shell and the corresponding energy level diagram is shown in Fig. 1.9. Among the rare earth ions, Eu^{3+} ion has a simple energy level scheme and the transitions are hypersensitive, i.e., they depend strongly on the chemical surroundings. Intense red emissions of Eu^{3+} ions are due to the intraconfigurational f-f transitions. Eu^{3+} emission line usually consists of narrow lines in the red spectral range due to the transition from the $^5D_0$ level to the ^7F_J (J = 0-6) levels of $4f^6$ configuration of Eu^{3+} ions. The probability of electronic transitions from the lowest $^5D_0$ excited state to the $^7F_{0\text{-}6}$ ground states differs depending on site symmetries. Due to non-degenerated ground ($^7F_0$) and excited ($^5D_0$) states together with non-overlapping $^{2S+1}L_J$ multiplets that give emission spectra with clear dependence on the host material structure and site symmetry. According to Judd-Ofelt theory, the electronic transitions from the Eu^{3+} $^5D_0$ state to low-lying levels with J = 0, 3, or 5 are both electric-dipole (ED) and magnetic-dipole (MD) forbidden.

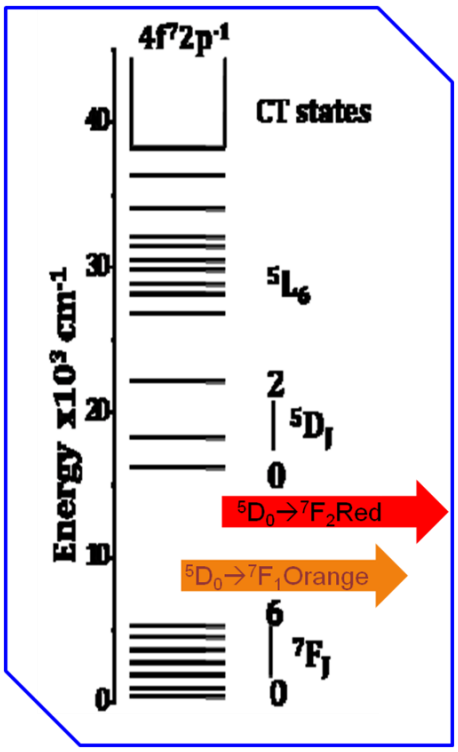

Fig. 1.9 Energy level diagram of Eu^{3+} ion

The luminescence of Eu^{3+} ions is determined greatly by the site symmetry and the strength of crystal field at the RE ion site. When Eu^{3+} is located at a low symmetry site, the hypersensitive forced electric dipole $^5D_0 \rightarrow {}^7F_2$ transition dominates over the allowed $^5D_0 \rightarrow {}^7F_1$ transition. In practical inorganic luminescent materials, both electric dipole and magnetic dipole transitions appear simultaneously, although their intensities are different, and in most cases, one of them is much stronger. Therefore, the asymmetric ratio reveals the distortion grade from the inversion symmetry of the local environment in the vicinity of Eu^{3+}in the host matrix (Du *et al*. 2011). The splitting of these transitions gives an insight into the crystal field effect at the activator sites. The appearance of $^5D_0 \rightarrow {}^7F_0$ transition of Eu^{3+} is an indication of lowering of Eu^{3+}crystal site symmetry as it is allowed only for Cs, Cn, Cnv site symmetries and shows a red shift with the increase in covalency of Eu^{3+}. The failure of Judd–Ofelt theory in the $^5D_0 \rightarrow {}^7F_0$ transition of Eu^{3+} is due to the mixing of two different states with different J values. The $^5D_0$ and $^7F_0$ levels are non-degenerate and the spectra associated with transitions between them should reflect the crystal-field (CF) splitting of the nominal ^7F_J (or $^{2S+1}L_J$) levels that depend on site symmetry. Further, the site-to-site variation in the local structure around Eu^{3+} will result in the broadening of $^5D_0 \rightarrow {}^7F_0$ transition. Hence Eu^{3+} ions are usually employed as an optical probe to investigate the coordination and environment around the cations substituted in the crystalline lattice.

Chapter 2

STRUCTURAL ASPECTS AND LITERATURE REVIEW OF RED PHOSPHORS IN THE PRESENT WORK

Eu^{3+} luminescence in various host lattices depend on crystal structure, local coordination environment, structural distortion, ordering, and disordering. In this context, an attempt has been made to manipulate the Eu^{3+} luminescence through suitable modifications of the host lattice. Some of the recent research works related to the luminescence properties of Eu^{3+} ions in pyrochlores, displaced pyrochlores and fergusonite type structure are discussed in this chapter. Finally, the motivation of the present research work is highlighted.

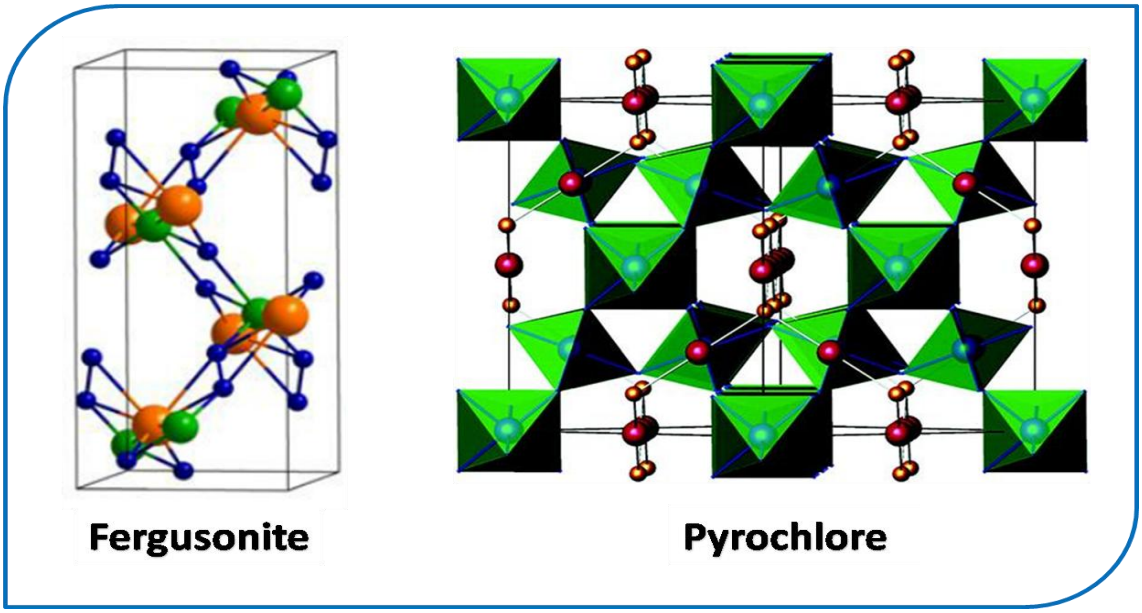

2. 1 Introduction

The research on red phosphors for WLEDs is still one of the hottest topics in solid state chemistry and materials science. The photoluminescence-controlling strategy for matching phosphors in LED applications includes: selection of crystal structures, modification of the chemical composition and coupling of activator to the host lattice and energy transfer process. The photoluminescence properties of Eu^{3+} activated phosphor depends on crystal structure, local coordination environment, covalence, structural distortion, structural ordering, and disordering. Hence, it is possible to tailor the luminescence properties of Eu^{3+} ions by controlling the local structure/coordination environment via substitutions and surface engineering. Exploration of suitable crystal structure will be the first step in the design of suitable red phosphors. The f-f transition of Eu^{3+} ions can be modified by different crystal field strength, so that emission can be tuned over a wide range in the visible light region. So, modification of chemical composition via cationic or anionic substitution can lead to the red shift of the emission peaks due to crystal field effect. Keeping all these facts in mind, a series of pyrochlore, displaced pyrochlore and fergusonite type Eu^{3+}-activated red phosphors were developed in the present work. Literatures on various pyrochlore and fergusonite type red phosphors were reviewed in this chapter.

2.2 Pyrochlore crystal structure

Pyrochlore oxides have attracted extensive attention as a host lattice for inorganic phosphors due to their unique properties such as high chemical stability, lattice stiffness, thermal stability, ability to incorporate a diverse range of elements at the A and B sites and to tolerate both cation and anion disorder etc. The pyrochlore structure is one of the oxygen- octahedron based families with general formula $A_2B_2O_7$ or $A_2B_2O_6O'$. The pyrochlore is a superstructure of the defect fluorite structure with exactly twice the lattice constant. Ideal fluorite is a simple crystal structure having a general formula AO_2. The A cation is eight coordinated with O^{2-} anions and occupying the tetrahedral holes within the cubic polyhedron. The A cation is located at 4a site and O^{2-} anions at 8c site.

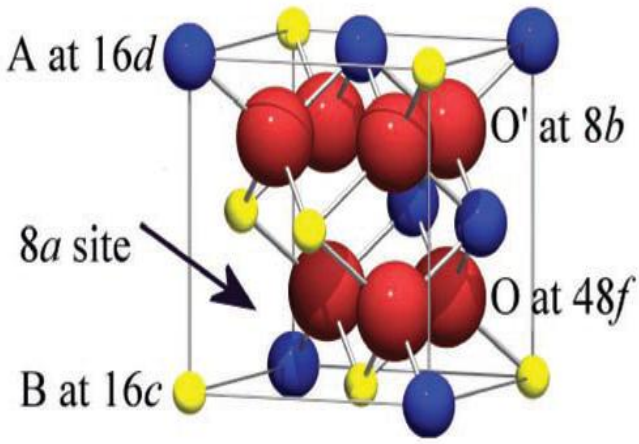

Fig. 2.1 Schematic illustration of one-eighth of a pyrochlore unit cell

The basic framework of the pyrochlore structure is a three dimensional corner sharing MO_6 octahedra, and A and B atoms are located on the 16d (1/2, 1/2, 1/2) and 16c (0, 0, 0) positions respectively. The larger A^{3+} cations in eightfold coordination with O^{2-} ions and smaller B^{4+} cations in sixfold coordination with O^{2-} ions are ordered alternatively in <1 1 0> direction. The oxygen has two distinct sites: the oxygen ions on the 48f (*x*, 1/8, 1/8) site which is bonded tetrahedrally to two A and B cations and the oxygen ions on the 8b (3/8, 1/8, 1/8) sites that are bonded tetrahedrally to four A cations. The third oxygen position is vacant in this structure, which is required to complete the anion arrangement in a fluorite lattice. This vacant anion site occurs at 8a (1/8, 1/8, 1/8). The A cations are located within scalenohedra (distorted cubes), while the B cations are located within trigonal antiprisms. All anions are tetrahedrally coordinated: the 8a anion site is surrounded by four B cations and the 8b anion site by four A cations. The A and B site coordination polyhedra are joined along edges, and the shape of these polyhedra changes as the positional parameter *x* of O_{48f} shifts to accommodate cations of different sizes. These two polyhedra have D_{3d} symmetry. For *x* = 0.3750 the materials have a defect fluorite structure and for *x* = 0.3125, the materials have the ideal pyrochlore structure (Subramanian *et al*. 1983). Thus, the 48f oxygen positional parameter *x* defines the polyhedral distortion and structural deviation from the ideal pyrochlore structure. The extensive compositional range known for pyrochlore compounds reflects the versatility of the A_2O' substructure: defect

pyrochlore form readily since this network can be partially occupied or even completely absent. The pyrochlore structure is therefore highly tailorable e.g., the identities and oxidation state of the B cations, which play a key role in electronic properties, can be controlled by achieving electroneutrality through deliberate choice of the A and O' ions and their concentrations.

The formation and stability of a pyrochlore structure is governed by the relative ionic radii or the ionic radius ratio (r_A/r_B) and the oxygen *x* parameter. Although the A cation must be larger than the B cation there is some variation in the limits of radius ratio values required for the formation of a pyrochlore structures. Typically for the formation of any pyrochlore compound, the ionic radius ratio of the A site cation to the B site must be between 1.46-1.80. Materials whose radius ratio is nearly 1.2 are found to crystallize in defect fluorite structure. In the pyrochlore structure, A_2O' chains weakly interact with the more rigid B_2O_6 network. Therefore, cation or anion vacancies in the A_2O' network of defect pyrochlores do not significantly reduce the stability of the lattice.

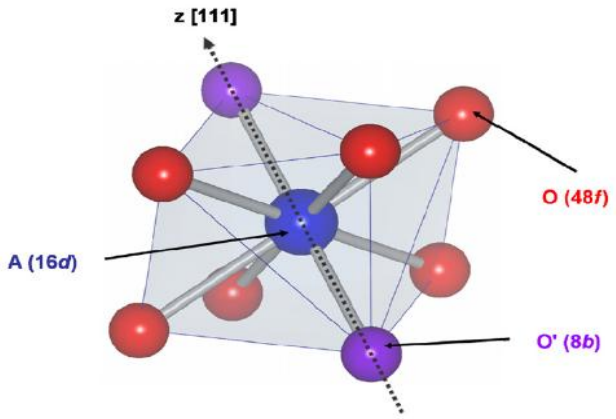

Fig. 2.2 AO_6 scalenohedra in the pyrochlore structure

It is perceived that the size difference between cations on A and B sites is supposed to be the driving force to stabilize the pyrochlore structure. Further interest in this area of pyrochlores is that they have a tendency to order-disorder transformation at elevated temperatures, which can be modified by the incorporation of cations, differing in size or valence from the host cations of the pyrochlore structure.

In most cases, the transitions from ordered pyrochlore to disordered fluorite structure occur by means of temperature, pressure, chemical substitution or high-energy irradiation. Disordering of the cation sites coupled with oxygen disorder on the anion vacancies within the pyrochlore unit cell results in defect fluorite structure. The anion disorder is marked by anions filling the vacant 8b anion site first with anions from the next nearest neighbor 48f site then by anions from the 8a site, while the cation disorder occurs upon the formation of anion vacancies on the 8a site. At that phase, A and B site cations disorder between 16c and 16d sites. The study of pyrochlore to fluorite phase transition requires a lot of attention since it governs the structural properties, which in turn influence the photoluminescence properties.

There are lots of research works related to the luminescence properties of pyrochlore phosphors. In the current study, stannate based pyrochlores have been selected as host lattice due to their interesting electrical, optical and magnetic properties as well as high thermal stability. Some of the research works related to the luminescence of lanthanide stannate pyrochlores are discussed in next section.

2.2.1 Literature review on pyrochlore red phosphors

The crystal field splitting of Eu^{3+} $^7F_1$ level in the pyrochlores $Ln_2Sn_2O_7$ (Ln = La^{3+}, Gd^{3+}, Y^{3+} and Lu^{3+}) and $Ln_2Ti_2O_7$ (Ln = La^{3+}, Gd^{3+}, Y^{3+} and Lu^{3+}) has been systematically examined by A. M. Srivastava. The splitting of the Eu^{3+} $^7F_1$ manifold in these materials increases with increasing size of the rare earth cation. Electrostatic point charge model is inadequate to account for this covalency/ligand polarizability contributions to the crystal field splitting. It was shown that the host lattice dependent changes in the polarizability of the oxygen ions occupying the 48f sites of the pyrochlore lattice is responsible for the variation in the splitting of the Eu^{3+} $^7F_1$ manifold in these materials. The polarization of the O_{48f}^{2-} electron density towards the Eu^{3+} ion is critical in determining the magnitude of the Eu^{3+} $^7F_1$ manifold splitting (Srivastava *et al*. 2009).

Cheng *et al*. synthesized a series of rare earth stannates, $Ln_2Sn_2O_7$ (Ln = Y, La, Pr, Nd, Sm, Eu, Tb, Dy, Ho, Er, Tm, Yb and Lu) via the assistance of a cetyltrimethyl ammonium bromide (CTAB) surfactant. Eu^{3+} activated $Ln_2Sn_2O_7$ nanocrystals emit a

dominating and intense line at 589nm (Cheng *et al*. 2007). It was found that excitation and emission intensity depends on the ionic radii of Ln^{3+} ions. $Y_2Sn_2O_7$:Eu^{3+} nanocrystal exhibits relatively the brightest luminescence.

Rare-earth zirconate $RE_2Zr_2O_7$ nanocrystals (RE = La, Nd, Eu and Y) possess either a pyrochlore structure or a defect fluorite structure, which depends on the ionic radius of RE^{3+} ions (Zhang *et al*. 2008). These phosphors exhibit emission in the UV and visible range due to different transition of RE ion. The PL properties were explained based on the transition between the valence band and a mid-gap state related to oxygen vacancies. Their luminescence properties intimately related to their intrinsic defect structure, and this work can be used to estimate the degree of disorder in the $A_2B_2O_7$ structure.

Eu^{3+} emission spectra in $La_2M_2O_7$ (M = Zr, Hf, Sn), were studied by Hirayama *et al.* in 2008. They observed that distortion of the $(EuO_8)^{n-}$scalenohedra increased with deceased ionic radii of M^{4+} ion. Also, the splitting width of $^5D_0$–$^7F_1$ transition increased with the distortion of the $(EuO_8)^{n-}$scalenohedra (Hirayama *et al.* in 1973). The peak wavelength of Eu^{3+} was affected by the average crystal structure of the host materials. The crystallinity is an important factor for understanding the luminescence color of Eu^{3+} in pyrochlore compounds.

The structural changes associated with transformation of bulk $Y_2Sn_2O_7$ into nanoparticles of $Y_2Sn_2O_7$ on the luminescence properties were investigated. A significant distortion in geometry and electron density distribution around Y^{3+}/Eu^{3+} ions was observed. The SnO_6 octahedron in $Y_2Sn_2O_7$ was more expanded in nanoparticles compared to bulk. The bulk sample exhibits typical ionic feature in Y/Eu-O bonds, while nanoparticle sample shows sharing of electron density along bond axis pertaining to covalent character (Nigam *et al*. 2013).

Fu *et al.* reported the luminescence of Eu^{3+}-doped nanocrystalline pyrochlore oxide $M_2Sn_2O_7$ (M = Gd and Y). It was found that tuning the base concentration was a crucial step for the control of the pure phase of the $M_2Sn_2O_7$ (M = Gd and Y) nanocrystals. The CTB energy of these crystals located at lower energy. The developed

samples show orange and red luminescence at single wavelength excitation due to the double split $^5D_0$-$^7F_1$ and $^5D_0$-$^7F_2$ transitions, which was attributed to the lattice distortion around Eu^{3+} ions (Fu *et al*. 2011).

To improve the luminescence properties of Eu in $Y_2Sn_2O_7$ host, they were dispersed in Y_2O_3 matrix. Their luminescence properties gets improved by the removal of surface effect by Y_2O_3 matrix and deterioration in the non-radiative contributions. Quantum efficiency of luminescence from $Y_2Sn_2O_7$: Eu - Y_2O_3 were found to be around 88% and was much higher than bulk and nanoparticles of $Y_2Sn_2O_7$: Eu and Y_2O_3: Eu phosphors (Sharma *et al*. 2016).

Photoluminescence properties of yttrium stannate ($Y_2Sn_2O_7$) phosphors doped with Tb, Eu and Dy was carried by Ege *et al*. A series of the emission lines corresponding to the characteristic 4f→4f intra-configuration forbidden transitions of Tb^{3+} were appeared and that main emission peak occurs at about 542 nm. They observed multiple emission lines at each of these ions due to the crystal field splitting of the ground state of the emitting ions. Eu-doped sample displayed intense and predominant emission peaks located at 580-650 nm corresponding to the $^5D_0 \rightarrow ^7F_j$ (j=l, 2, 3 and 4) transitions. Dy doped phosphor presented several luminescence bands from 450-800 nm and exhibit very good luminescence properties (Ege *et al*. 2013).

Fujihara *et al*. reported the multiband orange-red luminescence of Eu^{3+} Ions in the $Y_2Sn_2O_7$ pyrochlore structured host crystal. They observed simultaneous occurrence of five predominant orange-red band emissions at UV excitation due to doubly split magnetic dipole $^5D_0 \rightarrow ^7F_1$ and electric dipole $^5D_0 \rightarrow ^7F_2$ transitions. Inhomogeneous broadening was arising from the site-to-site variation of Eu^{3+} ions in the host crystal. Thus, they are able to synthesize a single-phase crystalline phosphor material having the chromaticity corresponding to a region between pink and yellowish pink Fujihara *et al*. 2005).

$Gd_2Sn_2O_7$:Eu^{3+} nanoparticles have been prepared by Liao *et al*. through microwave assisted hydrothermal method. They observed that pH value has a crucial role in the control of pure phases of nanocrystals. Intense emission peak at 587 nm

corresponding to the $^5D_0 \rightarrow {}^7F_1$ magnetic dipole transition of Eu^{3+} was observed at 391nm excitation which indicates that local symmetry of Eu^{3+} ions in the crystal lattice has inversion center (Liao *et al* 2017).

Nigam *et al*. studied the effect of annealing temperature on the structural and photoluminescence properties of Eu doped $Y_2Sn_2O_7$ nanoparticles. As the annealing temperature increases, the YO_8/EuO_8 polyhedra in the $Y_2Sn_2O_7$: Eu lattice become more symmetric. The extent of distortion of the YO_8/EuO_8 polyhedra is reflected in the luminescence parameters Ω_2 and Ω_4. The emission intensities of the Eu^{3+} ions in the nanoparticles are mainly decided by the surface Eu^{3+} ions, the concentration of which decreases with increasing temperature. They found that the incorporation of the nanoparticles in a poly (methyl methacrylate) (PMMA) matrix leads to a decrease in the $^5D_0$ lifetime due to the quenching of the excited states of surface Eu^{3+} ions through the vibrations of different structural units in PMMA (Nigam *et al*. 2013).

$Y_2Sn_2O_7$ nanocrystals with pyrochlore structure have been synthesized by a facile CTAB-assisted sol–gel route. The as-synthesized material display intense and prevailing emission at 589 nm due to the $^5D_0 \rightarrow {}^7F_1$ magnetic dipole transition of Eu^{3+} ions (Lu *et al*. 2004).

Luminescence properties of $La_2Sn_2O_7$:Eu^{3+} micronanospheres were studied by Fu *et al*. The samples exhibit orange-red luminescence at single wavelength excitation due to the double split $^5D_0$-$^7F_1$ and $^5D_0$-$^7F_2$ transitions. They reported that the splitting of $^5D_0$-$^7F_2$ transitions of Eu^{3+} ions may be due to the distortion of local symmetries of Eu^{3+} ions from inversion centre (Fu *et al*. 2008).

The luminescence properties of Eu^{3+}-doped and Eu^{3+}, Dy^{3+} codoped $La_2Sn_2O_7$ phosphor were investigated by Wang *et al*. The $^5D_0 \rightarrow {}^7F_1$ magnetic dipole transition was found to be more intense than $^5D_0 \rightarrow {}^7F_2$ electric dipole transition. Enhancement in emission intensity was observed by the codoping of Dy^{3+} ions due to the effective energy transfer from Dy^{3+} to Eu^{3+} ions (Wang *et al* 2006).

2.3 Importance of displaced-pyrochlore

If the total number of ions at the B site is more than the total number of ions at the A sites, some of the ions occupying the B site might be occupying the A site. This unconventional placement of small B type cations on the large A cation site results in the displacive disorder in the A_2O' network. A number of reports found in the literature suggest that displacive disorder in the A_2O' network is an inherent feature of the pyrochlore structure. Such pyrochlores are termed as misplaced-displacive cubic pyrochlore–pyrochlore which exhibit misplacement of traditionally octahedral B-site cations onto the larger A-sites, accompanied by displacive disorder in the A_2O' substructure to facilitate a lower coordination number for the smaller species. Their XRD patterns exhibit weak forbidden reflections (e.g. 442) which serve as a diagnostic flag for the displacement of atoms to lower symmetry positions in the space group and also they show relaxor behavior at low temperature. Detailed studies The A-site cations were found to be randomly displaced from the ideal eightfold coordinated positions along the six <1 1 2> directions, perpendicular to the O'-A-O' links. The O' ions were found to be randomly displaced along the <1 1 0> directions. Despite considerable recent efforts, however, the local crystal chemistry underlying such behavior still remains far from well understood. However, such displacive disorder can give the appearance of higher symmetry and the deviation of the pyrochlore A site symmetry from a perfect inversion centre and also the distortion of the scalenohedra can improve the luminescence.

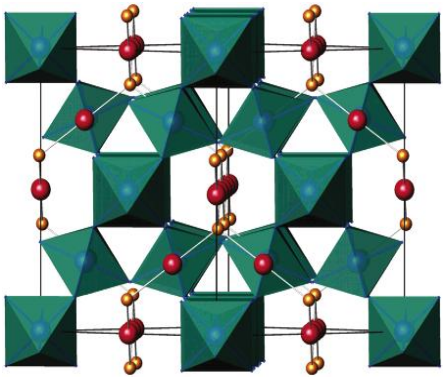

Fig. 2.3 Unit cell of displaced pyrochlore

2.3.1 Literature review on displaced pyrochlore

Roth *et al*. conducted the phase equilibria studies of the $CaO\text{-}TiO_2\text{-}Nb_2O_5$ system. They reported that some of the ions in the B-site can be mixed with larger Ca^{2+} ions on the A-sites by displacing it from the ideal 8-coordinated position to achieve a satisfactory coordination environment. Also, the developed pyrochlore were characterized by the displacive disorder in the A_2O' subnetwork. In the system, the A-type sites are ~75% occupied by Ca^{2+} in the ideal 16d position and ~25% by Ti^{4+}, which is displaced 0.7Å to partially occupy a ring of six 96g sites and reduce its effective coordination number to 5 (trigonal bipyramidal). The O' oxygens are disordered among a tetrahedral cluster of 32e sites displaced 0.48 Å from the ideal 8b site. These studies suggest that ~20% of the Ti in the A-type positions may occupy different displaced sites that result in distorted tetrahedral coordination, resulting in both five and four-coordinated Ti^{4+} in the system. The present pyrochlores exhibited dielectric relaxation due to the structural disorder (Roth *et al*. 2008).

The partial occupation of B site cations on the A site were reported in Ca-Ce-Ti-M-O (M = Nb or Ta) system. They also observed that some Ti ions might be occupying the A-sites, even though it is too small to occupy the large eightfold coordinated environment in pyrochlores. The weak characteristic reflection (442) of displaced pyrochlores was observed in both the Ti rich niobate and tantalite powder XRD patterns. Thus, the system involves the occupation of three cations (Ca, Ce and Ti) on the A-sites and two types of cations (Ti and Nb or Ta) on the B-sites. These semiconducting ceramic oxides were reported to be suitable candidate for applications in NTC thermistors (Deepa et al. 2009).

Levin *et al*. determined the stoichiometry of single-phase cubic bismuth zinc niobate to be $Bi_{3/2}Zn_{0.92}Nb_{1.5}O_{6.92}$ (BZN) in the pyrochlore structure ($A_2B_2O_6O'$) with partial Zn occupancy of both A and B sites. In addition, displacements from the ideal crystallographic positions were identified for both A and O' ions. The A-cations were found to be randomly displaced by ~0.39 Å from the ideal eight-fold coordinated positions along the six <112> directions perpendicular to the O'-A-O' links. In addition,

the O' ions were randomly displaced by ~0.46 Å along all 12 <110> directions. Crystal–chemical considerations suggest the existence of short-range correlations between the O' displacements and both the occupancy of the A-sites (Bi or Zn) and the directions of the A-cation displacements. The combined A cation and O' displacements change the coordination sphere of the A-cations from 8 to (5+3). The observed displacive disorder in the A_2O' network of the $Bi_{3/2}Zn_{0.92}Nb_{1.5}O_{6.92}$ structure were found to be responsible for both the high dielectric constant and the dielectric relaxation of this compound (Levin *et al*. 2002).

Phase equilibrium studies conducted by Vanderah *et al***.** in the Bi–Zn–Nb–O system revealed that a pyrochlore structure can accommodate up to 25% of small B cations on its A-site by the displacive disorder. In the system, the A sites were assumed to be occupied by a mixture of Bi^{3+}, Zn^{2+}, and vacancies. Even though the average structure retains cubic symmetry, the combined displacements of the A (0.39 Å) and O' (0.46 Å) ions change the coordination number of the A cations from 8 to (5 + 3), thus permitting the smaller Zn^{2+} ion to achieve a chemically reasonable environment, with fewer nearest oxygen neighbors, by local correlations of the displaced ions (Vanderah *et al***.** 2005).

Static displacive disorder of both the Bi and O' sites was observed in $Bi_2Ru_2O_7$ and $Bi_{1:6}M_{0:4}Ru_2O_7$ (M = Cu, Co) pyrochlores. This type of disorder is proposed to be a common feature of $A_2B_2O_7$ pyrochlores having a lone electronic pair on the A-site cation. This revealed that the off-center displacement of A-site cations can also occur when the A site is occupied by a small transition metal, because the A-site cavity is clearly too big for them to be placed in the ideal center position. Pyrochlore D_{3d} symmetry, as well as the disruption of the local symmetry by static A-site cation disorder determined the electronic behavior of Ru^{4+} pyrochlores (Avdeev *et al*. 2002).

The disordered structures and low temperature dielectric relaxation properties of two misplaced-displacive cubic pyrochlores were reported in the Bi_2O_3–$M^{II}O$–Nb_2O_5 (M = Mg, Ni) systems. The metal ion vacancies were found to be confined to the pyrochlore A site. The B_2O_6 octahedral sub-structure was found to be fully occupied and

well-ordered. The displacive shifts of the local A-site cations away from the ideal pyrochlore A-site positions for both systems were directed perpendicular to the local O'-A-O' axis. It seemed that both the concentration of M-site ions as well as vacancies on the pyrochlore A sites play crucial roles and that the dielectric relaxation properties of such Bi-pyrochlores were intimately dependent upon this local crystal chemistry (Nguyen *et al*. 2007).

Crystal chemistry and dielectric properties of chemically substituted $(Bi_{1.5}Zn_{1.0}Nb_{1.5})O_7$ and $Bi_2(Zn_{2/3}Nb_{4/3})O_7$ pyrochlores were investigated by Valant *et al*. The distortion in $Bi_2(Zn_{2/3}Nb_{4/3})O_7$ was suggested to result from the long-range coupling of the $6s^2$ lone-pair electrons of Bi^{3+} cations on the A-site position. They also examined the potential incorporation of tetravalent cations, such as Ti^{4+} and Zr^{4+}, onto the B-sites and larger trivalent cations, such as Gd^{3+}, onto the A-sites. The effect of the substitutions on the dielectric properties is correlated to the relative sizes of the A- and B-site occupants. They observed that the substitution of Gd cations into $(Bi_{1.5}Zn_{1.0}Nb_{1.5})O_7$ is more limited but can be extended by codoping with Ti cations (Valant *et al*. 2000).

Cubic bismuth pyrochlores in the Bi_2O_3-MgO-Nb_2O_5 system have been reported as promising dielectric materials due to their high dielectric constant and low dielectric loss. The presence of more than six vibrational models predicted for the ideal pyrochlore structure, indicated the additional atomic displacements of the A and O' sites from the ideal atomic positions in the samples. The high dielectric constants in the developed samples were ascribed to the long-range ordered pyrochlore structures since the electric dipoles formed at the superstructural direction could be enhanced (Zhang *et al*. 2013).

Gao *et al*. studied the effect of magnesium content on structure and dielectric properties of cubic bismuth magnesium niobate pyrochlores. The Raman vibration spectra studies revealed that the Mg^{2+} ions occupied B sites first and then entered A sites after the B sites were fully occupied. The microstructure significantly affected the dielectric properties of the samples. It was found that the dielectric constant and

dielectric loss of samples increased with the Mg^{2+} content, but the dielectric constant showed a slight decrease when N>1.1. This was due to the polarizability variation and structure disorder caused by the change of Mg^{2+} content. The dielectric constant was nearly temperature independent at lower Mg^{2+} content (N<0.8), but then it showed a tendency to decrease with the increasing temperature at higher Mg^{2+} content, which was found to be related to the disorder in the A sites (Gao *et al*. 2014).

A new member of Bi pyrochlore family with highest percentage of Fe^{3+} ion $(Bi_{1.88}Fe_{0.12})(Fe_{1.42}Te_{0.58})O_{6.87}$ were investigated by Babu *et al*. The developed pyrochlore crystallizes with displaced atomic A-sites similar to other Bi-based misplaced-displacive pyrochlores. They observed that ~6% of the Fe^{3+} were misplaced on the A-site. The higher number of Raman modes together with the presence of the low wavenumber modes confirm the displacive nature of the $(Bi_{1.88}Fe_{0.12})(Fe_{1.42}Te_{0.58})O_{6.87}$. The dielectric characterization exhibits a frequency diffusive and dispersive dielectric relaxation due to the multiwall hopping of displaced ions (Babu *et al* 2011).

The $(Bi_{1.5-2y}Zn_{1+2y}Nb_{1.5})O_{7-y}$ crystalline samples were also examined by Raman spectroscopy to look for further short range structural information. The results showed that the Nb/O and Zn/O stretching modes in the B site oxide octahedral almost do not change with the chemical constitution changing. It was found that the movable Zn^{2+} is inclined to occupy B site first and then enter into A site after the B site was stuffed (Hong *et al*. 2003).

Probing disorder in cubic pyrochlore $Bi_{1.5}Zn_{1.0}Nb_{1.5}O_7$ thin films were studied by Singh *et al*. The sharp increase in dielectric constant of thin film at high temperatures was related to disorder in cation and anion lattices. This phenomenon suggested that the large change in dielectric constant was due to a dynamical rise of dipolar fluctuations in the unit cell. It confirms the relaxation corresponds to the ionic hopping among the A and O' positions (Singh *et al*. 2010).

Tan *et al*. reported the distribution of Zn over A- and B-sites in the stoichiometric, $Bi_{1.5}ZnTa_{1.5}O_7$ and nonstoichiometric $Bi_{1.56}Zn_{0.92}Nb_{1.44}O_{6.86}$ systems.

They observed that the different-sized Zn^{2+} and Bi^{3+} ions occupy different positions within the A-sites. This is linked to off centre displacement of surrounding O(2) ions, allowing a local structure that gives reasonable Zn-O and Bi-O bond lengths. Also, Zn deficiency is accommodated by B-site vacancies. Off-centre displacement of both A-site ions provides a mechanism for satisfying the bonding requirements of the different-sized Bi^{3+} and Zn^{2+} ions. The flexibility in cation and oxygen site distributions and occupancies provides a basis to rationalize the unusual solid solution ranges which were significantly different for X = Nb, Ta and Sb (Tan *et al*. 2010).

2.4 Importance of fergusonite structure

The general formula of the fergusonite structure is ABO_4 with a space group C2/c (or often reported in its nonstandard setting I2/a)), Rare-earth niobates ($RENbO_4$), with fergusonite structure have been widely investigated by many researchers due to their interesting physical properties such as high dielectric constant, photocatalytic behavior and photoluminescence and excellent thermal and chemical stability. In $RENbO_4$, there are two crystalline forms, the high-temperature tetragonal phase corresponding to the scheelite structure and the low temperature monoclinically distorted monoclinic phase (fergusonite). The fergusonite structure of $RENbO_4$ is considered as a distorted scheelite structure with the cations deviating a little from the special Wyckoff positions and the anions dividing into two kinds of Wyckoff positions accompanied by fractional coordinate displacement, thereby inducing a lower symmetry. It is a three-dimensional framework consisting of irregular NbO_6 and REO_8 units. Niobium atoms having 2-fold symmetry forms shorter bonds to four oxygen atoms over a narrow range of distances (average Nb–O distances of 1.846(5) and longer bonds to two other oxygen atoms (an average Nb–O distance of 2.455(5) Å) to form the distorted NbO_6 unit. From this, the monoclinic fergusonite structure appears to be between the scheelite structure with isolated groups and crystal structures of niobates by means of octahedral niobate groups. The NbO_6 units form a one-dimensional zigzag chain propagating by edge-shared oxygen atoms along the c axis. Each shared edge consists of one longer Nb1-O2 bond and one shorter Nb1-O2 bond. If only the shorter Nb1–O1 and Nb1-O2 bonds are considered, the niobate unit is an isolated distorted tetrahedron. The Y atoms also

occupy a 4e site and are eight-coordinate with oxygen in a square antiprismatic geometry. The framework formed by edge-sharing YO_8 units can be considered to encapsulate the propagating chains of NbO_6 units to form a three-dimensional framework. As a result; the 1-D zig-zag chains of the NbO_6 polyhedral are isolated from each other, whereas the REO_8 polyhedral are interconnected in all three crystallographic directions. The fergusonite structural arrangement is shown in Fig. 2.4.

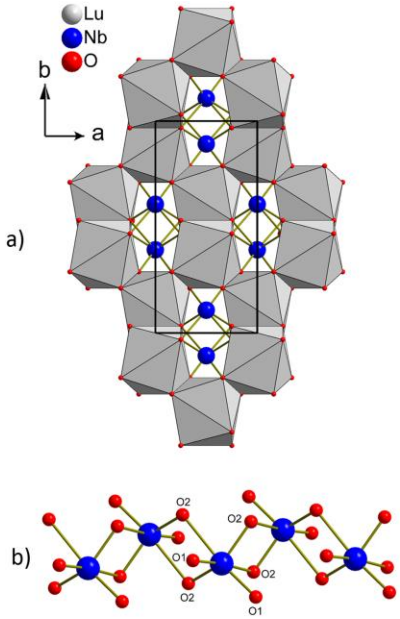

Fig. 2.4 Fergusonite type structure of rare earth niobates (a) framework of edge-sharing REO_8 units (b) propagation of the NbO_6 units.

2.4.1 Literature review on fergusonite type phosphors

$GdNbO_4$ has been considered as an essentially inert material in the visible region under excitation of UV light and electron beams. However it is possible to recreate blue emission of $GdNbO_4$ nanocrystalline phosphors. The host sensitized luminescence in $GdNbO_4$:Ln^{3+} (Ln^{3+} = Eu^{3+}/Tb^{3+}/Tm^{3+}) nanocrystalline phosphors with abundant color were investigated by Liu *et al*. Under the excitation of UV light and low-voltage electron beams, the $GdNbO_4$ nanocrystalline phosphor presented a strong blue luminescence from 280 to 650 nm centered around 440 nm, and the $GdNbO_4$:Ln^{3+} nanocrystalline phosphors showed both host emission and respective emission lines derived from the

characterize f-f transitions of the doping Eu^{3+}, Tb^{3+} and Tm^{3+} ions. They were succeeded in tuning the luminescence color of $GdNbO_4:Ln^{3+}$ nanocrystalline phosphors from blue to green, red, blue-green, orange, pinkish, white, etc. by varying the doping species, concentration, and relative ratio of the codoping rare earth ions in $GdNbO_4$ host lattice. Also single-phase white-light-emission has been realized in $Eu^{3+}/Tb^{3+}/Tm^{3+}$ triply doped $GdNbO_4$ nanocrystalline phosphors (Liu *et al*. 2016).

Yang *et al*. have prepared a single crystal $GdNbO_4:Ln^{3+}$ (Ln = Dy, Eu) phosphors via a hydrothermal procedure under high temperature high pressure conditions. The $GdNbO_4:Eu^{3+}$and $GdNbO_4:Dy^{3+}$ phosphors showed their characteristic emissions upon UV excitation. The $GdNbO_4:Dy^{3+}$single crystals exhibited a bright white emission under different excitation wavelengths with a relatively high quantum yield of 21.7%. The $GdNbO_4:0.05Eu^{3+}$ exhibited excellent bright red luminescence at 612 nm under near-UV excitation. The emission spectra were found to be narrow which resulted in improvement in quantum efficiencies of 43.2% (Yang *et al*. 2014).

The promising multi-modal luminescence (upconversion, downshifting and quantum cutting) properties of RE^{3+} (Tm^{3+}, Yb^{3+}) and Bi^{3+} activated GdNbO4 phosphors were investigated. This material produced intense blue and NIR emission via multi-modal optical processes. $Gd_{0.94}Tm_{0.01}Yb_{0.05}NbO_4$ produced intense upconverted blue and NIR and relatively weak red emission on NIR excitation. On UV excitation (λ_{exc} = 265 nm), $Gd_{0.99}Tm_{0.01}NbO_4$ sample produced intense down shifting blue emission due to the Tm^{3+} ion, overlapped with the emission of the $(NbO_4)^{3-}$ ion through strong energy transfer from $(NbO_4)^{3-}$ to Tm^{3+} ions. Interestingly, NIR QC has also been successfully observed in these phosphors through cooperative energy transfer from the $(NbO_4)^{3-}$ group to the Yb^{3+} ion, Bi(6s)-Nb(4d) to the Yb^{3+} ion and the Tm^{3+} ion to the Yb^{3+} ion, respectively (Dwivedi *et al*. 2015).

Lu *et al*. prepared nanocrystalline $GdNbO_4:Tm^{3+}$ and $GdNbO_4:Dy^{3+}$ phosphors via a Pechini-type sol–gel process. Under the excitation of UV light (264 nm), the $GdNbO_4:Tm^{3+}$ and $GdNbO_4:Dy^{3+}$ phosphors showed their characteristic emissions. They found that the blue cathodoluminescence of the $GdNbO_4:Tm^{3+}$ phosphor has higher

color purity and comparable intensity to the $Y_2SiO_5:Ce^{3+}$ commercial product. A single composition white light emitting in response to near UV and low-voltage electron beam excitation has also been realized in $GdNbO_4:Dy^{3+}$ phosphor. The developed phosphor exhibit good morphology, excellent CL and PL properties and high color purity (Lu *et al.* 2013).

$GdNbO_4:Eu^{3+}$ and $LuTaO_4:Eu^{3+}$ have been successfully prepared with different fluxes (NaCl, KCl, NaCl and KCl) via the molten salt method. Different morphologies of the phosphor were achieved with different fluxes. Large clusters in the absence of fluxes will change into small particles based on the addition of salts during the crystallization and transformation processes. Their photo-luminescent properties demonstrated the significant energy transfers from NbO_4^{3-} (TaO_4^{3-}) groups to Eu^{3+}. This suggested that both niobate and tantalite were efficient hosts to sensitize europium red emissions. $GdNbO_4:Eu^{3+}$ with NaCl flux gave much enhanced red emission whereas $LuTaO_4:Eu^{3+}$ synthesized with the assistance of mixed salts (NaCl–KCl) achieved the best luminescence (Lin *et al*. 2013).

Liu *et al*. prepared rare-earth (Eu^{3+} and/or Tb^{3+}) ions doped $YNbO_4$ phosphors by a Pechini-type sol-gel process. They observed that all the samples consist of fine and spherical grains of around 40-80 nm. The prepared $YNbO_4:A$ (A = Eu^{3+} and/or Tb^{3+}) phosphors showed the characteristic blue broadband emission (from 300 to 500 nm with a maximum around 403 nm) of the YNbO4 host lattice, the characteristic red emission of Eu^{3+} and Tb^{3+} under the ultraviolet light (around 255 nm) and low-voltage electron beams, This indicated the effective energy transfer from the $YNbO_4$ host lattices to Eu^{3+} (Tb^{3+}) ions. A single composition white-light-emitting has been realized in $YNbO_4:Eu^{3+}$, Tb^{3+} phosphor by varying the relative doping concentration of Eu^{3+} and Tb^{3+} ions (Liu *et al*. 2014).

Color-tunable luminescence was also observed in $YNbO_4:Ln^{3+}$ (Ln^{3+} = Dy^{3+} and/or Eu^{3+}) nanocrystalline phosphors. The samples showed the characteristic blue wide-band emission from the NbO_4 group, whitish light emission from Dy^{3+}, and red emission from Eu^{3+}. Single-phase white-light emission was observed in $YNbO_4:Dy^{3+}$

phosphors under the excitation of UV light and a low-voltage electron beam. The color tunable emission was observed by co-doping $YNbO_4:Dy^{3+}$ with the Eu^{3+} ion (Lu *et al*. 2015).

Choi *et al.* studied the effect of gadolinium incorporation on the optical characteristics of $YNbO_4:Eu^{3+}$ phosphors. They observed that luminescence intensity of $YNbO_4:Eu^{3+}$ phosphor increased with increasing the concentration of Gd^{3+} ions due to the energy migration process. They also reported that particle size of $(Y,Gd)NbO_4:Eu^{3+}$ phosphor could be controlled by using the NaCl flux. The peak intensity of $YNbO_4:Eu^{3+}$ phosphor with NaCl flux was found to be about 10% higher than the commercial phosphor $Y_2O_3:Eu^{3+}$. Highly anisotropic environment of Eu^{3+} ions in $(Y,Gd)NbO_4$ caused the CIE chromaticity coordinates shifted to the deep-red region (Choi *et al*. 2012).

2.5 Importance of the present work

In view of the importance of crystal structure of the host on the luminescence properties of Eu^{3+} ions, the current research work is an attempt to study the dependence of emission properties on structure, ordering of cations, and distribution of activator ions in host lattice. Major efforts have been made by many research groups in the world in the development of red phosphors. The literature review details the luminescence properties of Eu^{3+} ions in pyrochlore and fergusonite-type host lattice.

Most of the rare earth stannate pyrochlore phosphors discussed so far, exhibit intense and prevailing emission at 589 nm due to the parity allowed $^5D_0$-$^7F_1$ magnetic dipole transition. Accommodating cations with different valency and electronegativity in the crystal lattice can induce local distortion and modification in polarizability of chemical environment of Eu^{3+}, which can change the photoluminescent properties. For an enhanced parity forbidden red emission in pyrochlore phosphors, one has to destruct the inversion symmetry of Eu^{3+} site such that there will be a superior probability of mixing of CT band wave function with f-orbital resulting in relaxation of the parity selection rules. So, an attempt has been made to enhance the f-f transition intensity of rare earth stannate pyrochlore phosphors through phase transition from

ordered pyrochlore to defect fluorite and investigate their emission properties in correlation with their structures.

As always disorder can give the appearance of higher symmetry the deviation of pyrochlore from a perfect inversion center and also distortion of scalenohedra can improve the luminescence properties of Eu^{3+} ions. The misplaced-displacive cubic pyrochlores have been reported to be attractive candidate materials in low-temperature co-fired ceramic (LTCC) multilayer capacitor and integrated device applications, including frequency agile microwave devices and in semiconducting oxides and superconductors. However, up to now, no details of the photoluminescence work of these configurations have been reported. So, in the present study, the influence of partial substitution of small cation and medium size cation on both A and B sites of the pyrochlore type oxides on the photoluminescence properties was studied in detail. Thus, a new series of stannate/titanate based displaced pyrochlore type red phosphors were developed.

Commercially applied red phosphors exhibit a broad emission band with a large portion of emitted light lie outside the human eye sensitivity wasting energy in the infrared region. Therefore, narrow band red-emitting materials are necessary, which can be applied in high-power pc- LEDs. Our objective also includes the development of highly efficient intense narrow-band red emitting phosphors for practical applications. In the present work, the luminescence properties of Eu^{3+} in lanthanide niobate were enhanced by incorporating various aliovalent cations without altering the monoclinic fergusonite structure and developed narrow-band red emitting phosphors with high color purity.

The synthesized materials were characterized using various advanced techniques such as powder X-ray diffraction, Raman spectroscopy, Infrared spectroscopy, X-ray photoelectron spectroscopy, scanning electron microscopy with energy dispersive spectroscopy and X-ray dot mapping, transmission electron microscopy, absorption spectroscopy and luminescence spectroscopy.

Chapter 3A

PHOTOLUMINESCENCE PROPERTIES OF STANNATE BASED DISPLACED PYROCHLORE-TYPE RED PHOSPHORS: $Ca_{3-x}Sn_3Nb_2O_{14}:xEu^{3+}$

The influence of partial substitution of Sn in both A and B sites of the pyrochlore-type oxides, $Ca_{3-x}Sn_3Nb_2O_{14}:xEu^{3+}$ on the photoluminescence properties was studied using various advanced techniques. These phosphors exhibit strong absorptions at near UV and blue wavelength regions and emit intense multiband emissions due to Eu^{3+} $^5D_0$–$^7F_{0,\ 1,\ 2}$ transitions. The absence of characteristic MD transition splitting points out that local cation disorder exists in this type of displaced pyrochlores, reducing the D_{3d} inversion symmetry. The unusual forbidden intense sharp $^5D_0$–$^7F_0$ transition indicates a single site occupancy of Eu^{3+} with a narrower range of bonding environment, preventing the cluster formation.

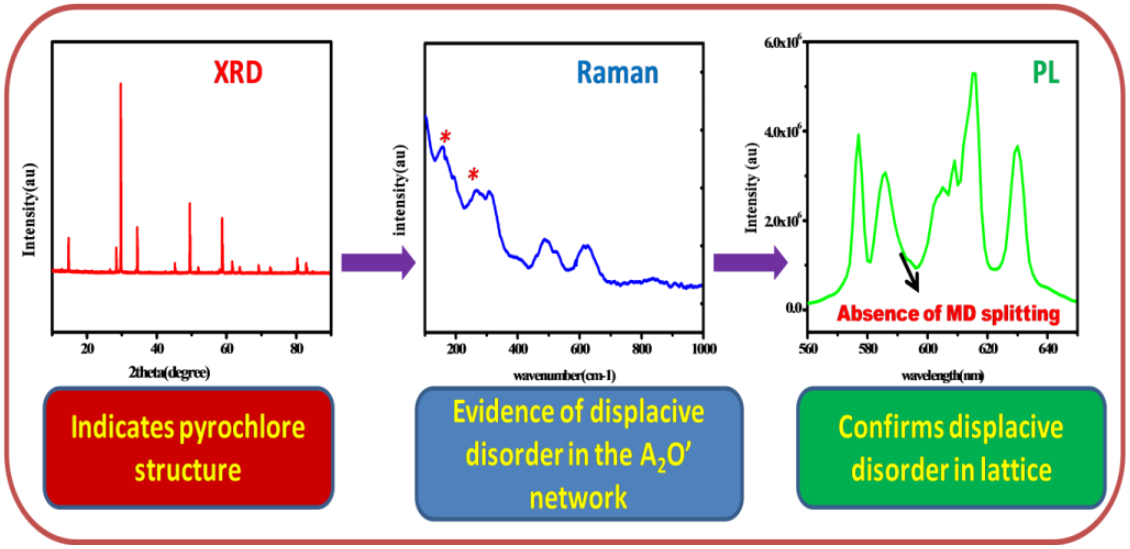

Sreena *et al. Dalton Trans.* **2015,** 44, 8718-8728.

3A. 1 Introduction

There is a great demand for inorganic phosphors with high chemical stability and luminescence efficiency for white light emitting diodes that can be effectively excited in the near UV or blue region. The luminescence efficiency of a phosphor material strongly depends on the local coordination structure at the luminescence centers, including factors such as the coordination number, interatomic distance, and symmetry and coordinating anion species. Due to the presence of intra-configurational f–f transitions, Eu^{3+} is preferably used as an activator in most inorganic red phosphors. The luminescence of Eu^{3+} ions is determined greatly by the site symmetry and the strength of crystal field at the RE ion site. When Eu^{3+} is located at a low symmetry site, the hypersensitive forced electric dipole $^5D_0 \rightarrow {}^7F_2$ transition dominates over the allowed $^5D_0 \rightarrow {}^7F_1$ transition (Blasse *et al*. 1994). The appearance of $^5D_0 \rightarrow {}^7F_0$ transition of Eu^{3+} is an indication of lowering of Eu^{3+} crystal site symmetry as it is allowed only for C_s, C_n, C_{nv} site symmetries and shows a red shift with the increase in covalency of Eu^{3+} (Capobianco *et al*. 1990; Du *et al*. 2011; Su *et al*. 2008; Parchur *et al*. 2012; Chen *et al*. 2004). Hence Eu^{3+} ions are usually employed as an optical probe to investigate the coordination and environment around the cations substituted in the crystalline lattice.

Pyrochlore oxides (cubic *Fd3m*) with the general formula $A_2B_2O_7$ have attracted extensive attention as a host lattice for inorganic phosphors due to its unique properties such as high chemical stability, lattice stiffness, thermal stability, ability to incorporate a diverse range of elements at the A and B sites and to tolerate both cation and anion disorder etc (Subramanian *et al*. 1983). If the total number of ions at the B site is more than the total number of ions at the A site, some of the ions occupying the B site might be occupying the A site (Deepa *et al*. 2011). This unconventional placement of small B type cations on the large A cation site results in the displacive disorder in the A_2O' network (Vanderah *et al*. 2005). Detailed studies by Levin et al. (Levin *et al*. 2002) determined the stoichiometry of single-phase cubic bismuth zinc niobate to be $Bi_{3/2}Zn_{0.92}Nb_{1.5}O_{6.92}$ (BZN) in the pyrochlore structure ($A_2B_2O_6O'$) with partial Zn occupancy in both A and B sites. In addition, displacements from the ideal crystallographic positions were identified for both A and O' ions. However, to date, only

the spectra of BZN have been reported despite the large number of bismuth-based pyrochlore compounds studied in the last few decades. The misplaced-displacive cubic pyrochlores have been reported to be attractive candidate materials in low-temperature co-fired ceramic (LTCC) multilayer capacitor and integrated device applications, including frequency agile microwave devices and in semiconducting oxides and superconductors (Roth *et al*. 2008; Randall *et al*. 2003; Ren *et al*. 2001; Hong *et al*. 2002). Up to now, no details of the photoluminescence work of these configurations have been reported.

Accommodating cations having different valencies and ionic radii in the pyrochlore A site can cause changes in the luminescence properties. As always, disorder can give the appearance of higher symmetry, and the deviation of the pyrochlore A site symmetry from a perfect inversion centre and also the distortion of scalenohedra can improve the luminescence. In this direction, new stannate pyrochlore phosphors, $Ca_{3-x}Sn_3Nb_2O_{14}$:xEu^{3+} have been prepared via a solid state reaction method in order to investigate the evolution of emission spectra with the partial occupancy of Sn in both A and B sites. The spectra show strong red luminescence through forced electric dipole transition ($^5D_0 \rightarrow {}^7F_2$) under the excitation either into the $^5L_6$ state with 394 nm or the $^5D_2$ state with 464 nm. Interestingly, there is no splitting observed in the MD transition $^5D_0 \rightarrow {}^7F_1$ in contrast to the pyrochlore D_{3d} symmetry. Further unusual forbidden intense sharp $^5D_0 \rightarrow {}^7F_0$ transition indicates low symmetry of Eu^{3+} ions with a uniform environment or without much site-to-site variation. The experimental details and the results of these phosphors are presented in this chapter.

3A. 2 Experimental

The pyrochlore type red phosphors with the general formula $Ca_{3-x}Sn_3Nb_2O_{14}$:xEu^{3+} (x = 0.05, 0.10, 0.15 and 0.20) were synthesized by the conventional solid state reaction method using $CaCO_3$, SnO_2, Nb_2O_5, and Eu_2O_3 (99.9% purity; Sigma-Aldrich, Steinheim, Germany) as the starting materials. The required stoichiometric amounts of these materials were weighed and then thoroughly wet mixed in an agate mortar with acetone as the wetting medium. The mixing is followed by drying in an air

oven at a temperature of 100°C. This process of mixing and drying was repeated thrice to obtain a homogeneous product. The obtained mixture was initially calcined at 1300°C for 6h in a platinum crucible in an air atmosphere furnace. The calcination was repeated at 1500°C for 6h with intermittent grinding until a phase pure compound was obtained. The calcined product was then ground into a fine powder for carrying further characterization.

The crystalline structure and the phase purity of the samples were analyzed by recording the X-ray powder diffraction (XRD) pattern using a PANalytical X'Pert Pro diffractometer having a Ni filtered Cu-Kα radiation with an X-ray tube operating at 40 kV, 30 mA and 2θ varying from 10 to 90° in 0.016 steps. The Raman spectra of the powder samples were acquired using an integrated micro-Raman system using a 633 nm helium-neon laser with a spatial resolution of 2 μm to analyse the structural aspects of the powder samples. The morphology of powder particles was studied using a scanning electron microscope (Carl Zeiss EVO 18) operated at 20 kV. The X-ray microchemical analysis and elemental mapping of the samples were carried out using a Silicon Drift Detector-X-Max^N attached with the SEM. The selected-area electron diffraction (SAED) patterns and high-resolution electron microscopy of the samples were taken using a TECNAI 30G^2 S-TWIN transmission electron microscope (FEI, The Netherlands) operating at 300 kV. Absorbance studies of the samples were carried out using a Shimadzu UV-3600 UV-Vis spectrophotometer in the 200-500 nm wavelength range using barium sulfate as a reference. The photoluminescence spectra of the prepared samples were obtained using a Spex-Fluorolog DM3000F spectrofluorimeter with a 450 W xenon flash lamp as the exciting source. The luminescence lifetime of the phosphors was recorded using the phosphorimeter attached to a Fluorolog®3 spectrofluorimeter. All the measurements were carried out at room temperature.

3A. 3 Results and discussion

3A. 3.1 Powder X-ray diffraction studies

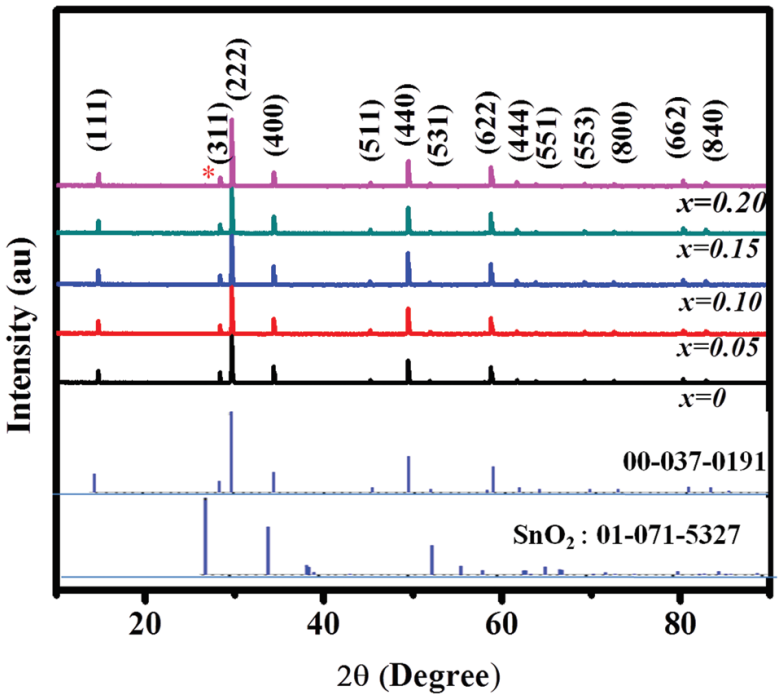

Fig. 3A.1 Powder X-ray diffraction patterns of $Ca_{3-x}Sn_3Nb_2O_{14}$:xEu^{3+} (x = 0, 0.05, 0.10, 0.15 and 0.20) red phosphors and the reference patterns for pyrochlore and SnO_2.

Fig. 3A.1 shows powder X-ray diffraction patterns of $Ca_{3-x}Sn_3Nb_2O_{14}$:xEu^{3+} (x = 0, 0.05, 0.10, 0.15 and 0.20) phosphors calcined at 1500°C. All the peaks can be well indexed to a cubic pyrochlore structure with a space group *Fd3m* (JCPDS file no. 037-0191). The sharp and intense peaks of the patterns indicate the crystalline nature of the samples. The presence of characteristic super-lattice peaks corresponding to the (111), (311), (511), (531), and (551) lattice planes evidence the formation of pyrochlore phase. Above 15 mol% doping, minor impurity SnO_2 peaks (marked as *) were observed in the XRD pattern. The ionic radii of Ca^{2+} and Eu^{3+} in eightfold co-ordination are 1.12 and 1.07 Å, respectively, and those of Sn^{4+} and Nb^{5+} in sixfold co-ordination are 0.81 and 0.64 Å, respectively (Shannon 1976). As the ionic radius of Ca matches with that of Eu, effective doping is possible. The bigger Ca^{2+} and Eu^{3+} ions occupy the A sites and the transition metals Sn^{4+} and Nb^{5+} occupy the B sites. Also, since the total number of Sn and Nb ions at the B-sites is more than the total number of Ca and Eu ions at the A-sites, some of the Sn ions might be occupying the A-sites because of its medium ionic radius according to the crystal chemical principle (Hong *et al*. 2003). In this case, the

occupation of randomly displacive Sn^{4+} ions makes the system remain in a disordered state, reducing the pyrochlore D_{3d} symmetry, as evidenced from the photoluminescence properties. Roth et al. had reported that some of the ions in the B-site can be mixed with larger Ca^{2+} ions on the A-sites by displacing it from the ideal 8-coordinated position to achieve a satisfactory coordination environment (Roth *et al.* 2008). The structural origin of this behavior is far from clear. From the chemical point of view, extensive displacive disorder is not perhaps unexpected; given the presence of rather small Sn^{4+} on the (6 + 2) fold coordinated pyrochlore A site and the difference in valence of the cations occupying the pyrochlore B site. This behavior has been observed in a number of pyrochlore systems (Vanderah *et al*. 2005) which exhibit static displacive disorder in the A_2O' network that facilitates reduced coordination numbers for the B type cations. The known limits of structural stability for the ideal cubic pyrochlore structure type suggest that it could not be possible for Sn^{4+} to occupy the A site without significant local structural distortion. These results confirm that the present pyrochlore oxides involve mixing of three cations (Ca, Sn and Eu) on the A site and the two types of cations (Sn and Nb) on the B-sites.

The radius ratio (r_A/r_B) is determined by the average ionic radius of the expected elements at the A site (Ca, Sn and Eu) to the B site elements (Sn and Nb). The average ionic radius of the cations occupying the A site and B site is calculated using the formula:

$$r_A = \frac{(3-x)r_{Ca} + x r_{Eu} + r_{Sn}}{4} \quad (3A.1)$$

$$r_B = \frac{2r_{Sn} + 2r_{Nb}}{4} \quad (3A.2)$$

The radius ratios of the prepared compounds were calculated accordingly and the values are listed in Table 3A.1. The data show that the ratio decreases with increase in Eu^{3+} ion concentration. The intensity variation of the characteristic superstructure peaks (111) is shown in Fig. 3A. 2.

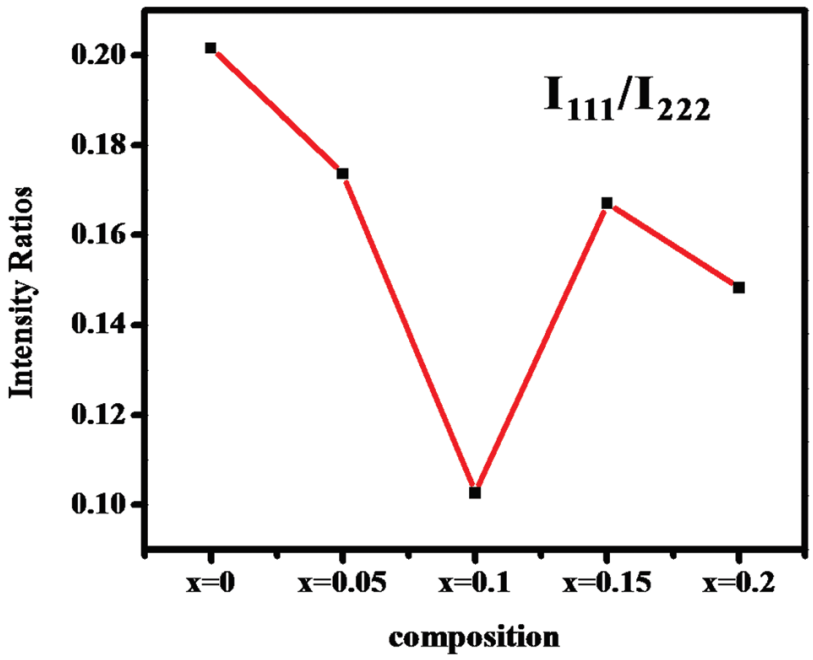

Fig. 3A.2 Variations of the super-lattice peak intensity ratio I_{111}/I_{222}.

Table 3A.1 Variation in lattice parameter, average crystallite size and radius ratio of $Ca_{3-x}Sn_3Nb_2O_{14}$:xEu^{3+} (x = 0, 0.05, 0.10, 0.15 and 0.20) red phosphors.

x	**Lattice Parameter(Å)**	**Average Crystallite size, Δd(μm)**	**Radius Ratio, r_A/r_B**
0	10.401	0.139	1.568
0.05	10.416	0.139	1.567
0.10	10.426	0.106	1.566
0.15	10.423	0.139	1.565
0.20	10.422	0.166	1.564

The decreasing trend of intensity ratio up to x = 0.10 indicates the probability of Eu^{3+} replacing the Ca (A-site) which reduces the radius ratio (r_A/r_B) and in turn decreases the order in the lattice. Such a variation in the intensities of super-structure peaks is associated with the variation in the oxygen position parameter. As the value of *48f* oxygen positional parameter x increases, A site scalenohedra become less distorted,

which is evident from the decreasing trend of asymmetric ratio with Eu^{3+} ion concentration which is further discussed in the later part. On further substitution, Eu^{3+} ion prefers to occupy the Sn displaced (A) site for maintaining the charge neutrality, which is further confirmed by the minor SnO_2 secondary phase in the XRD. Further the asymmetric ratio increased due to more distortion of the Eu^{3+} at the Sn site due to mismatch of the ionic radius and the displaced environment as discussed below. This led to the intensity ratio increase on higher substitution of Eu^{3+}. It was earlier reported that, as the radius ratio decreases, the pyrochlore structure tends to get converted from a well-ordered structure to disorder structure, in which the super-structure peaks diminish. Reducing the difference in ionic radius between A and B cations in the pyrochlore structure favors disordering. Disorder increases with increasing r_B and decreasing r_A (Minervini *et al*. 2000). The lattice parameters of the samples were calculated from the d-spacing. The lattice parameter increases with an increase in Eu^{3+} concentration up to 10 mol%, which is evident from the shift of the (222) peaks towards the left and after that it decreases. As Eu^{3+} replaces Ca^{2+} having a high ionic radius, the lattice value should decrease with an increase in Eu^{3+} concentration. Such inconsistency in the XRD pattern may be due to interstitial oxygen ions in the crystal lattice for maintaining the electrical neutrality of the system.

3A. 3.2 Raman spectroscopic studies

The crystalline $Ca_{3-x}Sn_3Nb_2O_{14}$:$x$$Eu^{3+}$ (x = 0, 0.05, 0.10, 0.15 and 0.20) samples were examined by Raman spectroscopy to look for further short range structural information, since Raman spectroscopy is an excellent tool to determine the local structure/disorder arising due to the anions in the materials (Vandenborre *et al*. 1983; Mandal *et al*. 2007). According to Group theoretical analysis, the Raman spectrum of a cubic pyrochlore structure has six optical Raman active modes which are given as:

$$\Gamma_{Raman} = A_{1g} + E_g + 4F_{2g} \qquad (3A.3)$$

These Raman active modes involve only the motion of oxygen atoms since A and B cations located at the inversion centre (D_{3d}) do not contribute to Raman active

vibrations. One of the F_{2g} modes is caused by the 8a oxygen sub-lattice vibration and the other F_{2g} Raman modes are related to *48f* oxygen sub-lattice vibrations in the cubic pyrochlore lattice (Gupta *et al*. 1996; Begg *et al*. 2001). The E_g mode can be assigned to B-O_6 bending vibrations and the A_{1g} mode to O-B-O bending vibrations, while F_{2g} modes represent a mixture of A-O and B-O bond stretching vibrations with bending vibrations.

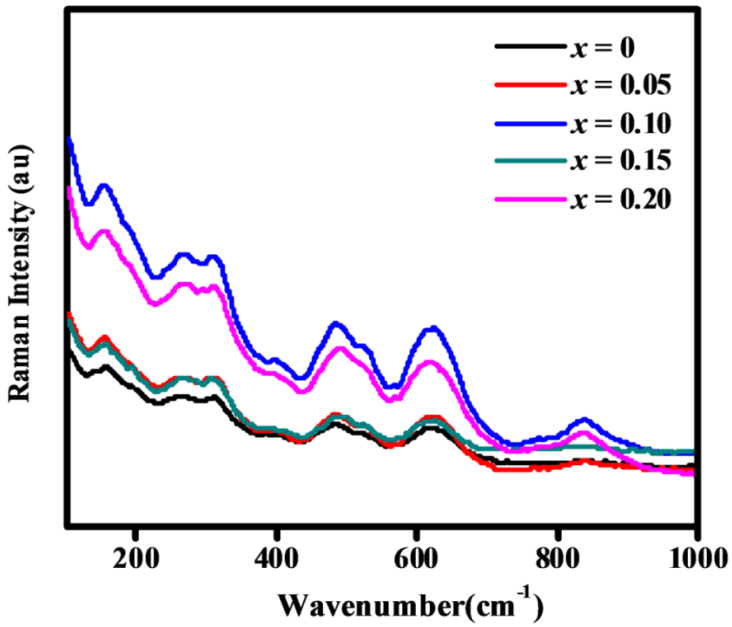

Fig. 3A.3 FT Raman spectra of $Ca_{3-x}Sn_3Nb_2O_{14}$:xEu^{3+} (x = 0, 0.05, 0.10, 0.15 and 0.20) phosphors.

Fig. 3A.3 represents the Raman spectra of all the samples in the series $Ca_{3-x}Sn_3Nb_2O_{14}$:xEu^{3+} (x = 0, 0.05, 0.10, 0.15 and 0.20) in the wave number ranging from 100 to 1000cm^{-1}. The Raman modes are assigned to symmetry species by referencing the previous literature (Vandenborre *et al*. 1983), and the proposed mode assignment is given in Table 3A.2. The Raman modes are broad as compared to that of well-ordered crystalline compounds, which is due to the inherent disorder in the system. This broadness is not due to small particle size because the sharp and narrow peaks in the XRD diagram and also the SEM analysis had shown that the particle size falls in the micrometer range. Thus the broadening due to a small particle size can be ruled out. Moreover, since all the Raman active vibrations involve oxygen motion the origin of

broadening is mainly due to structural disorder present in the system due to the existence of random vacancy from the statistical nature of the oxygen occupancy among various sites. However, the difference in the cation ion radius between A and B sites will affect the force constant of the A-O, A-O', and B-O vibrational modes; thus the whole Raman bands will have some extent of shift to the red or blue direction and even some new vibrational modes will emerge.

Table 3A.2 Raman mode frequencies with symmetry character and modes of vibration of $Ca_{3-x}Sn_3Nb_2O_{14}$:$x$$Eu^{3+}$ (x = 0, 0.05, 0.10, 0.15 and 0.20) red phosphors.

Wavenumber (cm^{-1})					Symmetry	Mode of vibration
x = 0	x = 0.05	x = 0.10	x = 0.15	x = 0.20		
155	155	154	154	153	F_{2g}	A-O stretching
264	266	269	270	272	F_{2g}	A-O stretching
304	306	304	305	303	E_g	O-B-O bond bending
485	487	488	490	493	A_{1g}	O-B-O bending with B-O stretching
621	620	620	619	619	F_{2g}	B-O stretching
840	840	838	835	834	A_{1g}	B-O stretching

After analyzing the Raman spectra based on the previously studied pyrochlore spectra, the typical modes of $Ca_3Sn_3Nb_2O_{14}$ were found to be located at 155, 264, 304, 485 and 621 cm^{-1}. The appearance of one extra Raman mode at the low frequency region (not observed for the ideal pyrochlore structure) in the system indicates the additional displacement of A and O' sites from the ideal atomic positions in the pyrochlore structure. Since the crystalline samples are composite pyrochlores, the A-O bonds include Ca-O and Sn-O bonds while B-O bonds include Nb-O and Sn-O bonds. The mode at 621 cm^{-1} corresponds to the Nb-O stretching modes. Similarly, the modes at 156 cm^{-1} and 266 cm^{-1} are related to the Sn-O stretching modes and the Ca-O stretching modes of A site, respectively. A new mode at nearly 840 cm^{-1} occurs in the doped

sample which may be due to the vibrational mode originating from localized short-range disorder of B site atoms and subsequent relaxation of the selection rules. In this complex compound, two species ions are located at A and B sites which would lead to two different vibrational modes corresponding to low frequency lines (155 cm^{-1} and 264 cm^{-1}); both are assigned to F_{2g} mode. The low frequency vibrations are due to the large cation displacements combined with octahedral deformations, which results in a large variation in the A-O bond length chemical environment. Further, when the A site (Ca^{2+}) is replaced by a smaller ion like Eu^{3+} in the present case results in the movement of oxygen atoms closer to the A site cation (along the bisector of the B-O-B angle), thereby decreasing the bond angle and increasing the B-O bond length. The variations of the F_{2g} mode around 155 cm^{-1} and the A_{1g} mode around 485 cm^{-1} suggest that excess Sn^{4+} and Eu^{3+} ions are occupying the A sites. As suggested by X-ray diffraction results discussed earlier, the Raman observations clearly corroborate the formation of a solid solution with Eu^{3+} incorporation into $Ca_{3-x}Sn_3Nb_2O_{14}$:$x$$Eu^{3+}$ (x = 0.05, 0.10, 0.15 and 0.20), since the peaks corresponding to the cubic pyrochlore structure are observed in all the samples. A close look at the peak positions for different Raman modes with Eu^{3+} content, as presented in Table 3A.2, reveals the hardening of F_{2g} (~264 cm^{-1}) mode with increasing Eu^{3+} concentration. The hardening of F_{2g} mode with increasing Eu^{3+} concentration may be due to the strengthening of the A-O bond as a result of Eu^{3+} doping, resulting in bond shortening and thereby shifting this stretching mode toward higher frequencies. On the other hand, the F_{2g} (~621 cm-^{1}) mode remains more or less the same with increasing the Eu^{3+} concentration as there is no change in the B site occupation. This indicates that the ion concentration in the B site does not change but the ion concentration in the A site changes with the chemical composition change. This observation of strengthening of a few modes gives a general indication of overall lattice strain and resulting local distortion in the system (Wan *et al*. 2009). Small distortions of the atomic positions caused by B cation species in pyrochlore structure compounds affect the force constant of the vibrational mode, resulting in a small shift in vibrational frequency. Thus, the full width at half maximum (*fwhm*) of a vibrational mode provides a measure of the level of localized short-range structural disorder in the material

(Mandal *et al*. 2006). From the structural analysis, it can be deduced that Sn^{4+} ions occupy the A site at a displaced position forming a displaced pyrochlore phase.

3A. 3.3 Morphological studies

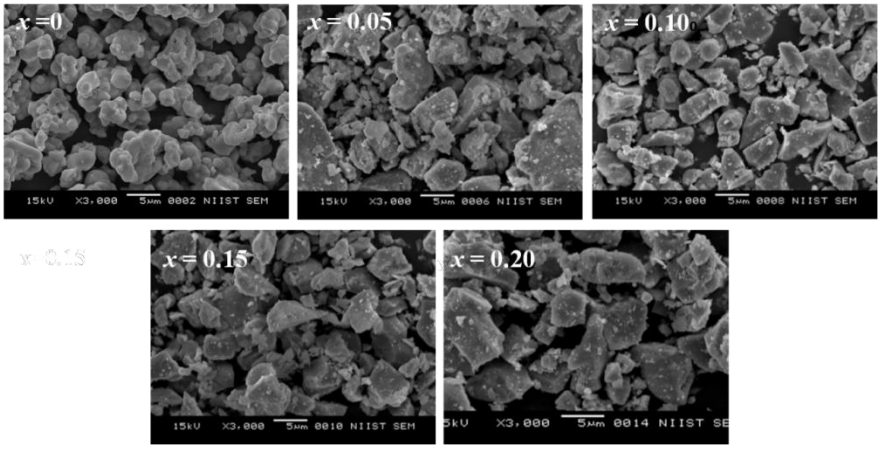

Fig. 3A.4 SEM images of $Ca_{3-x}Sn_3Nb_2O_{14}$:xEu^{3+} (x = 0, 0.05, 0.10, 0.15 and 0.20) samples.

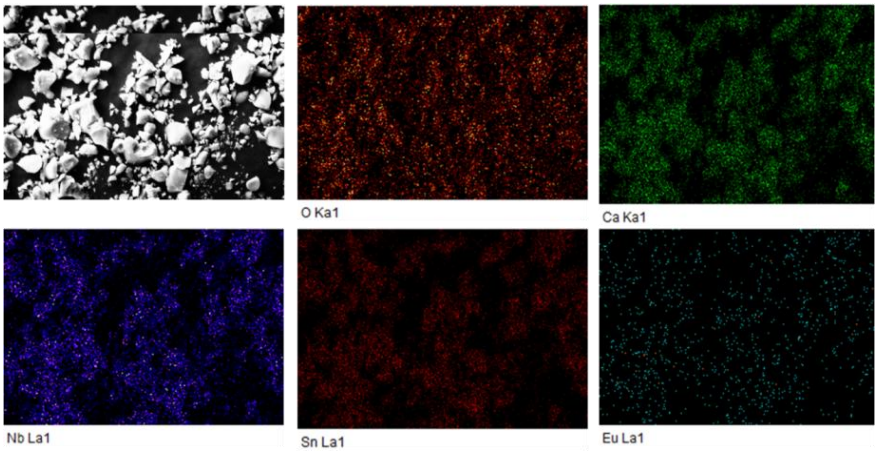

Fig. 3A.5 Elemental X-ray dot mapping of the typical $Ca_{2.85}Sn_3Nb_2O_{14}$:*0.15*Eu^{3+} phosphor synthesized at 1500°C.

Fig. 3A.4 shows the typical SEM micrographs of all the Eu^{3+}-doped samples. The overall morphologies of all the samples are more or less similar. The powder particles appear to be highly crystalline and are slightly agglomerated. The particles are in the scale of 1-5 μm in size with homogeneous nature. Elemental X-ray dot mapping analysis of the typical $Ca_{2.85}Sn_3Nb_2O_{14}$:0.*15*Eu^{3+} phosphor calcined at 1500°C for 6 h is shown in

Fig. 3A.5. This reveals that all the elements are uniformly distributed in the sample. The chemical composition of the developed phosphors was checked using energy dispersive spectrometry analysis attached with SEM (Fig. 3A.6) and we identified the presence of all expected elements and the obtained chemical compositions were close to the theoretical stoichiometry. EDS quantification with Eu^{3+} concentration confirms the increase of oxygen content in the lattice, indicating the presence of interstitial oxygen.

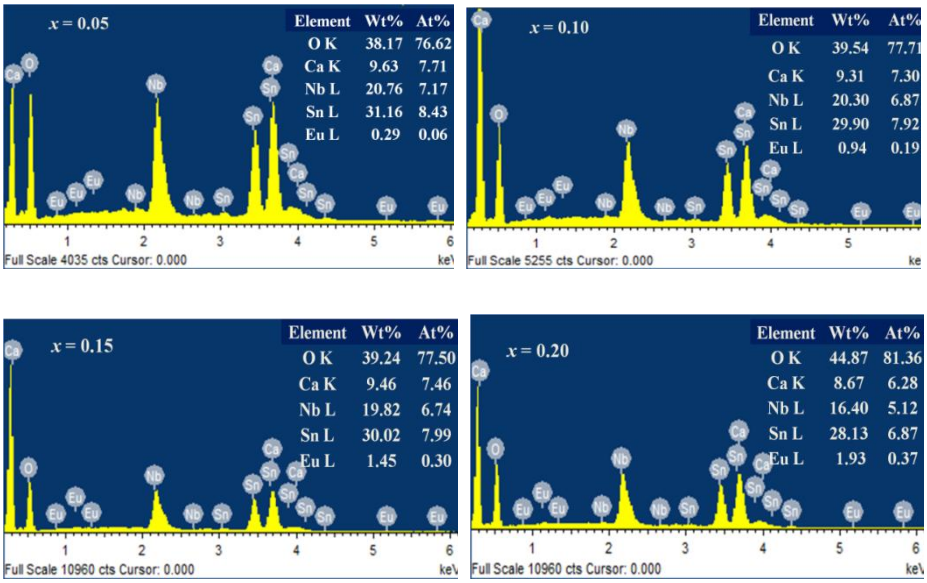

Fig. 3A.6 EDS spectra of $Ca_{3-x}Sn_3Nb_2O_{14}$:xEu^{3+}: (a) x = 0.05, (b) x = 0.10, (c) x = 0.15 and (d) x =0.20.

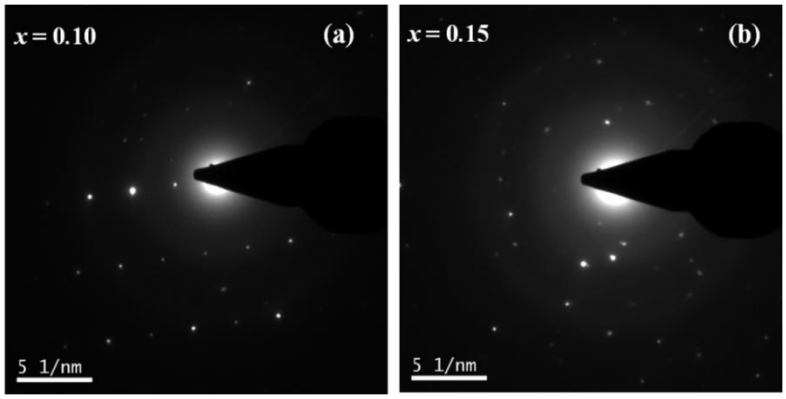

Fig. 3A.7 Selected area electron diffraction (SAED) patterns of (a) $Ca_{2.9}Sn_3Nb_2O_{14}$:*0.10*Eu^{3+} and (b) $Ca_{2.85}Sn_3Nb_2O_{14}$:*0.15*Eu^{3+} phosphors.

Fig. 3A.7 shows the typical SAED patterns of (a) $Ca_{2.9}Sn_3Nb_2O_{14}$:*0.10*Eu^{3+} and (b) $Ca_{2.85}Sn_3Nb_2O_{14}$:*0.15*Eu^{3+} phosphors calcined at 1500°C. The SAED pattern shows a polycrystalline nature of the material and the ordered diffraction maxima with weak super-lattice diffraction spots (a) further confirm the pyrochlore type unit cell in accordance with the literature (Kong *et al*. 2013). However, due to overlap of the diffraction spots from many crystals such an ordered pattern is not seen in Fig. 3A.7 (b).

3A.3.4. Absorbance and photoluminescence studies

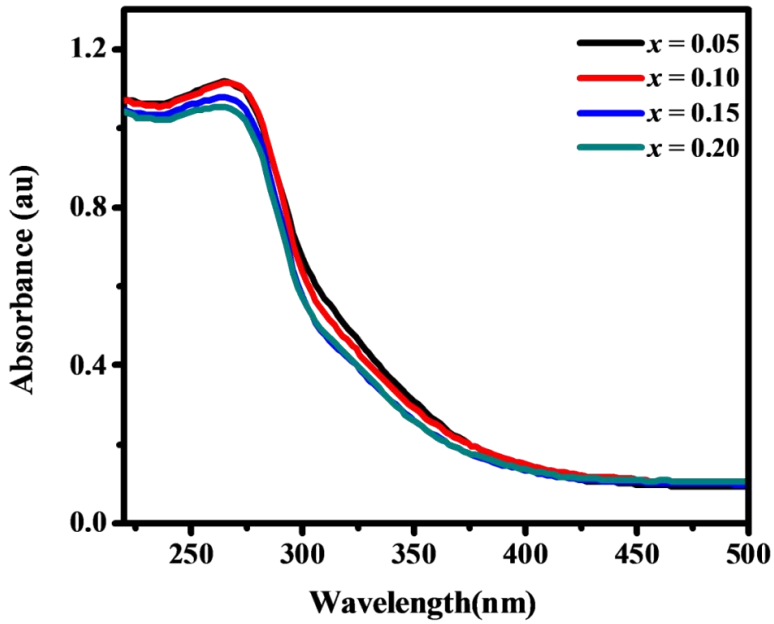

Fig. 3A.8 UV-visible absorption spectra of $Ca_{3-x}Sn_3Nb_2O_{14}$:xEu^{3+} (x = 0.05, 0.10, 0.15 and 0.20) red phosphors.

The UV-Vis absorption spectra of $Ca_{3-x}Sn_3Nb_2O_{14}$:xEu^{3+} (x = 0.05, 0.10, 0.15 and 0.20) phosphors are given in Fig. 3A.8. All the samples have a broad band of absorption in the UV region (200-375 nm) peaking at around 270 nm due to the ligand to metal charge transfer in the stannate/niobate groups and Eu^{3+}-O^{2-} in the host lattice. The degree of absorption of the Eu^{3+} level is increasing with Eu^{3+} concentration up to 15 mol%, and thereafter it gets decreased, indicating that the energy conversion from the CT states to the Eu^{3+} emitting levels is efficiently taking place. The absorption spectra showed a blue shift with increasing the concentration of Eu^{3+}, and the band gap was

calculated from the absorption spectra using Shapiro's method by extrapolating the onset of absorption to the wavelength axis and the estimated band gap energies are tabulated in Table 3A.3. Thus it is expected that the phosphors can be effectively excited in both UV and visible regions, which is further confirmed by the excitation spectra and it is one of the prerequisites for a phosphor material for pc-WLEDs.

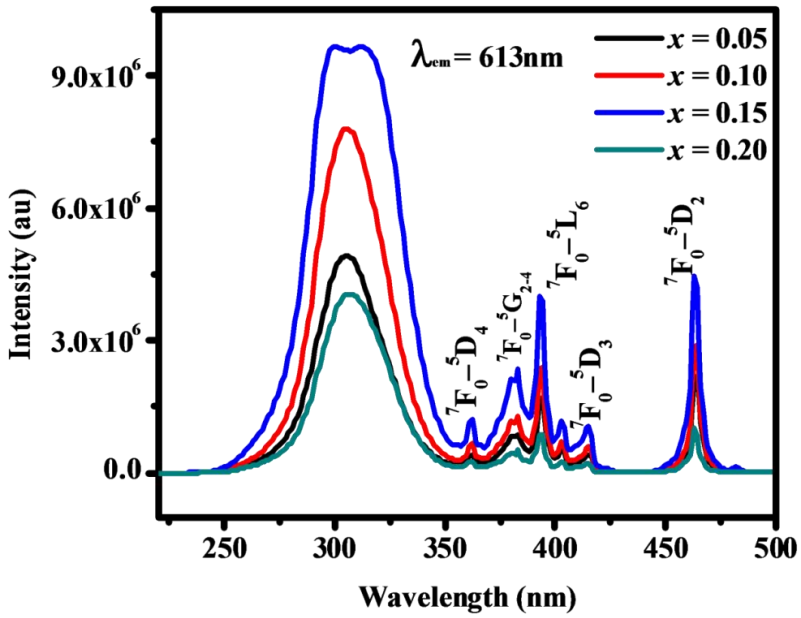

Fig. 3A.9 Excitation spectra of $Ca_{3-x}Sn_3Nb_2O_{14}$:xEu^{3+} (x = 0.05, 0.10, 0.15, 0.20) phosphors for an emission at 613 nm.

The influence of the partial substitution of Sn in both A and B sites of the pyrochlore-type oxides on the photoluminescence properties was investigated by recording the PL spectra of the developed phosphors at room temperature under identical instrumental conditions. The excitation spectra were recorded by monitoring the peak intensity at 613 nm. Fig. 3A.9 shows the excitation spectra of $Ca_{3-x}Sn_3Nb_2O_{14}$:xEu^{3+} (x = 0.05, 0.10, 0.15 and 0.20) phosphors which include a broad charge transfer (CT) band from 250-360 nm centered at 306 nm followed by a series of sharp peaks beyond 360 nm. The broad CT band is due to the merged effect of O_{2p}→Eu_{4f} and O_{2p}→Nb_{4d} charge transfer transitions. This broad band is mainly attributed to the charge transfer excitation of Eu^{3+} and the energy transfer transition from tin and niobium groups to the Eu^{3+} ions (Dutta *et al*. 2013). In complex hosts, the contributions

from more than one component in the CT band cannot be resolved due to spectral overlap (Mahesh *et al*. 2013). The CT band is red shifted with Eu^{3+} doping concentration. This shift can be attributed to an increase in covalency of Eu-O bonds and the coordination environment of the Eu^{3+} environment, which reduces the CT energy. The sharp peaks beyond 360 nm are due to the intraconfigurational (f-f) transitions of Eu^{3+} including the peaks with maxima at 362 nm ($^7F_0$-$^5D_4$), 382 nm ($^7F_0$-$^5G_{2-4}$), 394 nm ($^7F_0$-$^5L_6$), 412 nm ($^7F_0$-$^5D_3$) and 464 nm ($^7F_0$-$^5D_2$) (Thomas *et al*. 2012). The f-f transition peaks are less intense compared to the broad charge transfer band and are saturated for 15 mol% doping. Among them, the intensity of the peaks at 394 nm and 464 nm excitation wavelengths which are emission lines of near UV and blue LED chips is much stronger than the other transitions from Eu^{3+}. This implies that these samples can be effectively excited by radiation of wavelength in the near UV and blue regions.

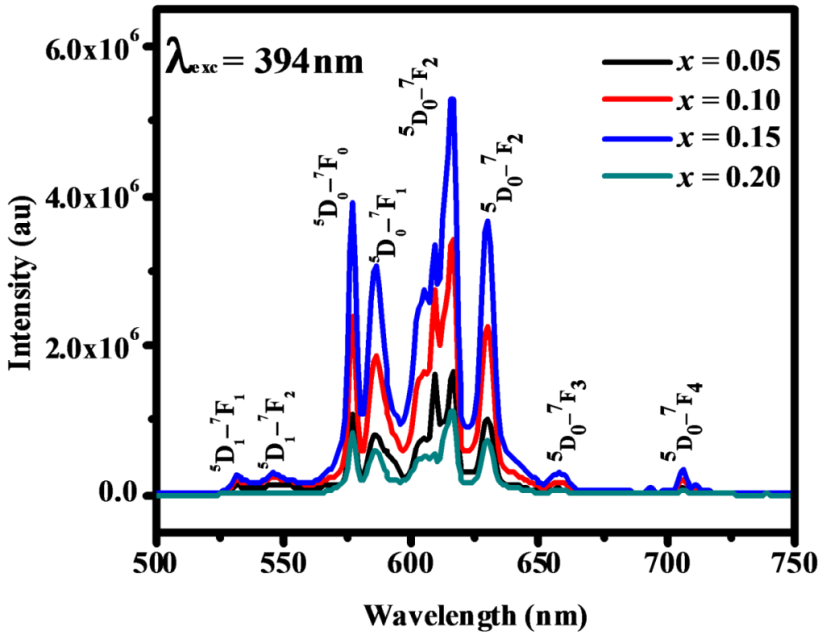

Fig. 3A.10 Emission spectra of $Ca_{3-x}Sn_3Nb_2O_{14}$:xEu^{3+} (x = 0.05, 0.10, 0.15, and 0.20) phosphors excited at 394 nm.

Fig. 3A.10 shows the emission spectra of $Ca_{3-x}Sn_3Nb_2O_{14}$:xEu^{3+} (x = 0.05, 0.10, 0.15 and 0.20) phosphors excited at 394 nm. The major emission peaks are observed at

575, 586, 614, 630 and 660 nm which can be assigned to $^5D_0$-^7F_J (J = 0, 1, 2, 3, 4) transitions of Eu^{3+} ions. According to J-O theory, (Wybourne *et al*. 2004; Judd *et al*. 1962) the emission lines are a cumulative effect of the magnetic dipole (MD) transition and the electric dipole (ED) transition depending on the specific environment of Eu^{3+}. When the Eu^{3+} ions are embedded in a site with inversion symmetry, the $^5D_0$-$^7F_1$ magnetic dipole transition is dominating, while in a site without inversion symmetry the $^5D_0$–$^7F_2$ electric dipole transition is the strongest. In the present system, the red emission peak at 613 nm is more dominant, which is due to the $^5D_0$-$^7F_2$ ED transition of Eu^{3+}, which indicates that Eu^{3+} occupies a non-centrosymmetric site (Blasse *et al*. 1979). The sharp emission without splitting at 586 nm, i.e. the orange region is assigned to MD transition ($^5D_0$-$^7F_1$) and it is insensitive to the site symmetry. When the RE ion is located in a site without inversion symmetry, the odd 4f-orbitals mix with either even 5d orbital or charge transfer orbital so that the parity selection rule is relaxed. For Eu^{3+} ions, the energy of the 5d orbital is higher than the CT band, so the mixing of the CT band with the f-orbital mainly contributes to the enhancement of forced ED transitions. Based on the D_{3d} symmetry at A site, the MD transition is expected to have splitting into two as observed in the normal pyrochlore (Lu *et al*. 2004). In contrast to this, no such splitting is observed in the present displaced pyrochlore system. As discussed in the earlier literature (Liu *et al*. 2009), displaced pyrochlores exhibit substantial displacive disorder in the A_2O' subnetwork. Dielectric relaxation is reported as the characteristic of a displacive disorder. Here, the luminescence results suggest that the single sharp emission due to MD transition is a characteristic of such displacive disorder pyrochlores due to loss of D_{3d} inversion symmetry.

One important observation is that the $^5D_0$-$^7F_0$ transition is more intense than the $^5D_0$-$^7F_1$ transition. It has been confirmed that $^5D_0$-$^7F_0$ is highly forbidden for both electric dipole and magnetic dipole transitions in a Eu^{3+} doped compound, (Wybourne *et al*. 2004; Judd *et al*. 1962; Ofelt *et al*. 1962) and therefore this abnormal phenomenon is not in agreement with Judd-Ofelt theory. Also the $^7F_0$ and $^5D_0$ levels are non-degenerate and the spectra associated with transitions between them should contain as many lines as the number of host non-equivalent sites (Du *et al*. 2011). The splitting in

this transition points out the dual or more non-equivalent site occupancy of Eu^{3+} ions (Binnemans *et al*. 1996). But, in our system, $^5D_0$-$^7F_0$ levels exhibit a sharp and single peak which offers the possibility of doping of Eu^{3+} ions to the Ca site. The unusually strong $^5D_0$-$^7F_0$ transitions have been reported in other materials, (Smentek *et al*. 2009; Souza *et al*. 2013; Pires *et al*. 1997; Piriou *et al*. 1997; Lakshminarasimhan *et al*. 2004; Fujishiro *et al*. 2013; Fujishiro *et al*. 2010) and there are different explanations for this phenomenon. One explanation is based on the mixing of two different states with different J values, the breakdown of the Wybourne-Downer mechanism and relativistic effects (Downer *et al*. 1988). Secondly, the appearance of $^5D_0$-$^7F_0$ transition of Eu^{3+} is an indication of lowering of Eu^{3+} crystal site symmetry as it is allowed only for C_s, C_n, C_{nv} site symmetries (Cockroft *et al*. 1991). Thirdly, the microstructure can also induce this transition (Piriou *et al*. 1997). It has been reported that the extra oxygen in the lattice is responsible for the unusually strongest $^5D_0$-$^7F_0$ transitions in Eu^{3+} doped Y_3SbO_7 (Wang *et al*. 2014). In our system, the last explanation is suitable because the lattice parameter calculated from the peak position in the XRD pattern confirms the presence of interstitial oxygen in the crystal lattice. The observation of this peak in the emission spectra indicates that forbidden $^5D_0$-$^7F_0$ transition can be relaxed by distortion of the Eu^{3+} environment. However, in the present system, the red emission intensity is more when compared to any other transitions and it increased with an increase in doping concentration. The enhanced ED transition intensity arises from the symmetry distortion of Eu^{3+} in most cases. Incorporation of cations with different valency and electronegativity into the crystal lattice was the reason for distortion of A site of the present pyrochlore system. The distortion of the A site symmetry and the red shift of the charge transfer energy leads to an intense $^5D_0$-$^7F_2$ hypersensitive ED transition under 394 nm excitation. The emission lines are similar for excitation wavelengths 394 (Fig. 3A.10) and 464 nm (Fig. 3A.11). However it is observed that the red emission intensity excited at the near UV region (394 nm) is greater than that of the emission excited at the blue region (464 nm).

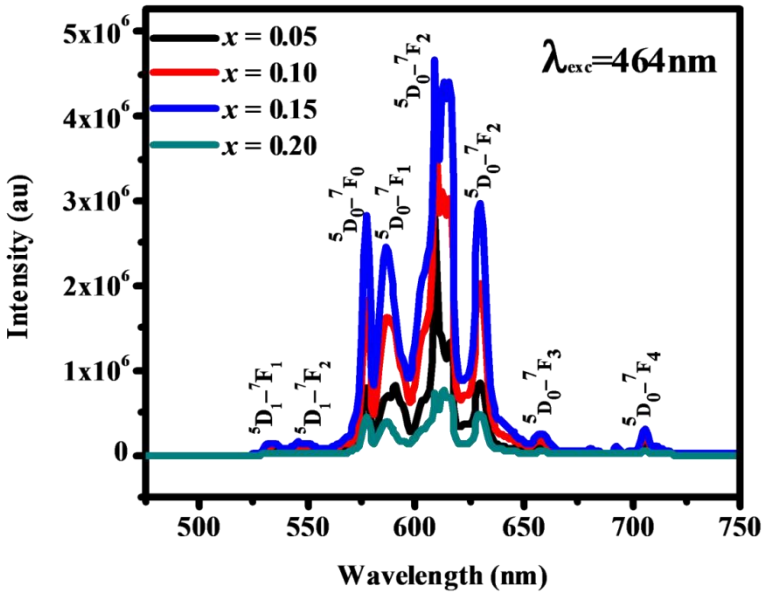

Fig. 3A.11 Emission spectra of $Ca_{3-x}Sn_3Nb_2O_{14}$:$x$$Eu^{3+}$ (x = 0.05, 0.10, 0.15, and 0.20) phosphors excited at 464 nm.

The asymmetric ratio (intensity of $^5D_0$-$^7F_2$/intensity of $^5D_0$-$^7F_1$) is a good measure of degree of distortion of the scalenohedron and the phase purity of the red color. The asymmetric ratio reveals the distortion grade from the inversion symmetry of the local environment in the vicinity of Eu^{3+} in the host matrix. For $Ca_{3-x}Sn_3Nb_2O_{14}$:$x$$Eu^{3+}$ (x = 0.05, 0.1, 0.15, and 0.2) phosphors, the asymmetric ratio decreases up to 15 mol% Eu^{3+} concentrations and then increases and the results are shown in Table 3A.3. The doping of Eu^{3+} ions to Ca^{2+} sites will decrease the amount of divalent ions in the crystal lattice, which can cause an increase in lattice symmetry and, as a result, the asymmetric ratio decreases. It can also be noted that the full width at half maximum (*fwhm*) of the red peak increases with an increase in Eu^{3+} doping concentration up to x = 0.15 and then decreases. This observation can be attributed to concentration quenching as shown in Fig. 3A.12 (Blasse *et al*. 1968; Enhai *et al*. 2011). In summary, the emission spectra of the present stannate based displaced pyrochlore-type red phosphors:$Ca_{3-x}Sn_3Nb_2O_{14}$:$x$$Eu^{3+}$, exhibit the allowed magnetic dipole transition, $^5D_0$-$^7F_1$, along with the forced electric dipole transition, $^5D_0$-$^7F_2$, and the forbidden transition, $^5D_0$-$^7F_0$, which are contrary to the D_{3d} symmetry of the pyrochlore structure. The presence of these transitions is mainly attributed to the distortion of

symmetry of the Eu^{3+} environment, mixing of $^5D_0$ states with the charge transfer states and the presence of interstitial oxygen in the lattice. Further, splitting of the $^5D_0$-$^7F_1$ transition is not observed as attributed to the displaced disorder in the lattice.

Table 3A.3 Asymmetric ratio, *fwhm* of the $^5D_0$-$^7F_2$ transition at 394nm excitation and the band gap energy of $Ca_{3-x}Sn_3Nb_2O_{14}$:xEu^{3+} (x = 0.05, 0.10, 0.15 and 0.20) phosphors

x	**Asymmetric Ratio**	***fwhm* (nm)**	**Energy gap, E_g (eV)**
0.05	1.94	7.90	3.60
0.10	1.82	11.72	3.64
0.15	1.69	13.70	3.86
0.20	1.84	10.51	3.89

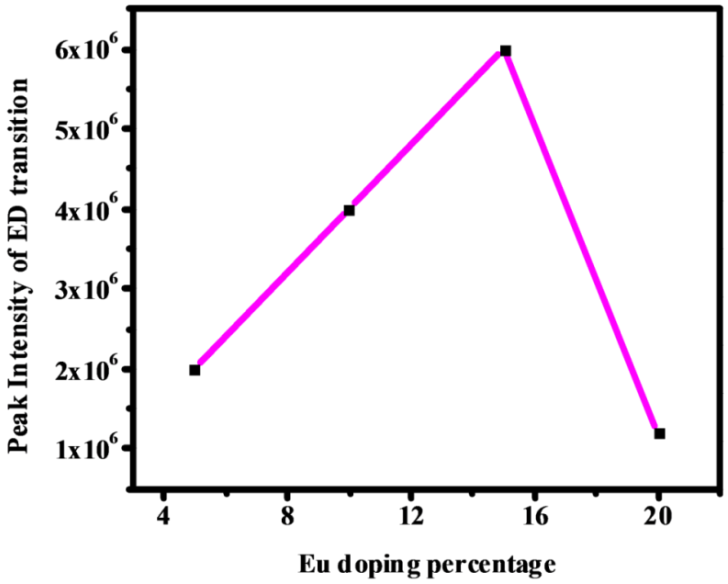

Fig. 3A.12 Peak intensities of 613 nm ED transition in $Ca_{3-x}Sn_3Nb_2O_{14}$:xEu^{3+} (x = 0.05, 0.10, 0.15, 0.20) phosphors under 394 nm

The photoluminescence decay curves for the $^5D_0$-$^7F_2$ transition of the prepared phosphors under 394 nm excitation for $Ca_{3-x}Sn_3Nb_2O_{14}$:xEu^{3+} (x = 0.05, 0.1, 0.15, and 0.2) is shown in Fig. 3A.13. All the decay curves can be fitted well using the single exponential decay function,

$$I = A\exp(-t/\tau) \qquad (3A.4)$$

where I, τ and A are intensity, decay time and fitting parameters respectively.

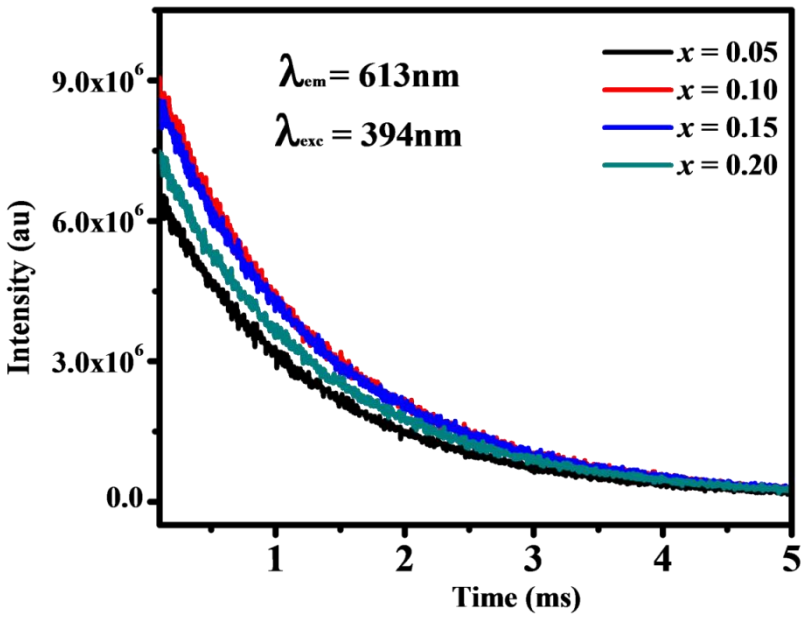

Fig. 3A.13 Lifetime decay curves of $^5D_0$-$^7F_2$ transition of Eu^{3+} (wavelength 613 nm) in $Ca_{3-x}Sn_3Nb_2O_{14}$:xEu^{3+} (x = 0.05, 0.10, 0.15 and 0.20) under 394 nm excitation.

Assuming that only radiative and non radiative processes are essentially involved in the depopulation of $^5D_0$ states of Eu^{3+} ion, the quantum efficiency (η) can be expressed as;

$$\eta = A_{rad} / (A_{rad} + A_{nrad}) \quad (3A.5)$$

where A_{rad} and A_{nrad} are the radiative and non-radiative transition probabilities respectively. The emission intensity (I) can be calculated as the integral intensity S of $^5D_0$-$^7F_{0-4}$ emission curves as;

$$I_{i-j} = \hbar\omega_{i-j} A_{i-j} N_i \sim S_{i-j} \quad (3A.6)$$

where i and j are the initial level ($^5D_0$) and the final levels ($^7F_{0-4}$), respectively; $\hbar\omega_{i-j}$ is the transition energy, A_{i-j} is the Einstein's coefficient of spontaneous emission, and N_i is the population of the $^5D_0$ emitting level. The experimental coefficients of spontaneous emission were then calculated according to the equation;

$$A_{0j} = A_{01} (I_{0j}/ I_{01}) (\nu_{01}/ \nu_{0j}) \quad (3A.7)$$

where ν_{01} and ν_{0j} are the energy baricenters of the $^5D_0$-$^7F_1$ and $^5D_0$-^7F_j energy levels determined from the emission peak of Eu^{3+} ion. A_{01} is the Einstein's coefficient of spontaneous emission between $^5D_0$ and $^7F_1$ energy levels.

In vacuum, the average refractive index (n) is 1.506 and $(A_{0-1})_{vac} = 14.64s^{-1}$ is considered. Then the value of A_{0-1} was expressed as,

$$A_{0-1} = n^3 (A_{0-1})_{vac} \sim 50s^{-1} \quad (3A.8)$$

The life time (τ) of the $^5D_0$ states, A_{rad} and A_{nrad} are related as;

$$A_{tot} = 1/\tau = A_{rad} + A_{nrad} \quad (3A.9)$$

On the basis of the emission spectra and lifetimes of the $^5D_0$ emitting level, the quantum efficiency (η) of the Eu^{3+} ion excited state can be determined using the equations 3A.5-3A.9 (Su *et al*. 2008; Peng *et al*. 2005; Linda Francis *et al*. 2014). The lifetime values and the calculated quantum efficiencies of the phosphors are listed in Table 3A.4. The lifetime of the $^5D_0$ excited state is mainly a result of the radiative and non-radiative decay rates. Here it is observed that the luminescence decay time of red emission (613 nm) of $Ca_{3-x}Sn_3Nb_2O_{14}$:$x$$Eu^{3+}$ (x = 0.05, 0.10, 0.15, and 0.20) remains almost constant (1.26-1.28 ms) though concentration quenching is observed beyond 15 mol% Eu^{3+}. To some extent here the concentration quenching is observed due to the secondary phase formation as evidenced from the XRD. As discussed above, the Eu^{3+} ion probably prefers to replace Sn instead of Ca at the A site of pyrochlore for maintaining the charge neutrality for higher substitution, leading to a minor SnO_2 secondary phase. However, the lifetime remains the same due to Eu^{3+} at a more distorted environment in a displaced position of the A site of the pyrochlore. The decay lifetimes (τ) are proportional to the transition probability. A heavier distortion of the crystallographic sites usually denotes the higher transition probability of Eu^{3+} ions. Thus the higher lifetime of the sample further confirms the more uniform distribution of Eu^{3+} ions in the $Ca_3Sn_3Nb_2O_{14}$ lattice (Yen *et al*. 2006). These long lifetimes could cause the emission to saturate when excited with high light intensities of commercial LEDs and attain the

saturation only at much higher intensities, due to the low absorption cross section of Eu^{3+}. The quantum efficiency calculated from the lifetime values was in the range of 27-30% with increasing Eu^{3+} concentration.

The Judd-Ofelt intensity parameters and the spectral parameters of the $Ca_{3-x}Sn_3Nb_2O_{14}$:xEu^{3+} (x = 0.05, 0.10, 0.15, and 0.20) phosphors tabulated in Table 3A.4 of this chapter is calculated from the emission spectrum for Eu^{3+} ion based on the $^5D_0 \rightarrow {}^7F_2$ and $^5D_0 \rightarrow {}^7F_4$ transitions and $^5D_0 \rightarrow {}^7F_1$ magnetic dipole allowed transitions as the reference. The integrated emission intensities associated with the radiative emission rates can be written as:

$$\frac{A_{0-2,4}}{A_{0-2,4}} = \frac{I_{0-2,4}}{I_{0-2,4}} \frac{h\nu_{0-2,4}}{h\nu_{0-2,4}} \tag{3A.10}$$

where I_{0-J} is the integrated emission intensity and $h\nu_{0-J}$ is the energy corresponding to transition $^5D_0 \rightarrow {}^7F_J$ (J = 1, 2, 4). The transition $^5D_0 \rightarrow {}^7F_J$ is left out due to their small emission intensities. The magnetic dipole radiative emission rate A_{0-1}has a value of ≈ 50 s^{-1}. The radiative emission rates $A_{0-2,\,4}$ are related to forced electric dipole transitions and they may be written as a function of the J-O intensity parameters:

$$A_{0-J} = \frac{64\pi^4(\nu_{0-2,4})^3 e^2}{3hc^3} \frac{1}{4\pi\epsilon_0} \chi \sum_{j=2,4,6} \Omega_j < \langle 5D_0 | U^{(J)} | 7F_{2,4} > \rangle^2 \tag{3A.11}$$

where, χ is the Lorentz local field correction factor given as function of the index of refraction n of the host $\chi = n(n^2+2)^{2/9}$. The non-zero square reduced matrix elements are solely $< \langle 5D_0 | U^{(2)} | 7F_2 > \rangle^2$=0.0032 and $< \langle 5D_0 | U^{(4)} | 7F_4 > \rangle^2$= 0.0023. Thus, using Equations (3A.10) and (3A.11) the values of $\Omega_{2,\,4}$ were obtained. The value of Ω_6 could also be estimated by analyzing the $^5D_0 \rightarrow {}^7F_6$ transition but in the present case, this emission could not be observed. The calculated Judd-Ofelt parameters have been used to predict some important radiative properties such as transition probabilities, radiative lifetime and branching ratios and lifetimes for the excited states of Eu^{3+} ions. The radiative transition probability for a transition $\Psi_J \rightarrow \Psi'_{J'}$ can be calculated from Eq. (3A.7) as $A_{rad}(\Psi_J, \Psi'_{J'}) = A_{J-J'}$.

The total radiative transition probability (A_T) can be calculated using the equation below:

$$A_T(\Psi_J) = \Sigma_{J'} A_{J-J'} \quad (3A.12)$$

The radiative lifetime $\tau_{rad}(\Psi_J)$ of an excited state in terms of A_T, is given by:

$$\tau_{rad}(\Psi_J) = \frac{1}{A_T(\Psi J)} \quad (3A.13)$$

The branching ratio $\beta(\Psi_J)$ corresponding to the emission from an excited level to its lower levels is given by:

$$\beta(\Psi_J) = \frac{1}{A_T(\Psi J)} \quad (3A.14)$$

The stimulated emission cross-section ($\sigma(\lambda_p)$) can be expressed as:

$$\sigma(\lambda_p)(J \rightarrow J') = \frac{\lambda_p^4}{8\pi c n^2 \Delta\lambda_{eff}} A_{rad}(J \rightarrow J') \quad (3A.15)$$

where λ_p is the peak wavelength and $\Delta\lambda_{eff}$ is its effective line width found by dividing the area of the emission band by its maximum height.

The J-O intensity parameters Ω_t (2 and 4) of the Eu^{3+} in the matrix $Ca_{3-x}Sn_3Nb_2O_{14}$:xEu^{3+} (x = 0.05, 0.10, 0.15 and 0.20) reveal information regarding the covalence and the surrounding of the metal ion. These intensity parameters provide information regarding the luminescence site symmetry, luminescence behavior and radiative probabilities of the activator ion in different host lattices. The parameter Ω_2 determines the covalency, polarizability and the asymmetric behavior of the activator and the ligand (short range effects) whereas Ω_4 are related to long range effects. The J-O intensity parameters $\Omega_{2\text{-}4}$ and other spectral parameters such as the branching ratio (β) and stimulated cross section (σ) were calculated as described (Som *et al*. 2014; Gupta *et al*. 2013). Since Ω_2 is most sensitive to the ligand environment, its value could reflect the asymmetry of the local environment at the Eu^{3+} ion site. The value of Ω_2 remains almost constant with Eu^{3+} concentration (up to 15 mol%) and then increases, indicating the increasing asymmetric nature of Eu^{3+} ion in the host. Generally the order of the

intensity parameters Ω_t is $\Omega_2 < \Omega_4$, but in our system the trend is reversed, $\Omega_2 > \Omega_4$. This change in trend is also in agreement with those reported previously (Raj *et al*. 2014, Kumar *et al*. 2014). It means that the efficiency for the $^5D_0$-$^7F_2$ transition becomes weak at the cost of the $^5D_0$-$^7F_1$ transition. The emission intensity could also be characterized by Ω_4 parameters. The continuous increase in the Ω_4 parameter with Eu^{3+} concentration suggests the increased efficiency of the $^5D_0$-$^7F_2$ transition, which is also evidenced in Table 3A.4. This is further supported by the increase in branching ratio of the $^5D_0$-$^7F_2$ transition compared with other transitions. The calculated value of radiative lifetime provided in Table 3A.4 indicates that this phosphor can be an effective luminescent material. The emission cross section (σ) changes differently for all the three transitions.

Table 3A.4 Spectral parameters, life time and quantum efficiency of $Ca_{3-x}Sn_3Nb_2O_{14}$:xEu^{3+} (x = 0.05, 0.10, 0.15 and 0.20) phosphors

x	J-O Intensity parameters		Transition	$A_{0\text{-}2,4}$ (s^{-1})	A_τ (s^{-1})	τ_{rad} (ms)	β (%)	σ (λ_p)	τ (ms)	η (%)
	Ω_2 (pm^2)	Ω_4 (pm^2)								
			$^5D_0$-$^7F_1$	___			22.97	132.93		
0.05	2.86	1.50	$^5D_0$-$^7F_2$	157.68	217.71	4.59	72.43	109.59	1.26	27.43
			$^5D_0$-$^7F_4$	3.95			1.81	496.94		
			$^5D_0$-$^7F_1$	___			22.89	141.81		
0.10	2.88	1.52	$^5D_0$-$^7F_2$	159.26	218.39	4.58	72.92	106.95	1.27	27.74
			$^5D_0$-$^7F_4$	4.01			1.84	489.27		
			$^5D_0$-$^7F_1$	___			23.05	148.48		
0.15	2.85	1.52	$^5D_0$-$^7F_2$	157.63	216.92	4.61	72.67	104.84	1.28	27.77
			$^5D_0$-$^7F_4$	3.99			1.84	491.99		
			$^5D_0$-$^7F_1$	___			20.96	183.95		
0.20	3.24	1.55	$^5D_0$-$^7F_2$	178.78	238.50	4.19	74.96	125.48	1.27	30.29
			$^5D_0$-$^7F_4$	4.09			1.71	592.69		

The CIE color coordinates of all four samples were calculated to be (0.60, 0.40) using the software CIE Calculator which is close to the NTSC standard values (0.67, 0.33) for a potential red phosphor. Thus, the developed red phosphors could be a suitable candidate for the red components in pc-WLEDs.

3A.4 Conclusions

A series of stannate based displaced pyrochlore type red emitting phosphors $Ca_{3-x}Sn_3Nb_2O_{14}$:$x$$Eu^{3+}$ (x = 0.05, 0.10, 0.15 and 0.20) were prepared by the conventional solid state reaction method for the first time. The influence of the partial substitution of Sn in both A and B sites of the pyrochlore-type oxides on the photoluminescence properties was studied in detail. Our results demonstrate that displacive disorder is not well evidenced by powder X-ray diffraction studies whereas Raman spectral studies indicate some amount of disorder in the lattice. Conversely photoluminescence studies exhibit intense multiband emissions due to Eu^{3+} $^5D_0$–$^7F_{0,\,1,\,2}$ transitions. The absence of characteristic MD transition splitting confirms the local cation disorder in this type of displaced pyrochlores. This can also be considered to be a characteristic of displaced pyrochlores in addition to the dielectric relaxation as reported in the literature.

Chapter 3B

EVOLUTION OF EMISSION SPECTRA WITH PARTIAL OCCUPATION OF Ti ON BOTH A AND B SITES OF THE PYROCHLORE STRUCTURE

In this chapter, the influence of partial substitution of less electronegative Ti^{4+} ion on both A and B sites of the pyrochlore-type phosphor, $Ca_{3-x}Ti_3Nb_2O_{14}:xEu^{3+}$ on the photoluminescence properties was studied. These phosphors exhibit intense sharp narrow red emissions due to Eu^{3+} $^5D_0$–$^7F_2$ transitions. A cross-cutting comparative study between titanate and stannate systems convince the role of electronegativity of B-site cation on the crystal field splitting of Eu^{3+} ions. The splitting of characteristic Eu^{3+} manifold is smaller in titanates relative to the stannate phosphors. Further, the fwhm of $^5D_0$-$^7F_2$ electric dipole transition were observed to be low for titanium substituted compositions which is ascribed to the difference in bonding environment of Ti and Sn in the host lattice.

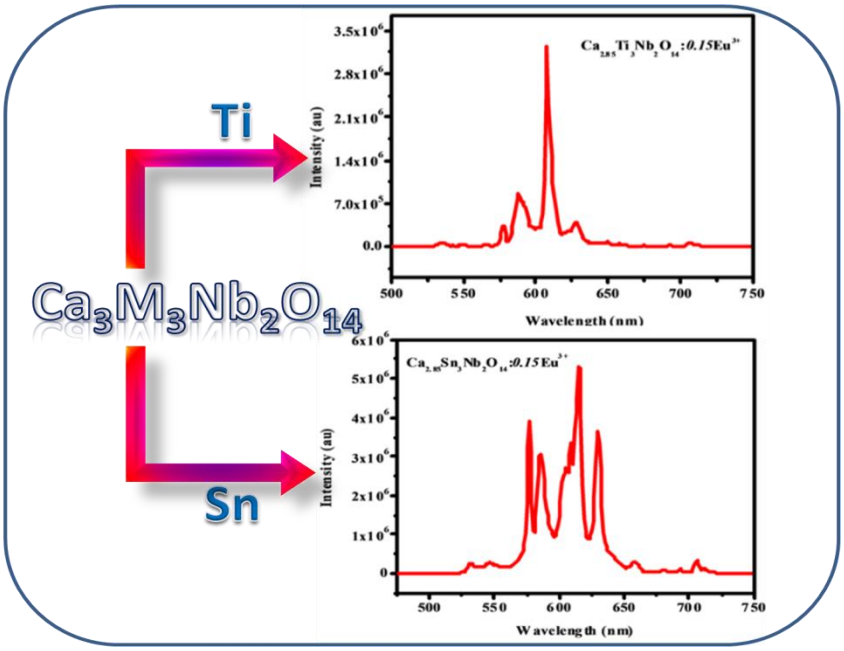

3B. 1 Introduction

The Eu^{3+} emission spectrum in solids afford a sensitive indication of structural variation because of its relatively simple energy level structure and serve as an extremely structural probe technique. Red luminescence of Eu^{3+} ions is due to their intraconfigurational f-f transitions and the emission wavelength depends mainly on the local environment in host crystals. At a site without inversion symmetry, Eu^{3+} ion exhibits hypersensitive forced electric dipole transition with emission wavelength in the range 610-615 nm. Hence for an enhanced red emission, either Eu^{3+} ion should occupy a site without inversion symmetry or charge transfer band energy should be lowered. A certain application of Eu^{3+} ion activated phosphors prefers monochromatic sharp emission rather than a multiband emission. For an ideal red phosphor for pc-WLED applications, electric dipole transition in the range 610-615 nm should have maximum intensity along with narrow *fwhm* and high asymmetric ratio. Consequently, it is more worthwhile to use crystalline host having lattice sites with little dispersion of symmetries.

In pyrochlore oxide host lattice, the crystal field splitting can be controlled upto some extent through A and B site modification. The crystal field splitting of Eu^{3+} levels in lanthanide stannate and titanate systems was scientifically examined by Srivastava (Srivastava *et al*. 2009). The crystal field splitting of Eu^{3+} levels in the pyrochlores depends on the covalency or ligand polarizability. The polarization of the $O^{2-}{}_{48f}$ electron density towards the Eu^{3+} ion is crucial in determining the magnitude of Eu^{3+} manifold splitting. According to Srivastava, rare earth cations with small ionic radii and high electronegativity polarize the $O^{2-}{}_{48f}$ electron density away from the Eu^{3+} ion, which decreases the splitting of Eu^{3+} manifold. Also, difference in the electronic configuration between Sn^{4+} and Ti^{4+} ion creates a significant difference between the natures of Sn^{4+} - $O^{2-}{}_{48f}$ and Ti^{4+} - $O^{2-}{}_{48f}$ bonding. The empty 3d orbitals of the Ti^{4+} ion are available for participate in π-bonding with the filled $O^{2-}{}_{48f}$ 2p orbitals whereas the filled $4d^{10}$ orbitals will not participate in π-bonding. Hence the transfer of charge out of the $O^{2-}{}_{48f}$ 2p orbital to the Ti^{4+} $3d^0$ orbital polarizes the ligand electron density away from the rare earth site

in titanate system. Consequently, the strength of crystal field at the Eu^{3+} site is different in stannate and titanate systems.

In the chapter 3A, the influence of partial substitution of higher electronegative tetravalent cation like Sn on both A and B sites on the photoluminescence properties was studied. The developed phosphor exhibits intense multiband emission due to Eu^{3+} $^5D_0$-$^7F_{0,\,1,\,2}$ transitions. Since Eu^{3+} emission spectrum depends on the strength of crystal field surrounding it, we tried to manipulate the emission spectra of the Eu^{3+}-pyrochlore phosphors by replacing higher electronegative Sn (1.8) with lower electronegative Ti (1.5) to obtain the host lattice of the general formulae $Ca_3Ti_3Nb_2O_{14}$. The evolution of emission spectra with partial substitution of Ti^{4+} ion on both A and B sites is also studied in detail. The spectra show strong red luminescence through forced electric dipole transition ($^5D_0 \rightarrow {}^7F_2$) under the 391 nm excitation with narrow *fwhm*. The absence of characteristic magnetic dipole transition ($^5D0 \rightarrow {}^7F_1$) splitting in contrast to the pyrochlore D_{3d} symmetry summit the local cation disorder exists in this system.

3B. 2 Experimental

3B. 2.1 Materials and Synthesis

The powder phosphors samples with the general formula $Ca_{3-x}Ti_3Nb_2O_{14}$:xEu^{3+} (x = 0, 0.05, 0.10, 0.15 and 0.20) were prepared via facile solid state reaction method. Individual oxides $CaCO_3$, TiO_2, Nb_2O_5, and Eu_2O_3 (99.9% purity; Sigma-Aldrich, Steinheim, Germany) were used as the starting materials. These oxides were weighed in the required stoichiometric ratio and then finely ground and mixed in an agate mortar using acetone as the wetting medium. The samples were dried in an air oven at a temperature of 100°C for half an hour. This procedure of mixing and drying was repeated three times to attain a homogeneous product. The mixed product was made into a pellet and then calcined on an alumina plate in an air atmosphere furnace. The samples were initially calcined at 1300°C for 6h and the calcination was repeated at 1500°C for 6h with intermittent grinding until a phase pure compound was obtained. The calcined pellet was then ground into fine powder for further characterization.

3B. 2.2 Characterization

The crystalline structure of the prepared powder samples was examined by recording the X-ray powder diffraction (XRD) pattern using a PANalytical X'Pert Pro diffractometer. The Raman spectra of the powder samples were obtained using an integrated micro-Raman system having a 633 nm helium-neon laser with a 2 μm spatial resolution. The morphology of powder particles was studied using a scanning electron microscope (Carl Zeiss EVO 18) operated at 20 kV. The elemental mapping of the samples was carried out using a Silicon Drift Detector-X-Max^N attached with the SEM. Absorbance study of the samples were carried out using a Shimadzu UV-3600 UV-Vis spectrophotometer in the 200-500 nm wavelength range using barium sulfate as a reference. The excitation and emission spectra were recorded at room temperature using a Spex-Fluorolog DM3000F spectrofluorimeter with a xenon flash lamp (450 W) as the excitation source. The luminescence lifetime of the phosphors was recorded using the phosphorimeter attached to a Fluorolog®3 spectrofluorimeter.

3B. 3 Results and discussion

3B. 3.1 Powder X-ray diffraction studies

The powder X-ray diffraction patterns of $Ca_{3-x}Ti_3Nb_2O_{14}$:xEu^{3+} (x = 0, 0.05, 0.10, 0.15 and 0.20) phosphors calcined at 1500°C is shown in Fig. 3B.1. The sharp and high intensity peaks proposes the high degree of crystallinity of the samples. It is very clear that all diffraction peaks of the product can be readily indexed to the cubic pyrochlore structure with a space group *Fd3m* (JCPDS file no. 037-0191). A close examination of powder XRDs shows no evidence to suggest the precipitation of any secondary phase from the solid solutions. Another interesting observation is that the intensity of characteristic superstructure peak (111) systematically diminishes with Eu^{3+} concentration (Fig. 3B.2). This can be elucidated based on the relative ionic sizes of the cations occupying both the A and B sites in the pyrochlore structure.

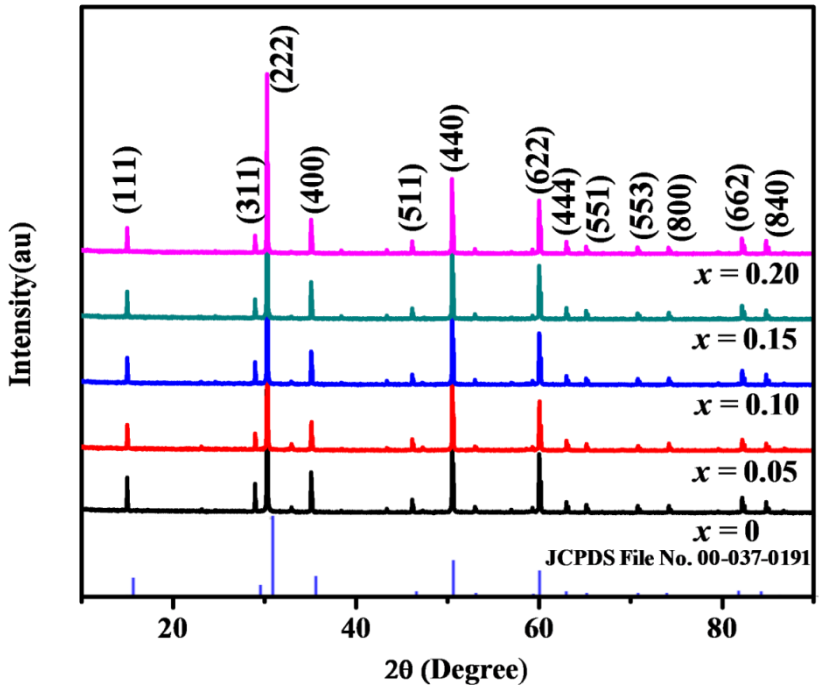

Fig. 3B.1 Powder X-ray diffraction patterns of $Ca_{3-x}Ti_3Nb_2O_{14}$:xEu^{3+} (x = 0, 0.05, 0.10, 0.15 and 0.20) red phosphors.

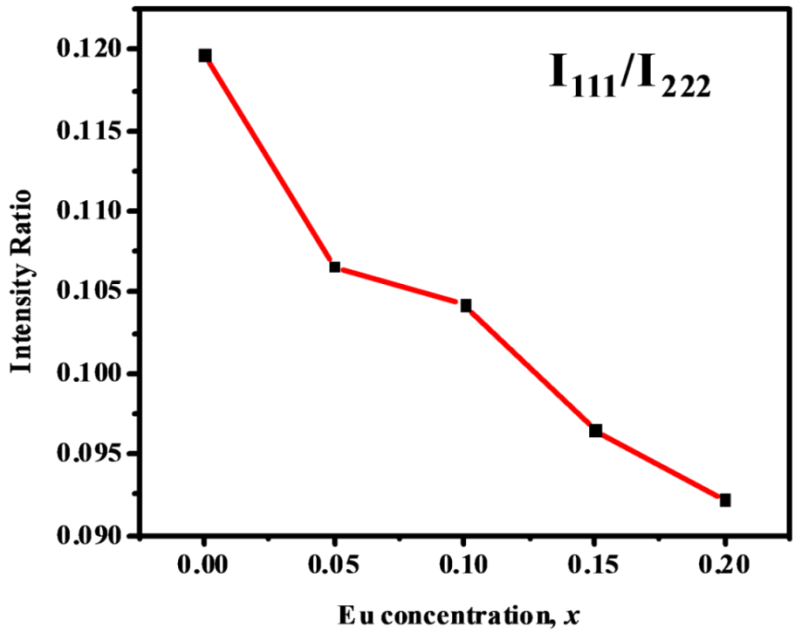

Fig. 3B.2 Variation of the superlattice peak intensity ratio I_{111}/I_{222} as a function of Eu^{3+} concentration in $Ca_{3-x}Ti_3Nb_2O_{14}$:xEu^{3+} (x = 0, 0.05, 0.10, 0.15 and 0.20).

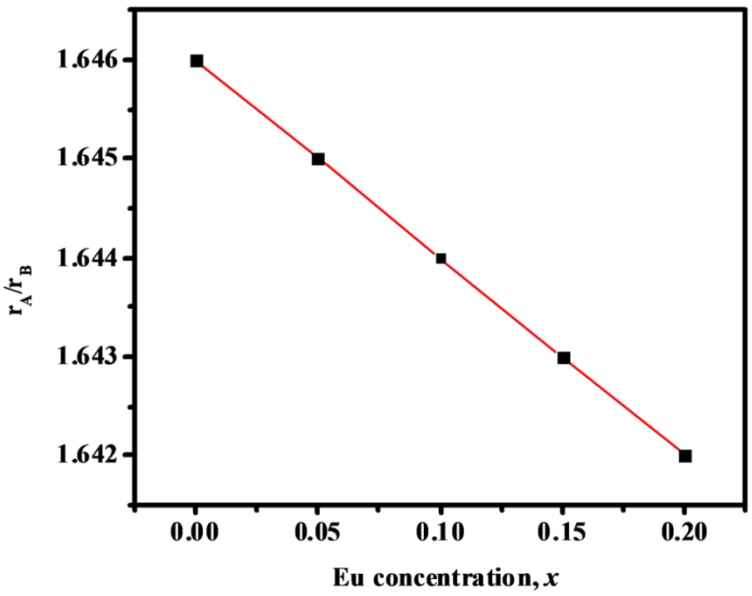

Fig. 3B.3 Variation of radius ratio with Eu^{3+} concentration in $Ca_{3-x}Ti_3Nb_2O_{14}$:xEu^{3+} (x = 0, 0.05, 0.10, 0.15 and 0.20) phosphor.

In these compounds, the ionic radius of Ca^{2+} and Eu^{3+} with eight- coordination is 1.12 and 1.07 Å, respectively, and those of Ti^{4+} and Nb^{5+} in six-coordination is 0.61 and 0.64 Å, respectively (Shannon 1976). The high ionic radii cations Ca and Eu occupy the A sites and the lower ionic radii cations of Ti and Nb occupy the B sites to keep the ratio of the ionic radius of cations at A site to that at the B site within the tolerance range (1.46-1.80). According to crystal chemistry principle, the site neutrality can be achieved by the distribution of Ti^{4+} cations over these two sites, allowing some excitability into this geometrically rigid structure. The partial occupation of the Ti^{4+} ion on both A and B sites induce significant local lattice distortion makes the system in a disordered state reducing the pyrochlore D_{3d} symmetry which is reflected in the emission spectra. But it is to be remembered that Ti is too small to occupy the large eightfold coordinated environment in the pyrochlores. But, recent studies of the pyrochlores in $((Ca_{1.5}Ti_{0.5})NbTi)O_7$ (Nguyen *et al*. 2008) and $CaO\text{-}TiO_2\text{-}(Nb,Ta)_2O_5$ (Roth *et al.* 2008) suggested that Ti^{4+} ions (up to 25% of the large A-sites) mixes with the much larger Ca^{2+} ions on the A-sites by displacing from the ideal eight-coordinated position to achieve satisfactory coordination environment. Based on these results, it is reasonable to assume that the present pyrochlore oxide involve mixing of three cations (Ca, Ti and

Eu) on A site and two types of cations (Ti, Nb) on the B sites. The radius ratio r_A/r_B were calculated accordingly (r_A and r_B are the average ionic radii of the A and B cations) and the values vary linearly from 1.646 to 1.642 (Fig. 3B.3), which is within the limiting radius required for the stabilization of pyrochlore type structure. It is well-known that (Minervini *et al*. 2000), as the radius ratio decreases the pyrochlore structure tends to get converted from a well-ordered structure to a somewhat disordered structure, where the super-structure peaks diminish.

To establish the crystal structure accurately, Rietveld analysis was carried out on all the samples using X'pert HighScore Plus software. The crystal structure of the samples was refined from powder X-ray data, in the *Fd3m* cubic space group. Eu^{3+} ions are expected to occupy the Ca^{2+} lattice position because of their similar ionic radius. Since Eu^{3+} ions can occupy Ca^{2+}/Ti^{4+} site (A site), it is difficult to make an assumption about the site of occupation of Eu^{3+} ions in the lattice. Based on the Rietveld refinement, a significant change in the *x* positional parameter of oxygen was obtained by varying the Eu^{3+} ion concentration which increases upto $x = 0.15$ and decreases thereafter. As the value of oxygen positional parameter *x* increases, A site scalenohedra becomes less distorted since the *48f* anions are somewhat shifted from the centre O_6O' stoichiometry. The electrostatic repulsion between the exposed Ti-site cations is compensated by the displacement of *48f* oxygen towards the Ti-site cation. Thus, *48f* oxygen *x* parameter is a measure of the degree of structural distortion of TiO_6 octahedra. From the structural analysis, we deduce that Eu^{3+} ions occupy the Ca^{2+} site upto $x = 0.15$ and on further substitution it prefers to occupy the Ti-displaced site for maintaining charge neutrality. Fig. 3B.4 shows the Rietveld refinement pattern of $Ca_{2.85}Ti_3Nb_2O_{14}$:*0.15*Eu^{3+} phosphor and the refinement results are given in Table 3B.1. From the table, it is seen that lattice parameter of the samples increases with an increase in Eu^{3+} concentration. As Eu^{3+} ion replaces Ca^{2+} having a high ionic radius, the lattice value should decrease. Such discrepancy in the XRD pattern may be due to interstitial oxygen ions in the crystal lattice for maintaining the electrical neutrality of the system. However, at higher concentrations with decreasing oxygen positional parameter Ti-O distance increases and increases the lattice parameter.

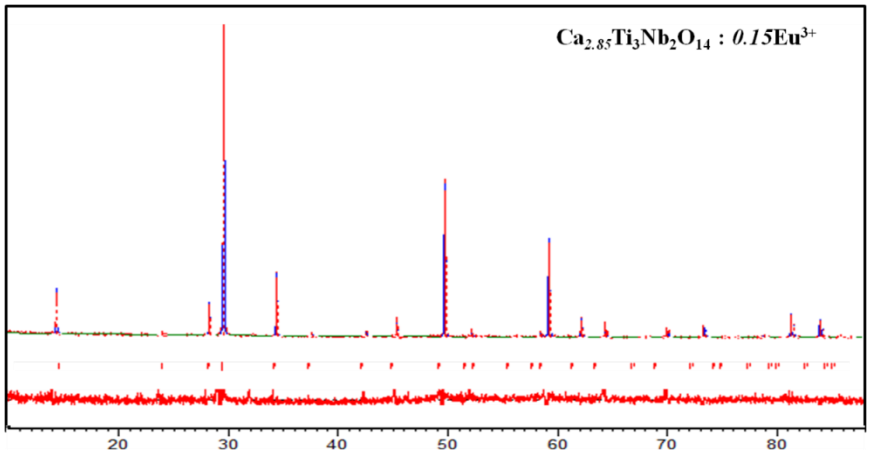

Fig. 3B.4 Observed, calculated and difference X-ray diffraction pattern of $Ca_{2.85}Ti_3Nb_2O_{14}$:*0.15*Eu^{3+} phosphor

Table 3B.1 Rietveld refinement results of $Ca_{3-x}Ti_3Nb_2O_{14}$:xEu^{3+} (x = 0, 0.05, 0.10, 0.15 and 0.20) red phosphors.

Sample	***x* = 0**	***x* = 0.05**	***x* = 0.10**	***x* = 0.15**	***x* = 0.20**
Phase	Pyrochlore	Pyrochlore	Pyrochlore	Pyrochlore	Pyrochlore
Unit cell	Cubic	Cubic	Cubic	Cubic	Cubic
Space group	*Fd3m*	*Fd3m*	*Fd3m*	*Fd3m*	*Fd3m*
Lattice constant (Å)	10.2162(9)	10.2166(1)	10.2174(9)	10.2178(9)	10.2187(9)
Flat background	78.6893	74.6906	79.4292	80.7046	78.7109
Coefficient 1	-34.9942	-31.8265	-33.6036	-36.0049	-35.4796
Coefficient 2	26.0352	24.12000	26.5289	28.5929	29.8435
Scale factor	0.000011	0.000008	0.000009	0.000009	0.000008
Oxygen *x* parameter	0.3248(5)	0.3267(3)	0.3272(6)	0.3272(5)	0.3201(5)
Caglioti parameters					
U	0.008(1)	0.016(2)	0.015(4)	0.009(1)	0.007(1)
V	-0.004(1)	-0.012(2)	0.000(3)	-0.006(1)	-0.006(1)
W	0.0031(3)	0.0056(4)	0.0051(6)	0.0034(3)	0.0039(3)
R parameters					
R_{exp}(%)	9.41	9.85	9.56	9.49	9.59
R_p(%)	9.57	9.81	9.16	8.93	8.96
R_{wp}(%)	12.72	13.25	12.11	11.87	11.71
R_{Bragg} (%)	4.75	3.89	3.97	3.26	3.76
GOF	1.83	1.81	1.60	1.57	1.49

3B. 3.2 Raman spectroscopic studies

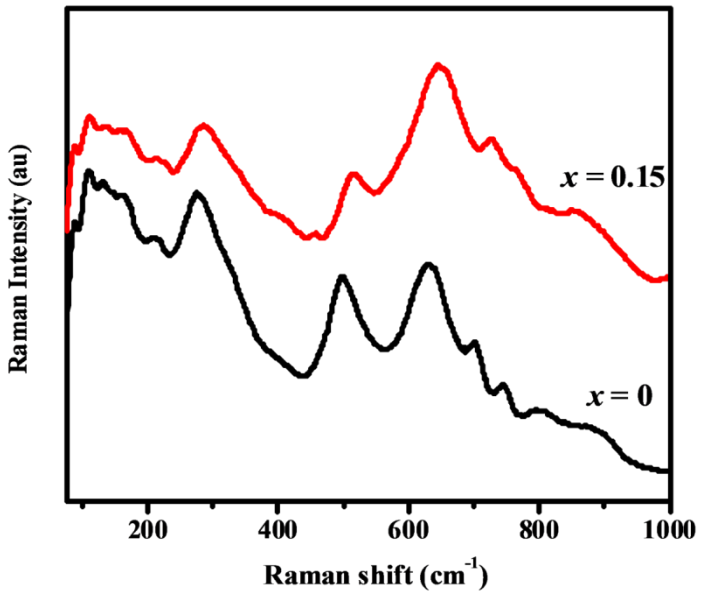

Fig. 3B.5 FT Raman spectra of $Ca_{3-x}Ti_3Nb_2O_{14}$:xEu^{3+} (x = 0 and 0.15) phosphors.

Table 3B.2 Raman mode frequencies with symmetry character and modes of vibration of $Ca_{3-x}Ti_3Nb_2O_{14}$:xEu^{3+} (x = 0 and 0.15) red phosphor.

Wavenumber (cm^{-1})		Symmetry	Mode of vibration
x = 0	x = 0.15		
109	112	F_{2g}	A-O stretching
210	223	F_{2g}	A-O stretching
278	288	E_g	O-B-O bond bending
500	515	A_{1g}	O-B-O bond bending with mixture of B-O stretching
630	632	F_{2g}	B-O stretching
747	770	A_{1g}	B-O stretching

$Ca_{3-x}Ti_3Nb_2O_{14}$:xEu^{3+} (x = 0 and 0.15) powder samples were examined by Raman spectroscopy for further structural information and is plotted in Fig. 3B.5. Raman modes of the undoped and 15mol% Eu^{3+} doped pyrochlore oxides are shown in Table 3B.2. The vibrational modes in the Raman spectra can be tentatively assigned to symmetry species by comparing with previously published Raman spectra of pyrochlore oxides. The Raman mode assignment in the present study has been done following Vandenborre's Raman spectroscopy work on pyrochlores (Vandenborre *et al*. 1983). Due to the inherent disorder in the system all Raman modes appears as broad

peaks as compared to that of well-ordered crystalline compounds. Similar to the stannate pyrochlore, the whole Raman bands will have some extent of frequency shift in the titanate system.

The typical Raman modes of $Ca_{3-x}Ti_3Nb_2O_{14}$:xEu^{3+} (x = 0 and 0.15) samples were found to be located at 109, 210, 278, 500 and 630 cm^{-1}. In contrast to the ideal pyrochlores, some extra Raman modes at the low frequency region were observed in the system which indicates the additional displacement of A and O' sites from the ideal atomic positions in the pyrochlore structure. Two species ions located at A and B site would lead to two different vibration bands. The lowest frequency lines, 109 and 210 cm^{-1} are undoubtedly assigned to the F_{2g} mode. The most notable difference is the significant increase of Raman shift at 210 cm^{-1} in intensity and full-width-at-half-maximum (*fwhm*) with increasing Eu^{3+} concentration. The peak observed at around 278 cm^{-1} can be assigned to E_g mode which is sensitive to the nature of cation associated with the Ti-O anion. Also prominently, the A_{1g} mode occurring at around 500 cm^{-1} shifts to higher wavenumbers with Eu^{3+} doping. The variation of F_{2g} mode (~ 210 cm^{-1}) confirm that excess Ti^{4+} ions entered the A sites. Since A_{1g} and E_g modes are the vibrations of TiO_6 octahedra, the increase in a force field is more likely because of shortening of Ti-O bond. As a result, Raman peaks appear at a higher frequency. But the broad bands of the Nb-O band and Ti-O stretching mode at about 630 cm^{-1} exhibited hardly any variation between the various crystalline pyrochlore compositions, that indicate the concentration of Nb^{5+} and Ti^{4+} ions at B site keeping stable but the ion concentration in A site varies with the chemical constitution change. Thus, from the Raman spectroscopy studies, it is reasonable to reckon that Ti^{4+} ions is inclined to occupy B site firstly, and then enter into A site after the B site was fully occupy.

3B. 3.3 Morphological studies

Scanning electron micrographs of all the Eu^{3+}-doped samples $Ca_{3-x}Ti_3Nb_2O_{14}$:xEu^{3+} (x = 0.05, 0.10, 0.15 and 0.20) are given in Fig. 3B.6. All the samples were slightly agglomerated and the particle sizes are in the range 1–5 μm. Elemental X-ray dot mapping analysis of the samples was also carried out to study the distribution

of elements in the sample. Fig. 3B.7 shows the typical X-ray dot mapping of $Ca_{2.85}Ti_3Nb_2O_{14}$:0.*15*Eu^{3+} phosphor. This confirms that all the elements are uniformly distributed in the sample.

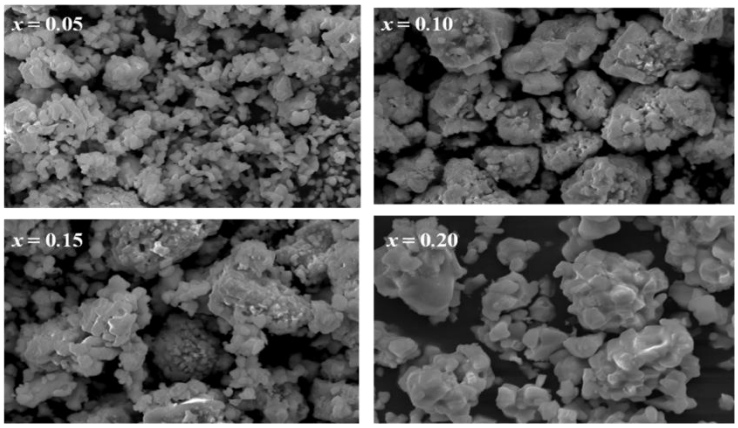

Fig. 3B.6 Scanning electron micrographs of $Ca_{3-x}Ti_3Nb_2O_{14}$:$x$$Eu^{3+}$ (x = 0.05, 0.10, 0.15 and 0.20) phosphor.

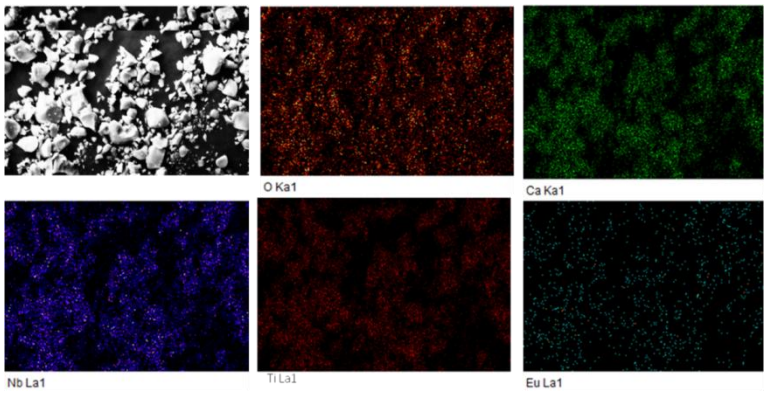

Fig. 3B.7 Elemental X-ray dot mapping of the typical $Ca_{2.85}Ti_3Nb_2O_{14}$:*0.15*Eu^{3+} phosphor synthesized at 1500°C.

3B.3.4. Optical studies

The UV-visible absorption spectra of $Ca_{3-x}Ti_3Nb_2O_{14}$:$x$$Eu^{3+}$ (x = 0, 0.05, 0.10, 0.15 and 0.20) phosphors are shown in Fig. 3B.8. The absorption spectra of all the samples exhibits a broad absorption band in the UV region (200-375 nm) with maxima at around 300 nm due to the charge transfer from the oxygen ligand to central titanate/niobate groups and Eu^{3+}-O^{2-} in the host lattice. The absorption edge shifted

towards higher wavelength side with increasing the concentration of Eu^{3+}, and the band gap energy calculated from the absorption spectra decreases and the estimated band gap energies are tabulated in Table 3B.2. It is noticeable that the intensity of absorbance of host is greater than that of doped samples indicating the efficient energy conversion from the charge transfer states to the Eu^{3+} emitting levels. Thus, the developed phosphors are excitable under both near UV and blue irradiation.

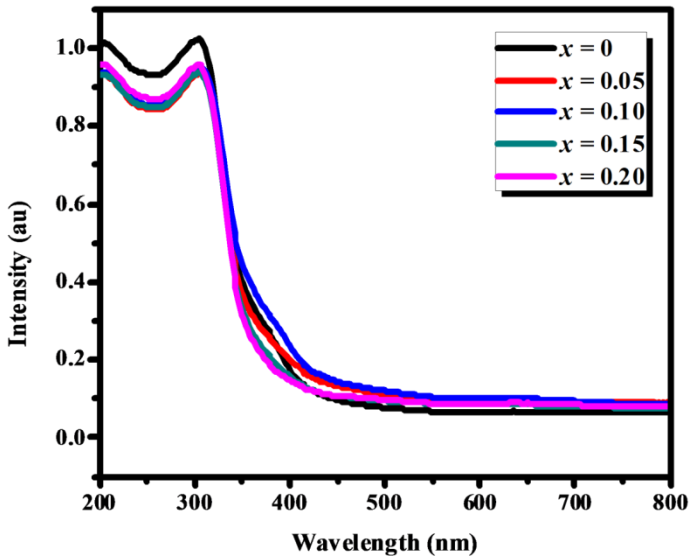

Fig. 3B.8 UV-visible absorption spectra of $Ca_{3-x}Ti_3Nb_2O_{14}$:xEu^{3+} (x = 0, 0.05, 0.10, 0.15 and 0.20) red phosphors.

Fig. 3B.9 shows the excitation spectra of $Ca_{3-x}Ti_3Nb_2O_{14}$:xEu^{3+} (x = 0.05, 0.10, 0.15 and 0.20) phosphors monitoring the emission of Eu^{3+} at 613 nm. A weak broad excitation band ranging from 250 to 350 nm peaking at 329 nm appears which can be attributed to the charge transfer (CT) band between the Eu^{3+} and the surrounding oxygen anions. However, the *fwhm* of CT band is more for titanate pyrochlores than the stannate pyrochlores. The CT band position, *fwhm* and intensity depend on the electronegativity difference between ligand and metal (Blasse *et al*. 1979). Although, the CT band position shifts to higher wavelength side with increasing the concentration of Eu^{3+} ion. Generally the CT band position of $O^{2-} \rightarrow Eu^{3+}$ lies in the wavelength region 230 nm taking into account of the electronegativities of O^{2-} and Eu^{3+} ions (Dorenbos *et al*. 2005). Moreover the CT band position is closely related to the coordination

environment of Eu^{3+} ions in the host lattice and the bond length of Eu^{3+} and anions. The band position is more or less fixed in VI coordination and varies in VIII and IX coordination as a function of Eu-O bond distance in the host lattice (Hoefdraad *et al*. 1975).

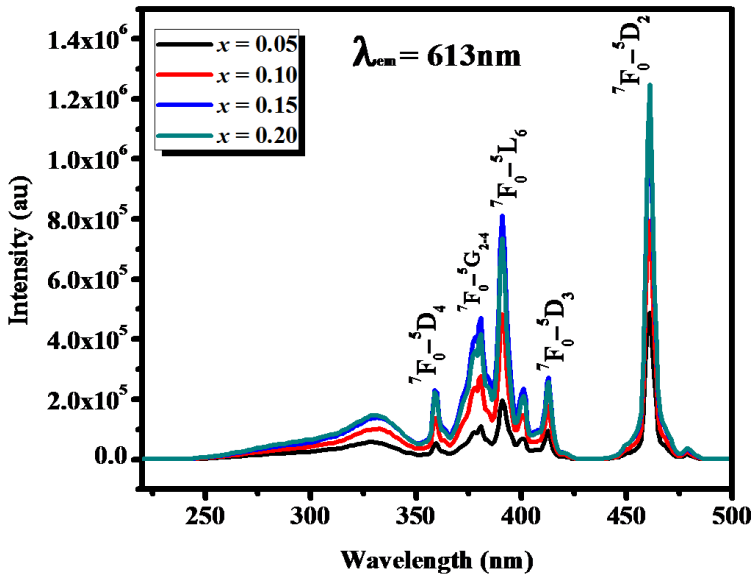

Fig. 3B.9 Excitation spectra of $Ca_{3-x}Ti_3Nb_2O_{14}$:xEu^{3+} (x = 0.05, 0.10, 0.15, 0.20) for an emission at 613 nm.

The O^{2-}- Eu^{3+} CT energy will decrease if we reduce the electronegativity of the surrounding ligands. It is noted that with decrease in the effective electronegativity of the A and B sites of pyrochlore phosphors, mixing of f-orbital and CT wave functions take place that in turn promote the f-f transitions. The sharp peaks observed beyond CT band are due to the intra-$4f^6$ configurations of Eu^{3+} ion. Since the intraconfigurational f-f transitions are not so much sensitive to the host lattice, there is no change in f-f transition peak position with Eu^{3+} concentration. However, the f-f transition peaks are more intense compared to the CT band. In addition, with the increase in Eu^{3+} concentration, the excitation lines at 391 and 461 nm become stronger, which are the emission wavelength of near UV and blue LED chips. Therefore, a red phosphor with high efficiency excited with near UV or blue light can be achieved by adjusting Eu^{3+} concentrations.

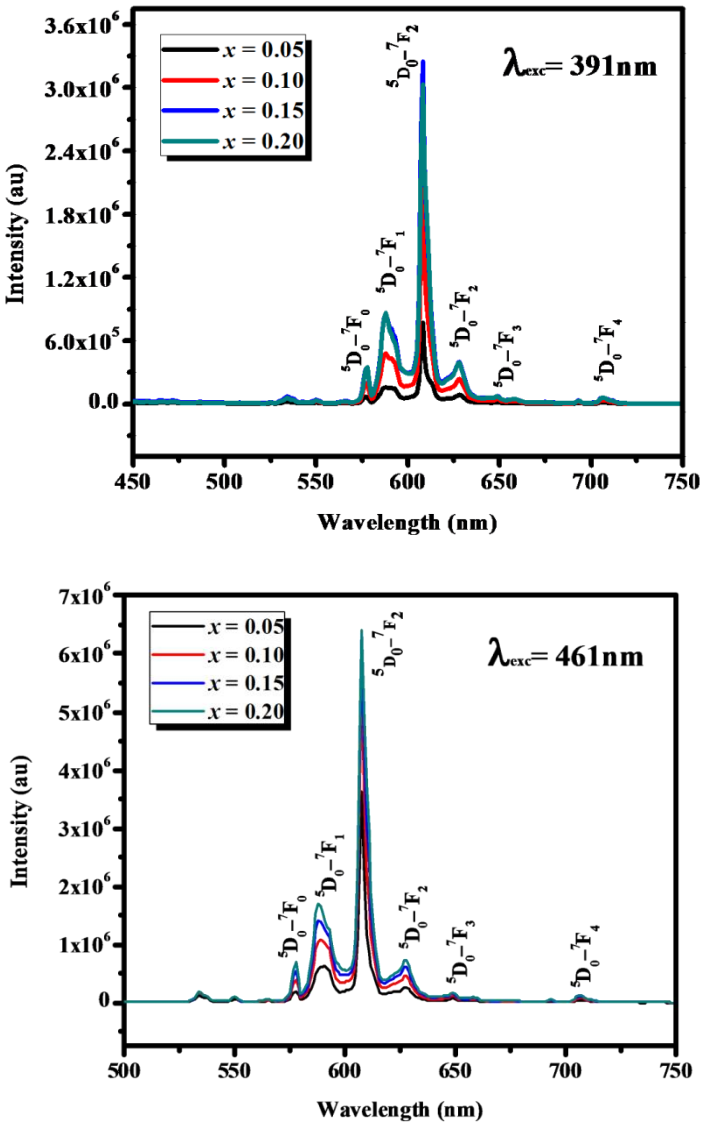

Fig. 3B.10 Emission spectra of $Ca_{3-x}Ti_3Nb_2O_{14}$:xEu^{3+} (x = 0.05, 0.10, 0.15, and 0.20) excited at 391 and 461 nm.

The emission spectra of $Ca_{3-x}Ti_3Nb_2O_{14}$:xEu^{3+} (x = 0.05, 0.10, 0.15 and 0.20) phosphors excited at 391 and 461 nm is shown in Fig. 3B.10. In all the samples, the intensity of $^5D_0$-$^7F_2$ electric dipole transition is higher than that of $^5D_0$-$^7F_1$ magnetic dipole transition, a clear indication of the occupation of Eu^{3+} ion in a noncentrosymmetic site in the host lattice. Also, the intensity of red emission increases with increase in doping concentration. The enhanced electric dipole transition arises from the symmetry distortion of Eu^{3+} ion in the host lattice. The asymmetric ratio of

$Ca_{3-x}Ti_3Nb_2O_{14}$:xEu^{3+} phosphor is more compared to $Ca_{3-x}Sn_3Nb_2O_{14}$:xEu^{3+} as given in Table 3B.3. Accommodation of cations with different valency and electronegativity to the crystal lattice was the reason for distortion of A site of present pyrochlore system. The doping of Eu^{3+} ions to Ca^{2+} site will decrease the amount of divalent cations in the lattice resulting in increase in lattice symmetry. This is confirmed by the asymmetric ratio value which decreases with Eu^{3+} doping. Moreover, the presence of the multiple peaks for $^5D_0$-$^7F_2$ transition is attributed to the Stark components of splitting of $^7F_2$ levels, perhaps due to the alteration of local crystal field strength of $Ca_3Ti_3Nb_2O_{14}$ host on account of Eu^{3+} doping.

Table 3B.3 Optical properties of $Ca_{3-x}Ti_3Nb_2O_{14}$:xEu^{3+} (x = 0.05, 0.10, 0.15 and 0.20) phosphors.

x	E_g (eV)	CTB (nm)	Asymmetric Ratio	Lifetime (ms)	Efficiency η (%)	Color Coordinates (x, y)
0.05	3.48	329	4.96	0.87	26.68	(0.57, 0.36)
0.10	3.39	331	4.59	0.89	26.72	(0.58, 0.36)
0.15	3.36	333	3.95	0.90	26.80	(0.60, 0.36)
0.20	3.33	334	3.66	0.93	27.16	(0.60, 0.37)

The full width half maxima of $^5D_0$-$^7F_2$ ED transition were observed to be low for titanate systems. In normal pyrochlore phosphors, based on D_{3d} symmetry at A site, the magnetic dipole transition is expected to have splitting into two. Similar to the stannate system, no such splitting is observed in the titanate phosphors. Hence, the presence of single sharp emission due to MD transition without splitting can be considered as an important characteristic of displaced pyrochlores. In contrast to the stannate phosphors, the $^5D_0$-$^7F_1$ transition is more dominant than $^5D_0$-$^7F_0$ transition in titanate system. However, $^5D_0$-$^7F_0$ transition appears as a single peak which confirms the single site occupancy of Eu^{3+} ions in the host lattice. A detailed comparison of luminescence properties of stannate and titanate systems are given in later part of this chapter. The emission profiles are similar for excitation under 391 and 461 nm. However it is observed that the red emission intensity excited at the blue region (461 nm) is greater compared to the excitation at near UV region (391 nm). Also, no concentration

quenching is observed in titanate phosphors at 461 nm excitation. This may be due to the difference in bonding of Ti in the host lattice. Since Eu^{3+} ions replaces Ca^{2+} ions in A site, the incorporation of Ti atoms to the A site can block resonance energy transfer between Eu^{3+} and neighbor ions and results in increased quenching concentration.

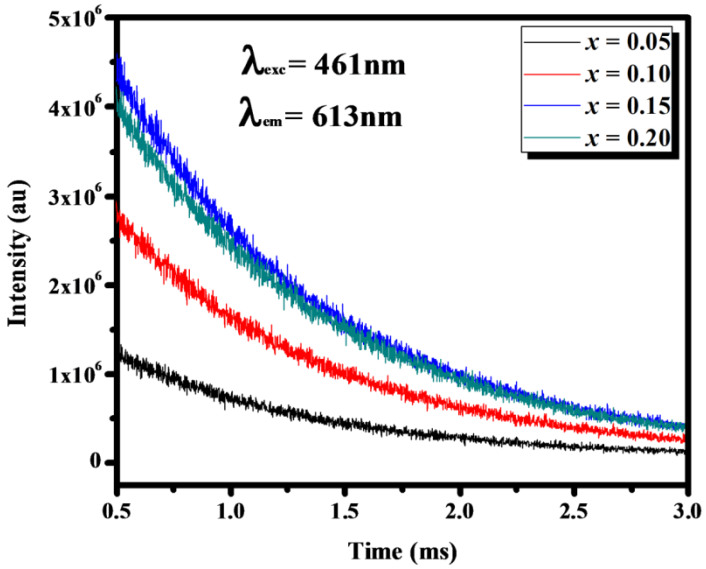

Fig. 3B.11 Lifetime decay curves of $^5D_0$-$^7F_2$ transition of Eu^{3+} (wavelength 613 nm) in $Ca_{3-x}Ti_3Nb_2O_{14}$:$x$$Eu^{3+}$ (x = 0.05, 0.10, 0.15 and 0.20) under 461 nm excitation.

The photoluminescence decay curves of $Ca_{3-x}Ti_3Nb_2O_{14}$:$x$$Eu^{3+}$ (x = 0.05, 0.10, 0.15, and 0.20) phosphors by monitoring at 613 nm with the excitation of 461 nm measured at room temperature is shown in Fig. 3B.11. The entire decay curves can be well fitted to a single exponential function, $I = Aexp(-t/\tau)$, where I, τ and A are intensity, decay time and fitting parameters respectively. Obviously, the lifetimes of Eu^{3+} ions gradually increases with increase in Eu^{3+} concentration which can be attributed to the decrease in nonradiative transition probability between Eu^{3+}-Eu^{3+} pair. From the life time values, quantum efficiency of the samples was also calculated and presented in Table 3B.3. It was found that the value increases from 26.68% to 27.16% with Eu^{3+} doping. The assessment of Judd-Ofelt intensity parameters Ω_t (2, 4 and 6) of the $Ca_{3-x}Ti_3Nb_2O_{14}$:$x$$Eu^{3+}$ (x = 0.05, 0.10, 0.15, and 0.20) phosphors calculated from the emission spectrum tabulated in Table 3B.4 support these results.

Table 3B.4 Judd-Ofelt intensity parameters of $Ca_{3-x}Ti_3Nb_2O_{14}$:*x*Eu^{3+} (*x* = 0.05, 0.10, 0.15 and 0.20) phosphors.

x	J-O Intensity parameters		Transitions	$A_{0\text{-}2,4}(s^{-1})$	$A_{\tau}(s^{-1})$	τ_{rad} (ms)	β(%)	$\sigma(\lambda_p)$ (pm^2)
	Ω_2	Ω_4						
0.05	2.38	0.12	$^5D_0$-$^7F_1$ $^5D_0$-$^7F_2$ $^5D_0$-$^7F_4$	— 137.31 3.23	191.69	5.22	26.08 71.63 1.69	116.39 248.77 300.07
0.10	2.34	0.11	$^5D_0$-$^7F_1$ $^5D_0$-$^7F_2$ $^5D_0$-$^7F_4$	— 134.65 2.99	188.78	5.29	26.49 71.33 1.58	115.32 236.61 263.68
0.15	2.28	0.11	$^5D_0$-$^7F_1$ $^5D_0$-$^7F_2$ $^5D_0$-$^7F_4$	— 131.59 2.92	185.64	5.39	26.93 70.88 1.57	118.18 217.77 332.92
0.20	2.26	0.10	$^5D_0$-$^7F_1$ $^5D_0$-$^7F_2$ $^5D_0$-$^7F_4$	------- 130.56 2.79	184.50	5.42	27.10 70.76 1.51	128.64 209.13 416.53

A better understanding of actual emission color of the phosphor is very important in the solid state lighting applications. The CIE chromaticity coordinates of $Ca_{3-x}Ti_3Nb_2O_{14}$:*x*Eu^{3+} (*x* = 0.05, 0.10, 0.15, and 0.20) phosphors were determined on the basis of its corresponding emission spectrum and the value is (0.60, 0.37), which is very close to the NTSC standard values (0.67, 0.33) for a potential red phosphor.

3B.3.5 Comparison between Sn and Ti systems

Powder XRD patterns of $Ca_{2.85}Sn_3Nb_2O_{14}$:*0.15*Eu^{3+} and $Ca_{2.85}Ti_3Nb_2O_{14}$:*0.15*Eu^{3+} phosphors calcined at 1500°C is shown in Fig. 3B.12. It is obvious that both compounds exhibit pyrochlore phase having space group *Fd3m*. Even though, XRD patterns looks to be similar there is some variations in the intensities of superstructure peaks.

Particularly, the intensities of peaks (111), (311) and (511) found to vary depending on the B site cation.

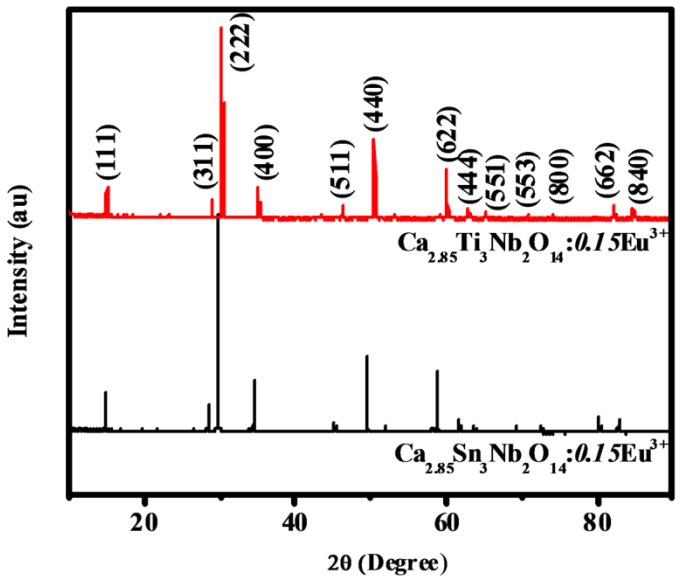

Fig. 3B.12 XRD patterns of $Ca_{2.85}Sn_3Nb_2O_{14}$:*0.15*Eu^{3+} and $Ca_{2.85}Ti_3Nb_2O_{14}$:*0.15*Eu^{3+} phosphors.

In general, the intensity of pyrochlore superlattice peak depends on the difference in average scattering power between A and B cation, ordering, distribution of oxygen vacancies, distortion in the anion array, displacement of *48f* oxygen from the ideal value etc (Radhakrishnan *et al*. 2009). Here, the intensity of superstructure peaks (111) and (311) is more pronounced in stannate than that in titanate system. However, the intensity of peak (511) is high in titanate compared to stannate pyrochlore. This change in intensity of superlattice peaks may be due to the change in crystal chemistry of B site cations including chemical bonding and covalency. The scattering power of Ti is much less than Sn, which leads to a significant decrease in the intensity of superstructure peak. Also, the extent of structural disorder in the system is also contributing to the decrease in peak intensity ratios.

Excitation spectra of $Ca_{2.85}Ti_3Nb_2O_{14}$:*0.15*Eu^{3+} and $Ca_{2.85}Sn_3Nb_2O_{14}$:*0.15*Eu^{3+} phosphors monitored for 613 nm emissions is shown in Fig. 3B. 13. It can be seen that full width half maximum (*fwhm*) of CT band in titanate phosphor is more compared to

that of stannates. The CT band have contributions from Eu^{3+}, Sn^{4+}/Ti^{4+} and Nb^{5+} ions. In both the systems, the contributions from Eu^{3+} and Nb^{5+} are almost same. The *fwhm* of CT band depends on the electronegativity difference between ligand and metal. The electronegativity of Sn (1.8) is higher than that of Ti (1.5). This change in *fwhm* may be related to the difference in energy levels of Sn/Ti ions. Further, CT band was located at longer wavelength (333nm) in titanate phosphors compared to stannate system. As report by Lin *et al*., the peak position of CT bands depends on the length of Eu-O bond and covalency (Lin *et al*. 1998). The shorter the Eu-O bond length, the shorter the CT band wavelength. Herein, the degree of covalency is weaker in the Sn host because Sn^{4+} attracts O^{2-} electron cloud most strongly since its electronegativity is large compared to Ti^{4+} ion. Hence, the electronic transition from the 2p orbital of O^{2-} to the 4f orbital of Eu^{3+} could be more possible in the Ti host than in the Sn one and hence CTB energy of Eu^{3+} decreases in stannate phosphors.

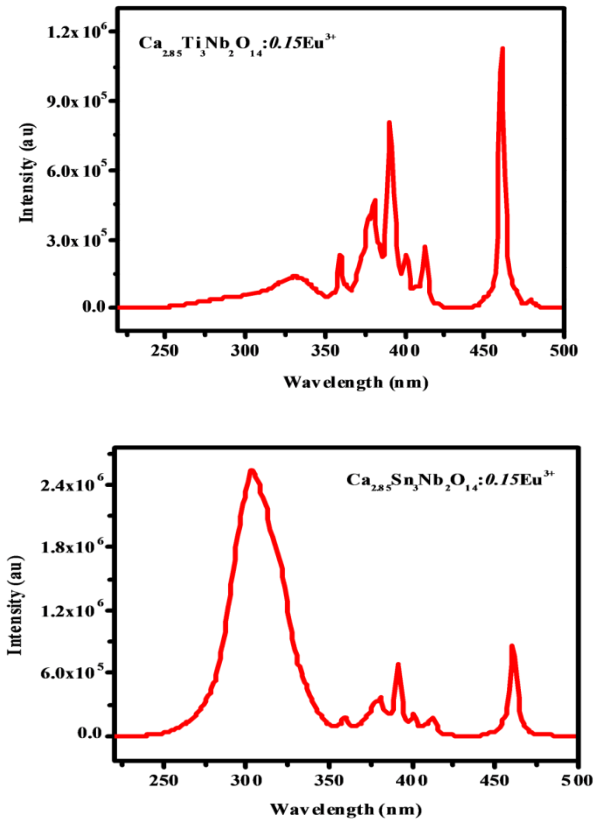

Fig. 3B.13 Photoluminescence excitation spectra of $Ca_{2.85}Ti_3Nb_2O_{14}$:*0.15*Eu^{3+} and $Ca_{2.85}Sn_3Nb_2O_{14}$:*0.15*Eu^{3+} phosphors monitored for 613 nm emission.

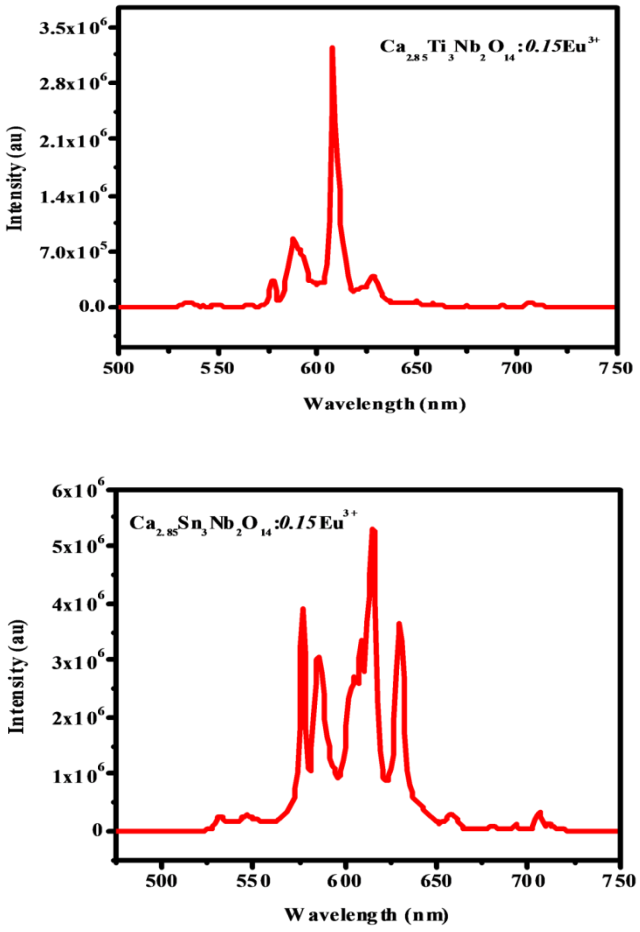

Fig. 3B.14 Photoluminescence emission spectra of $Ca_{2.85}Ti_3Nb_2O_{14}$:*0.15*Eu^{3+} and $Ca_{2.85}Sn_3Nb_2O_{14}$:*0.15*Eu^{3+} phosphors under 391 nm excitation.

The photoluminescence emission spectra of $Ca_{2.85}Ti_3Nb_2O_{14}$:*0.15*Eu^{3+} and $Ca_{2.85}Sn_3Nb_2O_{14}$:*0.15*Eu^{3+} phosphor under the 391 nm excitation is shown in Fig. 3B.14. The emission spectra consist of $^5D_0$-^7F_J (J = 0, 1, 2, 3, 4) transitions of Eu^{3+} ions. Because of the loss of inversion symmetry of pyrochlore A site, in both phosphors $^5D_0$-$^7F_2$ ED transition dominates over $^5D_0$-$^7F_1$ MD transition and its intensity is hypersensitive to the variations of bonding environment of the Eu^{3+} ion. Further, crystal field splitting and *fwhm* of $^5D_0$-$^7F_2$ ED transition depends on the A and B site cations. From the emission spectra, it can be seen that stannate phosphors exhibits intense multiband emission whereas sharp red emission is observed in titanate phosphors. Also, *fwhm* of red emission peak at 613 nm for titanate is low compared to that of stannate system. This is attributed to the difference in bonding environment of Ti and Sn in the host

lattice. As discussed earlier, the filled $4d^{10}$ orbitals of Sn^{4+} ion will not participate in π-bonding, while the empty 3d orbitals of Ti^{4+} are available for π-bonding. The strength of crystal field at the Eu^{3+} site is lower in titanate compared to stannate phosphor. The transfer of charge out of the O^{2-}_{48f} 2p orbital to the Ti^{4+} $3d^0$ orbitals via π-bonding polarizes the ligand electron density away from the rare earth site and hence electron density of O^{2-}_{48f} is shifted more towards Ti^{4+} ion than the Sn^{4+} ion. This results in the decrease in *fwhm* of red emission peak for titanate system. Moreover, this will render weaker crystal field at the Eu^{3+} site in titanate relative to stannate phosphors. The polarization of O^{2-}_{48f} towards the Ti^{4+} ions due to π-bonding in $Ca_3Ti_3Nb_2O_{14}$ results in smaller crystal field splitting.

3B.4 Conclusions

In summary, a series of titanate based displaced pyrochlore type red emitting phosphors, $Ca_{3-x}Ti_3Nb_2O_{14}$:$x$$Eu^{3+}$ (x = 0.05, 0.10, 0.15 and 0.20) were prepared via a high-temperature solid state reaction method. The influence of the partial substitution of less electronegative atom like Ti on both A and B sites of the pyrochlore-type oxides on the photoluminescence properties was studied in detail. The developed phosphors exhibit intense sharp red emission due to Eu^{3+} $^5D_0$-$^7F_2$ transitions with narrow full width half maximum (*fwhm*). The presence of the single sharp $^5D_0$-$^7F_1$ MD transition without splitting confirms the local cation disorder in this type of displaced pyrochlores. A cross-cutting comparative study between titanate and stannate systems convince the role of oxygen ion polarization on the crystal field splitting of Eu^{3+} ions. The splitting of Eu^{3+} manifold is larger in stannate than in titanate phosphors. Moreover, the *fwhm* of red emission peak at 613 nm for titanate is low compared to that of stannate system due to the difference in bonding environment of Ti and Sn in the host lattice. These results indicate that displaced pyrochlore system offers a lot of opportunities to manipulate the luminescence properties.

Chapter 4A

INFLUENCE OF STRUCTURAL DISORDER ON THE PHOTOLUMINESCENCE PROPERTIES OF Eu^{3+} DOPED RED PHOSPHORS: $Ca_2Y_{3-x}Nb_3O_{14}:xEu^{3+}$

Eu^{3+} doped pyrochlore type red phosphors, $Ca_2Y_{3-x}Nb_3O_{14}$ were prepared by a conventional solid state reaction route. The Eu^{3+} incorporation induces structural disorder in the lattice reducing the pyrochlore D_{3d} symmetry. The preferential occupation of Eu^{3+} ions on the B site conduces a higher coordination more than VI with disordered environment allowing forced electric dipole transitions. These phosphors emit intense red light due to forbidden electric dipole transition with more Stark splitting indicating the low symmetry of Eu^{3+} ions in the host. The Judd-Ofelt intensity parameters Ω_J supports the site symmetry and luminescence behavior of Eu^{3+} ions in the host. The disordered environment with special coordination of Eu^{3+} ions allows improved quantum efficiency (η = 34%) and CIE color coordinates (0.61, 0.38).

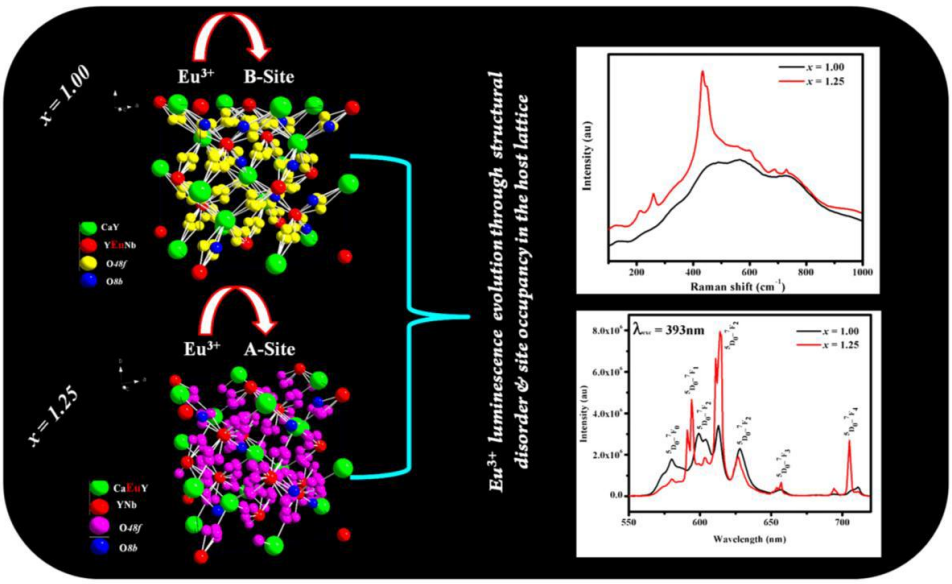

Sreena *et al. Chemistry Select.* **2016,** 1, 3413-3422

4A. 1 Introduction

In the last few decades, there have been extensive researches on pyrochlore type oxides due to their remarkable physical and chemical properties such as high thermal and chemical stability, lattice stiffness etc. In the pyrochlore structure, A_2O' chains weakly interact with the more rigid B_2O_6 network. Therefore, cation or anion vacancies in the A_2O' network of defect pyrochlores do not significantly reduce the stability of the lattice. Displacive disorder in the A_2O' network is observed in rare-earth-based pyrochlores such as $La_2Zr_2O_7$ (Tabira *et al*. 2001) but it is also often encountered in Bi-based pyrochlores (Lufaso M W *et al*. 2006; Vanderah *et al*. 2006; Levin *et al*. 2002) where it is attributed to the stereochemically active lone electron pair of Bi^{3+} ion (Shoemaker *et al*. 2011; Shoemaker *et al*. 2010). Studies of the local structure of BiZn/FeNbO pyrochlores by Krayzman et al. revealed that the displacement directions of the A-site ions are determined by the nature of A-site cations and the local B-site configurations (Krayzman *et al*. 2007). Avdeev *et al*. noted that the off-centering of the A-site cations can also occur when the A-site is occupied by small transition metal ions, because the A-site cavity is too big for them to maintain the ideal central position (Avdeev *et al*. 2002). This was further supported by the recent study on Ca-Ti-(Nb,Ta)-O pyrochlores (Roth *et al*. 2008). These pyrochlores exhibited a substantial displacive disorder without presence of lone electron pairs but with smaller Ti^{4+} ions on the A-site. Vanderah *et al*. reported that a pyrochlore structure can accommodate up to 25% of small B cations on its A-site by the displacive disorder (Vanderah *et al*. 2005). Such displacive disorder can give the appearance of higher symmetry and the deviation of the pyrochlore A site symmetry from a perfect inversion centre and also the distortion of the scalenohedra can improve the luminescence.

In view of the great importance of red phosphor towards the development of white LEDs in the lighting industry, the study of Eu^{3+} luminescence in the various host systems gains attraction. Among the different RE ions, Eu^{3+} is a good activator ion with red or red-orange emission in many inorganic hosts. Intense red emissions of Eu^{3+} ions are due to the intraconfigurational f-f transitions and their emission wavelength is determined primarily by the local environment in the host lattice (Peng *et al*. 2011;

Gupta *et al*. 2012; Khanna *et al*. 2013; Dordevic *et al*. 2014). Hence to study the influence of chemical environment on the nature of Eu^{3+} emission in different cationic sites and also to understand the preferential occupancy of Eu^{3+} in A and B site of the pyrochlore, we have synthesized Eu^{3+} substituted phases and studied their luminescence properties.

In the chapter 3A, the influence of partial substitution of small cation like Sn on both A and B sites of the pyrochlore type oxides on the photoluminescence properties was studied in detail. The photoluminescence spectra of the developed phosphors exhibit intense multiband emissions due to Eu^{3+} $^5D_0$-$^7F_{0,\,1,\,2}$ transitions. Despite lots of research work related to the occupation of small cation from B site to the A site of the pyrochlore oxides, there is not much work related to the occupation of medium size cation from A site to the B site so far. Hence, we plan to investigate the evolution of emission spectra with partial occupation of medium size cation on both A and B site of the pyrochlore oxides. In current study, cubic pyrochlore type $Ca_2Y_{3-x}Nb_3O_{14}$:$x$$Eu^{3+}$ phosphors were synthesized by high temperature solid state reaction to develop red emitting phosphors. In this pyrochlore, Ca^{2+} and Y^{3+} ions occupy the A site, Nb^{5+} ion occupies the B site. Since the total number of ions in the A site is more than that in the B site, some of the Y^{3+} ions in the A site might be occupying the B site because of its medium ionic radius. Another motivation was to investigate the luminescence properties and site occupancy of Eu^{3+} by considering different cationic sites of pyrochlore phosphors. Moreover, the luminescence characteristics were discussed based on their crystal structure.

4A. 2 Experimental

4A. 2.1 Materials and Synthesis

The pyrochlore type red phosphors, $Ca_2Y_{3-x}Nb_3O_{14}$: $x$$Eu^{3+}$ (x = 0, 0.10, 0.30, 0.50, 0.75, 1.00 and 1.25) were synthesized via a solid state reaction method. Fine powders of $CaCO_3$, Y_2O_3, Nb_2O_5 and Eu_2O_3 (Sigma–Aldrich, Steinheim, Germany) of 99.99% purity were used as the starting materials. These precursors were taken in the required stoichiometric ratio and then thoroughly wet mixed in an agate mortar with acetone as

the wetting medium with intermittent drying. The procedure of mixing and subsequent drying was repeated thrice so as to obtain a homogeneous product. This mixed product was made into a pellet and then calcined on an alumina plate at 1400°C twice for 6 hours in an air atmosphere electrical furnace. The calcined product was then ground into a fine powder for carrying further characterizations.

4A. 2.2 Characterization

X-ray powder diffraction (XRD) analysis was performed with a PANalytical X'PertPro diffractometer having Ni filtered Cu–K_α radiation with X-ray tube (40 kV, 30mA) and 2θ varied from 10 to 90º. Raman spectra of the powder samples were acquired using an integrated micro-Raman system of Labram HR800 spectrometer (Horiba Scientific) using a 633nm helium-neon laser with a spatial resolution of 2μm. Fourier transform infrared spectroscopy (FT-IR) data were collected on a (Perkin-Elmer Spectrum One FT-IR Spectrometer) over the range of wavenumber 1000-400 cm^{-1}, and the standard KBr pellet technique was employed. Morphological analysis of the powder was performed by means of a scanning electron microscope with JEOL JSM-5600 LV SEM. Energy dispersive analysis and elemental mapping of the samples were carried out using a Silicon Drift Detector–X-Max^N attached with a Carl Zeiss EVO SEM. EDS elemental mapping was conducted using the Aztec Energy EDS Microanalysis software. Absorbance study of the samples was carried out with a UV-vis-NIR spectrophotometer (Shimadzu, UV-3600) in the 400-700nm wavelength range using barium sulfate as a reference. The photoluminescence excitation and emission spectra of the prepared samples were obtained using a Spex-Fluorolog DM3000F spectrofluorimeter.

4A. 3 Results and discussion

4A. 3.1 Powder X-ray Diffraction Analysis

The phase purity of the samples was examined by X-ray powder diffraction (XRD) measurement and Fig. 4A.1 presents the XRD profiles of the $Ca_2Y_{3-x}Nb_3O_{14}$: xEu^{3+} (x = 0, 0.10, 0.30, 0.50, 0.75, 1.00 and 1.25) phosphors. No traces of impurities were

detected upto x = 1.00, indicating that upto this concentration, dopant Eu^{3+} ions have been effectively incorporated into the host lattice. All the diffraction peaks can be well indexed to a cubic pyrochlore structure with a space group *Fd3m* (JCPDS File No: 01–081-0841). However, at x = 1.25 barely visible traces of impurities are present. Additional diffraction peaks (marked as *) could be assigned to the traces of $YNbO_4$ (JCPDS File No: 00-023-1486). The sharp and regular sets of peaks suggest the high crystallinity of the samples.

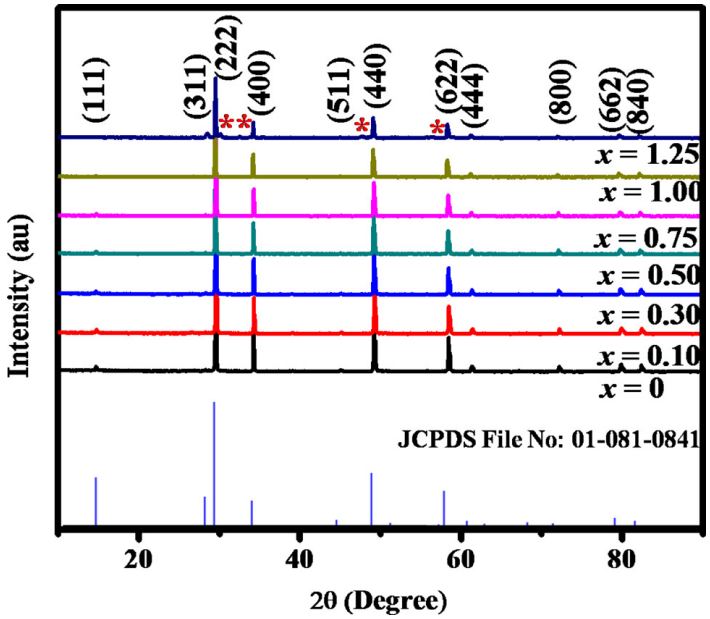

Fig. 4A.1 Powder XRD patterns of $Ca_2Y_{3-x}Nb_3O_{14}$: xEu^{3+} (x = 0, 0.10, 0.30, 0.50, 0.75, 1.00 and 1.25) red phosphors.

In pyrochlore structure having a general formula $A_2B_2O_7$ (where A and B are metal ions), A sites are occupied by larger metal ions and B sites are occupied by smaller metal ions. The ionic radii of Ca^{2+} and Y^{3+} in eightfold coordinations are 1.12 and 1.02Å respectively and that of Y^{3+} and Nb^{5+} in sixfold coordination are 0.90 and 0.64Å respectively (Shannon *et al*. 1976). Powder X-ray diffraction analysis confirms that the present system $Ca_2Y_3Nb_3O_{14}$ crystallizes in pyrochlore structure. For the stable pyrochlore to form some of the Y^{3+} ions might be occupying the B site because of its medium ionic radius, according to crystal chemistry principle. This unconventional substitution of medium size A-type cations on the B-site of pyrochlore has never been

reported. Eu^{3+} ions are incorporated into the lattice in order to investigate the evolution of emission spectra with partial occupation of Y^{3+} ions on both A and B site of the cubic pyrochlore. In all the cases the Eu^{3+} ions are expected to occupy the Y^{3+} ion site considering the matching ionic radius and valency. However due to the different site occupation of the Y^{3+} ion with different coordination environment, it is difficult to make the assumption. From the PL studies which is explained in the later part, we presume an occupation of Eu^{3+} ions in B-site (Y^{3+} ion site) in the pyrochlore structure upto x = 1.00. On further substitution, Eu^{3+} ion prefers to occupy the Y^{3+} ion in the A site which is further confirmed by the appearance of minor impurity $YNbO_4$ phases in the XRD.

In order to establish the crystal structure correctly, Rietveld refinements of all the XRD patterns were carried out using X'pert HighScore Plus software. The starting model used for the refinement of the $Ca_2Y_{2.9}Nb_3O_{14}$:*0.10*Eu^{3+} phosphor is shown in Table 4A.1. A pseudo-Voigt profile function was used to fit the XRD pattern. The background polynomial was refined with respect to a flat background and two other coefficients. Other profile functions including Caglioti parameters and the asymmetry parameter along with the structural parameters like lattice constant and the oxygen *x*-parameter were refined. The refined parameters obtained from the Rietveld analysis and their values corresponding to the best fit are listed in Table 4A.2. The refined R values suggest that the refinement is in good agreement with the space group in all respects. The result of the refinement of the phosphor $Ca_2Y_{2.5}Nb_3O_{14}$:*0.50*Eu^{3+} along with the difference plot is shown in Fig. 4A.2 which shows that the refinement leads to a good agreement between the calculated and observed patterns.

Table 4A.1 Starting structural model for $Ca_2Y_{2.9}Nb_3O_{14}$:*0.10*Eu^{3+} cubic pyrochlore

Atom	Position	Site occupancy	*x*	*y*	*z*
Ca	16d	0.5	0.5	0.5	0.5
Y	16d	0.5	0.5	0.5	0.5
Y	16c	0.225	0	0	0
Eu	16c	0.025	0	0	0
Nb	16c	0.75	0	0	0
O	48f	1	0.3195	0.125	0.125
O'	8b	1	0.375	0.375	0.37

Table 4A.2 Refined parameters obtained from the Rietveld analysis of the $Ca_2Y_{3-x}Nb_3O_{14}$: xEu^{3+} phosphors

Sample	***x* = 0**	***x* = 0.10**	***x* = 0.30**	***x* = 0.50**	***x* = 0.75**	***x* = 1.00**	***x* = 1.25**
Phase	Pyrochlore	Pyrochlore	Pyrochlore	Pyrochlore	Pyrochlore	Pyrochlore	Pyrochlore
Space group	*Fd3m*	*Fd3m*	*Fd3m*	*Fd3m*	*Fd3m*	*Fd3m*	*Fd3m*
Lattice Constant (Å)	10.4590(2)	10.4618(2)	10.4689(2)	10.4747(2)	10.4832(2)	10.4890(2)	10.4991(2)
Flat background	84.6983	77.0205	76.1278	72.3444	71.20042	102.4329	74.0366
Coefficient 1	-26.6949	-22.2764	-22.4440	-21.9785	-20.4246	-22.2938	-16.6308
Coefficient 2	23.7920	20.0131	20.6679	19.9576	19.1365	18.1941	10.3345
Scale factor	0.000012	0.000011	0.000010	0.000008	0.000007	0.000005	0.000004
Oxygen *x* parameter	0.385(2)	0.395(2)	0.397(2)	0.398(2)	0.398(2)	0.402(2)	0.403(2)
Caglioti parameters							
U	0.069(7)	0.048(9)	0.067(9)	- 0.08(1)	0.08(1)	0.09(1)	0.06(1)
V	-0.033(6)	-0.004(8)	0.024(7)	-0.028(8)	-0.036(8)	-0.04(1)	-0.02(1)
W	0.010(1)	0.005(1)	0.009(1)	0.010(1)	0.011(1)	0.011(2)	0.006(2)
Residual parameters							
Rexp (%)	11.73	12.35	12.55	12.99	13.37	8.47	14.07
Rp (%)	12.09	12.84	13.10	12.281	12.67	8.95	14.39
Rwp (%)	16.37	17.40	17.68	16.87	17.35	13.08	19.37
GOF	1.94	1.98	1.98	1.68	1.68	2.38	1.80

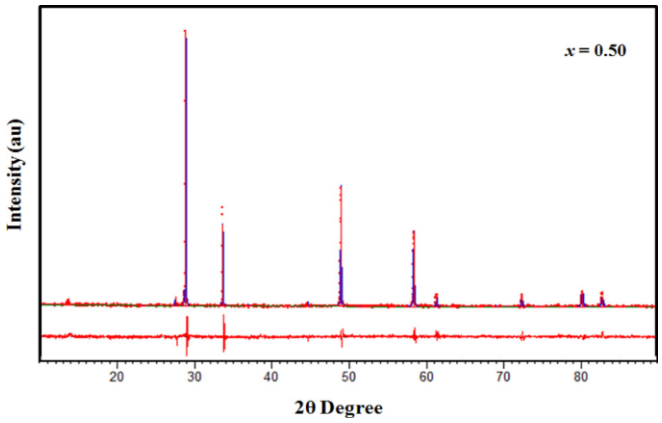

Fig. 4A.2 Observed (points), calculated (continuous line) and difference (bottom line) powder X-ray diffraction profiles of $Ca_2Y_{2.5}Nb_3O_{14}$:*0.50*Eu^{3+} phosphors

It can be seen that the lattice parameter increases with increase in Eu^{3+} concentration which suggests the replacement of Y^{3+} ions by larger Eu^{3+} ions in the lattice. Another observation is the variation of *48f* oxygen *x*-parameter which shows an increasing trend with Eu^{3+} concentration. As the 8a site in the pyrochlore unit cell is vacant, the *48f* oxygen tends to shift from its ideal tetrahedral position towards the two nearby B cations leading to a decrease in net B-O bond length. But as the lattice undergoes a disordering, the shift of oxygen towards the B cation decreases. This will lead to an increase in the *x*-parameter as well as in the B-O bond length. This facilitated to increase the average coordination more than VI. The increasing trend of *48f* oxygen *x*-parameter confirms the disorder induced by the incorporation of Eu^{3+} ion in the lattice.

Fig. 4A.3 shows the variation of characteristic superstructure peak (111) with Eu^{3+} concentration. Such variation in the intensities of superstructure peak is associated with the variation in the oxygen position parameter. Dickson *et al.* showed that the position of *48f* oxygen strongly influences the (111) Bragg refection from the crystal and the intensity of the (111) reflection tends to be zero as the *x*-parameter increases (Dickson *et al*. 1989). The ratio of the ionic radii of the A-site to B-site (r_A/r_B) was calculated by considering the occupation of Eu^{3+} ion on both Y^{3+} ion sites (A and B). The values listed in Table 4A.3 indicate that A site occupation of Eu^{3+} ion results in the increase of radius ratio and decrease on B site occupation. It has been earlier reported that, as the radius ratio decreases, the pyrochlore structure tends to get converted from a well ordered structure to disordered structure in which the superstructure peaks diminish. The disappearance of characteristic superstructure peak (111) with Eu^{3+} concentration suggests that Eu^{3+} ion might be occupying the Y^{3+} ion in B site. The decreasing trend of intensity ratio indicates the probability of Eu^{3+} replacing the Y^{3+} and in turn increases the disorder in the lattice. The diminishing of superstructure peak and the decreasing trend of radius ratio evidences the occupation of Eu^{3+} ion on Y^{3+} ion in the B site.

Table 4A.3 The crystal parameters of the prepared phosphor materials

x	Radius Ratio, r_A/r_B (A site)	Radius Ratio, r_A/r_B (B site)	Average Crystallite size, Δd(nm)	Lattice Strain (%)
0	1.517	1.517	67.16	0.81
0.10	1.519	1.514	70.19	0.77
0.30	1.522	1.509	61.44	0.89
0.50	1.525	1.504	70.18	0.78
0.75	1.530	1.498	70.19	0.78
1.00	1.534	1.492	63.98	0.99
1.25	1.538	1.496	98.34	0.55

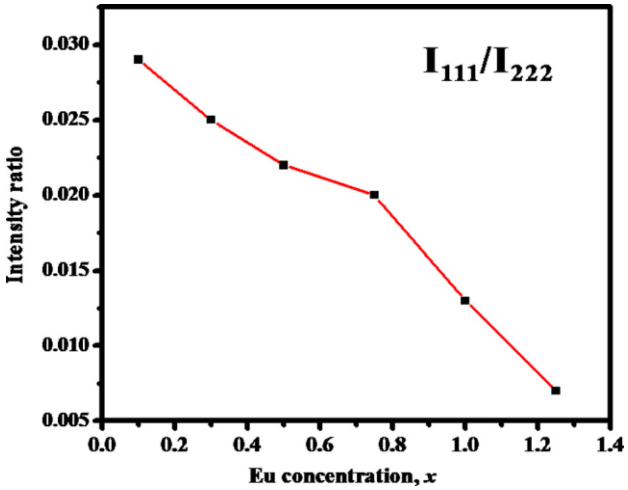

Fig. 4A.3 Variation of intensity ratio (I_{111}/I_{222}) in $Ca_2Y_{3-x}Nb_3O_{14}$: xEu^{3+} (x = 0, 0.10, 0.30, 0.50, 0.75, 1.00 and 1.25) phosphors.

The crystallite size and straininduced broadening of the samples are also determined with Williamson and Hall analysis, which is given by:

$$\frac{0.91\lambda}{\beta \mathrm{Cos}\,\theta} = \frac{0.9}{d_{avg}} + \frac{4\varepsilon \mathrm{Sin}\,\theta}{\lambda} \qquad (4A.1)$$

where 0.9 is the shape factor, λ is the $CuK_{\alpha 1}$ radiation of wavelength, β is the FWHM, ε is the strain, and θ is the scattering angle (Yogamalar *et al*. 2010). These samples have the

crystallite sizes in the range of 61-98 nm. The lattice strain ε associated with the lattice dislocation is found to be large (Table 4A.3) suggesting the disorder in the lattice.

4A. 3.2 Raman Spectroscopy Studies

To obtain the structural information of the local lattice distortion in the developed phosphors from the vibrational spectra, Raman scattering investigations were also carried out at room temperature. According to factor group analysis, there are 6 Raman active modes, (A_{1g} + E_g + $4F_{2g}$), $7F_{1u}$ infrared-active modes and $1F_{1v}$ acoustic mode for a cubic *Fd3m* pyrochlore structure with an ideal setting (McCauley R A *et al*. 1973; Vandenborre T A *et al*. 1983). In this ideal setting of the pyrochlore, Raman modes are only due to B_2O_6 sublattice vibrations whereas in the disordered pyrochlore structure the relaxation of the selection rule can result in the appearance of more Raman modes, including some infrared vibrational modes. The Raman spectra of the phosphor material as a function of Eu^{3+} concentration in the range of 100-1000 cm^{-1} are shown in the Fig. 4A.4. The sample with x = 1.25 showed some superimposed modes over the parent modes, which may be caused by secondary yttrium niobate phases according to XRD analysis. The mixed phases increased the number of Raman active modes (Arenas *et al*. 2010).

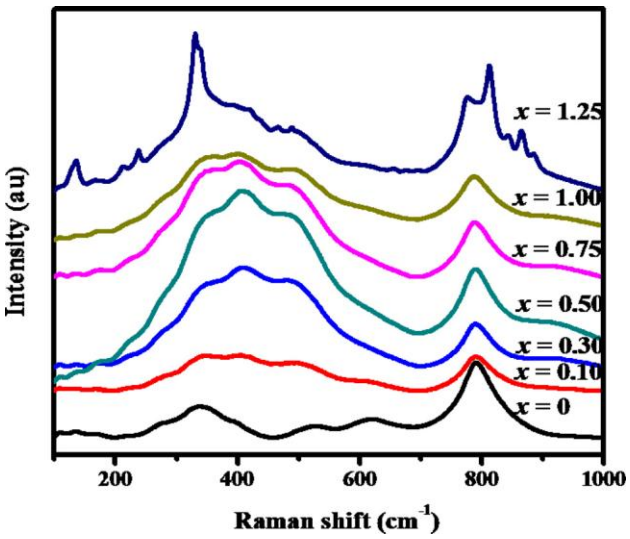

Fig. 4A.4 FT Raman spectra of $Ca_2Y_{3-x}Nb_3O_{14}$:xEu^{3+} (x = 0, 0.10, 0.30, 0.50, 0.75, 1.00 and 1.25) phosphors.

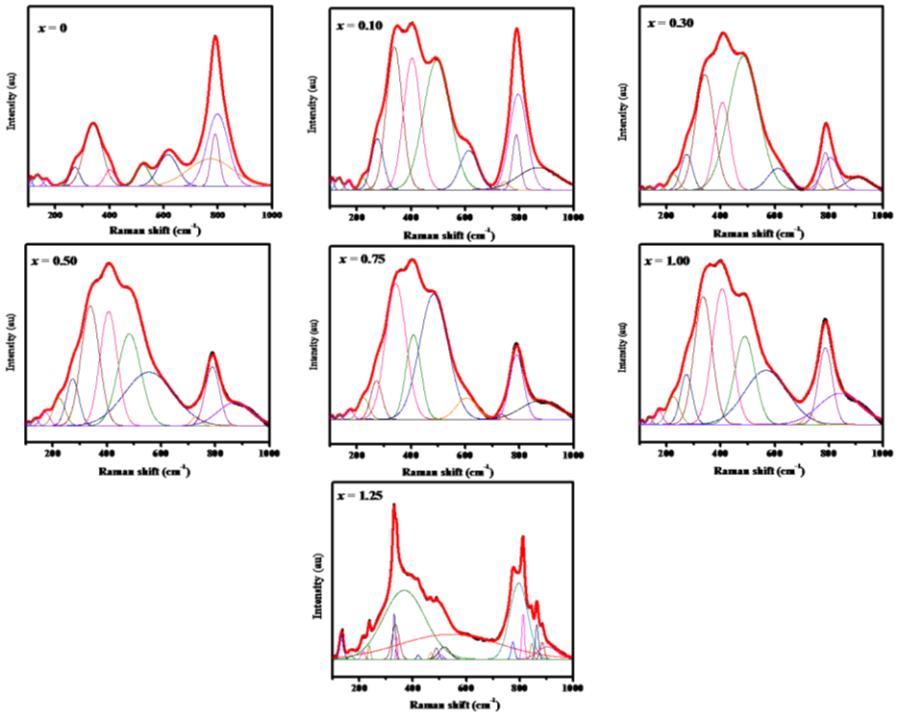

Fig. 4A.5 Sum of Lorentzian curves fit of the Raman spectra of the prepared phosphors. Experimentally measured spectra (red), fitted curves (thin line) and baseline (broken line) are shown.

Table 4A.4 Raman mode frequencies and the corresponding symmetry character of the $Ca_2Y_{3-x}Nb_3O_{14}$: xEu^{3+} (x = 0, 0.10, 0.30, 0.50, 0.75, 1.00 and 1.25) phosphors.

Wavenumber (cm^{-1})							Symmetry
x =0	x =0.10	x = 0.30	x = 0.50	x = 0.75	x = 1.00	x = 1.25	
108	108	109	109	109	109	109	F_{1u}
133	133	134	134	135	136	133	F_{1u}
168	170	172	172	172	172	213	F_{2g}
272	275	274	273	272	273	273	F_{2g}
339	338	341	338	343	335	339	E_g
401	403	406	406	408	408	419	F_{2g}
523	495	485	483	483	482	467	A_{1g}
615	613	612	610	604	--------	--------	F_{2g}
791	790	790	788	788	788	774	A_{1g}
804	865	869	874	878	883	884	F_{2g}

Clear visual inspection of the Raman spectra reveals the presence of more than 6 modes and some are overlapped. To resolve the spectra into modes, least square fitting with sum of the Lorentzian curves is carried out (Fig. 4A.5). The Raman mode assignment of the developed pyrochlore is carried out by comparing the wavenumber of modes with the modes reported in literature for different disordered pyrochlores (McCauley R A *et al*. 1973) and is presented in Table 4A.4. The Raman spectra show broad peaks as compared to that of well-ordered crystalline compounds, which is due to the greater deviation from ideal pyrochlore symmetry (D_{3d}). As such, materials with disorder will typically exhibit broader peaks within the Raman spectra.

The Raman spectra of the developed phosphors show only broad features at 100-300, 300-500, and 500-890 cm^{-1} which are "decorated" with various shoulders and weak sharper features. From previous studies on vibrational modes in pyrochlores, the highest-frequency features are associated with octahedral metal-oxygen stretching vibrations, the midrange vibrational modes are due to bending modes of MO_6 octahedra, and the lowest-frequency vibrations are due to large cation displacements associated with octahedral deformations. In pyrochlore, A-O atom interactions dominant at low frequencies and the B-O atom interactions prevalent at high frequencies. In the low wavenumber range, the modes observed at around 108 and 133 cm^{-1} were assigned to F_{1u} infrared vibrational modes. These low wavenumber modes, which are absent in pyrochlores with an ideal arrangement of atoms (Brown *et al*. 2004; Saha *et al*. 2008) are constantly seen in bismuth (Wang *et al*. 2006; Liu Y *et al*. 2009; Kamba *et al*. 2002) and rare earth based pyrochlores (Maczka *et al*. 2011) indicating their association with the ion displacements. Since no such ion displacement is observed in our system, the appearance of these modes may be due to the relaxation of the selection rules caused by the structural disorder.

In this complex compound, two species ions located at A and B site would lead to two different vibrational modes in the lowest frequency lines, 168 and 272 cm^{-1}. Here, Y^{3+} ions occupy partially on both A and B sites, therefore A-O bonds include Ca-O and Y-O bonds and B-O bonds include Y-O and Nb-O bonds. Thus the modes at 168 and 272 cm^{-1} are related to Y-O and Ca-O stretching modes, which are assigned to F_{2g} mode.

Similarly, the mode around 615 and 791 cm^{-1} are due to Y-O and Nb-O stretching modes of the B site. The E_g mode assigned to 339 cm^{-1} and F_{2g} mode assigned to 401cm^{-1} are principally due to stretching of B-O bond which causes a reaction from other O-B-O bonds. Two new modes appear at 495 and 804 cm^{-1} which results from the lowering of space symmetry due to local disorder in the B sub-lattice or from the existence of a significant amount of structural defects. The mode at 804 cm^{-1} sharply increasing probably means that B-O coordination environment is significantly more disordered. The lower A_{1g} mode assigned at 523 cm^{-1} may be due to O-B-O bond bending which disappears with Eu^{3+} ion substitution on the B cation (Y^{3+}) site. The higher frequencies consist of A_{1g} and F_{2g} vibrational modes, which are purely due to the B-O modes. The F_{2g} mode assigned to Y-O stretching (~615 cm^{-1}) decreases with Eu^{3+} ion concentration and finally disappears which may be due to the weakening of Y-O bond as a result of Eu^{3+} doping, thereby shifting this stretching mode toward lower frequencies. As *x* value increases, Y^{3+} ion concentration decreases and the Eu^{3+} ion concentration increases and when *x* becomes 1.00, it completely replaces the Y^{3+} ions in the B site. It is also noted that the Raman shift of the Nb-O stretching mode at 791 cm^{-1} almost do not change with increase in Eu^{3+} ion concentration. The variation of F_{2g} mode (~ 615 cm^{-1}) with Eu^{3+} ion concentration and the appearance of extra modes at 495 and 804 cm^{-1} confirm the replacement of Y^{3+} ions site by the Eu^{3+} ions in the B site. In summary, large number of modes in the Raman spectra of the developed pyrochlore appear as a result of the relaxation of selection rules caused by the lowering of cell symmetry due to the structural disorder. This supports our diffraction studies.

4A. 3.3 FT Infrared Spectroscopy (FT-IR) Studies

The IR spectra of the investigated compositions recorded in the range 400-1000 cm^{-1} are shown in Fig. 4A.6 and the tentative assignment is given in the Table 4A.5. Infrared active phonon modes have been assigned to specific bending and stretching vibrational modes, which originated from vibration and bending of metal-oxygen bond. The IR lattice vibration frequencies of some pyrochlore compounds with a formula $A_2B_2O_7$ have been studied (Du H *et al*. 2002; Chen M *et al*. 2005). There are seven IR-active optic modes originating from vibration and bending metal-oxygen bonds in the

infrared spectra of the pyrochlore oxides. The band (ν_1) at about 600 cm^{-1} is from the B-O stretching vibration in the BO_6 octahedron and the band (ν_2) at about 500 cm^{-1} is from the A-O' stretching vibration, and the band (ν_3) at about 400 cm^{-1} is from the A-O stretching vibration in the AO_6O_2' polyhedron of $A_2B_2O_7$, respectively.

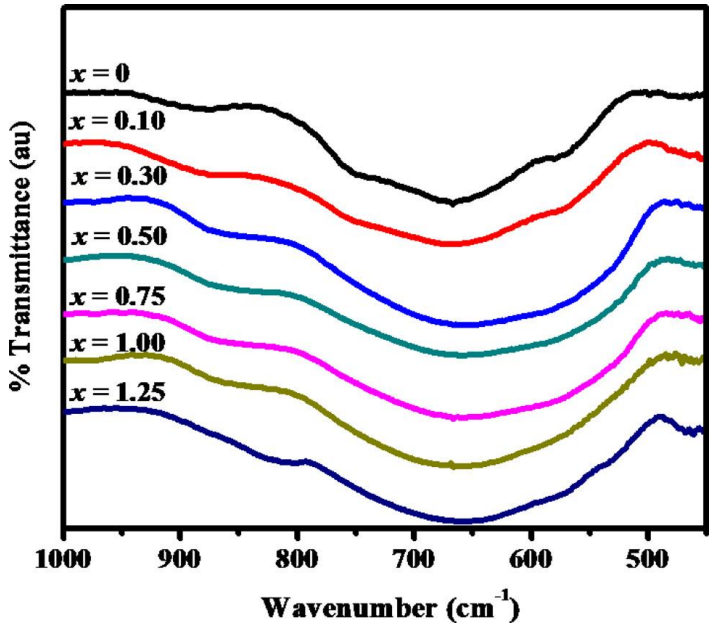

Fig. 4A.6 FT-IR spectra of $Ca_2Y_{3-x}Nb_3O_{14}$: $x$$Eu^{3+}$ (x = 0, 0.10, 0.30, 0.50, 0.75, 1.00 and 1.25) samples.

Table 4A.5 Assignment of characteristic vibrational modes obtained from FT-IR spectra of the developed phosphor materials

Mode Assignment	Wavenumber (cm^{-1})						
	x =0	x =0.10	x = 0.30	x = 0.50	x = 0.75	x = 1.00	x = 1.25
A-O'	873	873	872	872	871	871	871
B-O	753	759	799	808	809	813	815
B-O	667	667	667	666	667	667	667
A-O'	500	498	485	482	480	479	490

In the spectra, the vibration of shorter A-O' may correspond to the phonon mode at around 870 cm^{-1} and the vibration of longer bond may lead to a phonon mode at around 500 cm^{-1}. The phonon mode at 870 cm^{-1} show no significant difference in

resonant frequency as this mode is due to Ca-O' stretching vibrations. However, the mode at 500 cm^{-1} corresponds to the vibration of Y-O' shifts to lower frequencies. The band in the region 560-800 cm^{-1} can be ascribed to B-O stretching vibrations. The two phonon modes around 667 cm^{-1} and 760 cm^{-1}, are very close to each other but not well separated in the spectra. However, the assignment of the internal octahedral modes is based on the bonding character between B and O ions. The stretching vibration frequency of the bond is higher generally for bonding atoms with lighter mass. Hence, the phonon mode at 667 cm^{-1} is assigned to Nb-O while the phonon mode at 760 cm^{-1} is assigned to Y-O bond. Further, the frequency of the band at 760 cm^{-1} progressively increased with increase in Eu^{3+} concentration. The ν(B-O) value increased almost linear with increasing the lattice constant, or average radius of B site indicating that B-O bond strength enhanced with an increase in lattice constant. Furthermore, there is another dependence of the B-O vibrational frequency on the size of the B ion. The larger the B ion radius (with the same A ion) the higher the observed B-O vibrational frequency, indicating that force constant has increased. Thus FT-IR results indirectly points to the possibility that Eu^{3+} ions may be located in a more distorted environment in the lattice. The results obtained from diffraction, Raman and IR spectra studies confirm the occupation of medium size cation Y^{3+} on the B site from the A site of the pyrochlore oxide and doping by Eu^{3+} makes the system in a disordered state reducing the pyrochlore D_{3d} symmetry.

4A. 3.4 SEM and Microstructure

The surface morphology of the samples with Eu^{3+} doping concentration is shown in the Fig. 4A.7. The micrographs show that the sample consists of irregular particles and agglomerate to micron size. The morphology of the as prepared grains presents a smooth surface which may be advantageous for luminescence applications. The chemical composition of the developed phosphors was checked using energy dispersive spectrometry analysis attached with SEM. The EDS spectrum of the typical phosphor $Ca_2Y_{2.9}Nb_3O_{14}$:*0.10*Eu^{3+} is shown in Fig. 4A.8. EDAX microanalysis confirms the chemical homogeneity of the powders prepared by solid state route. No compositional variation was found upon probing different locations within each sample upto x = 1.00. However,

at x = 1.25 some variation occurs due to the formation of secondary phase as it is evidenced in the XRD analysis. Elemental X-ray dot mapping analysis shown in Fig. 4A.9 also reveals the uniform distribution of elements in the matrix.

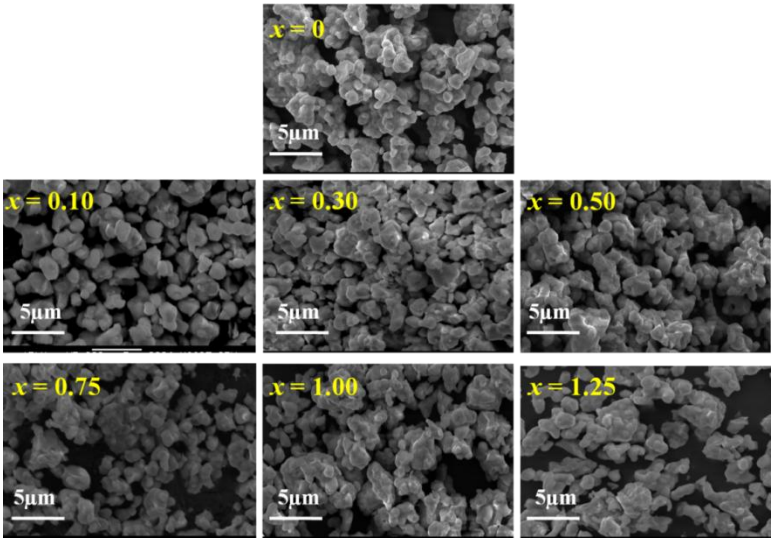

Fig. 4A.7 Surface morphology of the samples $Ca_2Y_{3-x}Nb_3O_{14}$:$x$$Eu^{3+}$ with different Eu^{3+} doping concentration synthesized at 1400°C.

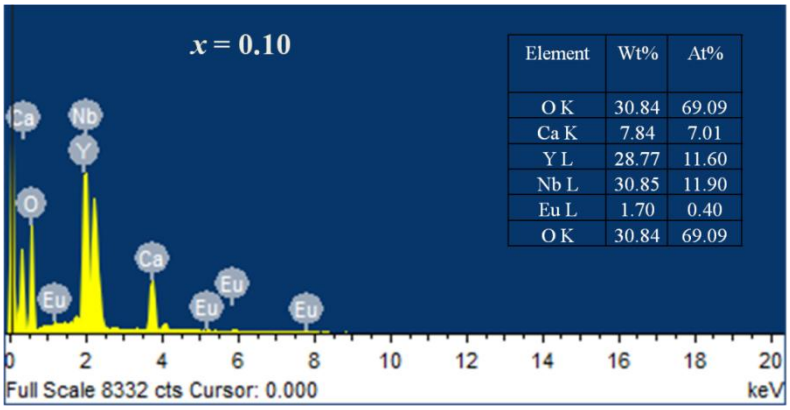

Element	Wt%	At%
O K	30.84	69.09
Ca K	7.84	7.01
Y L	28.77	11.60
Nb L	30.85	11.90
Eu L	1.70	0.40
O K	30.84	69.09

Fig. 4A.8 EDS spectrum of the typical $Ca_2Y_{2.9}Nb_3O_{14}$:*0.10*Eu^{3+} phosphor

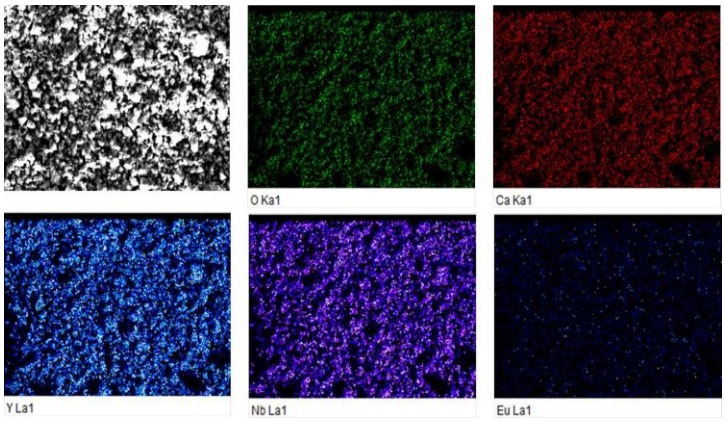

Fig 4A.9 Elemental X-ray dot mapping of typical $Ca_2Y_{2.9}Nb_3O_{14}$:*0.10*Eu^{3+} phosphor synthesized at 1400°C.

4A. 3.5 Absorbance and Photoluminescence Studies

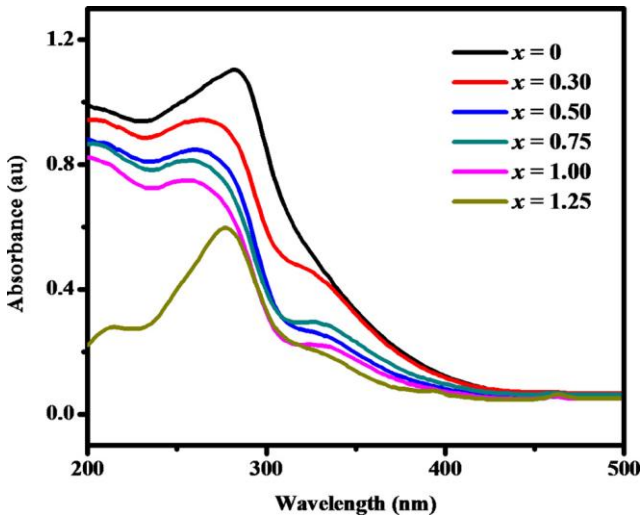

Fig. 4A.10 UV-visible absorption spectra of $Ca_2Y_{3-x}Nb_3O_{14}$: xEu^{3+} (x = 0, 0.30, 0.50, 0.75, 1.00 and 1.25) red phosphors.

The UV-visible absorption spectra of the $Ca_2Y_{3-x}Nb_3O_{14}$: xEu^{3+} (x = 0, 0.30, 0.50, 0.75, 1.00 and 1.25) phosphors synthesized by solid state reaction method is shown in Fig. 4A.10. The absorption spectra of all the samples exhibits a strong absorption band in the UV region (200-375 nm) peaking at 280 nm due to CT from the oxygen ligands to the central niobate groups in the host lattice and the shoulder absorption around 308 nm is corresponding to the CT from the oxygen ligands to Eu^{3+} ions. Similar observation

is made in the literature (Li K *et al*. 2015). In addition to the CT band, the Eu^{3+} doped samples show absorption peaks of the intra-4f transitions of Eu^{3+} at 393 nm (near UV) and 460 nm (blue). The absorption spectra showed a blue shift with increasing the concentration of Eu^{3+} resulting in increase of band gap and the values are listed in Table 4A.6. As can be seen from the absorption spectra, the CT absorptions of Nb group are decreasing with Eu^{3+} substitutions indicating energy transfer to the Eu^{3+} levels. This process influenced slight changes in the band gap values. It can be seen that the intensity of absorbance for $Ca_2Y_3Nb_3O_{14}$ is greater than that of europium-doped sample indicating that energy conversion from the CT states to the Eu^{3+} emitting levels is efficiently taking place. Thus, it is expected that these phosphors are excitable under both near UV and blue irradiation, which is one of the prerequisites for a phosphor material for pc WLEDs.

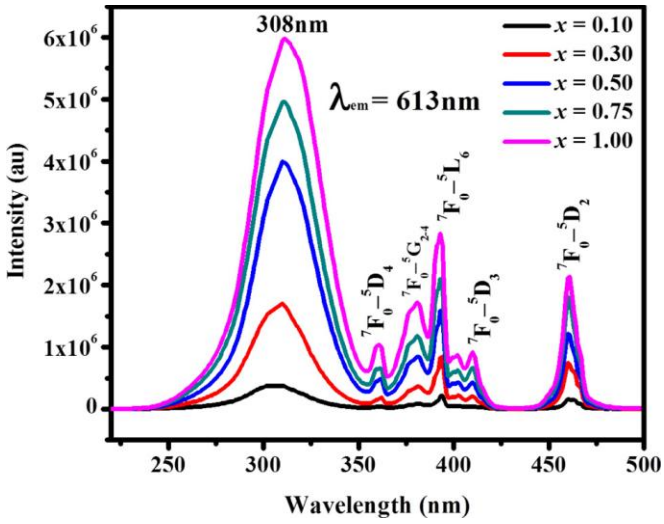

Fig. 4A.11 Excitation spectra of $Ca_2Y_{3-x}Nb_3O_{14}$: xEu^{3+} (x = 0.10, 0.30, 0.50, 0.75 and 1.00) red phosphors for an emission at 613 nm.

Fig. 4A.11 shows excitation spectra (λ_{em} = 613 nm) of the Eu^{3+} doped sample $Ca_2Y_{3-x}Nb_3O_{14}$: xEu^{3+} (x = 0.10, 0.30, 0.50, 0.75, and 1.00) phosphors. The excitation spectrum consists of a broad band in the region of 245–353 nm which is due to CT transitions from O^{2-} to Eu^{3+} and O^{2-} to Nb^{5+}. The CTB of Eu^{3+} generally lies in the range 250-300 nm and the energy for this process depends on the covalency of the Eu-O bond and the coordination environment of Eu^{3+}. NbO_6 groups have a strong absorption in the

250-310 nm regions. The observed CTB in the present excitation spectra corresponds to the merged effect of $O_{2p} \rightarrow Eu_{4f}$ and $O_{2p} \rightarrow Nb_{4d}$ charge transfer transitions. In this complex system, due to spectral overlap the contributions from more than one component in the CTB cannot be resolved for low concentrations.

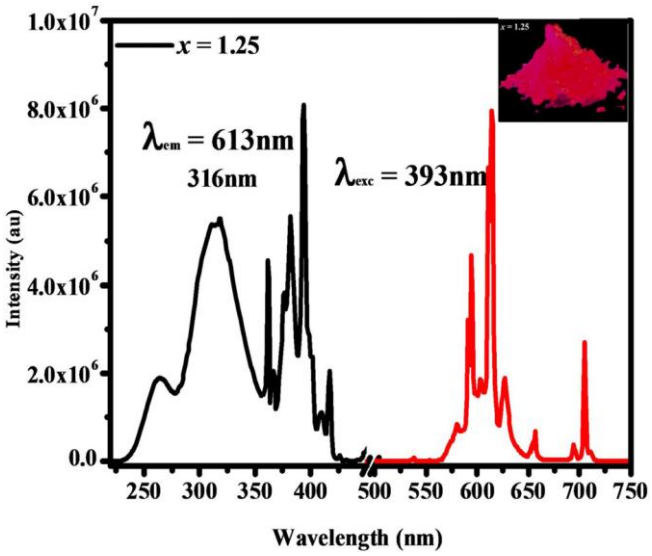

Fig. 4A.12 Excitation and emission spectrum of $Ca_2Y_{1.75}Nb_3O_{14}$:*1.25*Eu^{3+} phosphor. Inset is the luminescent photograph of the corresponding sample under the 393 nm (UV light) excitation.

It can be seen from the Fig. 4A.12 that as the Eu^{3+} concentration becomes 1.25, the CT band is shifted from 308 nm to 316 nm that might be due to the highly favorable low symmetry crystal structure of the system which enhances the electric dipole intra-4f transitions. This shift can be attributed to the increase in covalency of Eu-O bonds and the coordination environment of Eu^{3+} ions, which reduces the CT energy. The CTB position is closely related to the coordination state of Eu^{3+} ion in the host lattice and the bond length of Eu^{3+} and anions. The band position is more or less fixed in VI coordination and moves to lower energy with increase of bond distance in VIII coordination as in the expected line. In the present system, $[(Ca_2Y_2)(YNb_3)O_{14}]$, according to the stoichiometry, Eu^{3+} ions can occupy the VI coordinated B site upto x = 1.00 after which it is preferable to occupy the A site of the pyrochlore structure. This change in the symmetry of Eu^{3+} ions results in the shift of the CT bands to lower energy

for higher concentrations. Further, at x = 1.25, a lower intensity another CT band is observed at 253 nm in the excitation spectra which can be assigned to the CT band of the secondary phase $YNbO_4$ in the pyrochlore structure. Beyond this broad CT band, the sharp lines in the 360–500 nm are attributed to intra-configurational f-f transitions of Eu^{3+} in host lattice. Among them the peaks beyond 360 nm, that correspond to the $^7F_0 \rightarrow {}^5L_6$ (393 nm) and $^7F_0 \rightarrow {}^5D_2$ (460 nm) transitions are more intense which are matching well with the emission wavelengths of near UV and blue LED chips, respectively. This implies that these samples can be effectively excited by radiations of wavelength in the near UV and blue regions. The luminescent photograph of $Ca_2Y_{1.75}Nb_3O_{14}$:*1.25*Eu^{3+} phosphor under the 393 nm (UV light) excitation is shown in the inset of Fig. 4A.12.

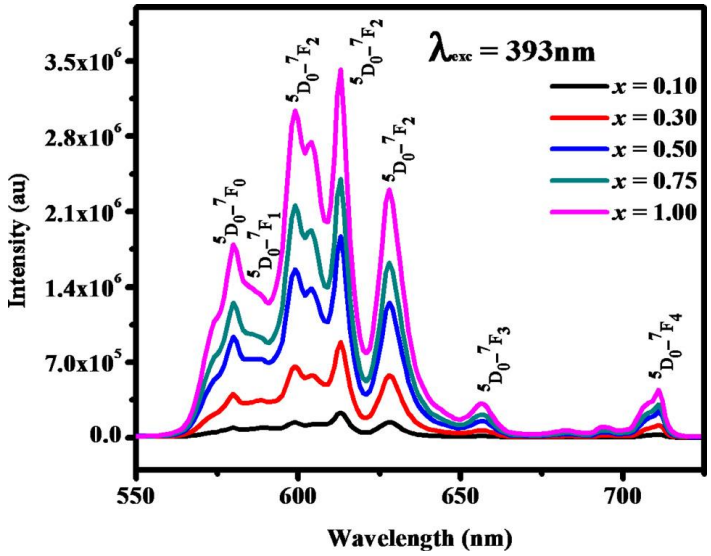

Fig. 4A.13 Emission spectra of $Ca_2Y_{3-x}Nb_3O_{14}$: $x$$Eu^{3+}$ (x = 0.10, 0.30, 0.50, 0.75 and 1.00) red phosphors excited at 393 nm.

Fig. 4A.13 shows the emission spectra of $Ca_2Y_{3-x}Nb_3O_{14}$: $x$$Eu^{3+}$ (x = 0.10, 0.30, 0.50, 0.75, and 1.00) phosphors excited at 393 nm. The spectra consists of series of peaks in the range of 560-720 nm corresponding to the characteristic transitions of Eu^{3+}, from the excited $^5D_0$ state to ^7F_J (J = 0-4) levels. Among all the transitions that were observed, $^5D_0$ - $^7F_1$ at 588 nm and $^5D_0$ - $^7F_2$ at 613 nm are special because of their peculiarity as symmetry-sensitive transitions and are generally known as magnetic dipole transition and hypersensitive electric dipole transition, respectively. When Eu^{3+}

ions are inserted into any chemical/ligand environment (crystal field), (2J+1) degenerate J-energy levels split into so-called Stark sub-levels by the ligand field effect and the number of levels depends on the local site symmetry of the metal ion. The substitution of Y^{3+} by Eu^{3+} may result in significant lattice distortion due to size differences. Further, the $^5D_0$-$^7F_0$ transition which is forbidden by both electric and magnetic dipole mechanisms is sensitive to the crystal field (Blasse *et al*. 1994).

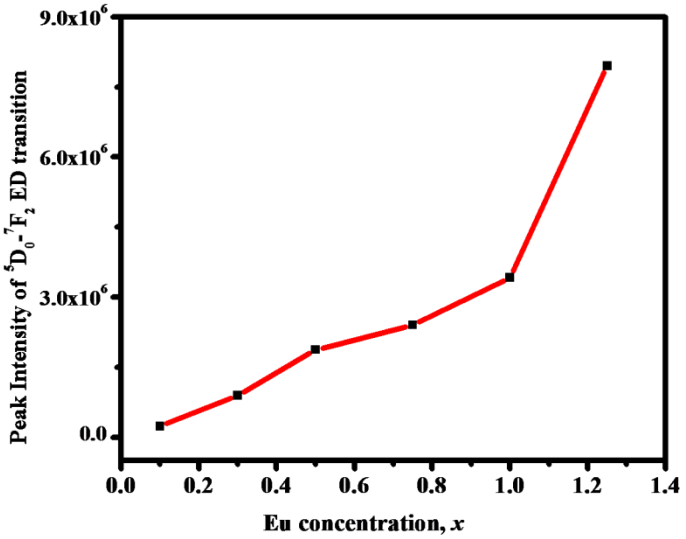

Fig. 4A.14 Peak intensities of 612 nm ED transitions of $Ca_2Y_{3-x}Nb_3O_{14}$:xEu^{3+} (x = 0.10, 0.30, 0.50, 0.75, 1.00 and 1.25) red phosphors under 393 nm excitation.

In the spectra, the weak emission peak centered at 580 nm belongs to the $^5D_0$ - $^7F_0$ transition is observed that is induced by role of crystal field in odd. The $^5D_0$-$^7F_0$ transition exists only when Eu^{3+} occupies sites with local symmetries of C_n, C_{nv}, or C_s. In the spectra, $^5D_0$ - $^7F_0$ (at 580 nm) transition appears as a broad single peak, because there is only one crystallographic site for Eu^{3+} ion in the lattice which is Y^{3+} ion due to the matching of ionic radius and valency. The emission bands of Eu^{3+} are broadened and split into several lines, indicating that Eu^{3+} ^7F_J levels appear Stark levels because of crystal field effect (Li Y C *et al*. 2007; Liu B *et al*. 2005). In the emission spectra, $^5D_0$ - $^7F_1$ transition appears as a single peak, and $^5D_0$ - $^7F_2$ split into four peaks. As always disorder can give the appearance of higher symmetry, the short range disorder present in the system improves the symmetry, which can slightly deviate from D_{3d} symmetry of

the structure that can lead to no splitting up of $^5D_0$ - $^7F_1$ transition. When excited by 393 nm (f-f transition of Eu^{3+}), the intensities of $^5D_0$ - $^7F_2$ and $^5D_0$ - $^7F_1$ transitions increase with *x*, and no quenching or saturation effect was observed (Fig. 4A.14). But as the Eu^{3+} concentration becomes 1.25, emission profile is drastically changed; indicating change in the symmetry of the Eu^{3+} ion occupying at the A site of the system (Fig. 4A.12).

To further assess the luminescence behavior with respect to temperature, we have carried out the PL measurements at Ln_2 temperature using Dewar and the glass sample probe attached to Flouorolog 3 Spectrofluorometer. It is observed that the emission profiles remain the same except the increase in intensity with Eu^{3+} substitution (Fig. 4A.15). This also further confirms the structural influence on the luminescence observed at low temperature. Even though XRD spectra showed hardly noticeable difference, photoluminescence spectroscopy clearly revealed the change of coordination and environment of Eu^{3+} ions in the host lattice. This observation indicates that luminescence spectroscopy is an effective method for investigating the coordination and environment around Eu^{3+} ions and could be used as an extremely structural probe technique.

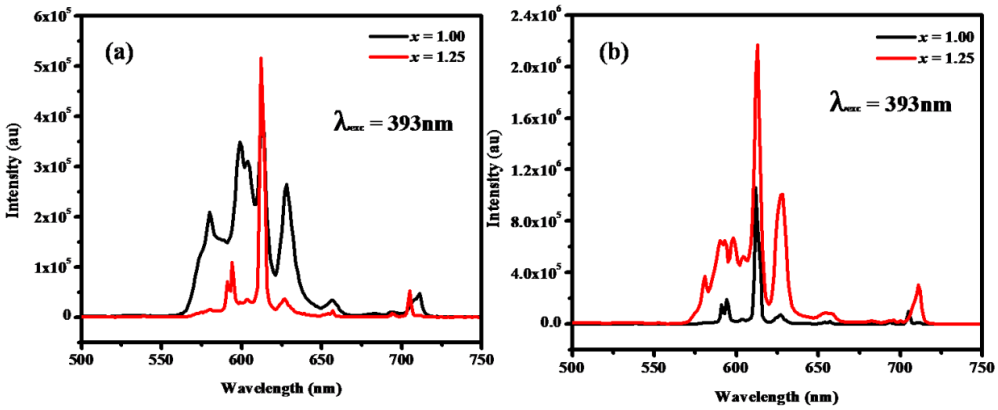

Fig. 4A.15 Emission spectra of $Ca_2Y_{3-x}Nb_3O_{14}$: xEu^{3+} (x = 1.00 and 1.25) phosphors recorded at (a) room temperature and (b) low temperature under 393nm excitation

The most sensitive parameter used for understanding symmetry around Eu^{3+} ion is the asymmetry ratio (R/O), which is defined as the ratio of the integral intensity of electric dipole transition to that of magnetic dipole transition (Chen D *et al*. 2015). The

asymmetry ratio is often regarded as a degree of symmetry distortion of the local environment around Eu^{3+} ions doped into the host lattice. Generally, a lower symmetry of the crystal field around Eu^{3+} leads to larger R/O. The values of R/O with different doping concentrations are shown in the Table 4A.6 which is confirmed by the Judd-Ofelt intensity parameters.

Table 4A.6 Optical parameters of $Ca_2Y_{3-x}Nb_3O_{14}:xEu^{3+}$ phosphors for different doping concentrations of Eu^{3+}

x	Band gap, E_g(eV)	Asymmetric Ratio	Life time (ms)		Efficiency η (%)	J-O Intensity Parameters		Color Coordinates (*x*, *y*)
			$^5D_0$-$^7F_2$	$^5D_0$-$^7F_0$		Ω_2 (pm^2)	Ω_4 (pm^2)	
0.10	3.08	2.58	0.89	1.03	30.51	3.66	5.86	(0.59, 0.39)
0.30	3.09	2.57	0.90	1.12	31.57	3.16	4.92	(0.59, 0.37)
0.50	3.37	2.55	0.91	1.14	34.38	2.91	4.37	(0.61, 0.38)
0.75	3.63	2.54	0.89	1.15	32.70	2.76	4.06	(0.61, 0.38)
1.00	3.78	2.52	0.93	1.10	34.14	2.65	4.06	(0.61, 0.38)
1.25	3.34	2.64	0.49	0.88	19.54	5.26	14.41	(0.63, 0.37)

To further substantiate the results of emission spectroscopy, photoluminescence decay measurements were carried out. The emission decay curves of Eu^{3+} ion recorded by monitoring the $^5D_0$ – $^7F_2$ transition of Eu^{3+} ion at 613 nm and $^5D_0$ – $^7F_0$ transition at 580 nm under excitation at 393 nm are presented in Fig. 4A.16 and Fig. 4A.17. For all samples decay profiles are exponential and can be reasonably well fitted to a single exponential function, indicating that only one de-excitation process is present. Life time values are similar upto x = 1.00, but they experience a sharp decrease at higher concentrations. The sudden decrease in life time value indicates the occupation of Eu^{3+} at a more distorted environment in the A site of the pyrochlore at higher doping concentration. Usually, for a given emitting ion, a long decay time is characteristic of the most symmetrical surrounding while a short decay value is observed when site distortion occurs. The efficiency of the phosphors was calculated from the life time values and the values are tabulated in Table 4A.6.

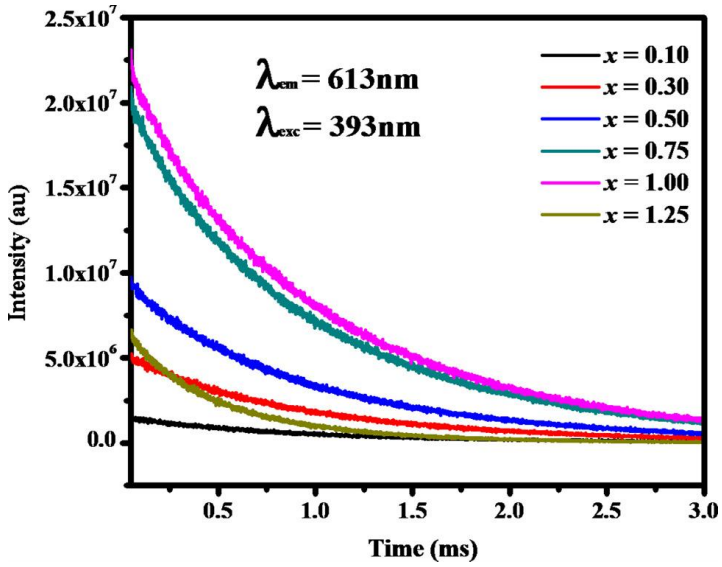

Fig. 4A.16 Life time decay curves of $^5D_0$-$^7F_2$ transition of Eu^{3+} (λ_{em} = 613 nm) in $Ca_2Y_{3-x}Nb_3O_{14}$: xEu^{3+}(x = 0.10, 0.30, 0.50, 0.75, 1.00 and 1.25) for 393 nm excitation.

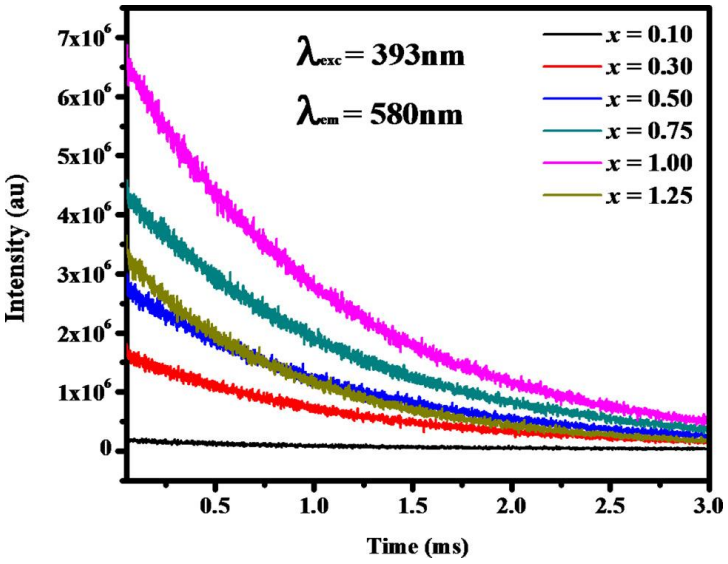

Fig. 4A.17 Decay curves of $^5D_0$-$^7F_0$ transition of Eu^{3+} (wavelength 580 nm) in $Ca_2Y_{3-x}Nb_3O_{14}$: xEu^{3+} (x = 0.10, 0.30, 0.50, 0.75, 1.00 and 1.25) under 393 nm excitation.

The detailed investigation of site symmetry and luminescence behavior of Eu^{3+} ions in the host was carried out by determining the Judd-Ofelt intensity parameters Ω_t (t = 2 and 4). The J-O intensity parameters and other spectral parameters are presented in Table 4A.6. The factor Ω_2 is related to the ligand environment, which can be clearly

understood by the significant change of its value with Eu^{3+} concentration and its value could reflect the asymmetry of the local environment at the Eu^{3+} ion site. The value of Ω_2 decreases with Eu^{3+} concentration upto x = 1.00 and then increases, indicating the increasing asymmetry nature of Eu^{3+} ion in the host, which is also confirmed by the variation in asymmetric ratio. Another important aspect is the order of intensity parameter, in general $\Omega_2 < \Omega_4$. This trend is observed in systems where Eu^{3+} ion is present in a higher coordinated site with a low degree of covalence of the metal-ligand bonds. This confirms the occupation of Eu^{3+} ion in higher coordinated Y^{3+}site, but sudden increase in the value of Ω_2 on further substitution of Eu^{3+} indicate the more distorted environment in the host lattice.

The CIE color coordinates (*x, y*) were calculated using the Color Calculator software to characterize the color emission. From the CIE coordinates, it can be seen that the color coordinates traverse a wide range from the light red to deep red region on varying the concentration of Eu^{3+}. The results show that tuning of red emission color is possible by the change of Eu^{3+} concentration in the host. The values of color coordinates were close to the NTSC standard values (0.67, 0.33) for a potential red phosphor.

4A. 4 Conclusions

A series of pyrochlore type red phosphor $Ca_2Y_{3-x}Nb_3O_{14}$: xEu^{3+} (x = 0.10, 0.30, 0.50, 0.75, 1.00 and 1.25) were prepared and their detailed structural, morphological and optical properties were carried out. The incorporation of Eu^{3+} ions induces some structural disorder in the lattice which is evidenced by the diminishing of characteristic superstructure peak (111) in the XRD pattern and the decreasing trend of radius ratio with Eu^{3+} doping. The presence of more than six Raman modes in the spectra supports the disorder present in the system. The absence of $^5D_0$-$^7F_1$ MD transition splitting with Eu^{3+} doping further confirms the short range disorder in the developed pyrochlore. These phosphors emit red light due to forced electric dipole transitions $^5D_0$ -$^7F_2$ with Quantum Efficiency (η = 34%) and CIE coordinates (0.61, 0.38) which make them promising phosphors for pc-LED applications.

Chapter 4B

INFLUENCE OF Sr SUBSTITUTION ON THE OPTICAL PROPERTIES OF $Ca_2Y_{3-x}Nb_3O_{14}$:xEu^{3+} PHOSPHORS

In this work, the influence of Sr^{2+} substitution in Ca^{2+} site on the photoluminescence properties of $Ca_2Y_3Nb_3O_{14}$:Eu^{3+} pyrochlore phosphor was studied. The Sr^{2+} incorporation induces structural disorder in the lattice reducing the pyrochlore D_{3d} symmetry and enhances the $^5D_0$-$^7F_2$ electric dipole transition. The abrupt change of $^5D_0$-$^7F_2$ life times with Sr^{2+} substitution further confirms the decrease in symmetry of Eu^{3+} ions to the pyrochlore D_{3d} symmetry. In the meantime, the emission color can be tuned from orange red to pure red due to the structural distortion of the activator Eu^{3+} ions. The assessment of Judd-Ofelt intensity parameters supports the site symmetry and luminescence behavior of Eu^{3+} ions in the host. These results propose that accommodation of bigger cations can effectively improve the luminescence properties of Eu^{3+}-activated phosphors.

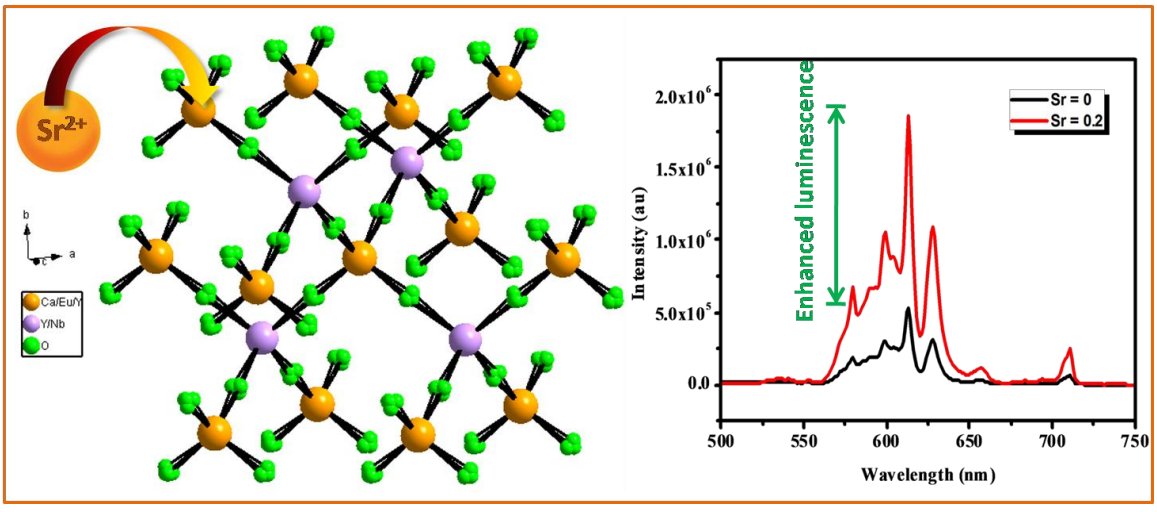

4B. 1 Introduction

The study of Eu^{3+} luminescence in various host systems has attained great importance in the solid state lighting technology owing to their high color purity and luminescence efficiency (Justel *et al*. 1998, Phillips *et al*. 2007). It is well known that the luminescence properties of Eu^{3+} ions highly depend on the crystal structure of the host lattice, doping site, doping concentration, ordering of the host lattice, uniformity in the activator distribution and various other factors (Dutta *et al*. 2013, Bünzli *et al*. 1989). Hence, it can be used as probe for site symmetry studies, covalency/polarizability of ligands, structure luminescence correlations, chemical bond differences in solids etc. As Eu^{3+} emission spectra can reflect any symmetry or covalent changes in the crystal structure, the substitution of cations in a phosphor with bigger or smaller ions is generally considered to create distortion around Eu^{3+} surrounding which is an effective way to tune various luminescence properties like the color coordinates, emission intensity etc (Tang *et al*. 2013). It is reported that, incorporation of cations with different valency and electronegativity to the crystal lattice can cause local distortion and modification in polarizability of chemical environment of Eu^{3+}, which can change the photoluminescent properties (Du *et al*. 2011, Lei *et al*. 2008, and Liu *et al*. 2007). The influence of effective positive charge of the central Eu^{3+} ions when it replaces a metal ion having lower oxidation state is also a thrust area of interest.

As discussed in chapter 4A, Eu^{3+} activated $Ca_2Y_3Nb_3O_{14}$ is a potential candidate to be used as a red phosphor in pc-WLED lighting industry. However further improvement in the emission properties of these phosphors could be achieved by the modifications in the host lattice. But, the addition of the cation should not disrupt the crystal phase formation of the lattice. Cation disorder in crystal lattices can enhance luminescence intensity and thermal stability of phosphors (Tanner *et al*. 2013, Zhao *et al*. 2017, Ji *et al*. 2015). Lin *et al*. have reported that cation disorder suppresses non-radiative processes through disruption of lattice vibrations and creates deep traps that release electrons to compensate for thermal quenching (Lin *et al*. 2017). The cation disorder within the host lattice improves the performance of WLED devices effectively. This idea can be confirmed in the cation substitution in $Ca_2Y_3Nb_3O_{14}$ host lattice. The

larger ionic radius and highly polarizable nature of Sr^{2+} ion may help to improve the emission properties of Eu^{3+} in $Ca_2Y_3Nb_3O_{14}$ host. Sr^{2+} ions doped into the luminescent materials can act as sensitizer or defect centres to enhance the luminescence properties. Thus, we attempted to introduce Sr^{2+} ions in place of the Ca^{2+} ions in $Ca_2Y_3Nb_3O_{14}$ host without altering the cubic pyrochlore structure. In this chapter, the luminescence properties of a series of $Ca_{2-y}Y_{2.80}Nb_3O_{14}$:*0.20*$Eu^{3+}$, *y*$Sr^{2+}$ phosphors are explained and the variation in the properties when Sr^{2+} was substituted to the Ca^{2+} site is discussed. In all the compositions, Eu^{3+} concentration was fixed to be x = 0.20. Substitution of Sr in place of Ca enhanced the CT band and f-f transition intensity of Eu^{3+} ions.

4B. 2 Experimental

4B. 2.1 Synthesis

In the present study, powder samples were synthesized via a high-temperature solid state reaction method. Fine powders of $CaCO_3$, Y_2O_3, Nb_2O_5, $SrCO_3$ and Eu_2O_3 (Sigma-Aldrich, Steinheim, Germany) of 99.99% purity were used as the starting materials for preparing $Ca_{2-y}Y_{2.80}Nb_3O_{14}$:*0.20*$Eu^{3+}$, *y*$Sr^{2+}$ phosphors. The chemicals taken in the required stoichiometric ratio were mixed, finely ground and made into a homogeneous mixture using an agate mortar and pestle in an acetone medium with intermittent drying. This powdered mixture was made into a pellet and then calcined on an alumina plate at 1400°C for 6 hours. Calcination was repeated at the same temperature and time, powdering and pelletizing after the first calcination. The properties of the phosphors thus prepared are studied using different characterization tools.

4B. 2.2 Characterization

The crystalline structure of the samples was examined with an Xray powder diffractometer (X'Pert Pro PANalytical, operated at 40 kV and 30 mA, Cu - Kα = 1.5406 Å, 2θ range = 10° - 90°). Morphological studies of powder particles were done by a scanning electron microscope (JEOL, JSM - 5600LV) operated at 15 kV. The excitation

and emission spectra were recorded on a Fluorolog HORIBA fluorescence spectrophotometer with a Xenon lamp (450 W) as the excitation source. Luminescence lifetime of the phosphors was recorded by the phosphorimeter attached to Fluorolog®3 spectrofluorimeter. CIE color coordinates of the samples were calculated using the Calc software.

4B. 3 Results and discussion

4B. 3.1 Powder X-ray Diffraction Analysis

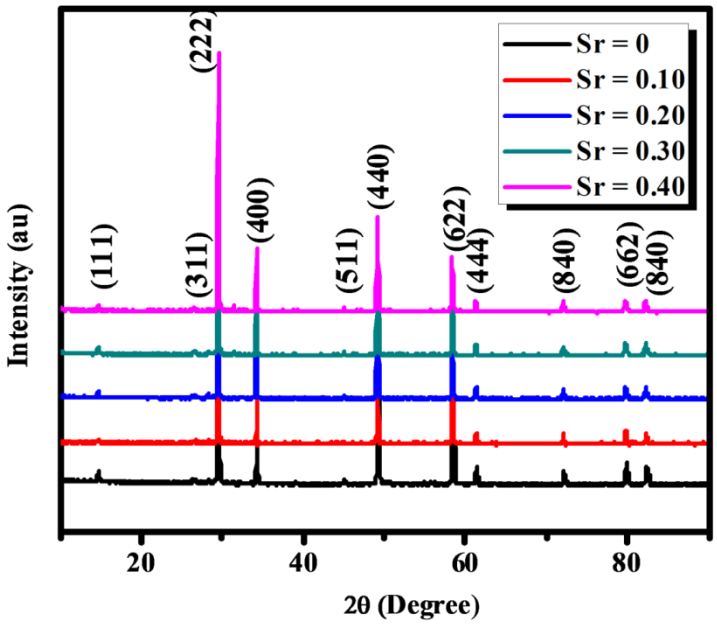

Fig. 4B.1 Powder XRD patterns of $Ca_{2-y}Y_{2.80}Nb_3O_{14}$:*0.20*$Eu^{3+}$, *y*$Sr^{2+}$ (y = 0, 0.10, 0.20, 0.30 and 0.40) phosphors.

Powder X-ray diffraction patterns of $Ca_{2-y}Y_{2.80}Nb_3O_{14}$:*0.20*$Eu^{3+}$, *y*$Sr^{2+}$ (y = 0, 0.10, 0.20, 0.30 and 0.40) phosphor samples were recorded and are presented in Fig. 4B.1. All peaks could be correctly indexed to the powder diffraction pattern of a cubic pyrochlore structure with a space group *Fd3m* (JCPDS File No: 01-081-0841) similar to the powder diffraction pattern of $Ca_2Y_3Nb_3O_{14}$ host lattice. This suggests that Sr^{2+} ion substitution cannot make any significant changes in the crystal structure but of course it will have some influence on the A-O_{8b} chains as it is bigger compared to Ca^{2+} ions. The solubility limit of Sr in place of Ca was found to be 20mol% after that some barely visible traces of

impurities are observed. Sr^{2+} ions are expected to substitute the Ca^{2+} ion site because of the matching ionic radius and valency.

To realize the extent of modification of the lattice with Sr substitution, Rietveld analysis of all the XRD patterns were carried out using X'pert HighScore Plus software. XRD patterns were fitted using a pseudo-Voigt profile function. Fig. 4B.2 shows the best fitted pattern of the observed, calculated, difference diffraction curve and Bragg positions of $Ca_{1.8}Sr_{0.2}Y_{2.8}Nb_3O_{14}$:*0.20*$Eu^{3+}$ phosphor obtained from the Rietveld refinement. Lattice parameter, selected bond distances along with R-factors are given in Table 4B.1. The values of R factors indicate a reliable structure model. It can be seen that lattice parameter and A-O_{8b} bond distance increases with increase in Sr substitution accounting its higher ionic size than Ca^{2+} ions. As discussed earlier, the shape of coordination polyhedra change with oxygen *x* parameter that determines the extent of distortion in the polyhedra A and B sites. From the refinement results, the variation of oxygen positional parameter (*x*) with Sr^{2+} ion substitution indicates the extent of distortion in the A site of pyrochlore, which has a strong influence on luminescence properties. Having heavier distortion around Eu^{3+} lattice, the local symmetry deviates from inversion center; parity forbidden transition is allowed gives strong red emission. This particular aspect is discussed in detail in luminescence section of the text. The crystal structure with cation surroundings of the samples was drawn using diamond software and representation of a typical $Ca_{1.8}Y_{2.80}Nb_3O_{14}$:*0.20*$Eu^{3+}$, *0.20*$Sr^{2+}$ phosphor is shown in Fig. 4B.3.

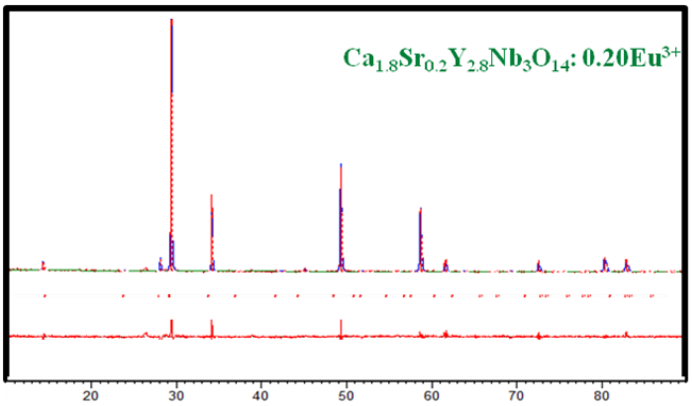

Fig. 4B.2 Refined pattern of $Ca_{1.8}Sr_{0.2}Y_{2.8}Nb_3O_{14}$:*0.20*$Eu^{3+}$ phosphor

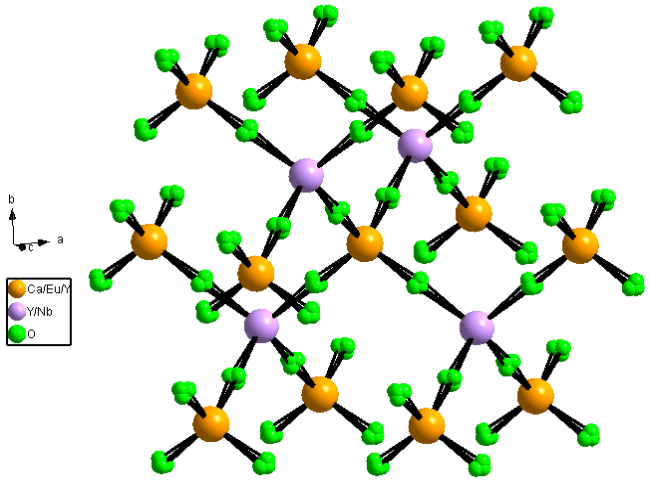

Fig. 4B.3 Crystal structure of $Ca_{1.8}Y_{2.80}Nb_3O_{14}$:*0.20*$Eu^{3+}$, *0.20*$Sr^{2+}$ phosphor

Table 4B.1 Structural parameters of $Ca_{2-y}Y_{2.80}Nb_3O_{14}$:*0.20*$Eu^{3+}$, *y*$Sr^{2+}$ (y = 0, 0.10, 0.20, 0.30 and 0.40) phosphor

Sample	Sr = 0	Sr = 0.10	Sr = 0.20	Sr = 0.30	Sr = 0.40
Phase	Pyrochlore	Pyrochlore	Pyrochlore	Pyrochlore	Pyrochlore
Unit cell	Cubic	Cubic	Cubic	Cubic	Cubic
Space group	*Fd3m*	*Fd3m*	*Fd3m*	*Fd3m*	*Fd3m*
Lattice constant (Å)	10.4644(3)	10.4739(3)	10.4795(3)	10.4858(4)	10.4910(4)
Flat background	40.8269	75.2165	74.6177	76.5264	78.1849
Coefficient 1	-12.7124	-18.7619	-20.1129	-19.2513	-17.6335
Coefficient 2	12.6163	16.3820	17.1458	15.3870	11.9769
Scale factor	0.000004	0.000007	0.000007	0.000007	0.000006
Oxygen parameter	0.334(1)	0.348(1)	0.353(1)	0.346(1)	0.346(1)
A-O_{48f} (Å)	2.151	2.139	2.111	2.270	2.271
A-O_{8b}(Å)	2.266	2.268	2.269	2.456	2.458
Caglioti parameter					
U	0.06(1)	0.12(2)	0.07(2)	0.19(2)	0.24(3)
V	-0.01(1)	-0.06(1)	-0.02(1)	-0.12(2)	-0.15(2)
W	0.007(2)	0.018(2)	0.011(3)	0.028(3)	0.033(4)
R parameters					
Rexp(%)	12.63	9.39	9.41	9.34	9.32
Rp(%)	12.39	10.36	9.65	10.37	10.32
Rwp(%)	16.89	14.23	13.41	14.39	14.78
RBragg (%)	8.95	7.76	6.83	8.15	7.35
GOF	1.79	2.29	2.02	2.37	2.51

4B. 3.2 Morphological Analysis

The SEM images of $Ca_{2-y}Y_{2.80}Nb_3O_{14}$:*0.20*$Eu^{3+}$, *y*$Sr^{2+}$ (y = 0 and 0.20) phosphors are shown in Fig. 4B.4. All the samples were slightly agglomerated and the particle size were found to be in the range 2-5μm. There is not much difference in the morphology of the samples with Sr^{2+} substitution.

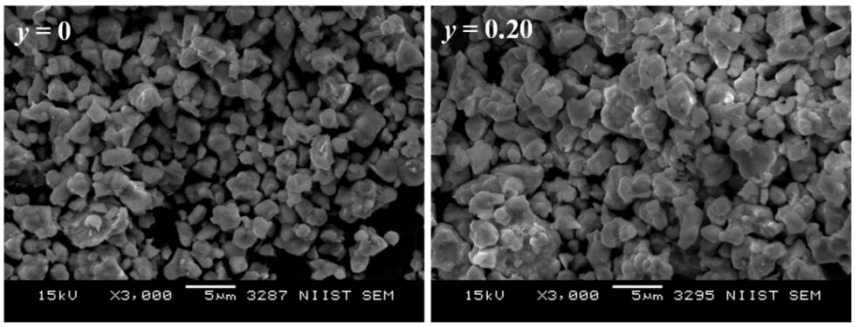

Fig. 4B.4 SEM images of $Ca_{2-y}Y_{2.80}Nb_3O_{14}$:*0.20*$Eu^{3+}$, *y*$Sr^{2+}$ (y = 0 and 0.20) phosphors

4B. 3.3 Photoluminescence Studies

Fig. 4B.5 presents the excitation spectra of the $Ca_{2-y}Y_{2.80}Nb_3O_{14}$:*0.20*$Eu^{3+}$, *y*$Sr^{2+}$ (y = 0, 0.10, 0.20, 0.30 and 0.40) phosphors for an emission at 613nm. The excitation spectra were similar to typical Eu^{3+} doped $Ca_2Y_3Nb_3O_{14}$ system. However, the intensities of CT band vary nonuniformly with Sr^{2+} ion substitution. It is well-known that the accommodation of cation with different valency and ionic radii in the pyrochlore A site can change the luminescence properties. The spectrum consists of a broad charge transfer band ranging from 250 to 350 nm and a series of sharp peaks beyond it. The most intense peaks at 393 nm and 463 nm are corresponding to the intra configurational f-f transitions of Eu^{3+} ions in the host lattice, which can be assigned to $^7F_0 \rightarrow {}^5L_6$ and $^7F_0 \rightarrow {}^5D_2$ transitions respectively. Since the Pauling's electronegativities of Ca and Sr are comparable (1 and 0.95) the CT band positions does not show any significant change. Even though, f-f transition intensities enhanced with Sr^{2+} substitution which can be attributed to the increased polarization and distortion in the lattice caused by the bigger ion substitution. The distortion of A site symmetry caused

by the incorporation of Sr^{2+} ions in the $Ca_2Y_3Nb_3O_{14}$ host lattice leads to an intense red emission.

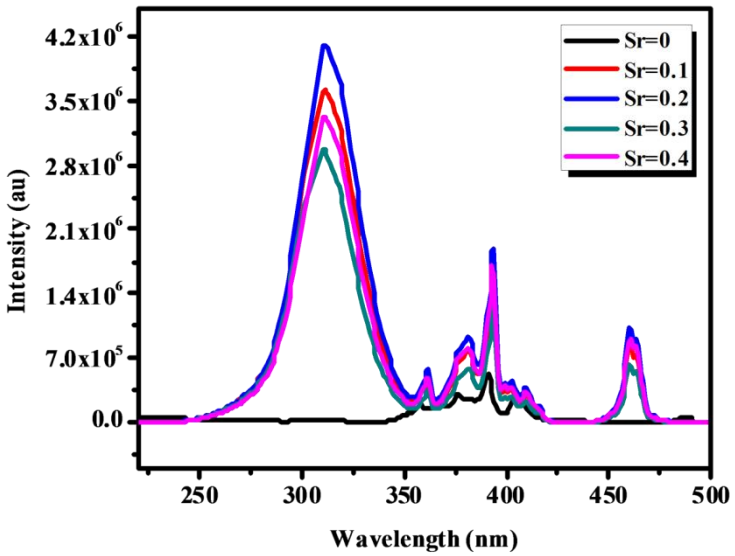

Fig. 4B.5 Excitation spectra of $Ca_{2-y}Y_{2.80}Nb_3O_{14}$:*0.20*$Eu^{3+}$, *y*$Sr^{2+}$ (y = 0, 0.10, 0.20, 0.30 and 0.40) phosphors for an emission at 613 nm.

The emission spectra of $Ca_{2-y}Y_{2.80}Nb_3O_{14}$:*0.20*$Eu^{3+}$, *y*$Sr^{2+}$ (y = 0, 0.10, 0.20, 0.30 and 0.40) phosphors under 393 nm excitation is shown in Fig. 4B.6. All the samples exhibited multiband emissions from all the f-f transitions of Eu^{3+}. The number of splits and the wavelengths of emission of Sr substituted phosphors were found to be identical with the emission spectra of Eu^{3+} doped $Ca_2Y_3Nb_3O_{14}$ phosphor. It can be clearly seen that emission intensities are enhanced with Sr^{2+} substitution and maximum intensity was observed for y = 0.20 substitution of Sr^{2+} in place of Ca^{2+}. However for higher substitutions of Sr^{2+}, the intensity was found to be declining. Fig. 4B.7 shows the dependence of experimental luminescence intensity all $^5D_o \rightarrow {}^7F_1$, $^5D_o \rightarrow {}^7F_2$, $^5D_o \rightarrow {}^7F_4$ emission intensities with respect to Sr^{2+} substitution (y = 0 – 0.30). The increased intensities could be attributed to the increased polarizable environment around the luminescent Eu^{3+} ion. The luminescence intensity greatly improves with the cation substitution. Therefore, the structural disorder induced by cation substitution can improve the luminescent efficiency of Eu^{3+}-doped phosphors. It is appreciable that the

emission intensity was increased to 3.5 times with Sr^{2+} substitution and this variation is shown in Fig. 4B.9.

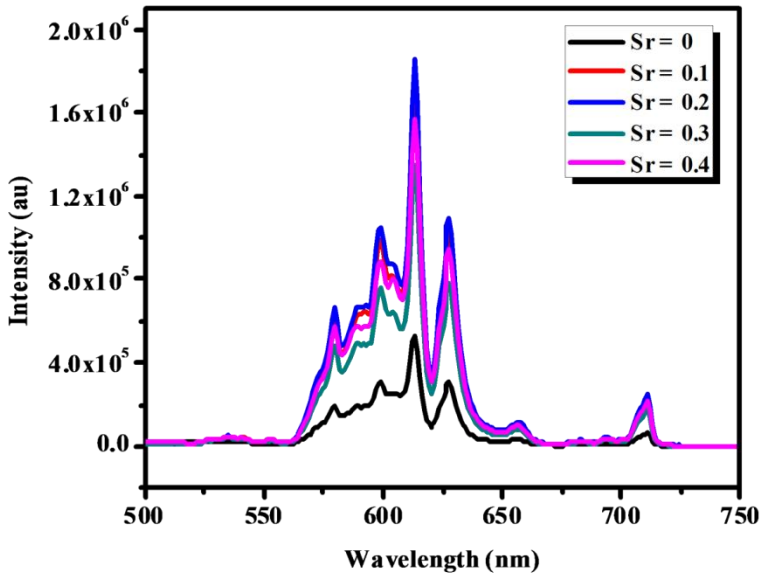

Fig. 4B.6 Emission spectra of $Ca_{2-y}Y_{2.80}Nb_3O_{14}$:*0.20*$Eu^{3+}$, *y*$Sr^{2+}$ (y = 0, 0.10, 0.20, 0.30 and 0.40) phosphors excited at 393 nm

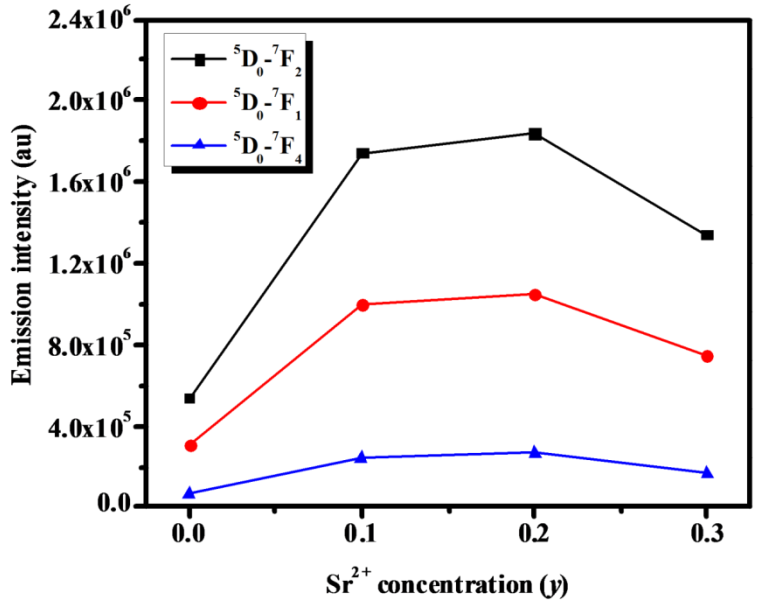

Fig. 4B.7 The variation of all $^5D_o \rightarrow {}^7F_1$, $^5D_o \rightarrow {}^7F_2$, $^5D_o \rightarrow {}^7F_4$ emission intensities with respect to Sr^{2+} substitution levels of $Ca_{2-y}Y_{2.80}Nb_3O_{14}$:*0.20*$Eu^{3+}$, *y*$Sr^{2+}$ (y = 0, 0.10, 0.20, and 0.30) phosphors excited at 393 nm.

Table 4B.2 Optical properties $Ca_{2-y}Y_{2.80}Nb_3O_{14}$:*0.20*$Eu^{3+}$, *y*$Sr^{2+}$ (y = 0, 0.10, 0.20, 0.30 and 0.40) phosphors.

y	Asymmetric ratio	Lifetime (ms)	Efficiency (%)	J-O Intensity Parameters		Color coordinates (*x*, *y*)
				Ω_2	Ω_4	
0	2.58	0.89	32.23	4.63	6.35	(0.52, 0.34)
0.10	1.78	0.93	39.64	6.06	8.32	(0.59, 0.37)
0.20	1.79	0.95	40.60	6.07	8.46	(0.60, 0.37)
0.30	1.77	0.83	34.72	5.97	8.28	(0.58, 0.37)
0.40	1.75	0.89	38.95	6.24	8.30	(0.58, 0.37)

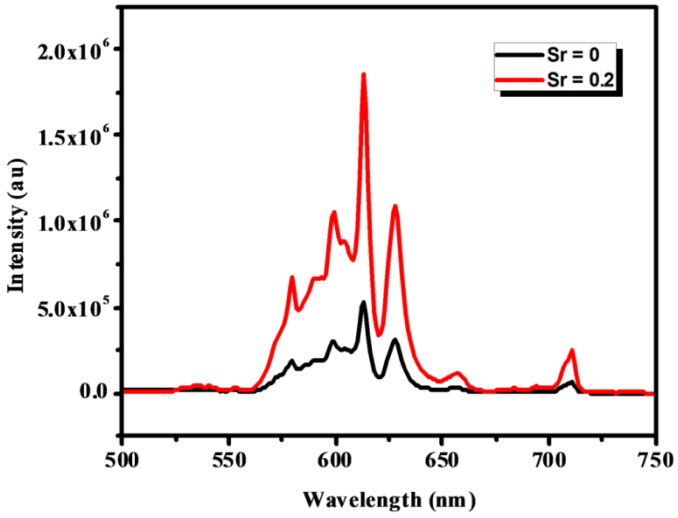

Fig. 4B.8 Comparison between the emission spectra of $Ca_{2-y}Y_{2.80}Nb_3O_{14}$:*0.20*$Eu^{3+}$, *y*$Sr^{2+}$ (y = 0, and 0.20) phosphors excited at 393 nm.

In the emission spectra, the hypersensitive electric dipole transition around 613 nm dominates over the allowed magnetic dipole transition and both the transitions got enhanced Sr^{2+} ions substitution. The difference in ionic radii would probably give rise to diversity in the sublattice structure around the Eu^{3+} ions. This in turn influences the spin-orbit coupling and the crystal field of Eu^{3+} ions. The ionic radius mismatch between Sr^{2+} and Ca^{2+} ions results in the deviation from the D_{3d} point symmetry. Size differences can induce the tilting of BO_6, which can influence the irregular coordination

in the AO_8 polyhedra. This phenomenon causes the distortion of Eu^{3+} surrounding the lattices, resulting in the strong ($^5D_0$-$^7F_2$) transition in the emission. Also, since three types of cations (Ca, Y and Sr) shared in the same lattice site (A site), Eu^{3+} ion loses its site symmetry, thereby enhancing the hypersensitive transitions. Recent experiments and calculations have confirmed that the introduction of cation disorder considerably improves luminescence efficiency of Eu-doped phosphors (Wang *et al*. 2013). Cation disorder suppresses nonradiative processes through the disruption of lattice vibrations and creates deep traps that release electrons to compensate for thermal quenching. Thus, the distortion caused by the accommodation of bigger Sr ions exhibit distinct influences on the luminescence of Eu^{3+} ions. It is worth noticing that emission intensity ratio of ($^5D_0$-$^7F_2$)/ ($^5D_0$-$^7F_1$) of $Ca_{2-y}Y_{2.80}Nb_3O_{14}$:*0.20*$Eu^{3+}$, *y*$Sr^{2+}$ (y = 0, 0.10, 0.20, 0.30 and 0.40) phosphors rapidly decreases with the Sr^{2+} ion substitution (Table 4B.2). This higher value is accountable for the red chromaticity of the phosphors.

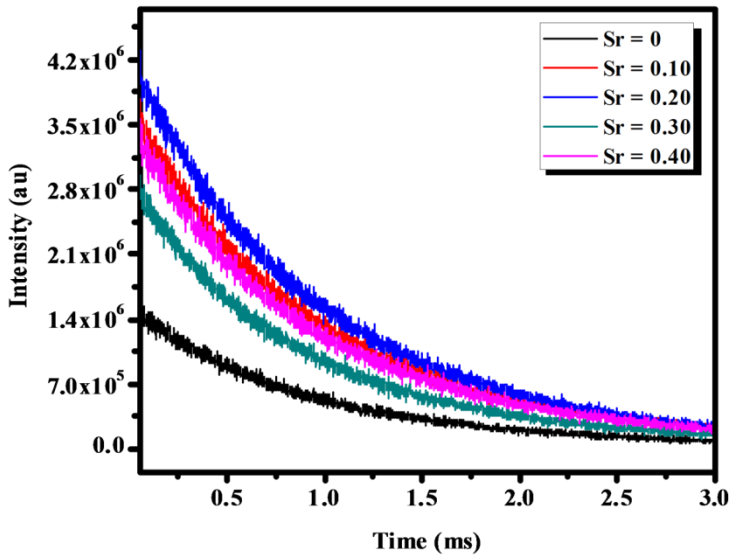

Fig. 4B.9 Decay curves of $^5D_0$-$^7F_2$ transition of Eu^{3+} (λ_{em} = 613 nm) in $Ca_{2-y}Y_{2.80}Nb_3O_{14}$:*0.20*$Eu^{3+}$, *y*$Sr^{2+}$ (y = 0, 0.10, 0.20, 0.30 and 0.40) phosphors at 393 nm excitation.

Fig. 4B.9 illustrates the fluorescence decay of the $^5D_0 \rightarrow {}^7F_2$ luminescence (613 nm) for the $Ca_{2-y}Y_{2.80}Nb_3O_{14}$:*0.20*$Eu^{3+}$, *y*$Sr^{2+}$ (y = 0, 0.10, 0.20, 0.30 and 0.40) phosphors. The curves show a single-exponential profile and can be fitted to a single exponential

function, signifying that only one de-excitation process is present. The obtained luminescence lifetimes are listed in Table 4B.2. The luminescence in Sr substituted phosphors presents a longer lifetime than that in Eu^{3+}-doped $Ca_2Y_3Nb_3O_{14}$ phosphors. This observation indicates that the cation disorder prolongs the luminescence lifetimes of Eu^{3+}-doped phosphors. Normally, the luminescence lifetime of Eu^{3+} ions could be influenced by several factors such as the changes of crystallographic surrounding, particle size, morphology of phosphors and so on. In our system, the increase of the lifetime could be resulted from the reduced transition rates of Eu^{3+} ions due to the surrounding structure changes. Meanwhile, the luminescence quantum efficiency calculated from the lifetime value improved due to the cation substitution in $Ca_2Y_3Nb_3O_{14}:Eu^{3+}$ phosphor and maximum efficiency is attained for 20mol% of Sr substitution. The luminescence behavior of Eu^{3+} ions with cation substitution is further confirmed by the J-O intensity parameters which is larger for Sr substituted samples. Significantly, structure distortions are responsible for luminescence changes.

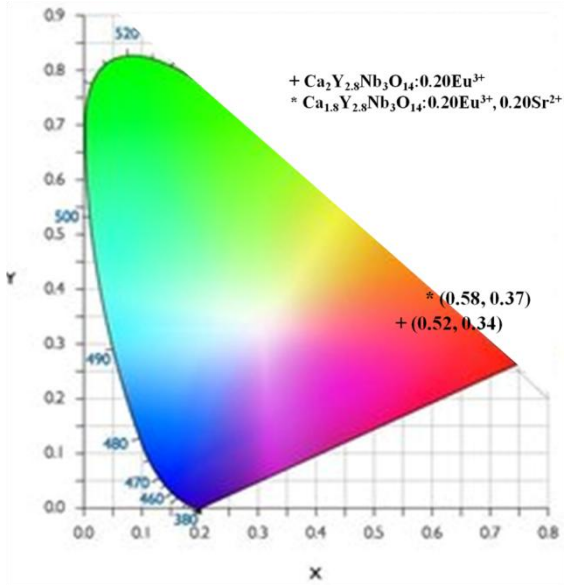

Fig. 4B.10 CIE chromaticity diagram for Eu^{3+} emission in $Ca_2Y_{2.80}Nb_3O_{14}$:*0.20*Eu^{3+} and $Ca_{1.8}Y_{2.80}Nb_3O_{14}$:*0.20*$Eu^{3+}$, *0.20*$Sr^{2+}$ phosphors under 393 nm excitation.

The CIE color coordinates (*x, y*) were calculated using the Color Calculator software to characterize the color emission and the values are listed in Table 4B.2. Fig.

4B.10 shows the CIE chromaticity diagram for Eu^{3+} emission in $Ca_2Y_{2.80}Nb_3O_{14}$:*0.20*Eu^{3+} and $Ca_{1.8}Y_{2.80}Nb_3O_{14}$:*0.20*$Eu^{3+}$, *0.20*$Sr^{2+}$ phosphors under 393 nm excitation. It can be seen that the emission color shifts to deep red region on varying the concentration of Sr^{2+} ions. These results show that tuning of red emission color is possible by the incorporation of bigger cations like Sr in the pyrochlore host lattice.

4B. 4 Conclusions

This study investigates the influence of cation substitution of $Sr^{2+} \rightarrow Ca^{2+}$ on the structural and optical properties of pyrochlore $Ca_2Y_2Nb_3O_{14}$:Eu^{3+} phosphors. All the samples were prepared via conventional high-temperature solid state reaction route. The Sr^{2+} cation substitution results in pyrochlore lattice distortion, which was confirmed by Rietveld structure refinements. The optimum doping concentration of Sr^{2+} ion was found to be y = 0.20. The introduction of cation disorder in $Ca_{2-y}Y_{2.80}Nb_3O_{14}$:*0.20*$Eu^{3+}$, $y$$Sr^{2+}$ (y = 0, 0.10, 0.20, 0.30 and 0.40) improves luminescence intensity, prolongs emission lifetime and increases excitation efficiency in the blue region. Meanwhile, the emission color can be tuned from origin red to pure red due to the structural distortion of the activator Eu^{3+} ions. These results suggest that substitution of bigger cations can effectively improve the luminescence properties of Eu^{3+}-activated phosphors.

Chapter 5A

EXPLOITATION OF Eu^{3+} RED LUMINESCENCE THROUGH ORDER-DISORDER STRUCTURAL TRANSITION IN RARE-EARTH STANNATE PYROCHLORE FOR WHITE LED APPLICATIONS

In this work, a series of Eu^{3+} doped $Ln_{2.85}YSnNbO_{10.5}$:0.15Eu^{3+} (Ln = La, Gd, Y and Lu) red phosphors were synthesized to explore the influence of phase evolution on the luminescence properties. The substitution of Ln^{3+} ions in the A site of the pyrochlore induces a structural transition from an ordered pyrochlore to a disordered fluorite structure with decreasing ionic radius. Their luminescence properties got enhanced with increased ordering of cations from Lu to La. The long range ordering, ligand polarizability and covalent nature of Eu^{3+} bonding influence the emission probability and improves the quantum efficiency of the La host. Eu^{3+} emission due to $^5D_0$-^7F_J transition is significantly improved with increase in the concentration of Eu^{3+} ions in the La host.

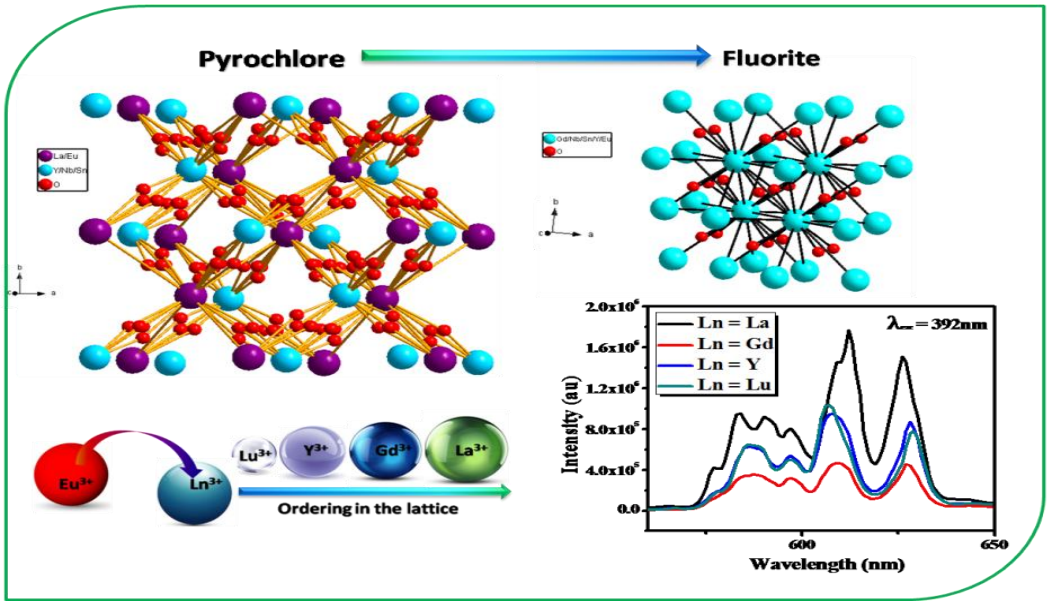

Sreena. *et al*. *Phys. Chem. Chem. Phys*. **2018**, 20, 24287-24299.

5A. 1 Introduction

The research efforts to develop novel phosphor materials for applications in next generation displays and solid state lighting remains a great challenge in the area of solid state lighting industry for the last few decades (Martínez *et al*.. 2011; Jiao *et al*. 2013; Jin *et al*. 2013). The main problem is the absorption by the phosphor of nUV (near ultra-violet)/blue light emitted by the InGaN LED chip, resulting in color change and luminous reduction. Therefore, the research for novel red-emitting phosphors with high efficiency, excellent chemical stability and effective absorption in the UV region is extremely desirable for applications in white light emitting diodes. Eu^{3+} ions are usually employed as an optical probe to investigate the coordination and environment around the cations substituted in the crystalline lattice due to the fact that the $^5D_0$ (or $^7F_0$) level is non-degenerate and the splitting of these emission (or absorption) transitions reflects the crystal-field (CF) splitting of the nominal ^7F_J (or $^{2S+1}L_J$) levels that depend on site symmetry (Lin *et al*. 2010; Chen *et al*. 2005; Dexpert-Ghys *et al*. 1981; Hölsä *et al*. 1981). So, our intimidating task is to find a suitable host lattice in which both electric and magnetic dipole transitions of Eu^{3+} ion are manifest.

Among the existing materials of interest, pyrochlores scores over other due to their inherent properties. Further interest in this area of pyrochlores is that they have a tendency to order-disorder transformation at elevated temperatures, which can be modified by the incorporation of cations, differing in size or valence from the host cations of the pyrochlore structure (Sickafus *et al*. 2000). In most cases, the transitions from ordered pyrochlore to disordered fluorite structure occur by means of temperature (Radhakrishnan *et al*. 2011), pressure (Zhang *et al*. 2008), chemical substitution (Panero *et al*. 2004) or high-energy irradiation (Lumpkin *et al*. 2007). Disordering of the cation sites coupled with oxygen disorder on the anion vacancies within the pyrochlore unit cell results in defect fluorite structure. The study of pyrochlore to fluorite phase transition requires a lot of attention since it governs the structural properties, which in turn influence the photoluminescence properties.

Among the various pyrochlore oxides the rare earth stannates, $Ln_2Sn_2O_7$ form a series of isostructural compounds and have been well investigated (Kennedy *et al*. 1997) due to their interesting electrical, optical and magnetic properties as well as high thermal stability. Lu *et al*. and Cheng *et al*. reported the luminescence properties of Eu^{3+} doped $Ln_2Sn_2O_7$ phosphors (Lu *et al*. 2004; Cheng *et al*. 2008). These phosphors exhibit intense and prevailing emission at 589 nm due to the parity allowed $^5D_0$-$^7F_1$ magnetic dipole transition. For an enhanced parity forbidden red emission in pyrochlore phosphors, one has to destruct the inversion symmetry of Eu^{3+} site such that there will be a superior probability of mixing of CT band wave function with f orbital resulting in relaxation of the parity selection rules. So, we tried to enhance the f-f transition intensity of rare-earth stannate pyrochlore phosphors by incorporating various rare-earth ions at the A site and Nb^{5+} ions at the B site. Thus, in the present study we made an attempt to vary the A site cation in the $Ln_{2.85}YSnNbO_{10.5}$:$0.15Eu^{3+}$ system by substituting various lanthanides (Ln = La, Gd, Y and Lu) so as to gradually transform the structure from an ordered pyrochlore to disordered fluorite through order-disorder transition. Detailed powder X-ray diffraction analysis supported by Raman spectroscopic studies has been performed to gain an insight into the structural changes occurring upon gradual substitution with various lanthanides and the results are discussed herein. Optical studies have been performed on these materials to correlate the trend in emission properties with the disorder induced in the structure upon lanthanide substitution.

5A. 2 Experimental

The phosphors $Ln_{2.85}YSnNbO_{10.5}$:$0.15Eu^{3+}$ (Ln = La, Gd, Y and Lu) and $La_{3-x}YSnNbO_{10.5}$:xEu^{3+} (x = 0.10, 0.30, 0.50, 0.75, 1.00 and 1.25) were prepared via conventional solid state reaction method using La_2O_3, Gd_2O_3, Y_2O_3, Lu_2O_3, SnO_2, Nb_2O_5 and Eu_2O_3 as starting materials. All the chemicals employed for the sample preparation were of analytical reagent (AR) grade and procured from Sigma Aldrich. The precursor chemicals were weighed in the required stoichiometric ratio and mixed in an agate mortar using acetone as the wetting medium. This process of mixing and drying was repeated thrice to obtain a homogeneous mixture. The obtained products were calcined

on an alumina plate at 1500°C for 6h. The calcined products were then ground into a fine powder for carrying characterizations.

The powder X-ray diffraction patterns were recorded to identify the crystalline phase of the calcined samples using PANalytical X'Pert Pro diffractometer. The structure refinement of XRD data was performed using commercial X'Pert Highscore Plus software. The Raman spectra of the prepared samples were acquired using an integrated micro-Raman system using a 633 nm helium-neon laser source with a spatial resolution of 2 μm to explore the structural aspects of the powder samples. The morphological analysis of the powder samples were performed using scanning electron microscope (JEOL, JSM-5600LV) operated at 15kV. Energy dispersive analysis and elemental mapping was carried out using a Silicon Drift Detector–X-Max^N attached with a Carl Zeiss EVO SEM. EDS elemental mapping was employed by Aztec Energy EDS Microanalysis Software. The absorbance study of the synthesized samples was carried out using Shimadzu, UV-3600 UV-visible spectrophotometer with barium sulfate as the reference. The excitation and emission spectra of the prepared samples were recorded on a Fluorolog HORIBA fluorescence spectrophotometer.

5A. 3 Results and discussion

5A. 3.1 Phase Evolution in $Ln_{2.85}YSnNbO_{10.5}$:$0.15Eu^{3+}$ (Ln = La, Gd, Y and Lu) Red Phosphor

It can be seen from the XRD patterns in Fig. 5A.1(a) that the diffraction peaks could be indexed to a cubic pyrochlore phase with a space group *Fd3m* for Ln = La and for the other lanthanides it could be indexed to a cubic fluorite type phase with a space group *Fm3m*. As pyrochlore is a superstructure of fluorite type unit cell, its diffraction pattern consists of a set of strong intensities representative of the average fluorite type structure along with an additional set of weak superstructure reflections. Therefore, the superstructure peaks contain all the information on the ordering process and the associated structural transition. It can be clearly seen that the intensities of weak superstructure peaks (111), (311) and (331) which are characteristic of the pyrochlore structure decreases gradually with lanthanide ion substitution. The intensity of

characteristic superstructure peaks depends on the size and atomic number of ions at the A site and diminishing in intensity suggests a phase transition from an ordered pyrochlore to the defect fluorite structure.

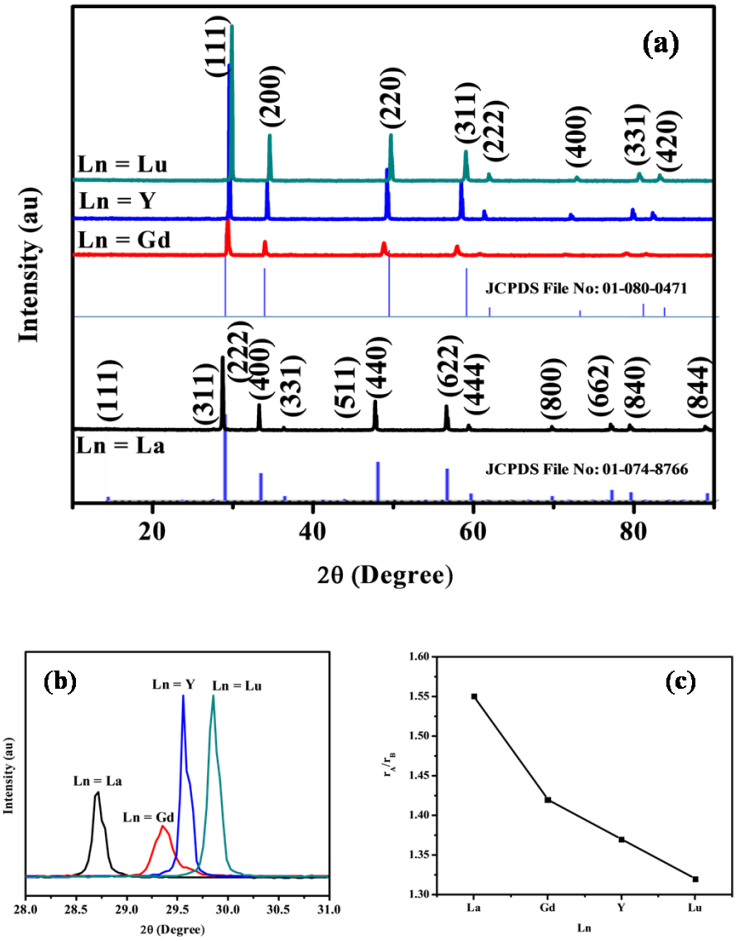

Fig. 5A.1 (a) Powder X-ray diffraction patterns of $Ln_{2.85}YSnNbO_{10.5}$:*0.15*Eu^{3+} (Ln = La, Gd, Y and Lu) phosphors. **(b)** The expanded view of the 2θ between 28 to 31°. **(c)** Variation of radius ratio with lanthanide substitution on the A site.

Fig. 5A.1 (b) represents the shift of main peak to higher angles with Ln is changed from La to Lu. Dickson et al. suggested that the weak (111) reflection is most sensitive to the oxygen *x*-parameter of *48f* oxygen (Dickson *et al*. 1986). In this system, only $La_{2.85}YSnNbO_{10.5}$:*0.15*Eu^{3+} crystallize into completely ordered pyrochlore while all the other lanthanides $Ln_{2.85}YSnNbO_{10.5}$:*0.15*Eu^{3+} (Ln = Gd, Y and Lu) exhibit defect fluorite phase. Therefore, oxygen *x*-parameter can be calculated only for La system and

so we can't draw any information about the structural transition from the oxygen *x*-parameter variation. Hence, the diminishing trend of characteristic superstructure peaks can be explained using radius ratio of cations at the A site to that at B site (r_A/r_B). As can be seen from the Fig. 5A.1(c) that, the radius ratio decreases gradually with the lanthanide ion substitution indicating the possibility of order-disorder phase transition which is in agreement with the observation from the XRD analysis. It was earlier reported that, as the radius ratio decreases the pyrochlore structure tends to get converted from well ordered structure to disordered structure in which the superstructure peaks intensity diminish. The decrease in radius ratio tends to distribute the cations randomly between A and B sites which in turn affect the scattering efficiency of certain lattice planes. As the lattice undergoes phase transition, X-ray scattering from these particular planes decreases and the corresponding superlattice peaks gradually disappear.

To validate the crystal structure and the space group in which the compound belongs, Rietveld analysis of all the four XRD patterns were carried out using commercial X'Pert Highscore Plus software. In all the cases, Eu^{3+} ions are expected to occupy the Ln^{3+} sites in view of the matching ionic radius and valency. At first, scale factor and background polynomial was fitted. The diffraction peak profile was fitted using pseudo-Voigt profile function and Caglioti profile parameters were refined. Oxygen *x*-parameter was refined only for the La substituted one. The refined parameters obtained from Rietveld analysis are given in Table 5A.1. A few typical refinement profiles after Rietveld refinement are shown in Fig. 5A.2.

It can be seen from the Table 5A.1 that the lattice parameter decreases with rare-earth ion substitution (La to Lu) at the A site which is reflected in the peak positions shifting towards higher angles (Fig. 5A.1b). As the structure transforms to defect fluorite for Ln = Gd, an abrupt change in lattice parameter occurs i.e., the lattice constant becomes about half of the ordered pyrochlore structure. This decrease in lattice parameter can be ascribed to the significant decrease in the ionic size at A site with substitution. Thus from XRD analysis, we can conclude that polymorphism exists in these family of compounds $Ln_{2.85}YSnNbO_{10.5}$:*0.15*Eu^{3+} (Ln = Gd, Y and Lu). This kind

of polymorphism arises from the progressive ordering of both anion and cations of the pyrochlore structure. As known, in a pyrochlore structure the A and B site cations have D_{3d} symmetry, whereas in a fluorite unit cell the site symmetry is O_h for the A cations. A fluorite unit cell contains only one equivalent cation site, while in a pyrochlore structure there are two non-equivalent cation sites. The occurrence of more superstructure peaks and the number of non-equivalent cation sites in $La_3YSnNbO_{10.5}$ points out a long range order which has a strong influence on the photoluminescence properties when compared to other lanthanide systems. The average crystallite size of the samples calculated from the XRD pattern using Scherrer equation was around 64 nm for La, Y and Lu host and about 43 nm for the Gd one. The small crystallite size of Gd host may be due to poor crystallinity compared to others which adversely affects the luminescence properties. This could be presumably due to Gd being in the phase boundary of the transition.

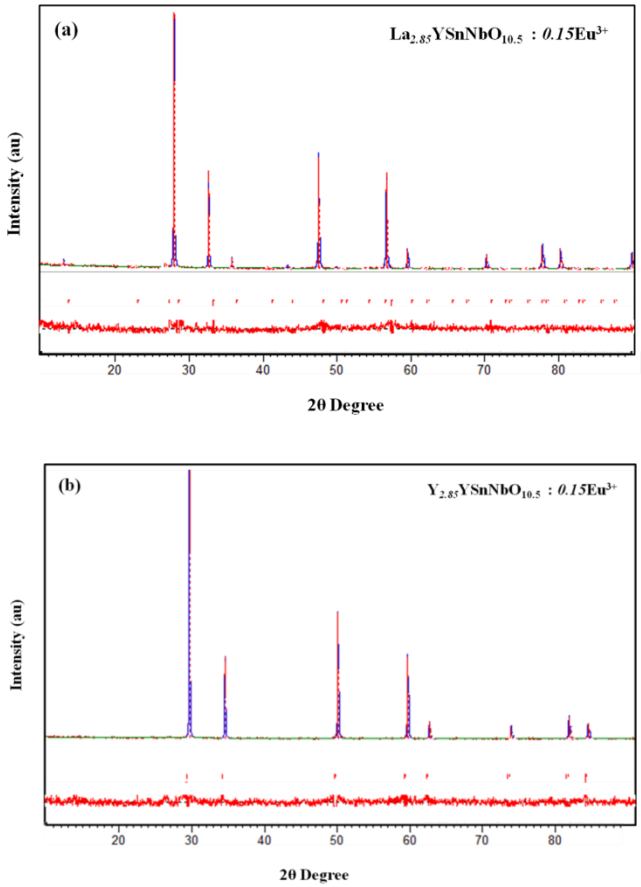

Fig. 5A.2 Refined pattern of $La_{2.85}YSnNbO_{10.5}$:*0.15*Eu^{3+} and $Y_{2.85}YSnNbO_{10.5}$: *0.15*Eu^{3+}.

Table 5A.1 Refined parameters from Rietveld Analysis of $Ln_{2.85}YSnNbO_{10.5}$:*0.15*Eu^{3+} (Ln = La, Gd, Y and Lu) samples

Sample	**La**	**Gd**	**Y**	**Lu**
Phase	Pyrochlore	Fluorite	Fluorite	Fluorite
Unit cell	Cubic	Cubic	Cubic	Cubic
Space group	*Fd3m*	*Fm3m*	*Fm3m*	*Fm3m*
Lattice constant (Å)	10.7772(2)	5.2837(4)	5.2325(8)	5.1899(1)
Oxygen *x* parameter	0.332(1)			
Caglioti parameters				
U	0.017(6)	-0.06(7)	0.019(4)	0.02(1)
V	0.003(5)	0.16(5)	-0.009(4)	0.03(1)
W	0.006(1)	0.00(1)	0.0067(8)	0.001(2)
R-factors				
R_{exp} (%)	12.70	9.09	9.69	9.74
R_p (%)	11.81	7.89	8.51	9.39
R_{wp} (%)	15.92	10.29	11.00	11.99
GOF	1.57	1.28	1.29	1.52

It is well-known that X-ray diffraction is more sensitive to disorder in the cation sublattice than in the anion sublattice since the X-ray scattering power of oxygen is very less compared to the heavy metal ions. However, Raman spectroscopy is very sensitive to metal-oxygen vibrations rather than metal-metal vibrations. Therefore, it is an excellent tool to explore the local disorder in the pyrochlore and thereby distinguish between ordered pyrochlore and defect fluorite phases (Glerup *et al*. 2001). Factor group analysis based on the site symmetries predicts six Raman active modes in ordered pyrochlores ($A_2B_2O_7$) with a space group *Fd3m* and Z = 8 and only one Raman active mode in defect fluorite (AO_2) with a space group *Fm3m* and Z = 4

In pyrochlore, $\Gamma_{(Raman)} = A_{1g} + E_g + 4F_{2g}$ (5A.1)

In fluorite, $\Gamma_{(Raman)} = F_{2g}$ (5A.2)

Here, E_g mode corresponds to B-O_6 bending vibrations and A_{1g} mode to O-B-O bending vibrations and F_{2g} mode is due to the A-O and B-O bond stretching vibrations with bending vibrations.

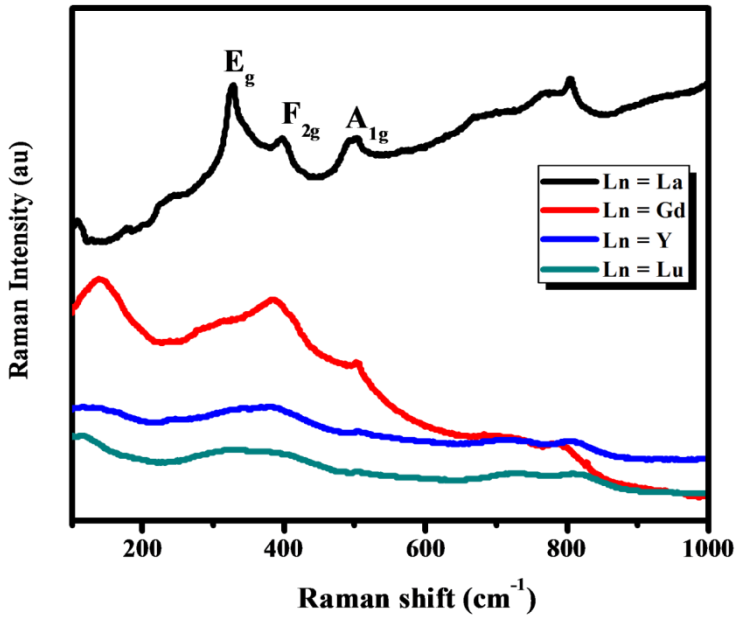

Fig. 5A.3 FT-Raman spectra of $Ln_{2.85}YSnNbO_{10.5}$:*0.15*Eu^{3+} (Ln = La, Gd, Y and Lu) phosphors.

Fig. 5A.3 shows the FT-Raman spectra of $Ln_{2.85}YSnNbO_{10.5}$:*0.15*Eu^{3+} (Ln = La, Gd, Y and Lu) phosphors in the wavenumber range 100-1000 cm^{-1} and the various modes are assigned according to the Raman measurements reported in the literature (Zhang *et al*. 2005; Scheetz *et al*. 1979)). It is clear from the spectra that only $La_3YSnNbO_{10.5}$ retain the ordered pyrochlore structure, Raman peaks successively broaden to a significant extent for all the other lanthanides (Ln = Gd, Y, and Lu). The distinct modes in the Raman spectra of $La_{2.85}YSnNbO_{10.5}$:*0.15*Eu^{3+} cubic pyrochlore could be assigned as E_g mode at ~ 325 cm^{-1}, F_{2g} mode at ~ 399 cm^{-1} and A_{1g} mode at ~ 500 cm^{-1}. One extra mode appearing at ~ 806 cm^{-1} may due to local disorder, vacancies and defects occur in the pyrochlore lattice and subsequent relaxation of the selection rules. This may lead to the appearance of less intense additional modes in the Raman spectra. Normally, F_{2g} modes of the pyrochlores are observed around 300, 400, 510 and 610 cm^{-1} due to a combination of B-O_6 bending, A-O bending/stretching, O-B-O bending, and B-O stretching vibrations. Due to the spectral overlap produced by the broadening of E_g and A_{1g} modes, the F_{2g} modes around 300, 510 and 610 cm^{-1} are absent in our spectrum. The less intense peak appearing at around 399 cm^{-1} is related to the 8b site oxygen

whereas the A_{1g} mode is related to the vibrations of 48f anion and increase in width of this mode point towards the degree of disorder in the 48f oxygen sites. F_{2g} mode involves the displacement of oxygen atoms on both 48f and 8a sites. Raman spectra of all compositions beyond La consist of broad bands and the broadness increases with lanthanide substitution. This broadening of Raman peaks with lanthanide substitution is mainly due to the partial disorder induced in the cationic sublattice. The disorder created due to the cationic substitution disrupts the translational periodicity and thereby relaxes the k = 0 selection rule (Arenas *et al*. 2010). As a result, phonons from all parts of the Brillouin zones contribute to the optical spectra results in broad bands. The appearance of these broad bands clearly indicate a phase transition from ordered pyrochlore to defect fluorite phase beyond Ln = La. These Raman spectroscopy results corroborates the conclusions drawn from the XRD studies, as discussed earlier. It is clear from the spectra that the peak intensity of E_g, A_{1g} and F_{2g} modes decreases with lanthanide substitution, indicating a progressive disordering of anion sublattice. For fluorite structured compounds, broad band occurring at around 399 cm^{-1} shift to higher wavenumbers with Ln^{3+} substitution. This can be attributed to the decreasing trend of ionic radius of Ln ions which is related to the lanthanide induced lattice contraction as evidenced from XRD studies. The replacement of Ln by smaller Ln cation will result in the movement of oxygen atoms close with the smaller Ln cation, thereby increasing the B-O bond. These results predict a linear relation between the ionic radius of Ln cations and O-B-O bond angles. The higher mass of A cations with the same B sites results in the shift of wavenumbers. Hence, the A site ionic radius play an important role in the magnitude of bond angles and the position of vibrational modes. Thus, Raman spectra mainly exhibit changes in fwhm and intensity of active modes with cationic substitution, which reflect the disorder of the cation sublattice.

SEM micrographs obtained for $Ln_{2.85}YSnNbO_{10.5}$:*0.15*Eu^{3+} (Ln = La, Gd, Y and Lu) phosphors are displayed in Fig. 5A.4. All the samples consist basically of sub-micron size agglomerates of irregular shape. It could be seen that the particle distribution was homogeneous and decrease in grain size is observed with the rare earth cation radius. EDS micrographs of $Ln_{2.85}YSnNbO_{10.5}$:*0.15*Eu^{3+} (Ln = La, Gd, Y and Lu) phosphors

calcined at 1500°C are given in Fig. 5A.5. Chemical compositions revealing atomic ratios are very close to that of the nominal composition. The chemical homogeneity of the as-prepared samples was examined using elemental X-ray dot mapping technique. The elemental maps of all the elements present in the sample shows a uniform density distribution, thus confirming that the activator distribution is homogeneous throughout the material. Elemental mapping of typical $La_{2.85}YSnNbO_{10.5}$:*0.15*Eu^{3+} phosphor is shown in Fig. 5A.6.

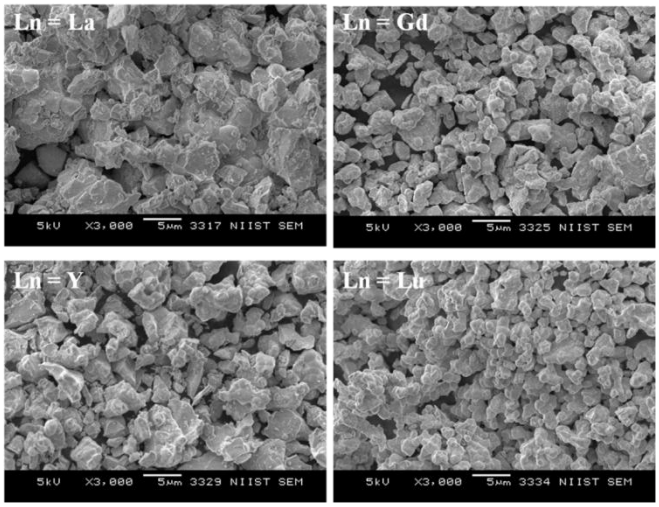

Fig. 5A.4 Scanning electron micrographs of $Ln_{2.85}YSnNbO_{10.5}$:*0.15*Eu^{3+} (Ln = La, Gd, Y and Lu) phosphors.

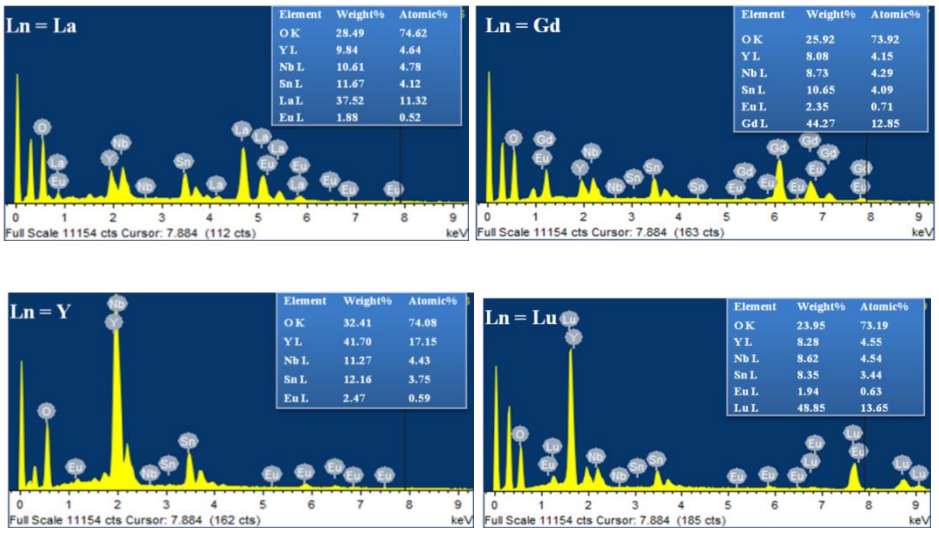

Fig. 5A.5 EDS spectra of $Ln_{2.85}YSnNbO_{10.5}$:*0.15*Eu^{3+} (Ln = La, Gd, Y and Lu)

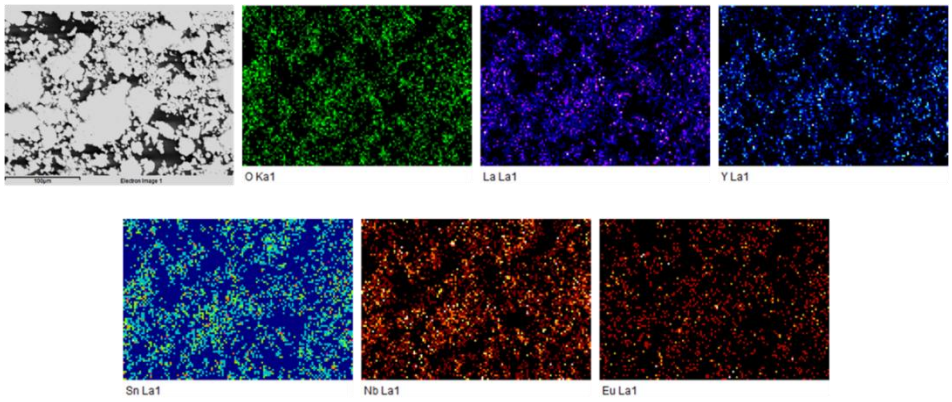

Fig. 5A.6 Elemental X-ray dot mapping of typical $La_{2.85}YSnNbO_{10.5}$:*0.15*Eu^{3+}

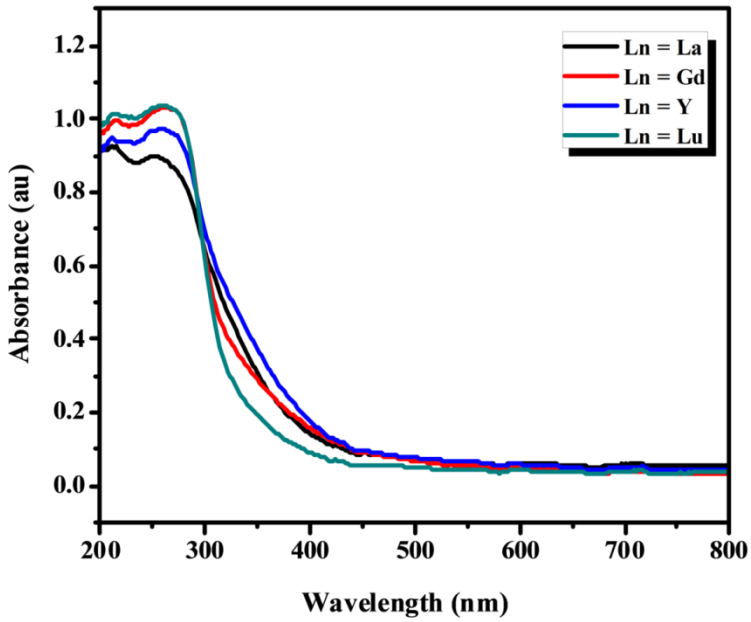

Fig. 5A.7 UV-visible absorption spectra of $Ln_{2.85}YSnNbO_{10.5}$:*0.15*Eu^{3+} (Ln = La, Gd, Y and Lu) phosphors.

The UV-visible absorption spectra of $Ln_{2.85}YSnNbO_{10.5}$:*0.15*Eu^{3+} (Ln = La, Gd, Y and Lu) phosphors synthesized by solid state method is shown in Fig. 5A.7. All the samples exhibit broad band of absorption in the UV region with a maximum at around 260 nm due to the charge transfer transition from oxygen ligand to Eu^{3+} ions and to the central stannate/niobate ions in the host lattice. It is clear from the spectra that the absorption edge shows a blue shift with decrease of Ln^{3+} ion radius. The band gap energy calculated using Shapiro's method by extrapolating the onset of absorption to

the wavelength axis also increases with lanthanide substitution (Table 5A.2). The band gap energy is usually found to increase with decreasing particle size due to quantum confinement effect (Choi *et al*. 2014). As seen from the SEM images that the particle size deceases as the lanthanide switches through La to Lu and hence band gap energy increases.

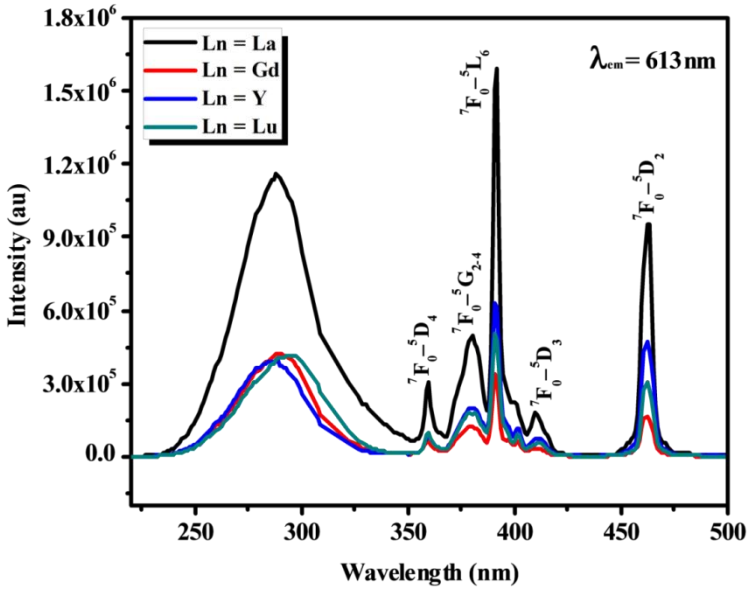

Fig. 5A.8 Excitation spectra of $Ln_{2.85}YSnNbO_{10.5}$:*0.15*Eu^{3+} (Ln = La, Gd, Y and Lu) phosphors for an emission at 613 nm.

In order to establish a correlation between the disorders induced into the system as a result of Ln^{3+} ion substitution and luminescence properties, all the samples were subjected to PL studies. Fig. 5A.8 shows the excitation spectra of $Ln_{2.85}YSnNbO_{10.5}$:*0.15*Eu^{3+} (Ln = La, Gd, Y and Lu) phosphors recorded under the same instrumental conditions. The excitation spectra of all the samples consist of a broad band from 250 to 350 nm, which is mainly attributed to the charge transfer from O^{2-} - Eu^{3+} and the central stannate/niobate groups in the host lattice. The excitation peaks of La, Gd, Y and Lu substituted compounds are centered at around 288, 290, 286 and 295 nm respectively. It is well known that CT band position is closely related to the coordination environment of Eu^{3+} ions in the host lattice and the covalence of Eu^{3+} - O^{2-} bonding. The band position is more or less fixed in VI coordination and varies in VIII

and IX coordination as a function of Eu-O bond distance in the host lattice (Hoefdraad *et al*. 1975). A shorter Eu-O bond length results in enhanced covalence leading to the red shift of CTB (Pei *et al*. 1991). The position of CTB for Gd and Lu host shifted towards the red side of La because the bond length of Eu^{3+}-O^{2-} in Gd and Lu systems is smaller than that in La system. However, the CTB position shows a blue shift when the Ln^{3+} ion is changed from Gd^{3+} to Y^{3+} and does not follow the trend of CTB variation as a function of bond distance. In the bond structure of Eu^{3+} - O^{2-} - Ln^{3+}, the degree of covalency is weaker in the Y host because Y^{3+} attracts O^{2-} electron cloud most strongly since it has the largest electronegativity and smaller ionic radius compared to Gd^{3+} ion. Hence, the electronic transition from the 2p orbital of O^{2-} to the 4f orbital of Eu^{3+} could be more possible in the Gd host than in the Y one and that's why CTB energy of Eu^{3+} decreases in the series of Y^{3+} to Gd^{3+} stannate phosphors. The sharp and narrow peaks beyond CTB are attributed to the intraconfigurational f-f transitions of Eu^{3+} ions in the host lattice. Among them, the peaks at 392 nm ($^7F_0$-$^5L_6$) and 463 nm ($^7F_0$-$^5D_2$) are much stronger which are matching well with the emission wavelength of near UV and blue LED chips. Although all the samples exhibit similar excitation profiles, the relative intensity between the intensity of CT band and f-f transitions are different. $La_{2.85}YSnNbO_{10.5}$:*0.15*Eu^{3+} phosphor exhibit intense excitation in the near UV region ($^7F_0$-$^5L_6$) which is stronger than the absorption in the CT region. Similarly, in the case of Y and Lu substituted ones f-f transitions are intense than CT band transition. However, Gd system exhibit weak excitation spectra compared to other samples. It has been proposed that the luminescence properties were strongly reliant on the crystallite size, particle size and the distribution of activator ions in the host matrix (Wang *et al*. 2007). The luminescence intensity enhanced with increasing crystallite size and particle size. As mentioned earlier in the XRD studies that, the crystallinity and crystallite size of Gd host is low compared to other lanthanides. This may be the reason for low PL intensity in the excitation spectra of Gd system which is also reflected in the emission spectra. The difference in the relative intensity of f-f transition and CT band may be related to their structures. Gd, Y and Lu substituted samples crystallize in fluorite structure which is a more disordered structure than the pyrochlore leading to the non-uniform distribution on Eu^{3+} ions. Also, these samples are less effective in transferring energy to

the activator when compared to La system. However, due to the intense excitation peaks in the near UV region, the developed phosphor material can effectively excited by radiation from near UV-LED chips based on GaN semiconductors for WLED applications.

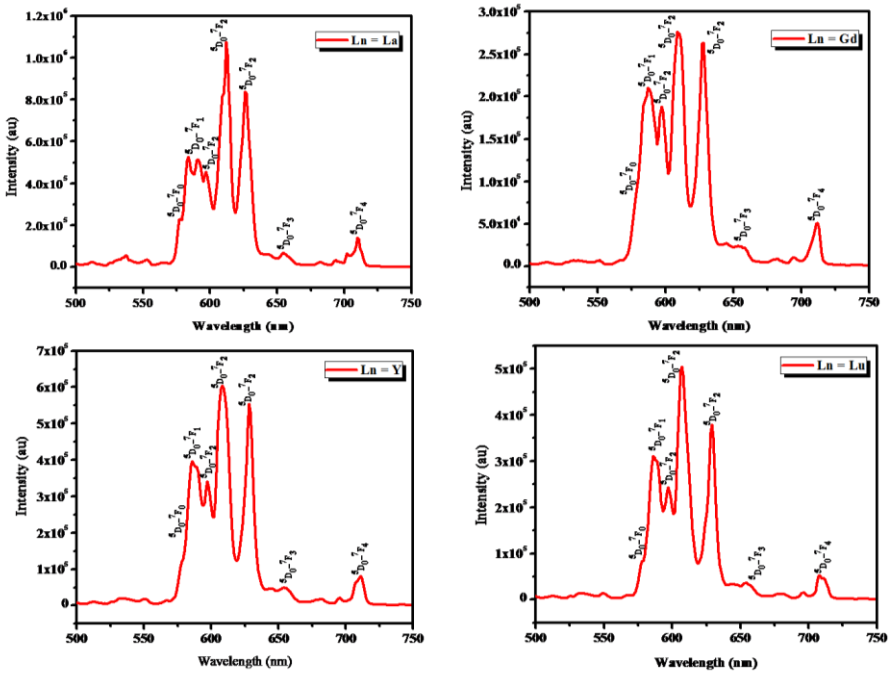

Fig. 5A.9 Emission spectra of $Ln_{2.85}YSnNbO_{10.5}$:*0.15*Eu^{3+} (Ln = La, Gd, Y and Lu) phosphors for an excitation at 392 nm.

The emission spectra of $Ln_{2.85}YSnNbO_{10.5}$:*0.15*Eu^{3+} (Ln = La, Gd, Y and Lu) phosphors excited at 392 nm is displayed in Fig. 5A.9. The emission spectra of all the samples follow the same trend as the variation in crystal structure. The spectra exhibits a group of emission lines ranging from 500 to 750 nm, corresponding to the transitions from the first excited state $^5D_0$ to the ground states ^7F_J (J = 0-4) in Eu^{3+} ions, and they strongly depend on their local environments in host lattice. In the spectra, $^5D_0$ – $^7F_0$ transition appear as a single peak indicate the single site occupancy of Eu^{3+} ion in the host lattice. Normally, $^5D_0$ – $^7F_0$ transition of Eu^{3+} ions is not split because both its excited and ground states are nondegenerated. This result is consistent with our structure models with the fact that the Eu^{3+} ions occupy only at the A site. Another interesting observation is the splitting of $^5D_0$ – $^7F_1$ transition into two lines A and B (λ_1 =

592 nm and λ_2 = 598 nm) for the La host, whereas a single sharp peak in the case of other lanthanide (Ln = Gd, Y and Lu) systems. As known, Eu^{3+} ions in the fluorite structure is located in a site with O_h symmetry where magnetic dipole transition ($^5D_0$ – $^7F_1$) will not split, while Eu^{3+} ions in the pyrochlore structure adopts D_{3d} symmetry will lead to the splitting of $^5D_0$ – $^7F_1$ transition (McCauley *et al*. 1980). The presence of single $^5D_0$ – $^7F_1$ transition indicates that the Gd, Y and Lu samples do not adopt the pyrochlore structure. The consistency in the published spectra of La host suggests that there is no break in symmetry and that the D_{3d} symmetry expected to the pyrochlore 16c site is preserved. McCauley et al (McCauley *et al*. 1973) reported that $^5D_0$ – $^7F_1$ transition of Eu^{3+} ions in D_{3d} symmetry occur along a particular direction. The $^5D_0$ level posses A_{1g} symmetry, while the $^7F_1$ level should split into two components of A_{2g} and E_g symmetry. The A_{1g} - E_g transition is allowed in the *x* and *y* direction, whereas A_{1g} – A_{2g} transition is allowed only in the *z* direction of the D_{3d} symmetry site. The *z* direction corresponds to the (111) crystallographic direction of the pyrochlore lattice, and *x* and *y* direction correspond to a direction perpendicular the (111) direction. For the $La_3YSnNbO_{10.5}$ sample, the relative intensity of A line to that of B line was found to be around 1.5 times. Hence, the A line is ascribed to the A_{1g} - E_g transition which occurs both along *x* and *y* direction, while the B line is ascribed to the A_{1g} – A_{2g} transition which occurs only along the *z* direction. In the pyrochlore structure, Ln/Eu-O_{8b} and Ln/Eu-O_{48f} bonds are parallel and perpendicular to the *z* direction of the D_{3d} symmetry. It can be seen that, for La host the peak wavelength of A_{1g} – A_{2g} transition became longer compared to the peak wavelength of Gd, Y and Lu host since the bond length of Ln/Eu-O_{8b} became shorter. But the A line is absent in Gd, Y and Lu host due to their defect fluorite structure. The splitting of $^5D_0$ – $^7F_1$ transition of Eu^{3+} ions in La host may be due to the distortion of EuO_8 scalenohedra, induces a larger splitting width of MD transition in the pyrochlore structure. These results corroborate structural variation enunciated in the structural analysis by XRD and Raman. Thus, Eu^{3+} luminescence is very sensitive to the local symmetry of the host lattice and can be used as structural probe to investigate the phase evolution with lanthanide substitution on the stannate pyrochlores.

Table 5A.2 Optical properties and intensity parameters of $Ln_{2.85}YSnNbO_{10.5}$: *0.15*Eu^{3+} (Ln = La, Gd, Y and Lu) phosphors.

Sample	Band gap (eV)	CTB (nm)	Asymmetric Ratio	Life time (ms)	Ω_2 (10^{-20}) cm^2	Ω_4 (10^{-20}) cm^2	Efficiency (%)
La	3.70	288	2.42	0.86	7.86	1.12	46.51
Gd	3.81	290	1.47	1.21	4.24	0.81	40.10
Y	3.76	286	1.77	1.11	4.82	0.76	40.07
Lu	3.83	295	2.07	1.09	4.75	0.70	38.86

The emission lines between 600 and 640 nm are attributed to the electric dipole transitions ($^5D_0$ – $^7F_2$) of Eu^{3+} ions in Ln host lattice. It can be seen that, in all the samples the intensity of $^5D_0$ – $^7F_2$ transition is much stronger than that of $^5D_0$ – $^7F_1$ transition. When the lattice around Eu^{3+} ions is distorted, their local symmetry deviates from inversion center leading to red emission. Rietveld analysis indicate that doped Eu^{3+} ions substitute for the La^{3+} site with D_{3d} inversion symmetry in $La_3YSnNbO_{10.5}$ sample prevailing the allowed $^5D_0$ – $^7F_1$ transition. Since the ionic size difference between La^{3+} (1.16 Å, CN 8) and Eu^{3+} (1.07 Å, CN 8) is more, the substitution of Eu^{3+} ions in the La^{3+} site can lead to the distortion of octahedra reducing the symmetry of crystal field surrounding the Eu^{3+} ions. Thus, the distortions of the A site symmetry and the red shift of the charge transfer band lead to highly intense red emission. Concerning the luminescence in defect fluorite system (Ln = Gd, Y and Lu), the $^5D_0$ – $^7F_2$ transition dominates over the $^5D_0$ – $^7F_1$ transition, which is against the O_h symmetry of the defect fluorite structure. In the defect fluorite phase, most of the Eu^{3+} ions locate in sites without centrosymmetry, relax the selection rules and allow the forbidden electric dipole transition. To gain more insight into the possible structural changes surrounding the Eu^{3+} ions with Ln^{3+} substitution, asymmetric ratio was calculated from the emission spectra (Table 5A.2). Higher asymmetric ratio for La host compared to other Ln host suggests that Eu^{3+} ions are indeed having a more distorted environment in La host. This is further supported by the increased red emission observed in La host due to its long range ordering. Defect fluorite phases contain short rang ordering that give rise to diffuse scattering that will decrease the intensity of red emission. The decrease in

asymmetric ratio with Ln^{3+} ions results in decrease in the extent of distortion in the lattice. As a result, the probability of $^5D_0 - {}^7F_2$ transition decreases for other Ln (Ln = Gd, Y and Lu) systems. Besides the asymmetric ratio of luminescence, lifetime corresponding to the excited state of Eu^{3+} ions and the decay profiles are also very sensitive to the changes in the environment around Eu^{3+} ions.

Fig. 5A.10 shows the fluorescence decay curves corresponding to the $^5D_0$ transition of Eu^{3+} ions in $Ln_{2.85}YSnNbO_{10.5}$:*0.15*Eu^{3+} (Ln = La, Gd, Y and Lu) phosphors under 392 nm excitation. The decay curve is found to be a single exponential for all the samples suggesting the single site occupancy of Eu^{3+} ions in the host lattice. Generally, long decay time is the characteristic of the symmetrical surrounding while a short decay time is observed when site distortion occurs. The short decay time obtained La host may be due to the occupation of Eu^{3+} ions in a more distorted environment in the A site (Ln^{3+} site) of pyrochlore structure as evidenced from the asymmetric ratio variation. The quantum efficiency value calculated from the lifetime and emission spectra (Soares Santos *et al*. 2003; Su *et al*. 2008) was found to be maximum (46.51%) for La host. As known, the host crystal structure plays a crucial role on the efficiency of rare earth activated phosphors. The Eu^{3+} ions have much higher luminescence efficiency in *Fd3m* phase than that in *Fm3m* phase.

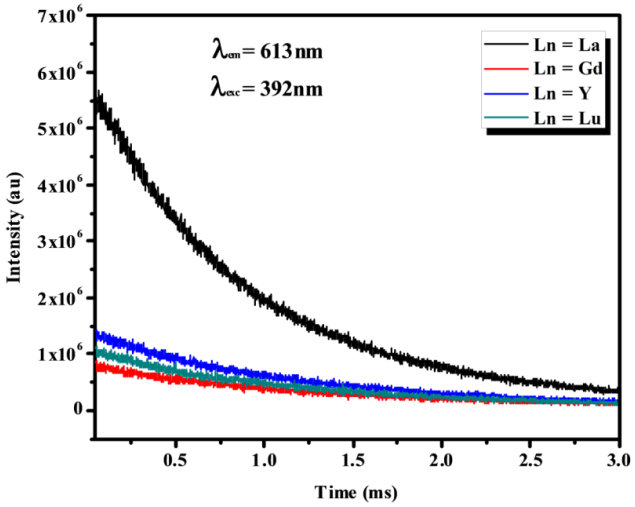

Fig. 5A.10 Decay curves of $Ln_{2.85}YSnNbO_{10.5}$:*0.15*Eu^{3+} (Ln = La, Gd, Y and Lu) phosphors for an emission at 613 nm.

To further substantiate the change in Eu^{3+} ion environment with Ln^{3+} ions, the Judd-Ofelt intensity parameters Ω_λ (λ = 2 and 4) were calculated from the emission spectra and decay curves as described elsewhere (Peacock *et al*. 1975). The intensity parameters are a measure of degree of polarizability around Eu^{3+} ions, the nature of forced electric dipole transition and the dynamic coupling mechanisms operating in the sample. Higher value of above parameters signifies an increase in polarizability and covalent character of the Eu^{3+} environment. These parameters can also be used for finding out the changes in the local environment associated with variation in the crystal structure. The parameter Ω_2 decides the covalency, polarizability and the asymmetric behavior of the activator and the ligand (short range effects), whereas Ω_4 details the long range effects. In the present study, Ω_λ parameters were calculated taking $^5D_0 - {}^7F_2$ transition as the reference. From the data given in Table 5A.2, it is clear that Ω_2 and Ω_4 values are maxima for La host indicating that the extent of covalent character or electron density around Eu^{3+} ions is high for the La host. The higher the Ω_2 parameter, the lower is the environmental chemistry around Eu^{3+} ions (Pokhrel *et al*. 2015). The decrease in the value of Ω_2 for the other lanthanide hosts suggests decrease in the extent of polarizability around Eu^{3+} ions, results in the decrease of disorder around Eu^{3+} ions. This decrease in the extent of disorder is also evident from the decrease in asymmetric ratio. Moreover, the value of Ω_4 decreases from La to Lu suggesting the increased efficiency for $^5D_0 - {}^7F_2$ transition in the La host. In general, the order of intensity parameter is $\Omega_2 < \Omega_4$, but in our case the trend is reversed. This variation of trend in the intensity parameters is in agreement with the reported ones (Ishihara *et al*. 1994). The higher values of Ω_2 compared with Ω_4 suggest that the contribution of lower rank components of the crystal field has have more influence than the higher rank components. The nature of intensity parameter ($\Omega_2 > \Omega_4$) further validates the covalency existing between the Eu^{3+} ions and the ligands as well as the asymmetry around the metal ion site. These results are in conformity with the conclusions drawn from PL spectra. All these results point out that the La system exhibit better luminescence properties compared to other Ln cations and hence further studies were confined to this system.

5A. 3.2 Effect of Eu^{3+} Doping in $La_3YSnNbO_{10.5}$ Host Lattice

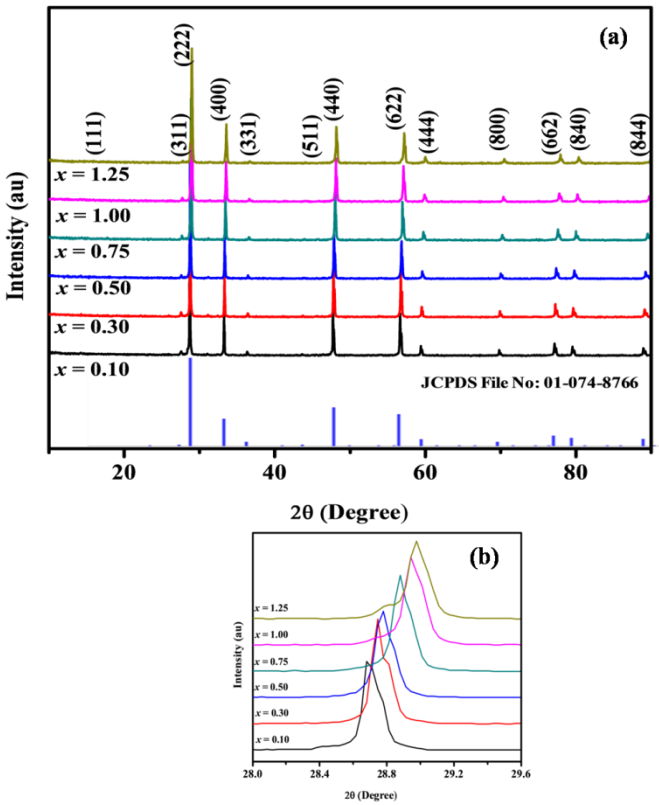

Fig. 5A.11 (a) Powder X-ray diffraction patterns of $La_{3-x}YSnNbO_{10.5}$:xEu^{3+} (x = 0.10, 0.30, 0.50, 0.75, 1.00 and 1.25) phosphors. **(b)** The expanded view of the (222) reflection at 29°

Powder XRD patterns of $La_{3-x}YSnNbO_{10.5}$:xEu^{3+} (x = 0.10, 0.30, 0.50, 0.75, 1.00 and 1.25) phosphors are given in Fig. 5A.11. All the XRD peaks are indexed in reference to the pyrochlore type unit cell with *Fd3m* space group. The presence of sharp and narrow peaks reveal the crystallinity and phase purity of all the samples and no impurity peaks were observed upon increasing the doping concentration of Eu^{3+} ions. Also, in the XRD patterns of Eu^{3+} doped samples, the peak positions are shifted slightly towards the higher angles and these results in lattice contraction (Table 5A.3). This is due to the substitution of La^{3+} ion (1.16 Å, CN 8) by a slightly smaller Eu^{3+} ion (1.07 Å, CN 8). The peak shift of the XRD pattern with Eu^{3+} concentration shown in Fig. 5A.11 (b) confirms the effective substitution of Eu^{3+} ions into the lattice. The SEM images of all

the samples shown in Fig. 5A.12 reveal that the particles are agglomerated and are few microns in size.

Table 5A.3 Refined parameters from Rietveld Analysis of $La_{3-x}YSnNbO_{10.5}$:xEu^{3+} (x = 0.10, 0.30, 0.50, 0.75, 1.00 and 1.25) phosphors

Sample	***x* = 0.10**	***x* = 0.30**	***x* = 0.50**	***x* = 0.75**	***x* = 1.00**	***x* = 1.25**
Phase	Pyrochlore	Pyrochlore	Pyrochlore	Pyrochlore	Pyrochlore	Pyrochlore
Unit cell	Cubic	Cubic	Cubic	Cubic	Cubic	Cubic
Space group	*Fd3m*	*Fd3m*	*Fd3m*	*Fd3m*	*Fd3m*	*Fd3m*
Lattice constant (Å)	10.7694(3)	10.7570(3)	10.7393(3)	10.7222(3)	10.7018(4)	10.6834(6)
Oxygen parameter	0.329(2)	0.332(2)	0.333(2)	0.336(2)	0.336(2)	0.337(2)
Caglioti parameters						
U	0.019(7)	0.028(6)	0.039(8)	0.046(9)	0.06(2)	0.22(4)
V	0.000(6)	-0.006(6)	-0.010(8)	-0.014(9)	-0.01(1)	-0.10(3)
W	0.003(1)	0.005(1)	0.008(2)	0.009(2)	0.010(3)	0.025(6)
R-factors						
R_{exp} (%)	13.12	12.88	12.85	12.32	12.08	12.05
R_p (%)	13.66	13.02	12.49	12.46	12.88	13.57
R_{wp} (%)	18.13	17.11	16.36	16.19	16.44	17.51
GOF	1.91	1.76	1.62	1.73	1.85	2.11

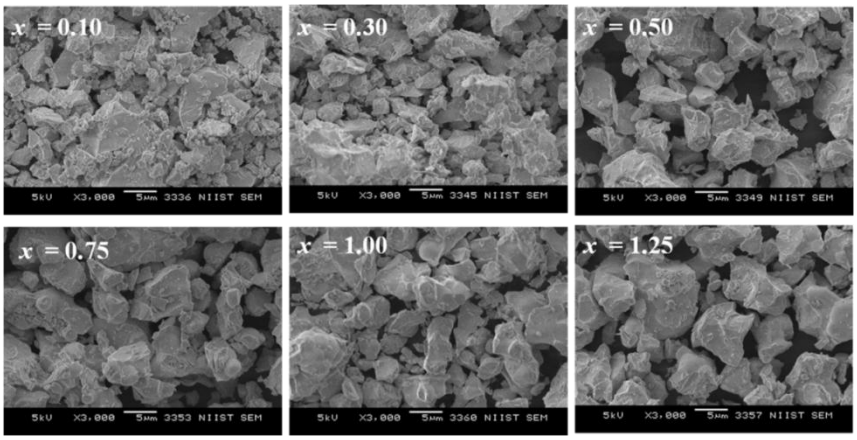

Fig. 5A.12 Scanning electron micrographs of $La_{3-x}YSnNbO_{10.5}$:xEu^{3+} (x = 0.10, 0.30, 0.50, 0.75, 1.00 and 1.25) phosphors.

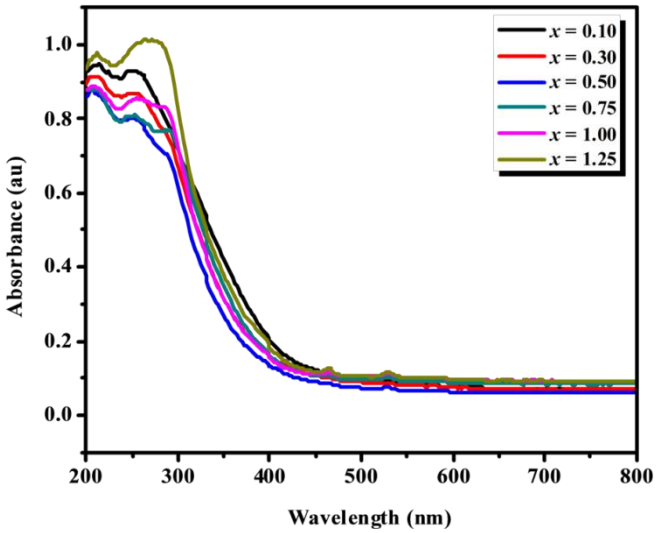

Fig. 5A.13 UV-visible absorption spectra of $La_{3-x}YSnNbO_{10.5}:xEu^{3+}$ (x = 0.10, 0.30, 0.50, 0.75, 1.00 and 1.25) phosphors.

Fig. 5A.13 shows the UV-visible absorption spectra of $La_{3-x}YSnNbO_{10.5}:xEu^{3+}$ (x = 0.10, 0.30, 0.50, 0.75, 1.00 and 1.25) phosphors. It can be seen that the entire samples exhibit a good absorption in the UV region peaking at around 258 nm attributed to the charge transfer from O^{2-} to the Eu^{3+} ions in the sample. The degree of absorption of Eu^{3+} level is increasing with Eu^{3+} concentration suggesting the effective energy transfer from CT states to Eu^{3+} ions. The band gap energy calculated from the absorption spectra increases with increase in Eu^{3+} concentration and the estimated band gap energies are given in Table 5A.4. Thus, these materials are suitable for application as phosphors in near-UV excited LEDs.

To investigate the influence of activator concentration on the photoluminescence properties, excitation and emission spectra were recorded at room temperature. Fig. 5A.14 displays the excitation spectra of $La_{3-x}YSnNbO_{10.5}:xEu^{3+}$ (x = 0.10, 0.30, 0.50, 0.75, 1.00 and 1.25) compositions by monitoring the red emission of Eu^{3+} at 392 nm. It was noticed that the Eu^{3+} doping hardly affect the excitation and emission profiles except the change in intensity. However, the substitution of La^{3+} with Eu^{3+} caused a significant red shift of the excitation peaks from about 289 to 320 nm due to the increase in covalency of Eu-O bond and the coordination environment of Eu^{3+}

ions. The drastic change in the CT band might be due to the highly favorable low symmetry crystal structure of the system which enhances the electric dipole transitions. Moreover, the f-f transition intensities got enhanced due to the increased polarization and distortion in the lattice.

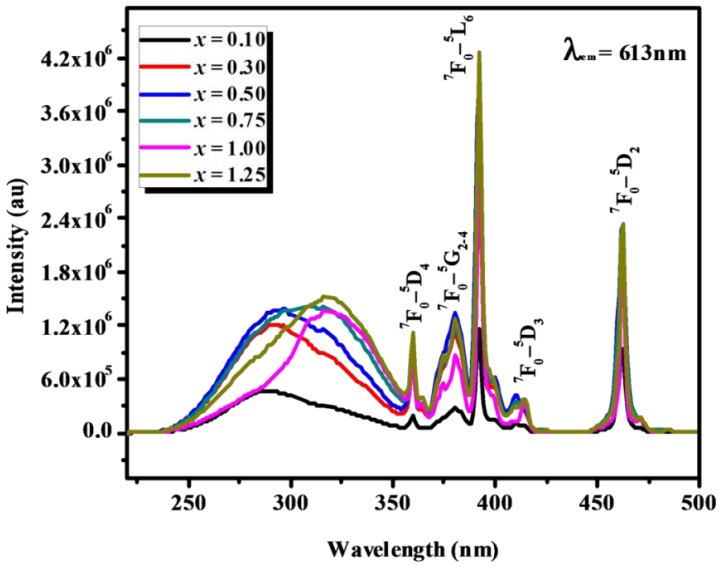

Fig. 5A.14 Excitation spectra of $La_{3-x}YSnNbO_{10.5}$:xEu^{3+} (x = 0.10, 0.30, 0.50, 0.75, 1.00 and 1.25) phosphors for an emission at 613 nm.

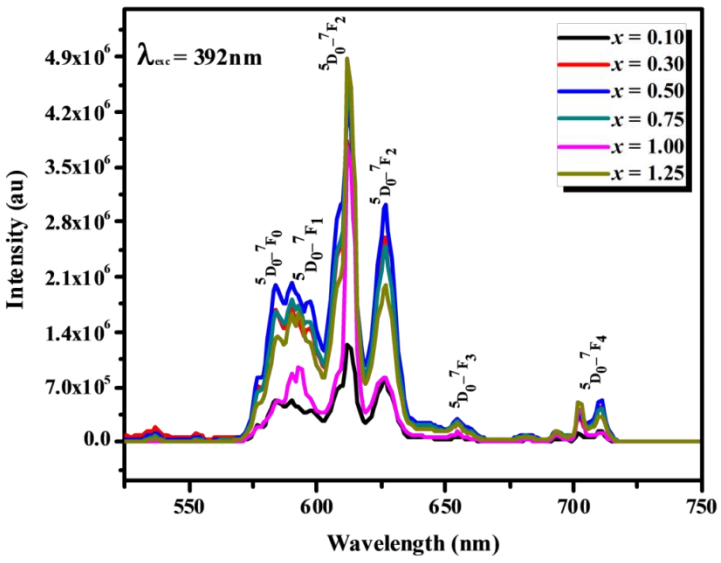

Fig. 5A.15 Emission spectra of $La_{3-x}YSnNbO_{10.5}$:xEu^{3+} (x = 0.10, 0.30, 0.50, 0.75, 1.00 and 1.25) phosphors under 392 nm excitation.

It is obvious from Fig. 5A.15 that PL emission intensity of Eu^{3+} increases with increasing doping concentration which indicates that $La_3YSnNbO_{10.5}$ host can accept Eu^{3+} in high concentrations without concentration quenching. The enhanced electric dipole transition intensity arises from symmetry distortion of Eu^{3+} ions. Substitution of Eu^{3+} ions on the sites of La^{3+} ions in the D_{3d} crystalline field and the influence of coordination environment caused the Eu^{3+} ions deviated from the inversion center and had low crystal field symmetry. The lower the symmetry is, the more is the splitting degree and that's why the $^5D_0$-$^7F_1$, $^5D_0$-$^7F_2$ and the $^5D_0$-$^7F_4$ transitions of Eu^{3+} ions splits. This symmetry variation is reflected in the asymmetry values (Table 5A.4) which shows an increasing trend with Eu^{3+} ion doping.

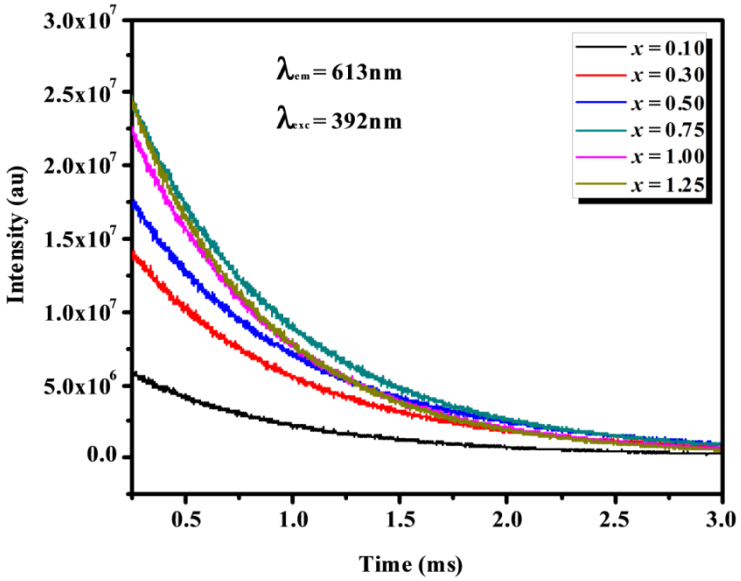

Fig. 5A.16 Lifetime decay curves of $^5D_0$-$^7F_2$ transition of Eu^{3+} in $La_{3-x}YSnNbO_{10.5}$:xEu^{3+} (x = 0.10, 0.30, 0.50, 0.75, 1.00 and 1.25) phosphors under 392 nm excitation.

Fig. 5A.16 show the fluorescent decay time of the $^5D_0$-$^7F_2$ transition of as prepared samples under the 392 nm excitation. The decay curves are found to be nearly single exponential and the obtained lifetime values increase with increase in Eu^{3+} ion substitution resulting in improved quantum efficiency. This is further supported by the J-O intensity parameters given in Table 5A.4. The increase in Ω_2 value with Eu^{3+} ion concentration indicates the increase in asymmetry nature of Eu^{3+} ion in the host which is also clearly indicated by the asymmetry ratio. Hence, it can further confirm that the

crystal symmetry around Eu^{3+} ion was decreased with increasing the concentration of Eu^{3+} ions. The continuous increase in the Ω_4 parameter with Eu^{3+} concentration also implies the increased efficiency of the $^5D_0$–$^7F_2$ transition. The trend observed in the J-O intensity parameters ($\Omega_2 > \Omega_4$) further validates the covalency existing between the Eu^{3+} ion and ligands as well as the asymmetry around the metal ion site.

Table 5A.4 Optical properties of $La_{3-x}YSnNbO_{10.5}$:xEu^{3+} (x = 0.10, 0.30, 0.50, 0.75, 1.00 and 1.25) phosphors

x	Band gap (eV)	CTB Peak (nm)	Asymmetric Ratio	Lifetime (ms)	Ω_2 (10^{-20}) cm^2	Ω_4 (10^{-20}) cm^2	Efficiency (%)	Color coordinates (*x*, *y*)
0.10	2.79	289	2.16	0.77	8.39	0.75	42.90	(0.57, 0.35)
0.30	3.14	293	2.33	0.77	8.42	0.77	43.19	(0.60, 0.38)
0.50	3.22	296	2.42	0.78	10.91	0.81	58.02	(0.61, 0.37)
0.75	3.30	308	2.56	0.80	11.08	0.96	59.07	(0.62, 0.37)
1.00	3.33	316	3.16	0.81	11.35	1.04	64.43	(0.63, 0.36)
1.25	3.46	320	4.02	0.88	12.55	1.13	64.59	(0.63, 0.37)

The improvement in luminescence properties with Eu^{3+} doping bring out rich luminescence color for the Eu^{3+} doped $La_{3-x}YSnNbO_{10.5}$:xEu^{3+} (x = 0.10, 0.30, 0.50, 0.75, 1.00 and 1.25) phosphors. Based on the emission spectra of the phosphors, the Commission International d'Eclairage (CIE) coordinates were calculated using the CIE color calculator software and the values are given in Table 5A.4. The calculated color coordinates of all the samples were found to be (0.63, 0.37) which is close to the NTSC standard values (0.67, 0.33) for a potential red phosphor.

The Eu^{3+} emission spectrum in this system offers an ample scope to understand the influence of structural variation on photoluminescence properties because of its relatively simple energy level structure. The luminescence spectra in the various lanthanide hosts exhibit distinct luminescence characteristics. Eu^{3+} ion could obtain highly efficient luminescence in the $La_3YSnNbO_{10.5}$ *Fd3m* phase than that in *Fm3m* phase. It is well known that the selection rules and f-f transition probability between states depend highly on the crystal field environment around Eu^{3+} ions. Thus, difference

in Eu^{3+} luminescence in various lanthanide hosts may be due to the different environment around Eu^{3+} ions. The structural variation in these closely related structures greatly affects the luminescence properties. The formation of cation ordering on the metal site and the polarization of electron density around O^{2-} anions towards or away from the Eu^{3+} ion are the important factors that govern the luminescence. The structural analysis reveals the structural variation from the ordered pyrochlore to disordered fluorite structure upon lanthanide substitution. The degree of ordering of cations is La > Gd > Y > Lu. Due to the more ordered structure of La host lattice resulting in a more uniform distribution of Eu^{3+} ions, the La system showed better luminescence properties. Another important factor that influences the Eu^{3+} luminescence is anion polarizability around Eu^{3+} ions which depend on the ionic radii and electronegativity of host cations. The anion polarizability also depends on the nature of cations with which they are bonded. It is reported that the anion polarizability decreases when the anion is bonded to cations which are small and highly charged. Moreover, the anion polarizability decreases with increasing electronegativity of the coordinating cations (Dorenbos *et al*. 2002). The Pauling's electronegativity values are 1.10, 1.20, 1.22 and 1.27 for La, Gd, Y and Lu host respectively (Allred *et al*. 1961). Based on the respective ionic radii and electronegativity, we can anticipate that the anion polarizability is highest in La and least in Lu host. Consequently, in the series of isostructural compounds, the anion polarizability is expected to vary as La > Gd > Y > Lu. So, the oxygen electron density is more tightly bonded by Lu^{3+} ions than by La^{3+} ions. Thus, we can conclude that larger and least electronegative La^{3+} ions are less able to attract the O^{2-} electron density towards them compared to the smaller and least electronegative Lu^{3+} ions. When Eu^{3+} ions are incorporated into the host lattice, due to inductive effect the shift of the centre of negative charge density around O^{2-} ions towards Eu^{3+} ions will be highest in La than in Lu host. As a result, the distance between the centre of charge density on O^{2-} ions and Eu^{3+} ions will be minimum in La and maximum in Lu host. Finally, we note that the splitting of $^7F_1$ transition in La host is due to the significant contribution of covalency/ligand polarizability to the crystal field. Thus, the host lattice dependent changes in the polarizability of the oxygen ions occupying the 48f sites of the pyrochlore lattice is responsible for the splitting of Eu^{3+} $^7F_1$ transition.

5A. 4 Conclusions

In the present work**,** we made an attempt to vary the A site cations in the $Ln_{2.85}YSnNbO_{10.5}$:*0.15*Eu^{3+} system by substituting various lanthanides (Ln = La, Gd, Y and Lu) so as to gradually transform the structure from an ordered pyrochlore to disordered fluorite through order-disorder transition. Detailed powder X-ray diffraction analysis supported by Raman spectroscopic studies evidence the structural changes occurring upon the gradual substitution with various lanthanides. Rietveld analysis performed on the powder X-ray diffraction data of these solid solutions also confirms the structural transitions. The luminescence properties are also correlated with their crystal structures. Eu^{3+} ion could obtain highly efficient luminescence in the $La_3YSnNbO_{10.5}$ *Fd3m* phase than that in *Fm3m* phase. The degree of ordering of cations in the system is La > Gd > Y > Lu. The luminescence intensity and quantum efficiency are closely related to the degree of ordering of cations in the lattice. Due to the more ordered structure of La host lattice resulting in a more uniform distribution of Eu^{3+} ions, the La system showed better luminescence properties. The splitting of $^5D_0$-$^7F_1$ magnetic dipole transition of Eu^{3+} ions in La host due to the distortion of EuO_8 scalenohedra indicate that peak wavelength of Eu^{3+} was affected by the crystal structure. The distortion of the A site symmetry and the red shift of the charge transfer band with higher concentrations of Eu^{3+} ions in $La_3YSnNbO_{10.5}$ system enhanced the electric dipole transition lead to improved quantum efficiency. All these results demonstrate that Eu^{3+} ions can be employed as an optical probe to investigate the phase evolution with lanthanide substitution on the stannate pyrochlores.

Chapter 5B

PHOTOLUMINESCENT EVOLUTION INDUCED BY PHASE TRANSITION IN RARE-EARTH STANNATE PYROCHLORE PHOSPHORS

Eu^{3+} doped $Ln_4YSn_2NbO_{14}$ (Ln = La, Gd, Y and Lu) red phosphors were synthesized via solid state route. The Ln^{3+} induces a structural transition from an ordered pyrochlore to a disordered fluorite structure with increased ordering of cations from Lu to La. These phosphors exhibit strong absorption in the near UV region and emit red luminescence under 392nm excitation which is also correlated with their crystal structures. These results suggest that rare-earth stannate system offers a lot opportunity to manipulate the Eu^{3+} red luminescence through order-disorder structural transition.

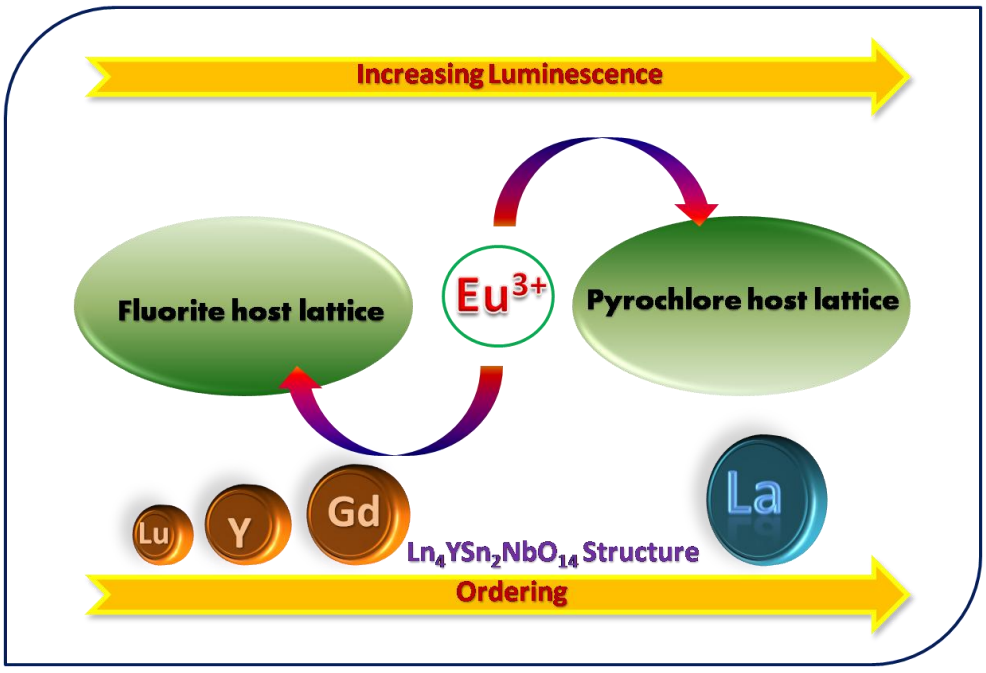

5B. 1 Introduction

The order-disorder transition from pyrochlore to fluorite structure has been extensively studied for their potential applications as ionic conductors, nuclear waste storage materials and luminescent materials. A decrease of the average value of the ionic radius r_A and elevated temperatures were found to resulting mixed occupancy of the cation sites and partial occupancy of the normally vacant oxygen site. This process is also promoted by decreasing the ionic size difference between A and B cations in the pyrochlore structure. Further, it is of interest to note that many of the defect fluorite phases contain short to intermediate range ordering that give rise to diffuse scattering and satellite reflections in electron diffraction patterns. So, optical spectroscopy may be able to detect short to intermediate range ordering due to the compositional/displacive structural modulation. For the RE stannate series $Ln_2Sn_2O_7$, the pyrochlore structure tends to be more unstable as the RE ion radius decreases, and $Gd_2Sn_2O_7$ always lies at the phase boundary between ordered pyrochlore and defect fluorite structure. The coordination number of the cations increases with increasing size of Ln cation as the pyrochlore approaches the phase boundary. This change in coordination tends to reflect an increase in local disorder across the pyrochlore series. The information about Ln cation local structure can be acquired by their luminescence studies. As Eu^{3+} emission spectrum can reflect any symmetry or covalent changes within the crystal, the nature of compositionally induced phase transformation were explored using Eu^{3+} emission spectroscopy.

In the chapter 5A, the correlation between the structural transformation and the emission properties were discussed in detail in the $Ln_3YSnNbO_{10.5}$ (Ln = La, Gd, Y and Lu) system. The system undergoes a phase transformation from ordered pyrochlore to defect fluorite structure by the substitution of Ln^{3+} ions in the A site of the pyrochlore. Further, their luminescence properties enhanced with increased ordering of cations from Lu to La. The more ordered structure of La host lattice favors more uniform distribution of Eu^{3+} ions and improves the quantum efficiency of La host. Thus in the present investigation, an attempt has been made to incorporate more Sn ions in the B site to obtain the host lattice of the general formulae $Ln_4YSn_2NbO_{14}$ (Ln = La, Gd, Y and

Lu) and investigate the influence of phase evolution on the luminescence properties. In addition, the results of order-disorder transformation in the system are discussed in correlation with their optical properties. To study the influence of long range ordering and coordination of cations associated with the structural transition on the photoluminescence properties, the activator doping concentration was fixed at x = 0.15 in all the prepared samples. The effect of Eu^{3+} doping concentration on the emission characteristics in relation to the phase evolution were also discussed in this chapter.

5B. 2 Experimental

$Ln_{3.85}YSn_2NbO_{14}$:$0.15Eu^{3+}$ (Ln = La, Gd, Y and Lu) and $La_{4-x}YSn_2NbO_{14}$:xEu^{3+} (x = 0.10, 0.30, 0.50, 0.75, 1.00 and 1.25) phosphors were prepared by a conventional high temperature solid-state reaction method. Stoichiometric amounts of La_2O_3, Gd_2O_3, Y_2O_3, Lu_2O_3, SnO_2, Nb_2O_5 and Eu_2O_3 (Sigma Aldrich, 99.99% purity) were weighed and thoroughly mixed in an agate mortar using acetone as the mixing medium. The homogeneous mixtures thus obtained were calcined at 1500°C for 6h. The calcined samples were then ground into a fine powder for further characterizations.

Powder X-ray diffraction (XRD) analysis was performed with a PANalytical X'Pert Pro diffractometer having Ni filtered CuKα radiation with X-ray tube operating at 40kV, 30mA, in the 2θ range 10-90°. Structure refinement of XRD data was performed by Rietveld analysis using X'Pert Highscore Plus software. Raman spectra were recorded using an integrated micro-Raman system with a 633 nm helium-neon laser source at a spatial resolution of 2 μm. The morphology of the powder samples was studied by a scanning electron microscope (JEOL, JSM-5600LV) operated at 15kV. Energy dispersive analysis and elemental mapping was carried out using a Silicon Drift Detector–X-Max^N attached with a Carl Zeiss EVO SEM. EDS elemental mapping was employed using Aztec Energy EDS Microanalysis Software. The absorbance study of the synthesized samples was carried out using Shimadzu, UV-3600 UV-Visible spectrophotometer using barium sulfate as the reference. The photoluminescence and lifetime of the prepared samples were obtained using a Spex Fluorolog DM3000F spectrofluorimeter using a 450W xenon lamp as the excitation source.

5B. 3 Results and discussion

5B. 3.1 Powder X-ray Diffraction Studies

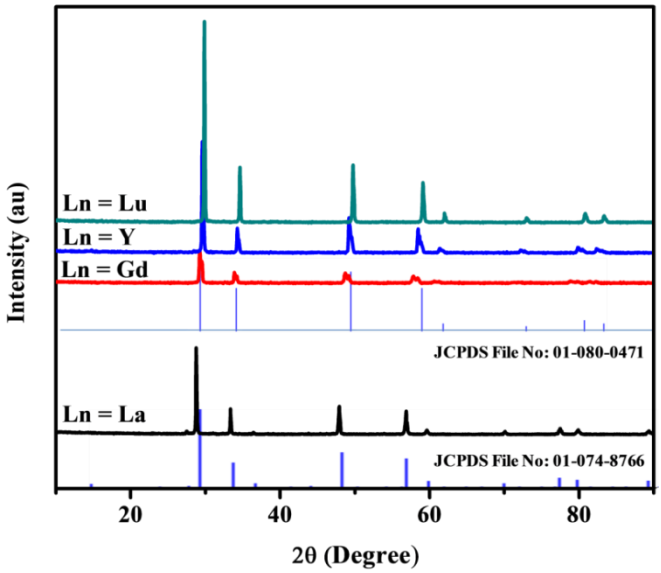

Fig. 5B.1 Powder XRD patterns of $Ln_{3.85}YSn_2NbO_{14}$:*0.15*Eu^{3+} (Ln = La, Gd, Y and Lu) phosphors.

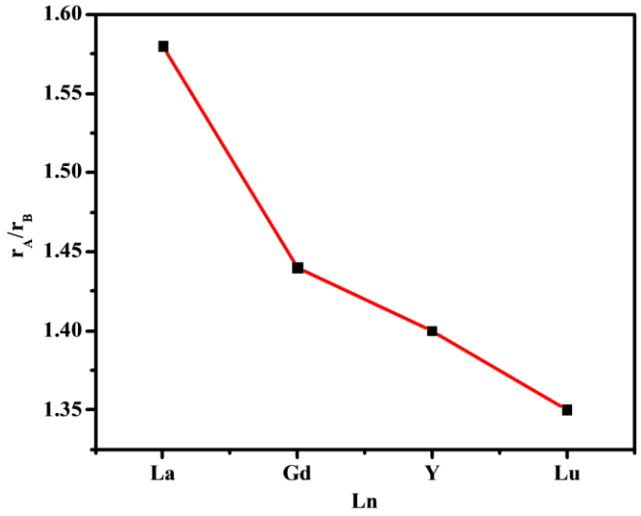

Fig. 5B.2 Variation of radius ratio (r_A/r_B) with Ln^{3+} ions (Ln = La, Gd, Y and Lu) on the A site of the pyrochlore structure.

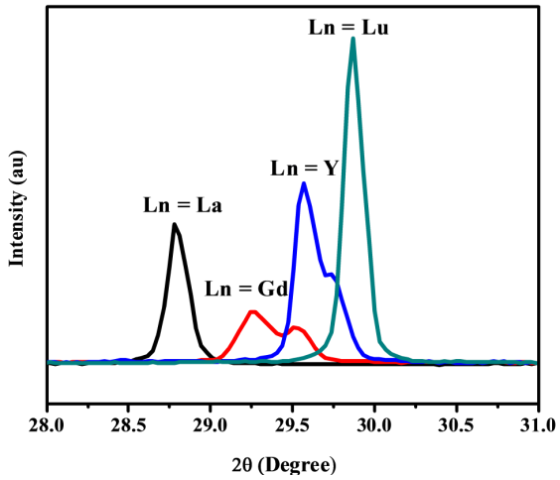

Fig. 5B.3 Shift of the main diffraction peak with Ln^{3+} ions (Ln = La, Gd, Y and Lu)

In order to determine the phase formation of $Ln_{3.85}YSn_2NbO_{14}$:*0.15*Eu^{3+} (Ln = La, Gd, Y and Lu) solid solutions and to characterize their structure, detailed X-ray diffraction studies have been carried out. The room temperature X-ray diffraction patterns of all the samples are shown in Fig. 5B.1. It can be seen that the structure of the crystal lattice is dependent on the ionic radius of the Ln ions. It is well known that pyrochlore structure is a superstructure of the fluorite structure characterized by the ordering of ions in the lattice due to the ionic radii of cations involved. Therefore, the diffraction pattern of pyrochlore is basically that of the fluorite structure along with an additional set of weak superstructure reflections (111), (311), (331) and (511), which corresponds to ordering in the lattice (Heremans *et al*. 1995). Moreover, the intensity of these characteristic superstructure peaks depends on the size and atomic number of cations in the A site and also on the degree of antisite occupation of cations in A and B site. It is worth noting that the sample Ln = La is crystallized in a pyrochlore structure. The incorporation of other lanthanides (Ln = Gd, Y and Lu) to the lattice will decrease the cationic size difference (r_A/r_B) thus disrupting the lattice order (Fig. 5B. 2). This disordering of the lattice is manifested by the disappearance of the superstructure peaks in the XRD pattern. It clearly indicates that the addition of Ln^{3+} ions to the lattice disrupts the ionic order resulting in the disappearance of superlattice peaks and that they are crystallized in a defect fluorite structure with *Fm3m* space group. The diminishing of characteristic superlattice peaks and the decreasing trend of radius ratio

suggest the possibility of order-disorder transition with decreasing ionic radius of Ln ions. Fig. 5B.3 shows a close examination of the main diffraction peaks. It can be seen that diffraction peak shift towards higher angles as Ln is changed from La to Lu indicting a decrease in the lattice spacing resulting from the incorporation of lanthanides of decreasing ionic radii.

A detailed structural analysis was carried out by Rietveld refinement of the diffraction data using X'Pert Highscore Plus software. At first, the scale factor and background parameters were fitted. A pseudo-Voigt profile function was used to fit the diffraction peak. Caglioti profile parameters and the asymmetry parameter along with structural parameters like lattice constant and oxygen *x* parameter were refined. The refined parameters and their values corresponding to best fit are given in Table 5B.1. Sample with Ln = La was best fitted using the *Fd3m* space group, while all the other lanthanides (Ln = Gd, Y and Lu) were fitted with *Fm3m* space group. The results of Rietveld refinement for two typical samples (Ln = La and Y) are shown in Fig. 5B.4. The observed, calculated and difference patterns are displayed there. The patterns show good agreement between observed and calculated diffraction profiles. Moreover, Rietveld analysis yielded accurate values for the lattice parameter, which confirmed the observation in Fig. 5B.3. From the Table 5B.1, we can see that the lattice parameter decreases with the substitution of Ln^{3+} ions of deceasing ionic radii (La to Lu) at the A site. The calculated lattice parameter as a function of Ln^{3+} ions are shown in Fig. 5B.5, wherein the lattice parameter of the fluorite type sample has been doubled to fit the graph. The variation of lattice parameter is in agreement with Vegard's law, according to which the lattice parameter of a mixture will have a linear relation with those of the components of via the composition (Vegard *et al*. 1921). In this system, Eu^{3+} ions are supposed to occupy the Ln^{3+} ion sites because of the similar ionic radius and valency. One interesting characteristic of the pyrochlore is that the oxygen ion on the *48f* site has a variable *x* coordinate. In a perfectly defect fluorite structure, the *x* coordinate has a value 0.375 at a tetrahedral position related to ideal cubic array of atoms. But as the lattice undergoes disordering, the shift of *48f* oxygen towards B cation decreases. However, only La system crystallizes into pyrochlore structure and all the other

lanthanide (Ln = Gd, Y and Lu) exhibits defect fluorite phase. Hence, oxygen *x*-parameter can be calculated only for La system. The incorporation of more Sn^{4+} ions in the B site of pyrochlore structure induces structural disorder in the lattice which has a strong influence on the luminescence properties. Thus, XRD analysis suggests that as a sufficient amount of Ln^{3+} ions is introduced into the lattice, the lattice preferentially orders with respect to cations, which may be attributed to structural transition.

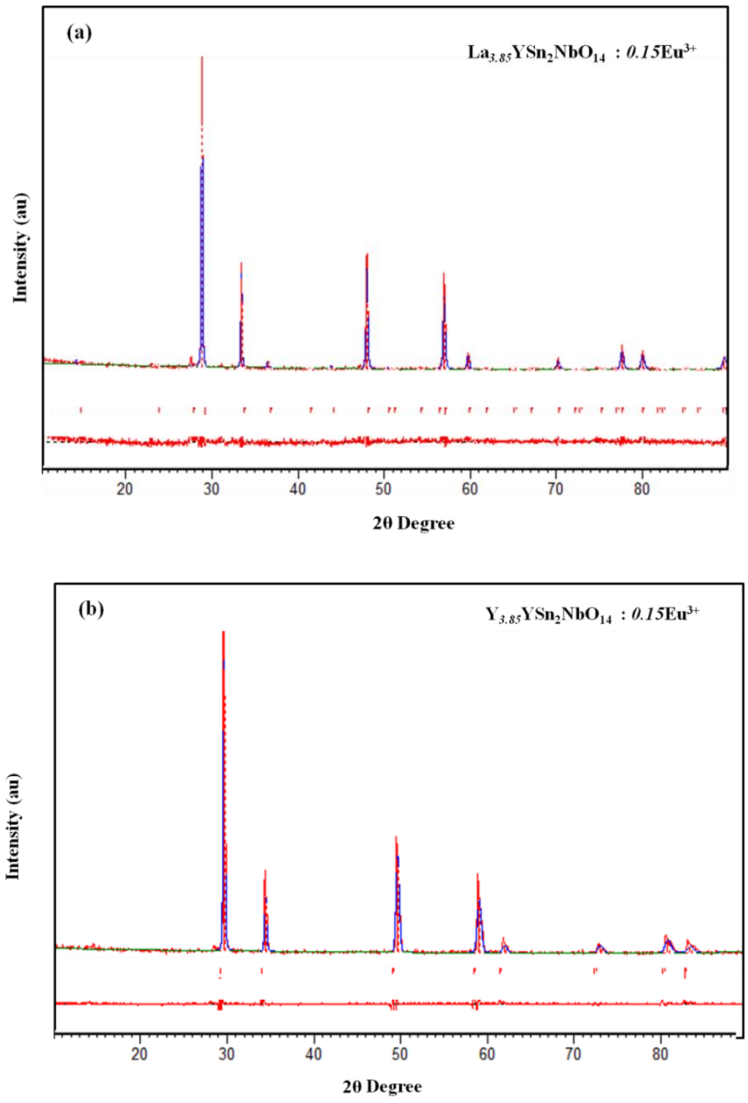

Fig. 5B.4 The observed, calculated and difference XRD patterns of **(a)** $La_{3.85}YSn_2NbO_{14}$:*0.15*Eu^{3+} **(b)** $Y_{3.85}YSn_2NbO_{14}$: *0.15*Eu^{3+} phosphors

Table 5B.1 Refined parameters from Rietveld Analysis of $Ln_{3.85}YSn_2NbO_{14}$:*0.15*Eu^{3+} (Ln = La, Gd, Y and Lu) phosphors

Sample	La	Gd	Y	Lu
Phase	Pyrochlore	Fluorite	Fluorite	Fluorite
Unit cell	Cubic	Cubic	Cubic	Cubic
Space group	*Fd3m*	*Fm3m*	*Fm3m*	*Fm3m*
Lattice constant (Å)	10.7404(6)	5.2690(2)	5.2214(6)	5.1818(2)
Oxygen *x*-parameter	0.332(2)			
Caglioti parameters				
U	0.21(4)	2.88(9)	0.9(2)	0.05(2)
V	-0.06(3)	-0.1(8)	-0.1(2)	0.02(1)
W	0.016(6)	0.0(1)	0.02(3)	0.002(3)
R-factors				
R_{exp} (%)	13.68	10.57	10.18	10.27
R_p (%)	13.79	11.45	14.93	9.72
R_{wp} (%)	17.83	14.98	19.59	12.71
GOF	1.70	2.00	3.70	1.53

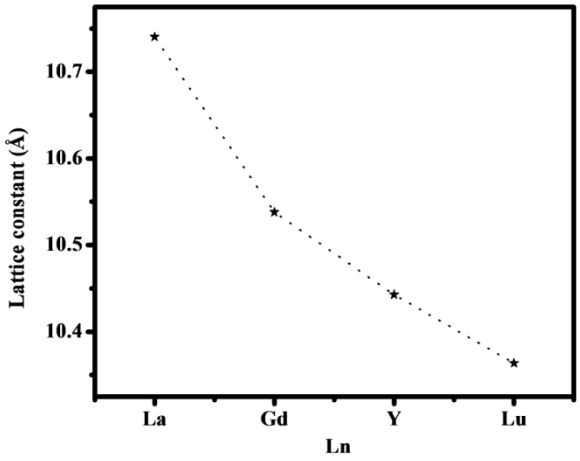

Fig. 5B.5 Variation of lattice parameter with Ln^{3+} ion (Ln = La, Gd, Y and Lu) substitution on $Ln_{3.85}YSn_2NbO_{14}$:*0.15*Eu^{3+} phosphors.

5B. 3.2 Raman Spectroscopy Studies

Raman spectroscopy is an effective tool for distinguishing an ordered pyrochlore structure from a defect fluorite structure. Factor group analysis based on the site

symmetries has shown that ordered pyrochlores possess six Raman active modes and only one Raman active mode present in defect fluorite structure. The FT Raman spectra of $Ln_{3.85}YSn_2NbO_{14}$:*0.15*Eu^{3+} (Ln = La, Gd, Y and Lu) phosphors in the range 100-1000cm^{-1} is shown in Fig. 5B.6. The bands in the Raman spectra are assigned to symmetry by comparing with the published Raman spectra of pyrochlores (Vandenborre *et al*. 1983). The lowest frequency lines observed between 177 and 220cm^{-1} in La system are assigned to the F_{2g} mode. The prominent peaks in the spectra are the E_g band at ~326 cm^{-1}, F_{2g} band at ~399 cm^{-1} and A_{1g} band at ~512 cm^{-1} and the other bands are very weak in intensity.

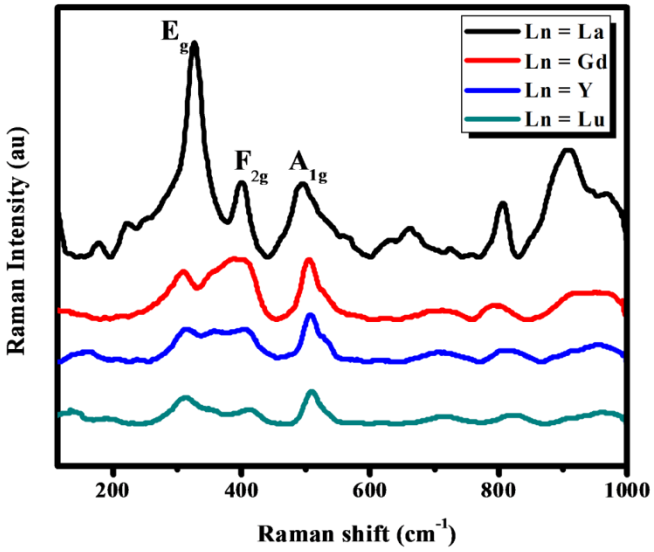

Fig. 5B.6 FT-Raman spectra of $Ln_{3.85}YSn_2NbO_{14}$:*0.15*Eu^{3+} (Ln = La, Gd, Y and Lu) phosphors.

In general, with Ln ion substitution line broadening, minor shift in the position and the appearance of new features in the spectra are observed. The E_g mode at ~326 cm^{-1} is related to the *48f* oxygen in the pyrochlore structure, whereas F_{2g} band at ~399 cm^{-1} is related to the 8b oxygen. Detailed observation indicates that intensity of these modes tends to diminish with Ln^{3+} ion substitution. This implies that addition of Ln^{3+} ions into the lattice disturb the arrangement of both the 48f and 8b oxygen ions leading to an overall disorder of the anion sublattice. The broadening of Raman modes with Ln ions may be due to the partial disorder induced into the cation sublattice by the Ln

substitution. Such disorder created due to the presence of dopant ions in an ordered lattice, disrupts the translational symmetry and relaxes the k = 0 selection rule. Consequently, the phonons from all parts of the Brillouin zone contribute to the optical spectra resulting in broad Raman bands. This clearly indicates the gross transformation of the ordered pyrochlore structure to a completely disordered fluorite structure by the substitution of Ln^{3+} ions of decreasing ionic radius. Also a small peak ~804 cm^{-1} is observed in La system which may be due to the second order scattering or structural defects in the system. Further, a new peak at ~908 cm^{-1} appears in the La system. According to Michel *et al*., the feature at the ~908 cm^{-1} implies a random distribution of seven oxygen ions over eight anion sites in pyrochlore compounds, i.e. complete anionic disorder due to increased lattice strain from the substitution of mismatched atoms (Michel *et al*. 1976). Another interesting observation in the Raman spectra is the shift in peak positions. Prominently, A_{1g} mode shifts to higher wavenumbers with decreasing ionic radius from La to Lu with the same B site. The constants depend on the spatial ordering of the octahedra rather than the nature of A and B cations and may vary with the nature of bond. Since A_{1g} mode is related to the vibrations of BO_6 octahedra, the increase in force field is more likely because of a lengthening of B-O bond in lanthanide samples. As a result, higher mass of A cation with the same B cation results in slightly higher wavenumbers for all Raman active modes. This is in line with the XRD data where the unit cell volume decreases with Ln^{3+} ions of decreasing ionic radii.

5B. 3.3 Morphological Studies

The as-prepared lanthanide phosphors $Ln_{3.85}YSn_2NbO_{14}$:*0.15*Eu^{3+} (Ln = La, Gd, Y and Lu) shows similar particle morphology and is given in Fig. 5B.7. All the samples exhibit typical polycrystalline nature, with grains falling in a range of 1-3μm. It can be found that grain size decreases with the rare earth ion substitution. The EDS spectra of all the samples were recorded and the atomic mass percentages were found to be in well agreement with the theoretical stoichiometry. Elemental X-ray dot mapping studies further revealed the uniform distribution of Eu^{3+} ions in the host lattice. EDS spectra and X-ray dot mapping images of $La_{3.85}YSn_2NbO_{14}$:*0.15*Eu^{3+} phosphor is given in Fig. 5B.8.

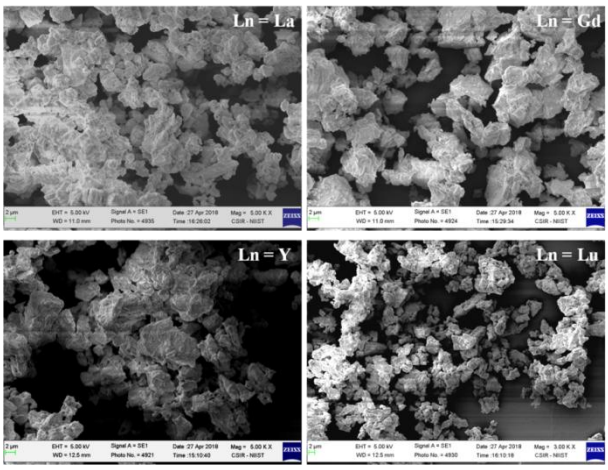

Fig. 5B.7 Scanning electron micrographs of $Ln_{3.85}YSn_2NbO_{14}$:*0.15*Eu^{3+} (Ln = La, Gd, Y and Lu) phosphors.

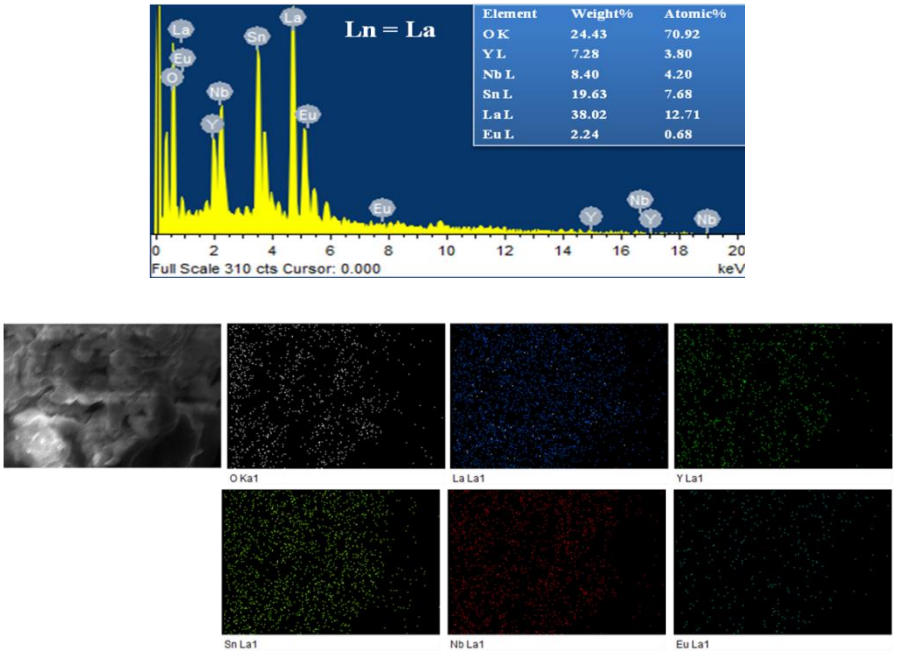

Fig. 5B.8 EDS spectra X-ray dot mapping of $La_{3.85}YSn_2NbO_{14}$:*0.15*Eu^{3+} phosphor.

5B. 3.4 Optical Studies

Fig. 5B.9 shows the UV-visible absorption spectra of the as-prepared $Ln_{3.85}YSn_2NbO_{14}$:*0.15*Eu^{3+} (Ln = La, Gd, Y and Lu) phosphors. All the samples have the absorptions located in the UV range due to the charge transfer from oxygen ligands to Eu^{3+} ions and to the central stannate/niobate groups in the host lattice. The wavelength

at the absorption edge, λ is determined as the intercept on the wavelength axis for a tangent drawn on the absorption spectra. The absorption edge shifted towards the lower wavelength side with decrease of Ln^{3+} ion radius resulting in the increase of band gap energy (Table 5B.2). This is in line with SEM images where the band gap energy increases with decreasing particle size due to quantum confinement effect. The absorption spectra of all the three samples show good absorption in the UV region pointing to the applicability of these phosphor materials in UV LED chip.

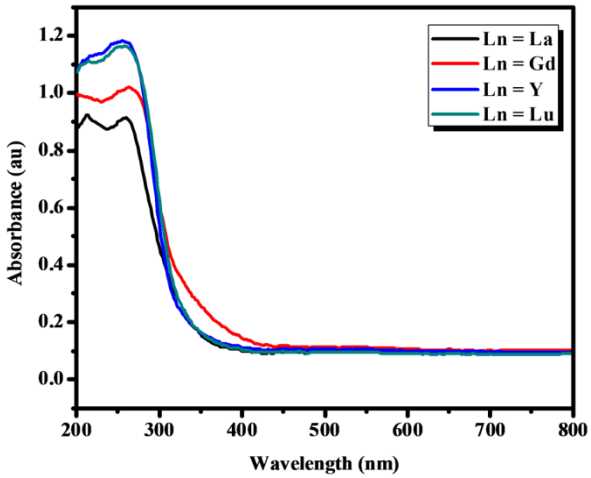

Fig. 5B.9 UV-visible absorption spectra of $Ln_{3.85}YSn_2NbO_{14}$:*0.15*Eu^{3+} (Ln = La, Gd, Y and Lu) phosphors.

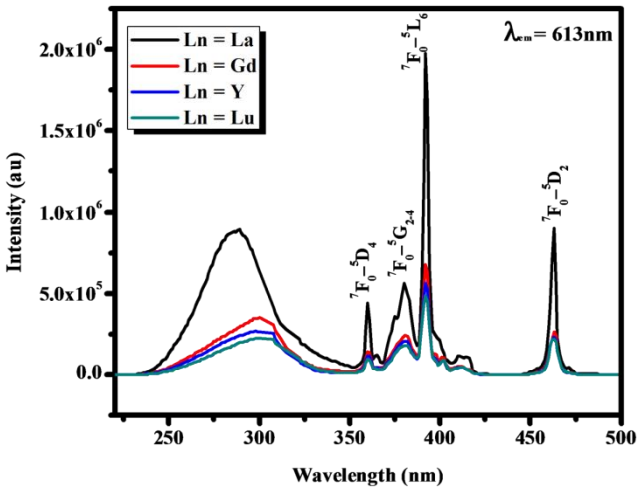

Fig. 5B.10 Excitation spectra of $Ln_{3.85}YSn_2NbO_{14}$:*0.15*Eu^{3+} (Ln = La, Gd, Y and Lu) phosphors for an emission at 613 nm.

Fig. 5B.10 shows the excitation spectra of $Ln_{3.85}YSn_2NbO_{14}$:*0.15*Eu^{3+} (Ln = La, Gd, Y and Lu) phosphors obtained by monitoring the emission of Eu^{3+} $^5D_0 - {}^7F_2$ transition at 613nm. A broad excitation band ranging from 250 to 350 nm appears which can be ascribed to a charge transfer band (CTB) between the Eu^{3+} and the surrounding oxygen anions or host excitation. However, a series of sharp peaks centered from 360 to 470 nm due to the intra-$4f^6$ transitions of Eu^{3+} are observed. The CTB maxima for La, Gd, Y and Lu substituted compounds are 288, 299, 302 and 304 nm respectively. This means that substituting Ln^{3+} with Eu^{3+} ions resulted in significant red shift of the excitation peaks. It is generally recognized that the CTB of Eu^{3+} in oxide host depends greatly on the covalence of Eu^{3+} - O^{2-} bonding. The red shift of the CT band with Ln^{3+} ions suggests the decrease in the covalency of Eu-O bond. To understand the shift of Eu-O CT band, the optical electronegativity of the ligand ion was studied using Jorgensen empirical equation of charge transfer:

$$\Delta_{Eu\text{-}O} = [\chi \text{ (ligand)} - \chi (Eu^{3+})]\ 3x10^4\ cm^{-1} \quad (5B.1)$$

where $\Delta_{Eu\text{-}O}$ is the peak position of the Eu-O CT band and χ (ligand) and $\chi(Eu^{3+})$ are the optical electronegativities of the ligand ion (O^{2-}) and Eu^{3+} ion respectively (Jorgensen 1971). From the peak position values ($\Delta_{Eu\text{-}O}$) of the CT band, we have calculated the difference in electronegativity [χ (O^{2-}) – χ (Eu^{3+}) values of the various lanthanides. The difference in electronegativity decreases with decreasing Ln^{3+} ionic radius, indicating decrease in ionic strength. Eu^{3+} ions replacing La^{3+} ions site have D_{3d} inversion symmetry, and all the other lanthanides possess O_h symmetry. Due to the difference in coordination number and ionic sizes, the environment of Eu^{3+} is disturbed by the incorporation of Ln^{3+} ions. This will induce more covalency in the Eu-O CT band. Even though, all the samples exhibit similar excitation profiles, the intensities of CT band and f-f transitions are different, which are stronger in the La system. The intensity of excitation peak due to due to $^7F_0$-$^5L_6$ transition is in the order La >Gd > Y > Lu. Due to the intense excitation peaks in the UV region, these phosphor materials can be used with near UV InGaN chip for WLED applications. Interestingly, the intensity of CT band and f-f transitions gets improved in $Ln_{3.85}YSn_2NbO_{14}$:*0.15*Eu^{3+} sample than the $Ln_{2.85}YSnNbO_{10.5}$:*0.15*Eu^{3+} phosphor discussed in the chapter 5A. This means the

incorporation of more Sn^{4+} ions in the B site creates more distortion in the lattice and enhances the luminescence properties.

The f-f transitions of Eu^{3+} ions depend strongly on the site occupation and the environment around Eu^{3+} ions in various hosts with different structures. The luminescence emission spectra shown in the Fig. 5B.11 details the variation in the emission intensities due to the transitions from the excited states $^5D_0$ to the ground states ^7F_J (J = 0, 1, 2, 3, 4) in different lanthanide samples. Although all the samples exhibit same emission profiles, crystal field splitting and relative intensity between each transitions are different which is in accordance with the crystal structure. The spectra consist of profiles ranging from 500 to 750 nm, corresponding to the transitions from the excited $^5D_0$ state to the ground states ^7F_J (J = 0-4) of $4f^6$ configuration of Eu^{3+} ions. The $^5D_0$ – $^7F_0$ transitions of Eu^{3+} ions, which occupy only one crystallographic site in the host lattice, is not split because both of its excited and ground states are non-degenerated. No splitting of the $^5D_0$-$^7F_0$ transition (~578nm) observed in the PL spectra of $Ln_{3.85}YSn_2NbO_{14}$:$0.15Eu^{3+}$ indicates that Eu^{3+} ions occupy only one site. This is also consistent with our structure models used for the Rietveld analysis with the fact that Eu^{3+} ions occupy only the A site of the host lattice. It is worth noting that $^5D_0$ – $^7F_1$ magnetic dipole transition of Eu^{3+} ion were split into two lines for the La system, while it appears as single peak in other lanthanides. This indicates that Eu^{3+} ions were located in a site with D_{3d} symmetry in the La substituted phosphor. This consistency in the published spectra suggests that there is no break in symmetry and that D_{3d} symmetry expected to the pyrochlore is preserved in La system. The peak wavelengths of $^5D_0$ – $^7F_1$ MD transition were observed at λ_1 = 586 nm (A line) and λ_2 = 593 nm (B line) respectively. The relative intensity of A line with respect to the B line is found to be more. Hence the A line corresponding to the A_{1g} - E_g transition occurs along x and y direction, while the B line due to the A_{1g} – A_{2g} transition occurs only along the z direction. The distortion of EuO_8 scalenohedra caused by the accommodation of cations of large ionic radius like La induces a larger splitting width of MD transition in the pyrochlore structure. Based on the O_h symmetry of the fluorite structure, no such splitting is observed in other lanthanides. These results are consistent with the

structural variation. These results suggest that manipulation of Eu^{3+} red luminescence is possible through order-disorder structural transition in rare-earth stannate pyrochlore phosphors.

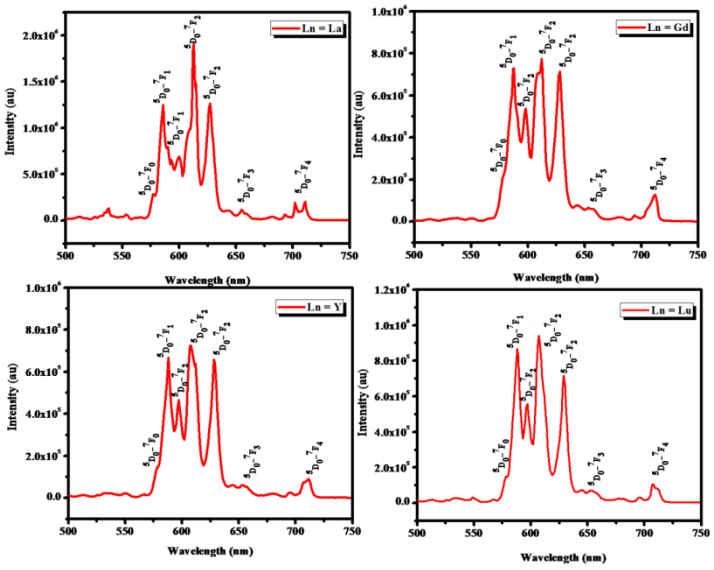

Fig. 5B.11 Emission spectra of $Ln_{3.85}YSn_2NbO_{14}$:*0.15*Eu^{3+} (Ln = La, Gd, Y and Lu) phosphors under 392 nm excitation.

According to the pyrochlore D_{3d} symmetry at the A site, only $^5D_0$ – $^7F_1$ MD transition is allowed. But this assessment is against our results wherein the intensity of $^5D_0$ – $^7F_2$ ED transition is more than that of allowed $^5D_0$ – $^7F_1$ MD transition. The doping of Eu^{3+} ions in the La^{3+} site leads to the distortion of octahedra reducing the symmetry of crystal field surrounding the Eu^{3+} ions, due to the large ionic size difference between La^{3+} and Eu^{3+} ions resulting in an enhanced red emission. This is confirmed by the asymmetry variation (Table 5B.2) which is high for La system compared to that of other Ln host indicating that Eu^{3+} ions are situated in a more distorted environment in La host. The short range ordering in defect fluorite phases give rise to diffuse scattering and decrease the intensity of red emission. Besides asymmetric ratio, assessment of J-O intensity parameters also provide information about the Eu-O covalency and the asymmetry behaviour of the activator and the ligand. Higher value of Ω_2 for La host suggests the strong covalent nature of the Eu^{3+} bonding with the surroundings. The Ω_2 values decreases from La to Lu suggests decrease in the extent of polarizability around

Eu^{3+} ions. In addition, the value of Ω_4 increases from Lu to La and show maximum for La suggesting the increased efficiency for the $^5D_0$ – $^7F_2$ transition. The order of Ω_t parameter is $\Omega_2 > \Omega_4$, which confirms the covalency existing between the Eu^{3+} ions and the ligands as well as the asymmetry around the metal ion site. The assessment of J-O intensity parameters suggests the increased polarizability and efficiency from Lu to La system.

Table 5B.2 Optical properties and intensity parameters of $Ln_{3.85}YSn_2NbO_{14}$:*0.15*Eu^{3+} (Ln = La, Gd, Y and Lu) phosphors.

Sample	Band gap (eV)	CTB (nm)	Asymmetric Ratio	Life time (ms)	Ω_2 (10^{-20}) cm^2	Ω_4 (10^{-20}) cm^2	Efficiency (%)
La	3.64	288	2.75	0.77	8.31	1.23	46.51
Gd	3.69	299	1.41	1.17	4.24	0.73	43.48
Y	3.79	302	1.57	1.10	4.56	0.71	37.26
Lu	3.83	304	1.69	0.94	5.01	0.49	33.40

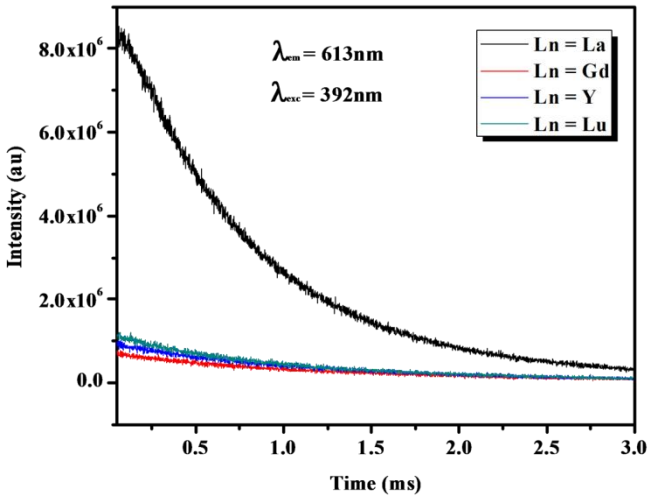

Fig. 5B.12 Decay curves of Eu^{3+} emission in $Ln_{3.85}YSn_2NbO_{14}$:*0.15*Eu^{3+} (Ln = La, Gd, Y and Lu) phosphors.

The fluorescence decay curves for $^5D_0$ states in $Ln_{3.85}YSn_2NbO_{14}$:*0.15*Eu^{3+} (Ln = La, Gd, Y and Lu) phosphors under 392 nm excitation is shown in Fig. 5B.12. All decay

curves could be fitted well using the single exponential function: I = A exp (-x/τ), where I, τ and A are intensity, decay time and fitting parameter respectively. This indicates the single site occupancy of Eu^{3+} ions in the Ln host lattice. The lifetime is found to be small for La host due to the occupation of Eu^{3+} ions in a more distorted environment in the A site (Ln^{3+} site) of pyrochlore structure. Lifetime values and the efficiencies of the phosphors are given in Table 5B.2. It is very clear that the photoluminescence properties among the prepared phosphor materials were better in the system in which Ln cation has the highest ionic radius. This is ascribed to the structural variation in the crystal lattices by varying the Ln cations. It can be understood that the pyrochlore *Fd3m* structure offers better site occupation for Eu^{3+} for f-f transitions leading to enhanced red emissions than the fluorite *Fm3m* phase.

5B. 3.5 Effect of Eu^{3+} Doping in $La_4YSn_2NbO_{14}$ Host Lattice

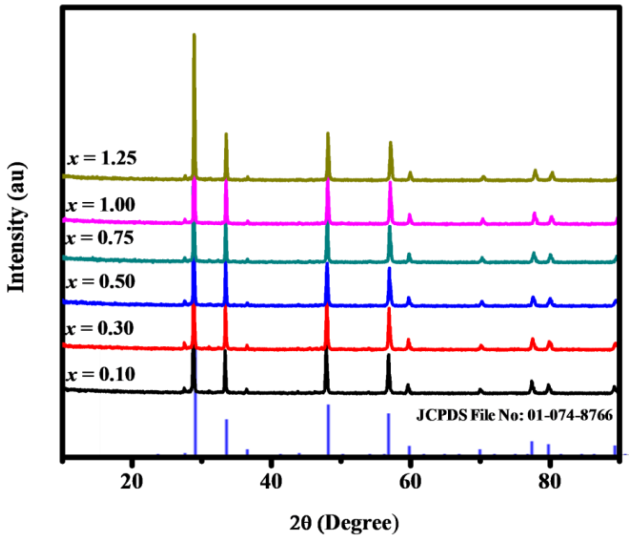

Fig. 5B.13 Powder X-ray diffraction patterns of $La_{4-x}YSn_2NbO_{14}$:xEu^{3+} (x = 0.10, 0.30, 0.50, 0.75, 1.00 and 1.25) phosphors.

Powder X-ray diffraction patterns of $La_{4-x}YSn_2NbO_{14}$:xEu^{3+} (x = 0.10, 0.30, 0.50, 0.75, 1.00 and 1.25) phosphors given in Fig. 5B.13 reveal the crystallinity and phase purity of all the samples and they are in good agreement with the powder diffraction pattern of pyrochlore type unit cell (space group: *Fd3m*). No impurity peaks were observed in the XRD patterns on increasing the doping concentration of Eu^{3+} ions,

which suggests that doping of a small percentage of Eu^{3+} ions does not change the crystal structure. The substitution of the La^{3+} ion (1.16 Å, coordination number, CN = 8) by slightly smaller Eu^{3+} ion (1.07 Å, CN = 8) results in the lattice contraction (Table 5B.3), which is confirmed by the shift of XRD peaks of $La_{4-x}YSn_2NbO_{14}$:xEu^{3+} towards the higher 2θ angle side with increasing Eu^{3+} content (De Dood *et al*. 2005). The shift of the XRD peak towards right shown Fig. 5B.14 confirms the effective substitution of Eu^{3+} ions into the lattice.

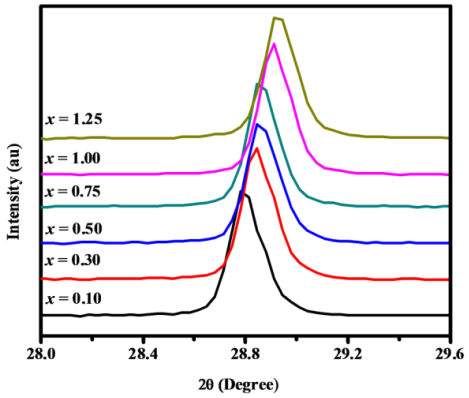

Fig. 5B.14 The expanded view of the (222) reflection at 29°.

Table 5B.3 Refined parameters from Rietveld Analysis of $La_{4-x}YSn_2NbO_{14}$:xEu^{3+} (x = 0.10, 0.30, 0.50, 0.75, 1.00 and 1.25) phosphors

Sample	***x* = 0.10**	***x* = 0.30**	***x* = 0.50**	***x* = 0.75**	***x* = 1.00**	***x* = 1.25**
Phase	Pyrochlore	Pyrochlore	Pyrochlore	Pyrochlore	Pyrochlore	Pyrochlore
Unit cell	Cubic	Cubic	Cubic	Cubic	Cubic	Cubic
Space group	*Fd3m*	*Fd3m*	*Fd3m*	*Fd3m*	*Fd3m*	*Fd3m*
Lattice constant (Å)	10.7488(6)	10.7370(6)	10.7284(6)	10.7145(6)	10.7013(5)	10.6891(6)
Oxygen *x* parameter	0.330(2)	0.330(2)	0.330(2)	0.332(2)	0.335(2)	0.337(2)
Caglioti parameters						
U	0.12(4)	0.14(4)	0.09(4)	0.18(4)	0.12(3)	0.26(5)
V	0.00(3)	-0.03(3)	0.03(3)	-0.05(3)	-0.02(2)	-0.09(3)
W	0.006(5)	0.012(5)	0.002(5)	0.015(5)	0.010(4)	0.021(6)
R-factors						
R_{exp} (%)	13.79	13.43	13.51	13.47	13.14	13.03
R_p (%)	14.08	14.36	13.82	13.22	12.38	11.83
R_{wp} (%)	18.04	18.44	17.59	16.99	16.19	15.34
GOF	1.71	1.89	1.70	1.59	1.52	1.39

Fig. 5B.15 and 5B.16 display the excitation spectra and emission spectra of $La_{4-x}YSn_2NbO_{14}$:xEu^{3+} (x = 0.10, 0.30, 0.50, 0.75, 1.00 and 1.25) phosphors.. It can be seen that increase in the Eu^{3+} content doesn't change the shape and peak positions of the excitation and emission spectra although the intensity changes. However, a significant red shift of the excitation peaks from 287 to 297 nm was observed by the substitution of Eu^{3+} ions on the La^{3+} ion site due to the increase in covalency of Eu-O bond and the coordination environment of Eu^{3+} ions. The red shift of CT band due to the highly favorable low symmetry crystal structure of the system enhances the red emission. Also, both the excitation and emission intensities increases as the Eu^{3+} doping was increased which indicates that $La_4YSn_2NbO_{14}$ host can accept Eu^{3+} in high concentrations without concentration quenching. The enhanced electric dipole transition intensity arises from symmetry distortion of Eu^{3+} ions. This is further confirmed by the asymmetric ratio variation given in Table 5B.4 which shows an increasing trend with Eu^{3+} doping suggesting that doping of Eu^{3+} ions on the sites of La^{3+} ions perturb the symmetry of the host structure. As a result, $^5D_0$-$^7F_1$, $^5D_0$-$^7F_2$ and the $^5D_0$-$^7F_4$ transitions of Eu^{3+} ion splits. Thus long range ordering and ligand polarizability influenced significantly the emission probabilities, intensity and the quantum efficiency of these phosphor materials.

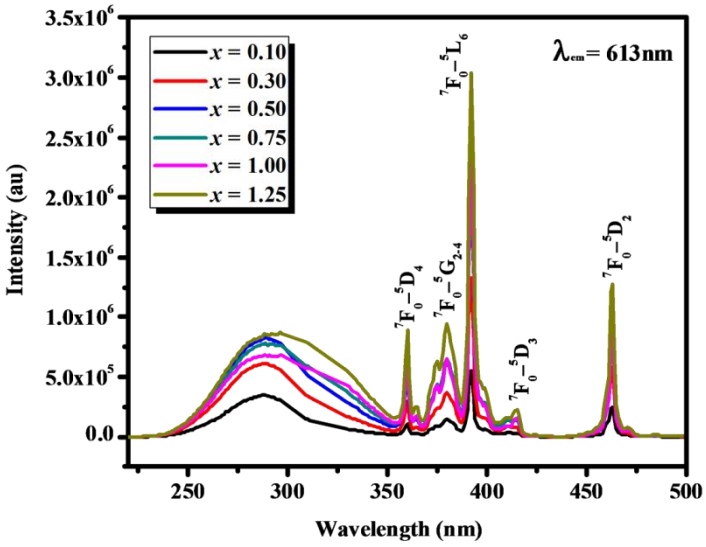

Fig. 5B.15 Photoluminescence excitation spectra of $La_{4-x}YSn_2NbO_{14}$:xEu^{3+} (x = 0.10, 0.30, 0.50, 0.75, 1.00 and 1.25) phosphors.

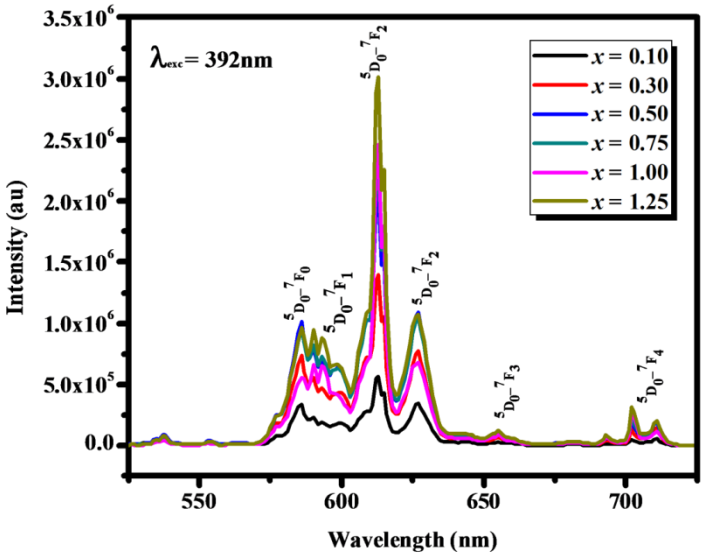

Fig. 5A.16 Emission spectra of $La_{4-x}YSn_2NbO_{14}$:xEu^{3+} (x = 0.10, 0.30, 0.50, 0.75, 1.00 and 1.25) phosphors under 392 nm excitation.

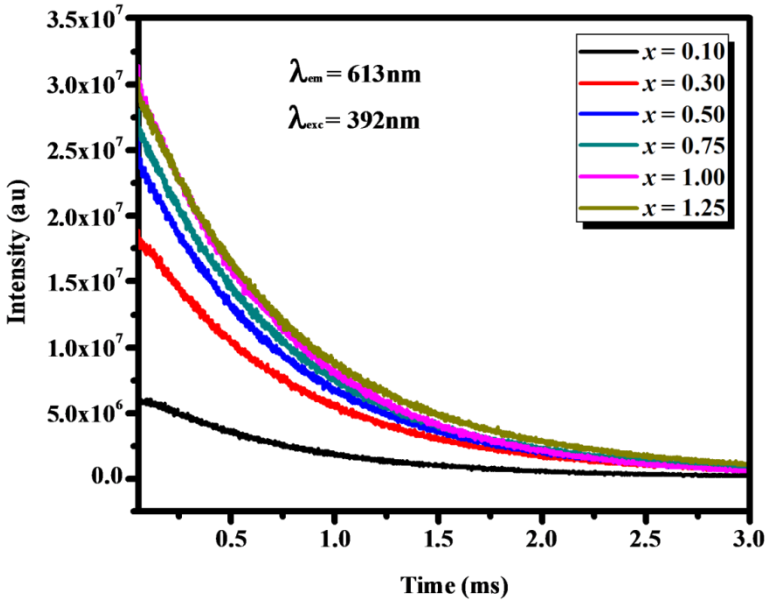

Fig. 5B.17 Decay curves of $^5D_0$-$^7F_2$ transition of Eu^{3+} in $La_{4-x}YSn_2NbO_{14}$:xEu^{3+} (x = 0.10, 0.30, 0.50, 0.75, 1.00 and 1.25) phosphors under 392 nm excitation.

The fluorescent decay curves of the $^5D_0$-$^7F_2$ transition of as prepared samples under the 392 nm excitation are shown in Fig. 5B.17. The lifetime values show an increasing trend with Eu^{3+} ion doping resulting in improved quantum efficiency. The

assessment of J-O intensity parameters given in Table 5B.4 corroborates these results. The incorporation of more Sn^{4+} on the B site of the pyrochlore structure induces more structural distortion in the lattice and improves the red emission and quantum efficiency.

Table 5B.4 Optical properties of $La_{4-x}YSn_2NbO_{14}:xEu^{3+}$ (x = 0.10, 0.30, 0.50, 0.75, 1.00 and 1.25) phosphors

x	CTB (nm)	Asymmetric Ratio	Lifetime (ms)	Ω_2 (10^{-20}) cm^2	Ω_4 (10^{-20}) cm^2	Efficiency (%)
0.10	288	3.19	0.71	7.30	1.05	40.34
0.30	290	3.22	0.72	8.11	1.29	43.64
0.50	291	3.34	0.72	8.12	1.31	48.36
0.75	292	3.78	0.75	10.69	1.79	54.06
1.00	294	3.83	0.76	11.39	1.94	60.87
1.25	298	4.77	0.77	11.76	2.02	67.26

5B. 4 Conclusions

A series of $Ln_{3.85}YSn_2NbO_{14}:0.15Eu^{3+}$ (Ln = La, Gd, Y and Lu) red phosphors were prepared and their structural and photoluminescence properties have been studied. Substitution of various lanthanides (Ln = La, Gd, Y and Lu) transform their crystal structure from an ordered pyrochlore to disordered fluorite through decreasing ionic radius. Powder X-ray diffraction analysis along with Raman spectroscopic studies confirms the phase transition. Studies revealed that the La host showed better luminescence properties in terms of emission intensity, asymmetric ratio and quantum efficiency in accordance with their crystal structures. It was observed that more ordering occurs in the lattice when Ln site is doped from Lu to La. The long range ordering and ligand polarizability influenced significantly the emission probabilities, intensity and quantum efficiency of these phosphor materials.

Chapter 6A

NARROW-BAND RED EMITTING PHOSPHOR, $Gd_3Zn_2Nb_3O_{14}:Eu^{3+}$ WITH HIGH COLOR PURITY FOR PHOSPHOR-CONVERTED WHITE LEDs

In this work a narrow band red emitting $Gd_3Zn_2Nb_3O_{14}:Eu^{3+}$ phosphor was synthesized and characterized in order to improve the color qualities of warm white light emitting diodes. The structural and luminescence property analysis corroborates the occupancy of Eu^{3+} ions in the Gd^{3+}/Zn^{2+} ion site (A site). The developed phosphor exhibits a strong red emission peaking at 613 nm with a fwhm of merely ~ 3.50 nm under the 392 nm excitation. The relative emission intensity was found to be maximum at x = 0.40 and is 3.9 times higher than that of the commercial red phosphor under the 392 nm excitation. These phosphors with remarkable CIE chromaticity coordinates (0.64, 0.35), good CCT values along with high color purity (94.2%) might have significant applications in display devices and evidence as an efficient red phosphor

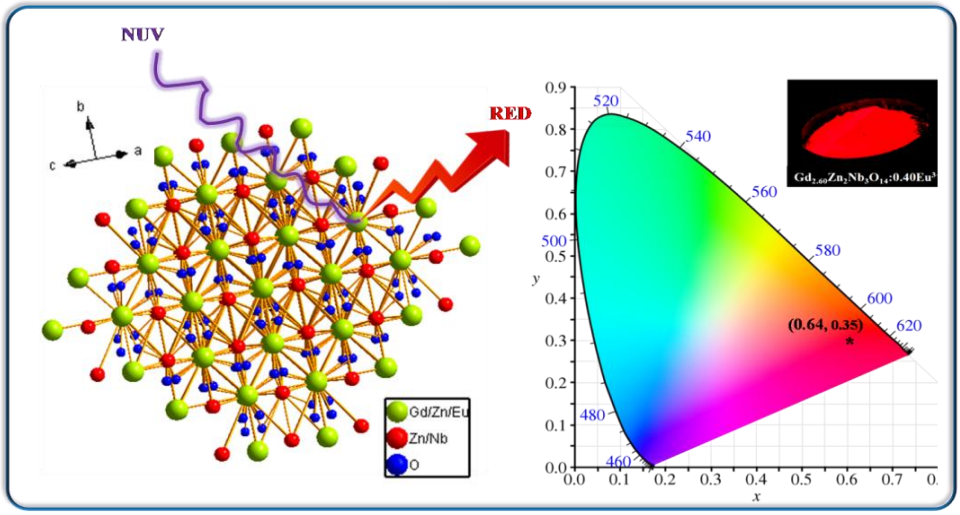

Sreena *et al. J. Alloys Compd.* **2018,** 751, 148-158.

6A. 1 Introduction

The development of an efficient illumination-grade white light with a lower correlated color temperature (CCT: 2700-4000 K), higher color rendering index (CRI > 85) and high luminous efficacy remains a key challenge in the area of solid-state lighting industry (Pust *et al*. 2014; Tsai *et al*. 2015; Pust *et al*. 2015). Research has been going on to improve the color rendition and enhance the visual energy efficacy of illumination grade white light sources, by adapting the pc-LED emission to the visual sensitivity of the human eye, resulting in a high luminous efficacy. Commercially applied red phosphors exhibit a broad emission band with a large portion of emitted light lie outside the human eye sensitivity wasting energy in the infrared region. Therefore, narrow band red-emitting materials are necessary, which can be applied in high-power pc- LEDs, with blue light output of the (Ga,In)N semiconductor LED >100 W/cm^2. The narrow full width half maximum (*fwhm*) of the red emitting spectrum can be obtained by optimizing the crystal structure, local symmetry, and an available number of sites for activators via varying the host composition, activator elements, stoichiometry, concentration, and so on. Lots of researchers have been developing new kinds of narrow-band red phosphors that will be suitable for warm white pc-WLED applications.

Among the state-of-art of red phosphors, Eu^{2+} and Ce^{3+} doped nitrides are most commercialized (Wan *et al*. 2017; Yiyao *et al*. 207; Li *et al*. 2017; Yuan *et al*. 2017) for applications in illumination-grade white pc-LEDs, however, they suffer from rather broad emission bands, which limit the achievable luminous efficacy values of high-luminance warm-white pc-LEDs because a significant part of the emitted light is produced outside the sensitivity range of human eye above 700 nm. Also, the harsh synthetic conditions (high temperature, high pressure, water free, etc.) and the serious re-absorption problem between nitride phosphors and YAG: Ce^{3+} should also be considered (Smet *et al* .2011). Red phosphors, such as those with rare-earth activated sulfides, molybdates/tungstates, and nitrides have been studied and utilized for warm WLEDs with a high CRI value of 80 and low CCT values of 2000-4700K. However, these red phosphors exhibit several limitations such as strong emission quenching with

temperature, high sensitivity to hydrolysis (due to the ionic nature of binary sulfides) and the toxicity of the hydrolysis products which limits the practical applications. Narrow band red emitting phosphors doped with Mn^{4+} ions have shown potential applications in the field of solid state lighting because of their high thermal stability and low cost preparation (Jia *et al*. 2018; Shao *et al*. 2017; Li *et al*. 2017). But they exhibit intense narrow band red emission at approximately 630-650 nm, which is insensitive to human eye. Hence, we tried to develop Eu^{3+} doped oxide based narrow band red phosphor using the conventional solid state reaction method.

The Eu^{3+} activated phosphors have attracted more attention since the $^7F_0$-$^5L_6$, and $^7F_0$-$^5D_2$ transition wavelengths match well with the emission wavelength of near-UV InGaN and blue GaN chips, respectively. As band gap between $^5D_0$ level and the highest component of the ground state multiplet (^7F_J) is very high, they can then give highly intense narrow red band emissions. So there is immense interest on Eu^{3+} doped red phosphors for which the narrower the red emission, the better will be the CRI (Katelnikovas *et al*. 2012). Generally, Eu^{3+} activated phosphors possess high CRI values but exhibit low absorption in blue or near UV region because of the dynamics of rare earth ion, which depends on the interaction between the rare earth ion and the host, such as local environment around the dopants, the doping concentration, the distribution of activator ions in the host lattice and the energy transfer from the host lattice to the activator ions. The absorption of Eu^{3+} ions can be increased by selecting a suitable host lattice where absorption is increased due to the increased optical pathway of the incident photons.

Niobium-containing oxides have attracted a great deal of attention due to their interesting physical properties, such as high dielectric constants, photocatalytic behavior, and photoluminescence and mechanical and chemical stability (Li *et al*. 2015; Yang *et al*. 2014). $GdNbO_4$ is essentially inert in the visible region under the excitation of UV light and electron beams. Blasse and Bril have explained that the absence of luminescence in $GdNbO_4$ is due to the energy transfer from NbO_6 groups to gadolinium ions, and the concentration quenching of gadolinium ions. Even though $GdNbO_4$ still has the potential to be a good host lattice material for rare earth ions due to its chemical

stability, the self-activated luminescent center NbO_4 group, and the sensitization of Gd^{3+} (Liu *et al*. 2007). ZnO is a direct wide energy band gap (3.37eV) material with a large exciton binding energy (60meV) at room temperature and has been used as a host material for the doping of rare earth and transition metal ions (Islam *et al*. 1996). Hence, possible solution to improve the luminescent properties of $GdNbO_4$ is by substituting Zn^{2+} ions for part of Gd^{3+} ions without altering the monoclinic crystal structure. Unfortunately, to the best of our knowledge so far as the related research about the Zn substituted $GdNbO_4$ system is rarely reported. Therefore, in this work, a series of novel narrow red-emitting phosphors $Gd_{3-x}Zn_2Nb_3O_{14}$:xEu^{3+} were prepared and characterized for their crystal, morphological and optical properties. Also, investigate the influence of partial occupation of Zn in both A and B sites on the photoluminescence properties in detail. This phosphor emitted a red light peaking at 613 nm with a narrow *fwhm* of 3.50 nm under the 392 nm excitation which is highly perceived by the human eye and led to excellent chromatic saturation of the red spectra.

6A. 2 Experimental Section

6A. 2.1 Synthesis

The phosphors $Gd_{3-x}Zn_2Nb_3O_{14}$:xEu^{3+} (x = 0, 0.10, 0.20, 0.30, 0.40 and 0.50) were prepared by a conventional high temperature solid-state reaction method using Gd_2O_3, ZnO, Nb_2O_5, and Eu_2O_3 (99.99% purity; Sigma-Aldrich, Steinheim, Germany) as the starting materials. The constituent chemicals taken in the required stoichiometric ratios were mixed thoroughly in an agate mortar with acetone as the mixing agent. The mixture was then dried by keeping in hot air oven at 100°C. The procedure of mixing and subsequent drying was repeated thrice to obtain a homogeneous mixture. The mixture was then calcined on a sintered alumina plate in an air atmosphere electrical furnace at 1400°C for 6 h. The calcination was repeated at 1500°C for 6 h with intermittent grinding until a phase pure compound was obtained. The calcined product was then ground into a fine powder for carrying out further characterization.

6A. 2.2 Characterization

The crystal structure and the phase purity of the calcined samples were identified by recording the powder X-ray diffraction (XRD) patterns using a PANalytical X'pert Pro diffractometer. The surface chemical composition and the oxidation states of the constituent elements present in the sample were analyzed using X-ray photoelectron spectroscopy (XPS) PHI 5000 Versa probe II having Al Ka monochromatic source. The particle size and morphology analysis of the samples were performed on a scanning electron microscope (JEOL, JSM-5600LV) with an acceleration voltage of 15 kV. Energy dispersive analysis and elemental mapping of the samples was carried out using a Silicon Drift Detector X-Max^N attached with a Carl Zeiss EVO SEM. EDS elemental mapping was conducted using the Aztec Energy EDS Microanalysis Software. The photoluminescence excitation and emission spectra of the prepared samples were recorded on a Fluorolog HORIBA fluorescence spectrophotometer with a Xenon lamp (450 W) as the excitation source.

6A. 3 Results and discussion

6A. 3.1 Structural studies

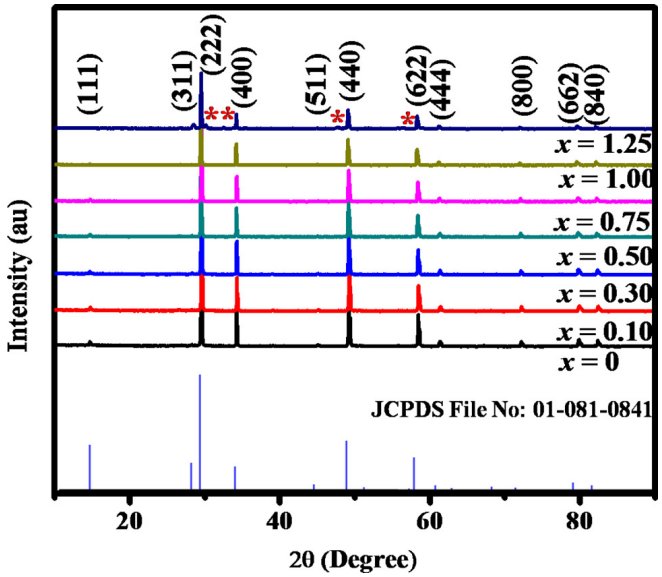

Fig. 6A.1 Powder X-ray diffraction patterns of $Gd_{3-x}Zn_2Nb_3O_{14}$:xEu^{3+} (x = 0, 0.10, 0.20, 0.30, 0.40 and 0.50) phosphors calcined at 1500°C.

A series of $Gd_{3-x}Zn_2Nb_3O_{14}$:xEu^{3+} (x = 0, 0.10, 0.20, 0.30, 0.40 and 0.50) phosphors have been successfully synthesized by a high temperature solid-state reaction method. As is given in Fig. 6A.1, it can be seen that all the diffraction peaks of the samples indexed to the pure phase of $GdNbO_4$ (JCPDS: 01-085-0520; monoclinic phase; space group: C2/c). The sharp and narrow peaks of the XRD patterns indicated that the sample was crystallized well, which was beneficial for luminescence applications. No additional diffraction peaks that could be attributed to the impurities are observed in the diffraction pattern, indicating that Eu^{3+} ions can be completely made solid solutions into the $Gd_3Zn_2Nb_3O_{14}$ compound and their introduction does not induce significant changes in the crystal structure. The $GdNbO_4$ crystal belongs to the fergusonite-type structure, ABO_4. In the present system [$(Gd_{0.75}Zn_{0.25})(Zn_{0.25}Nb_{0.75})O_{3.5}$], the A-site is occupied by Gd^{3+} ions, and Nb^{5+} ions occupy the B site; while Zn^{2+} ions might be occupying both A and B-sites because of its medium ionic radius according to the crystal chemical principle (Sreena *et al*. 2016). In this case, the occupation of indiscriminately displacive Zn^{2+} ions make the system in a disordered state reducing the symmetry, as evidenced from the emission studies. From the chemical point of view, some of the Zn^{2+} ions can be mixed with Gd^{3+} ions in the A site resulting in the disorder in A-O network. Thus in the present system, the partial occupation of Zn^{2+} ions in the A site induce significant local structural distortion. Eu^{3+} ions are expected to substitute the Gd^{3+} lattice positions in the host lattice because of their similar ionic radii (r(Gd^{3+}, CN= 8) = 1.053 Å, r(Eu^{3+}, CN = 8) = 1.066 Å, (where CN is coordination number)) and valency. This is evidenced by the shift in the diffraction peaks towards lower angles with respect to increasing Eu^{3+} doping concentrations. This shift can be explained by the Bragg's equation, $n\lambda = 2d\sin\theta$, where d is the interplanar spacing, θ is the half diffraction angle, n is an integer and λ is the wavelength of X-ray used (Balmer *et al*. 2001). The decrease in 2θ value will lead to the expansion of lattice volume and the values are listed in Table 6A.1. However, from the structural analysis it is difficult to make an assumption about the site occupation of Eu^{3+} ions in the lattice, since the Eu^{3+} ions can occupy the Gd^{3+}/Zn^{2+} ions site (A site). From the XPS and PL studies we deduce that Eu^{3+} ions will occupy the Gd^{3+} ion site up to x = 0.40 and on further substitution, Eu^{3+} ion prefers to occupy the Zn^{2+} ion in the A site for maintaining the charge

neutrality. To achieve the charge balance, Eu^{3+} ions may form pairs by trapping an interstitial O^{2-} ions and replace a couple of neighboring Zn^{2+} ions and is evidenced by the variation of O1s spectral regions in the XPS spectra. This is further confirmed by the varying trend of asymmetry ratio and lifetime with Eu^{3+} ion concentration which is discussed in detail in later part. Thus, according to the radius analysis we conjecture that Eu^{3+} ions will occupy the Gd^{3+} ion site up to x = 0.40. The lattice parameters and unit cell volume of $Gd_3Zn_2Nb_3O_{14}$ were compared with the parent compound $GdNbO_4$. The cell volume decreases with the introduction of Zn^{2+} ion due to the lower ionic radius of Zn^{2+} than Gd^{3+}. The average crystallite size (Δd) of the samples can be calculated from the Debye-Scherrer equation, $\Delta d = 0.91\lambda/\beta\cos\theta$, where λ is the wavelength of X-ray used, β and θ are the half width of the X-ray diffraction lines and half diffraction angle 2θ respectively (Langford *et al*. 1978). The instrumental broadening was rectified using silicon as the external standard. The estimated average crystallite size of the sample is found to be in the range 63-85 nm and the values are listed in Table 6A.1. It is observed that on doping, the crystallite size increases up to x = 0.40 and then decreases monotonously.

Table 6A.1 Variation of lattice parameter, lattice volume and average crystallite size of pure $GdNbO_4$ and $Gd_{3-x}Zn_2Nb_3O_{14}$:xEu^{3+} (x = 0, 0.10, 0.20, 0.30, 0.40 and 0.50) phosphor

Sample	**$GdNbO_4$**	***x* = 0**	***x* = 0.10**	***x* = 0.20**	***x* = 0.30**	***x* = 0.40**	***x* = 0.50**
Lattice constant							
***a* (Å)**	7.1115	7.1112	7.1114	7.1118	7.1122	7.1129	7.1135
***b* (Å)**	11.0959	11.0951	11.0970	11.0975	11.0977	11.0992	11.1009
***c* (Å)**	5.1067	5.1067	5.1068	5.1071	5.1072	5.1077	5.1083
β (°)	131.146	131.144	131.138	131.134	131.132	131.128	131.123
Cell Volume (Å^3)	303.446	303.438	303.500	303.590	303.612	303.736	303.866
Crystallite size (nm)	63.79	63.79	63.79	85.04	85.08	85.09	63.79

The $Gd_3Zn_2Nb_3O_{14}$ crystal belong to the monoclinic fergusonite type structure ($GdNbO_4$) with a space group C2/c, the crystal structure, as well as the coordination environment are displayed in Fig. 6A.2. The fergusonite structure is only a slightly distorted scheelite structure with the cations deviating a little from the special Wyckoff positions and the anions dividing into two kinds of Wyckoff positions accompanied by fractional coordinate displacement, thereby inducing a lower symmetry (Errandonea *et al*. 2009). It is a three dimensional framework consisting of irregular NbO_6 and GdO_8 units. The NbO_6 units form a one-dimensional zigzag chain propagating by edge-shared oxygen atoms along the c axis. The framework formed by edge-sharing GdO_8 units can be considered to encapsulate the propagating chains of NbO_6 units to form a three-dimensional framework.

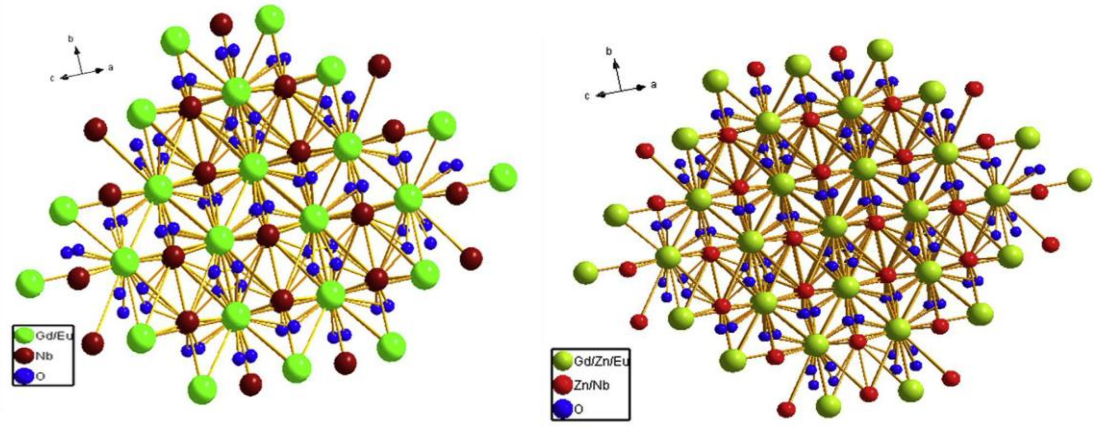

Fig. 6A.2 Schematic illustration of the monoclinic fergusonite-type crystal structure $Gd_{0.80}NbO_4$:*0.20*Eu^{3+} and $Gd_{2.60}Zn_2Nb_3O_{14}$:*0.40*Eu^{3+}.

6A. 3.2 X-ray photoelectron spectroscopy studies

X-ray photoelectron spectroscopy is a renowned technique to explore the surface chemical composition, the oxidation states of the constituent elements present in the sample. The survey scan spectra of the $Gd_{2.60}Zn_2Nb_3O_{14}$:*0.40*Eu^{3+} phosphor synthesized at 1500°C is shown in Fig. 6A.3, which clearly confirms the presence of Gd, Zn, Nb, O, and Eu from their corresponding binding energies. The binding energy data were calibrated using C1s peak at 284.7 eV for the charge shift rectifications, and its binding energy generally remains constant irrespective of the chemical state of the

sample. The presence of core-level photoelectron peaks at 1021.3 and 1046.4 eV corresponding to Zn $2p_{1/2}$ and Zn $2p_{3/2}$ confirms the presence of Zn^{2+} ions in an oxide environment (Tay *et al*. 2006). The appearance of peaks at around 205 and 142 eV corresponding to the binding energies of Nb 3d and Gd 4d, respectively (Fig. 6A.4c and a). Also, the binding energy of Gd 4d and Zn 2p3 increases with increase in Eu^{3+} concentration upto x = 0.40 and thereafter decreases. This variation in the binding energy values signifies the change of site occupation of Eu^{3+} ions in the lattice. The O1s spectral regions have been used to gain information concerning the presence of oxygen vacancies present in the sample. The high resolution XPS scan spectra of O1s for different Eu^{3+} concentration shown in Fig. 6A.4d showed a BE = 528.7 eV, ascribed to the lattice oxygen in the Zn-O-Zn network. The peak associated with O1s bonds is generally originating from the oxygen within the crystal lattice in the form of O^{2-} (or metal-oxygen bond). The intensity of O1s increases monotonously with doping up to 40 mol% and thereafter decreases. Also, it is observed the BE of O1s remains the same with Eu^{3+} doping up to x = 0.40; but shift to higher energy (530 eV) on further doping. The shifting of BE signifies the possibility of change in the chemical environment around Eu^{3+} ions (Moulder *et al*. 1995). Moreover, the *fwhm* of the O1s peak decreases with Eu^{3+} doping up to x = 0.40 and increases on further doping which also signifies the variation in the site of occupation of Eu^{3+} ions. As mentioned earlier in the XRD studies, the site of the occupation of Eu^{3+} ions changes when the Eu^{3+} concentration becomes 0.50, which is confirmed by the XPS study that doping changes the chemical environment around Eu^{3+} ions. The doping of Eu^{3+} ions in the nonisovalent site (Zn^{2+} ion site) creates defects and oxygen vacancy in the lattice and quenches the luminescence properties.

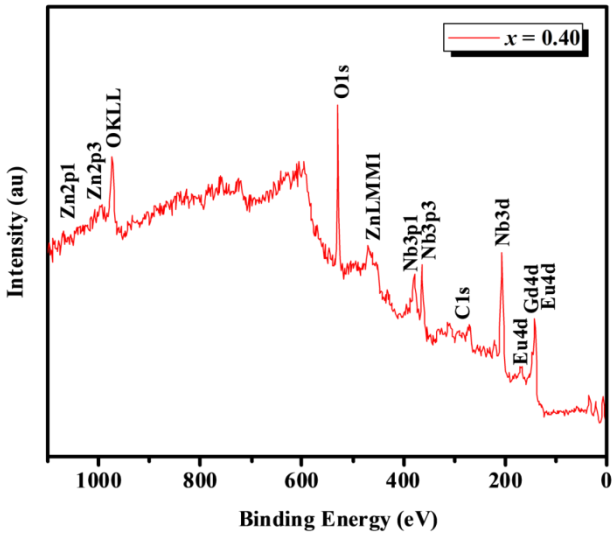

Fig. 6A.3 XPS Survey Scan Spectra of $Gd_{2.60}Zn_2Nb_3O_{14}$:*0.40*Eu^{3+} phosphor synthesized at 1500°C.

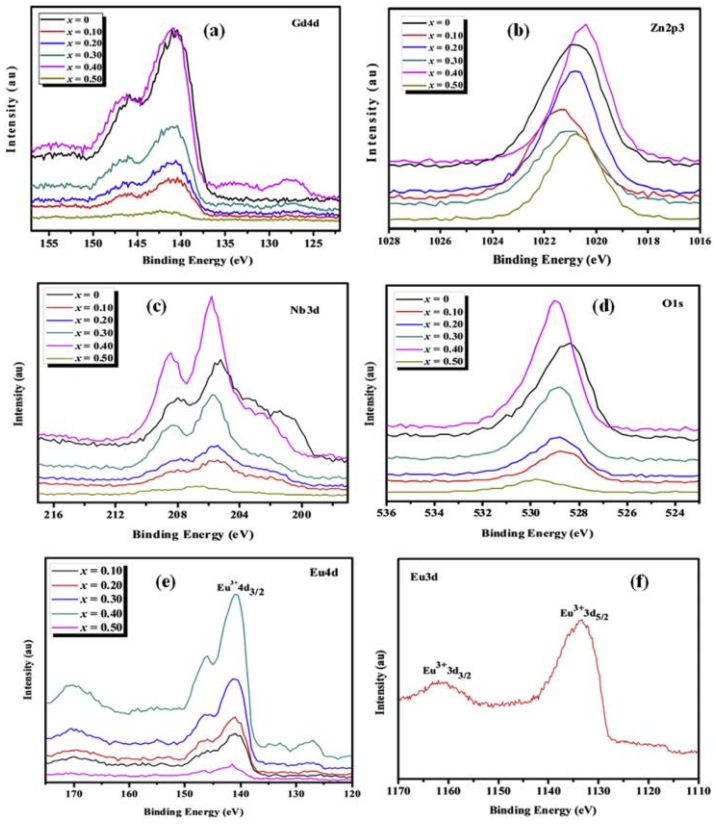

Fig. 6A.4 (a) High resolution XPS scan of the Gd 4d (b) Zn 2p3 (c) Nb 3d (d) O1s (e) Eu 4d (f) Eu 3d regions.

The high-resolution XPS scan spectra for the Eu 4d and Eu 3d regions are shown in Fig. 6A.4e and f, respectively. The presence of two peaks at around 1133.5 and 1161.7 eV can be assigned to Eu^{3+} $3d_{5/2}$ and $3d_{3/2}$ core levels, respectively; both peaks are due to multiple spin-orbit interactions and are consistent with the reported values (Singh *et al*. 2014). The BE difference between the two peaks is about 28.2 eV which is in agreement with the literature values for oxygen surrounded Eu ions, which confirms the possibility of the presence of trivalent Eu ions in the samples. Due to the final state effects and charge transfer co-excitations, normally the core-level photoelectron spectra of the rare earth compounds exhibit a characteristic satellite peaks. As a result, additional peaks are also present at the low binding energy side of Eu^{3+} ions shown in Fig. 6A.4e. A broad peak occurs at around 141.4 eV corresponds to Eu $4d_{3/2}$ which is attributed to the spin-orbit splitting and no peak at around 127.1 eV corresponding to Eu^{2+} ($4d_{5/2}$) are observed. This confirmed that the high probability of the presence of Eu^{3+} ion present in the sample and is also confirmed from excitation and emission study. The broadness arises from the multiplet splitting owing to the strong exchange interaction between the 4d core holes and the partly filled 4f shell. The BE separation between the satellite and the spin-orbit splitting is around 8.2 eV is in good agreement with the previous reports of Eu^{3+} containing oxide materials. The intensity of this peak also increases with doping and reaches a maximum at 40 mol%, beyond that it exhibits a sudden decrease which may be due to the difference in the site of occupation. The analysis of peak positions and binding energies in the XPS spectra in the region corresponding to the $3d_{5/2}$ and $3d_{3/2}$ core levels of the Eu ion confirms that Eu is present in Eu^{3+} oxidation states in the system. Thus, the XRD and XPS results designate that our sample can be acknowledged as crystalline and pure phases.

6A. 3.3 Morphological studies

The crystalline morphology of the $Gd_{3-x}Zn_2Nb_3O_{14}:xEu^{3+}$ (x = 0, 0.10, 0.20, 0.30, 0.40 and 0.50) phosphor was checked by scanning electron microscopy and is shown in Fig. 6A.5. It is clearly seen from the images that the samples are composed of aggregate particles with sizes ranging from 1 to 5 μm and display approximate spherical morphologies, basically agreeing with the results estimated from the Scherrer equation.

Not much difference in particle size and morphology were observed upon varying the Eu^{3+} concentration. The energy dispersive X-ray spectroscopy measurements shown in the Fig. 6A.6 confirm the presence of the Gd, Zn, Nb, O and Eu in the typical sample $Gd_{2.6}Zn_2Nb_3O_{14}$:*0.40*Eu^{3+} and the obtained chemical compositions were close to the theoretical stoichiometry. Also, the elemental X-ray dot mapping analysis (Fig. 6A.7) indicates that the Eu^{3+} ions are homogeneously dispersed in the host lattice.

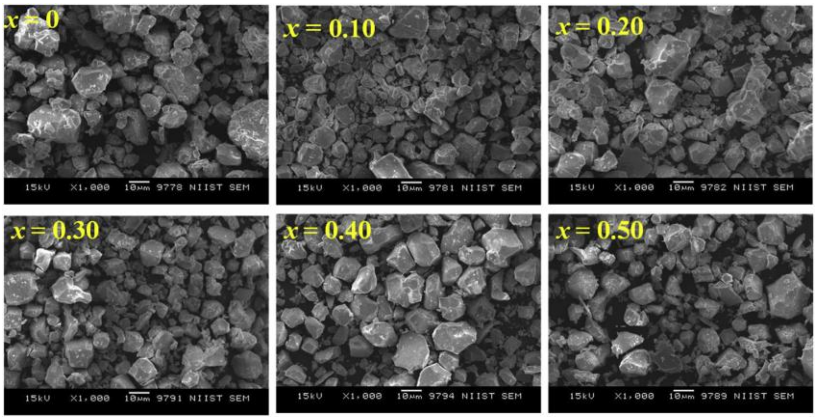

Fig. 6A.5 SEM micrographs of $Gd_{3-x}Zn_2Nb_3O_{14}$:xEu^{3+} (x = 0, 0.10, 0.20, 0.30, 0.40 and 0.50) phosphor.

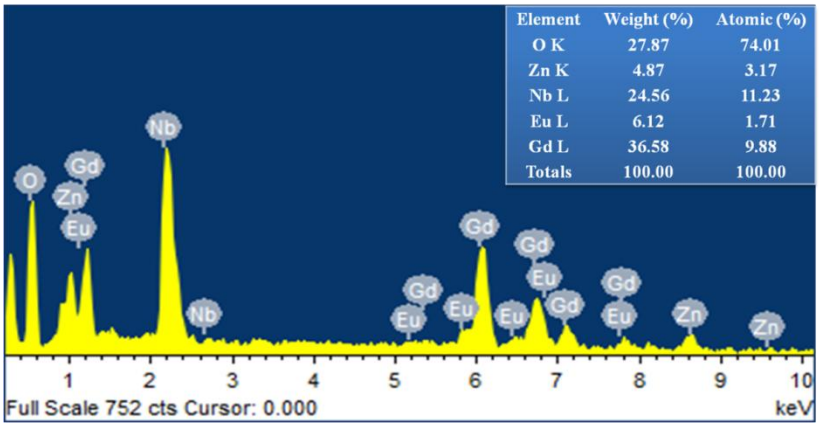

Fig. 6A.6 Energy dispersive X-ray spectroscopy measurements of the typical $Gd_{2.60}Zn_2Nb_3O_{14}$:*0.40*Eu^{3+} phosphor synthesized at 1500°C**.**

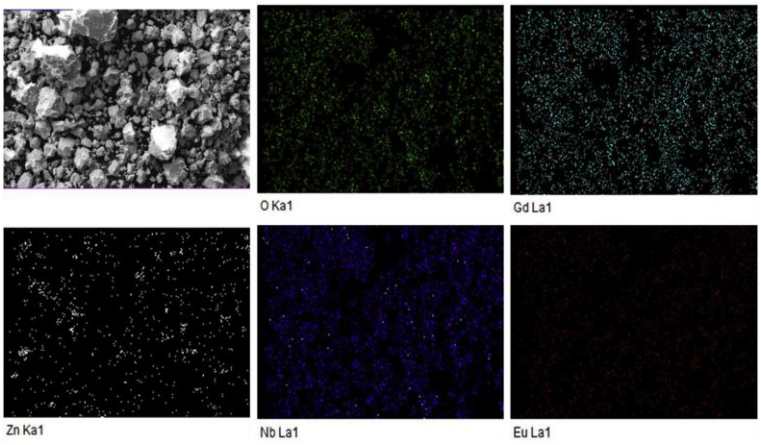

Fig. 6A.7 Elemental X-ray dot mapping of typical $Gd_{2.60}Zn_2Nb_3O_{14}$:*0.40*Eu^{3+} phosphor synthesized at 1500°C.

6A. 3.4 Optical studies

$GdNbO_4$ is known as self-activated phosphor since it contain niobate groups (NbO_4^{3-}) in the lattice and they emit blue light under UV or X-ray excitation. Fig. 6A.8 shows the excitation and emission spectra of $GdNbO_4$ host lattice for an emission at 440 nm. The excitation spectra consist of a broad band ranging from 200 to 350nm peaking at 270 and 300 nm. The band at 270 nm is attributed to the $O^{2-} \rightarrow Nb^{5+}$ charge transfer transition and that at 300 nm corresponds to the characteristic f-f transition of Gd^{3+} ($^8S_{7/2} \rightarrow {}^6P_{7/2}$) within the $4f^6$ configuration. The excitation band corresponding to the NbO_4^{3-} group in $GdNbO_4$ is weak compared to the Gd^{3+} ion transition, which indicates that considerable amount of energy absorbed by the NbO_4^{3-} group, is transferred to the Gd^{3+} ions in the lattice (Blasse *et al*. 1970; Blasse *et al*. 1976). A weak luminescence is observed under the excitation of NbO_4^{3-} group due to the $^3T_1$, $^3T_2 \rightarrow {}^1A_1$ transition of the NbO_4^{3-} group, and the rest energy is transferred to Gd^{3+} ion, which is then quenched because of its high concentration. A strong blue emission is observed on excitation with 300 nm owing to the NbO_4^{3-} group. The emission color can be tuned from blue to red by the addition of Eu^{3+} ions in $GdNbO_4$ host lattice. In the present study, we tried to enhance the f-f transition intensity of $GdNbO_4$:Eu^{3+} phosphors by incorporating Zn^{2+} ions to obtain the general formula $Gd_3Zn_2Nb_3O_{14}$ and investigate their photoluminescence properties in detail.

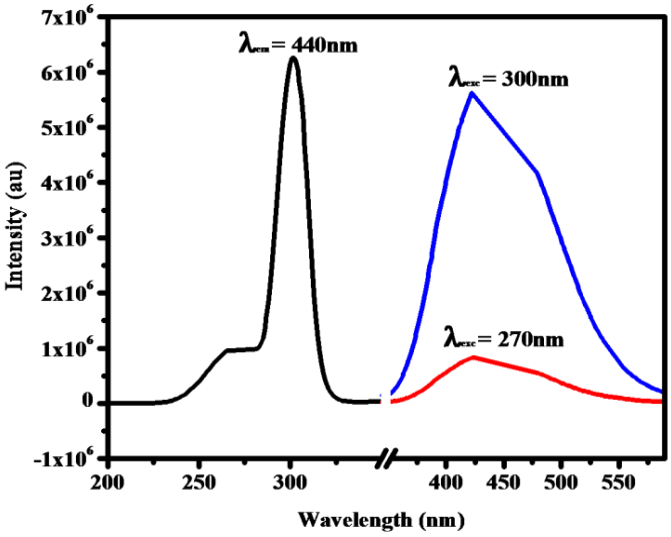

Fig. 6A.8 Excitation and emission spectra of $GdNbO_4$ at 270 nm and 300 nm excitation

The photoluminescence excitation spectra of the samples monitored at 613 nm is shown in Fig. 6A.9. The excitation spectra consist of a broad band from 220 to 320 nm with maxima at 270 nm and 300 nm and a series of narrow lines in the range 320-500 nm. The first excitation band at 270 nm can be assigned to the $O^{2-} \rightarrow Nb^{5+}$ charge transfer transition and the second band at 300 nm is ascribed to the charge transfer from the completely filled 2p orbitals of O^{2-} to the partially filled f-f orbitals of the Eu^{3+} ions ($O^{2-} \rightarrow Eu^{3+}$) (Parchur *et al*. 2011; Dutta *et al*. 2013). The presence of excitation peak of the NbO_4^{3-} group in the excitation spectra of Eu^{3+} ions implies the existence of efficient energy transfer from the NbO_4^{3-} group of the host to Eu^{3+} ions. The CT band is shifted to higher wavelength side with an increase in Eu^{3+} concentration. This shift can be attributed to an increase in covalency of Eu-O bonds and the coordination environment of the Eu^{3+} environment, which reduces the CT energy. The parity forbidden intraconfigurational f-f transitions of Eu^{3+} is also strengthened by borrowing intensity from the lowest strong absorption band (CT) by nonradiative energy transfer process. The CTB position is closely related to the coordination state of Eu^{3+} ion in the host lattice and the bond length of Eu^{3+} and anions. The band position is more or less fixed in VI coordination and moves to lower energy with an increase of bond distance in VIII coordination as a function of Eu-O bond distance in the lattice (Hoefdraad *et al*. 1975).

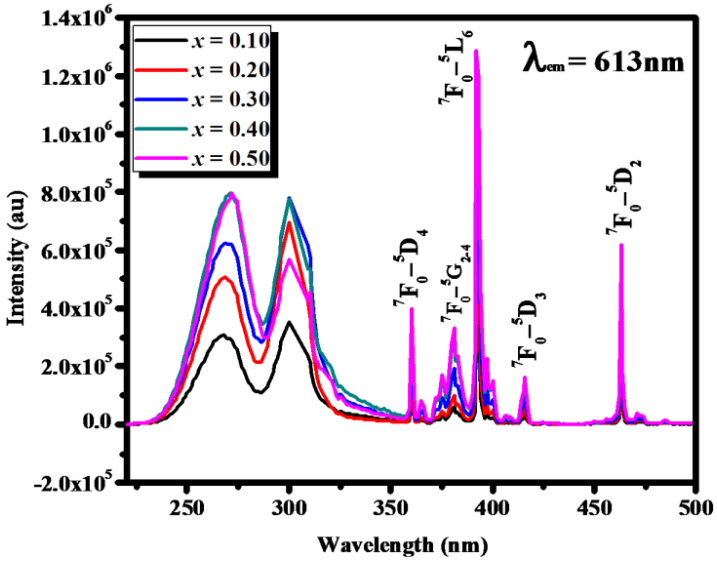

Fig. 6A.9 Photoluminescence excitation spectra of $Gd_{3-x}Zn_2Nb_3O_{14}$:xEu^{3+} (x = 0.10, 0.20, 0.30, 0.40 and 0.50) red phosphors for 613 nm emission.

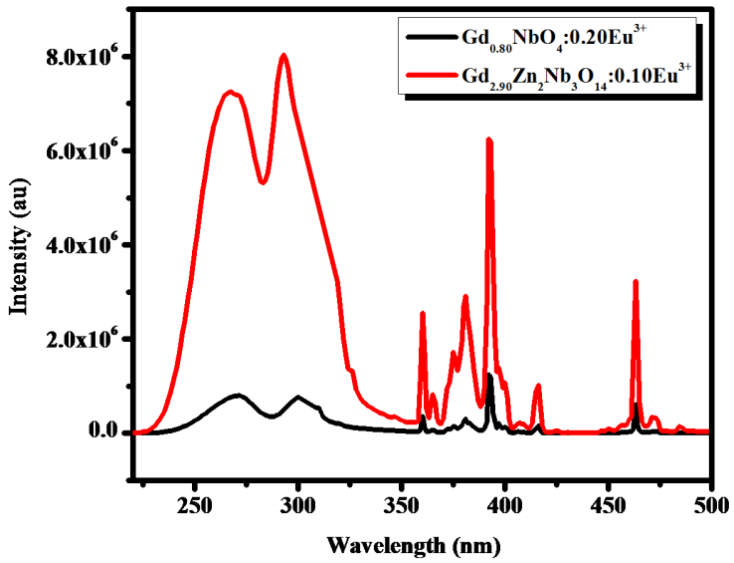

Fig. 6A.10 Comparison of photoluminescence excitation spectra of $Gd_{0.80}NbO_4$:*0.20*Eu^{3+} and $Gd_{2.90}Zn_2Nb_3O_{14}$:*0.10*Eu^{3+} red phosphor for 613 nm emission.

Comparing the excitation spectra of $Gd_{2.90}Zn_2Nb_3O_{14}$:*0.10*Eu^{3+} with that of $Gd_{0.80}NbO_4$:*0.20*Eu^{3+} (Fig. 6A.10), it can be seen that the broad excitation band are almost identical, except the excitation intensity. The CT band and f-f transition intensities are got enhanced with Zn^{2+} incorporation into the $GdNbO_4$ host lattice. The

series of sharp excitation bands present between 320 and 500 nm are associated with the typical intra 4f transitions of Eu^{3+} ions that centered at 360, 392, 415 and 463 nm were attributed to the $^7F_0 \rightarrow {}^5D_4$, $^7F_0 \rightarrow {}^5L_6$, $^7F_0 \rightarrow {}^5D_3$ and $^7F_0 \rightarrow {}^5D_2$ respectively. Among these, the intensity of peaks at 392 and 463 nm are stronger than other transitions which are matching well with the emission wavelengths of near UV and blue LED chips, respectively. This suggests that $Gd_{3-x}Zn_2Nb_3O_{14}:xEu^{3+}$ phosphor is suitable to be used for near UV and blue LED exciting red phosphor for white lighting device.

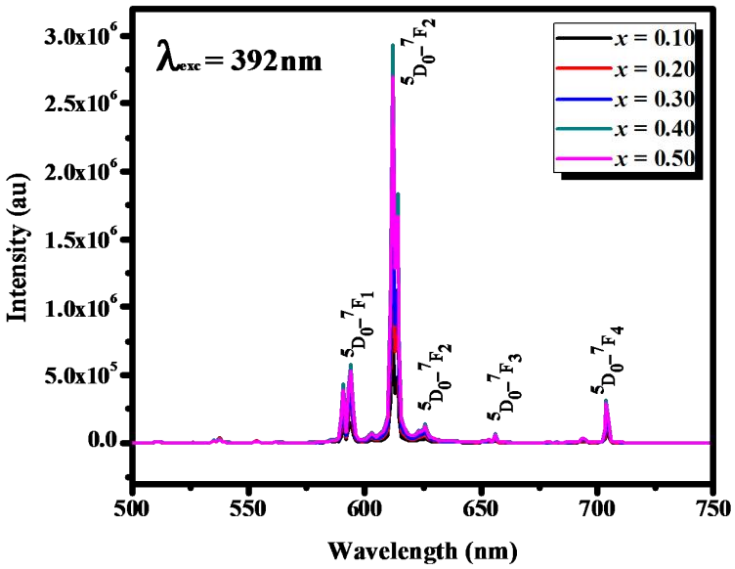

Fig. 6A.11 Photoluminescence emission spectra of $Gd_{3-x}Zn_2Nb_3O_{14}:xEu^{3+}$ (x = 0.10, 0.20, 0.30, 0.40 and 0.50) red phosphors under 392nm excitation.

Fig. 6A.11 shows the emission spectrum of $Gd_{3-x}Zn_2Nb_3O_{14}:xEu^{3+}$ phosphor with different Eu^{3+} concentrations under the 392 nm excitation. The strongest emission peak located at 613 nm is attributed to the $^5D_0$ - $^7F_2$ transition of Eu^{3+} ion. Three other weak peaks at 594, 656 and 703 nm are assigned to the $^5D_0$ - $^7F_1$, $^5D_0$ - $^7F_3$ and $^5D_0$ - $^7F_4$ transition of Eu^{3+}, respectively. The positions of the red emission peaks of Eu^{3+} ions have no obvious shift with increasing Eu^{3+} ion concentration, suggesting that doping of Eu^{3+} ions does not induce significant changes in the crystal structure. Also, no emission from NbO_4^{3-} group could be detected in the emission spectra revealing the highly efficient non-radiative energy transfer from the NbO_4^{3-} group to Eu^{3+} ions. From the emission spectra, one can observe that the intensity of $^5D_0$ - $^7F_2$ transition is much

stronger than that of the $^5D_0$ - $^7F_1$ transition, which is beneficial for obtaining a phosphor with good color purity. This suggests that Eu^{3+} ions occupied the site without inversion symmetry, which is in accordance with the crystal structure of $Gd_3Zn_2Nb_3O_{14}$.

In this system, the doped Eu^{3+} ions will occupy the site of the Gd^{3+} ion, where the Gd^{3+} ion bonded to four vertices of NbO_4 tetrahedron with Nb-O = 2.146 Å and two edges of NbO_4 tetrahedron with Gd-O = 1.1916 Å, forming a GdO_8 distorted triangulate dodecahedron. The dodecahedron can be visualized to give Gd^{3+} ions D_{2d} site symmetry which has very low inversion symmetry. This agrees with the nature of Eu^{3+} ion local environment and the structure of single crystal that favors the placing of Eu^{3+} ion on the lattice, where the local site symmetry is highly distorted and is evidenced by the splitting of the $^5D_0$ - ^7F_J levels due to the crystal field effect. It can be clearly seen from the emission spectra that the photoluminescence intensity of Eu^{3+} ion increases monotonically with increasing Eu^{3+} doping concentration and reaches a maximum at x = 0.40 and decreases thereafter. As discussed in the structural analysis, Eu^{3+} ions replace the Gd^{3+} ions is probable to have low inversion symmetry. The possibility of next nearest neighbor for Eu^{3+} ion with different doping concentrations can be assumed as: Gd^{3+} - O^{2-} - Eu^{3+} - O^{2-} - Gd^{3+}; Zn^{2+} - O^{2-} - Eu^{3+} - O^{2-} - Zn^{2+}; and Gd^{3+} - O^{2-}- Eu^{3+} - O^{2-} - Zn^{2+}; Zn^{2+} - O^{2-}- Eu^{3+} - O^{2-} - Gd^{3+}; Gd^{3+} - O^{2-} - Zn^{2+} - O^{2-} - Eu^{3+}; etc. At higher doping level, the local environment of Eu^{3+} to the nearest neighbor changes. Since three types of cations occupies in the same lattice site, Eu^{3+} loses its site symmetry and enhanced the hypersensitive transitions. The Eu^{3+} ion transition probability depends on the polarization of the electron density around the O^{2-} anions towards or away from the Eu^{3+} ion. The anion (O^{2-}) polarizability in turn depends on the ionic radii and electronegativity of host cations. Moreover, the anion polarizability decreases with increasing electronegativity of the surrounding cations. Considering the Pauling's electronegativity and ionic radii of the coordinating cations, we can realize that anion polarizability is highest in Gd and least in Zn. So, the oxygen electron density is more tightly bonded by Zn^{2+} ions than by the Gd^{3+} ions. The smaller and most electronegative Zn^{2+} ions attract the O^{2-} electron density towards them relative to the larger and least electronegative Gd^{3+} ions. Hence, when Eu^{3+} ions are incorporated into the host lattice,

the shift of the centre of electron density around O^{2-} ions will be higher in Gd^{3+} than Zn^{2+} ions. So the distance between the Eu^{3+} ion and the centre of electron density on the O^{2-} ion will be least in Gd^{3+} than Zn^{2+} ions. Thus, ligand polarizability and long range ordering influenced greatly on the emission probabilities and intensity.

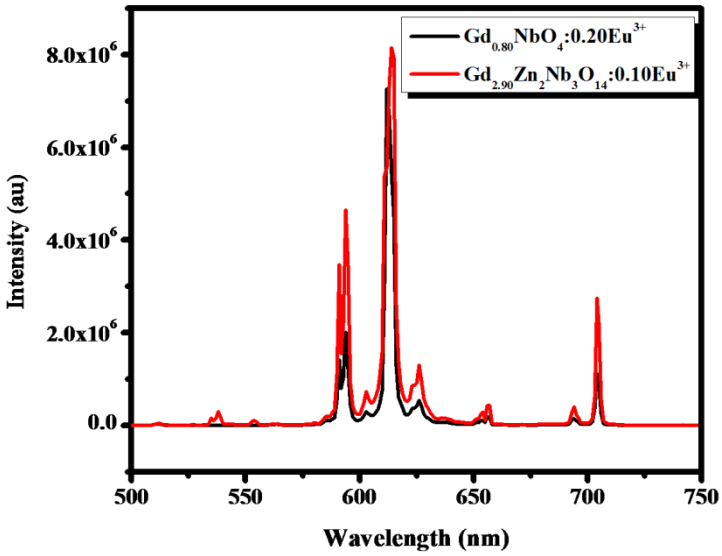

Fig. 6A.12 Comparison of emission spectra of $Gd_{0.80}NbO_4$:*0.20*Eu^{3+} and $Gd_{2.90}Zn_2Nb_3O_{14}$:*0.10*Eu^{3+} red phosphor under 392nm excitation.

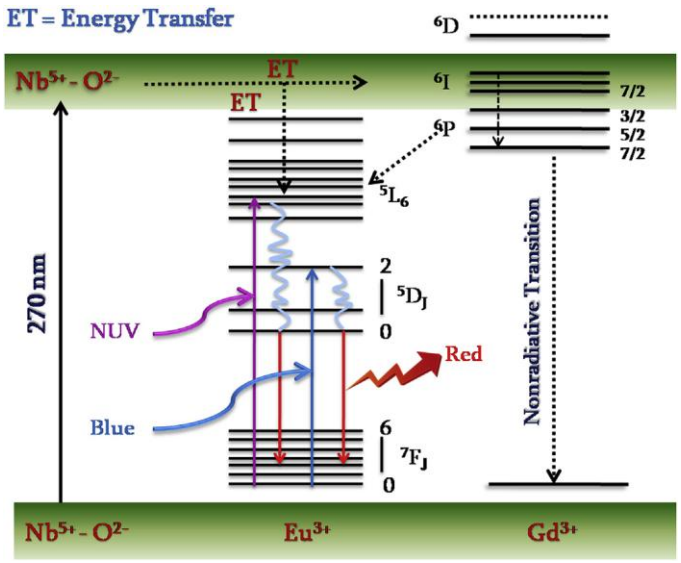

Fig. 6A.13 Model illustrating the energy transfer from NbO_4 group ($O^{2-} \rightarrow Nb^{5+}$ charge transfer band) to Gd^{3+} and Eu^{3+} ions.

The photoluminescence emission spectra of $Gd_{2.90}Zn_2Nb_3O_{14}$:*0.10*Eu^{3+} were compared with that of $Gd_{0.80}NbO_4$:*0.20* Eu^{3+} under the same experimental conditions and equating the same Eu^{3+} concentrations (Fig. 6A.12). It can be clearly seen that the emission intensity gets improved by the Zn^{2+} addition. This result indicates that the introduction of Zn^{2+} into $GdNbO_4$ would perturb the symmetry of the matrix. Hence, we can conclude that the enhanced electric dipole transition intensity arises from the symmetry distortion of Eu^{3+} ions in the lattice. The distortion of the A site symmetry and the red shift of the charge transfer energy leads to an intense $^5D_0$ - $^7F_2$ hypersensitive electric dipole transition under 392 nm excitation. The emission from higher energy was attributed to the low energy vibration of NbO_4^{3-} groups. The multiphonon relaxation by NbO_4^{3-} groups was not able to overpass the gap between the higher energy levels ($^5D_1$, $^5D_2$ and $^5D_3$) and the $^5D_0$ level of Eu^{3+} ion completely, which results in emission from these higher energy levels.

A simple model illustrating the energy transfer from NbO_4 group ($O^{2-} \rightarrow Nb^{5+}$ charge transfer band) to Gd^{3+} and Eu^{3+} ions, the concentration quenching of Gd^{3+}, and the characteristic emission of Eu^{3+} in $Gd_3Zn_2Nb_3O_{14}$ is shown in Fig. 6A.13. For the $Gd_{3-x}Zn_2Nb_3O_{14}$:*x*Eu^{3+} sample, under UV light excitation, the NbO_4 absorb UV efficiently, and a charge transfer from O^{2-} ligand to Nb^{5+} metal ion occurs. After the excitation, the excitation energy is transferred from the NbO_4 group ($O^{2-} \rightarrow Nb^{5+}$ charge transfer band) to Gd^{3+} ion; the energy migrates over the Gd^{3+} sublattice until it is trapped by Eu^{3+} ion and gives its characteristic red emission. Since the energy level difference of ^6G_J and ^6P_J of Gd^{3+} is close to that of $^7F_1$ and $^5D_0$ states of Eu^{3+}, the Gd^{3+} in ^6G_J state can excite Eu^{3+} from $^5D_0$ state by resonance energy transfer, which results in energy transfer from Gd^{3+} to Eu^{3+}. In addition to this, the presence of the absorption due to NbO_4^{3-} ions in the excitation spectra for Eu^{3+} emission further indicates the efficient energy transfer to the Eu^{3+} ions. It is also evidenced in the emission spectra where no emission from NbO_4^{3-} could be detected revealing the highly efficient non-radiative energy transfer from the NbO_4^{3-} ions to Eu^{3+} ions.

To gain more insight into the change of the Eu^{3+} structural surroundings, we have calculated the ratio of integrated emission intensities of electric and magnetic

dipole transitions. The variation of asymmetry ratio with Eu^{3+} ion concentration is tabulated in Table 6A.2 which decreases up to x = 0.40 and thereafter increases. Also, the asymmetry ratio of $Gd_{3-x}Zn_2Nb_3O_{14}$:$x$$Eu^{3+}$ is more than that of pure $Gd_{0.80}NbO_4$:*0.20*Eu^{3+} phosphor, which is another confirmation for the symmetry distortion caused by the Zn^{2+} addition in the lattice. Usually, a lower symmetry of the crystal field around Eu^{3+} leads to larger asymmetry ratio. The more severe distortion ensures stronger photoluminescence emission, which may result in high color purity. The full width half maximum (*fwhm*) of the red emission calculated from the emission spectrum is ~3.50 nm. Such narrow band emission enables the high color purity of $Gd_3Zn_2Nb_3O_{14}$:Eu^{3+} phosphor and helps to improve the luminous efficiency of the radiation since the emitted light is concentrated mainly in the visible spectral region to which the human eye is sensitive. The high symmetry around the activator site with high coordination number and with the same distance between the activator and ligand is required for reducing the inhomogeneous emission broadening. The rigid and ordered network decreases the nonradiative relaxation and will finally lead to a sufficiently narrow band red emitting phosphors.

The photoluminescence decay curves of the samples also reveal the dependence of the activator concentration on photoluminescence properties and the decay time could provide vital information of the concentration quenching in the energy transfer process. The fluorescence decay lifetime measurements for Eu Eu^{3+} emission λ_{exc} = 392 nm, λ_{em} = 613 nm) with increasing Eu^{3+} concentration is shown in Fig. 6A.14. The decay curves can be well fitted using a first order exponential function as given by, $I = Aexp(-t/\tau)$, where I is the intensity at time t, A is the fitting parameter and τ is decay lifetime. The single decay time indicates the uniform chemical environment of Eu^{3+} ion in the matrix. It can be seen that the lifetime value obtained from the decay curves increases monotonically and reaches a maximum at x = 0.40 and then rapidly decreases with further increasing the Eu^{3+} concentration. The decrease in lifetime value indicates the occupation of Eu^{3+} at a more distorted environment in the A site (Zn^{2+} ion site) at higher doping concentration as evidenced form XRD studies. Usually, a decrease in decay value is observed when site distortion occurs and the decay lifetimes (τ) are proportional to

the transition probability. The lower photoluminescence efficiency (Table 6A.2) of the as-prepared phosphors strongly indicate that there should be significant structural distortion in the lattice with Eu^{3+} doping which could result in changes of the matrix phonon energy.

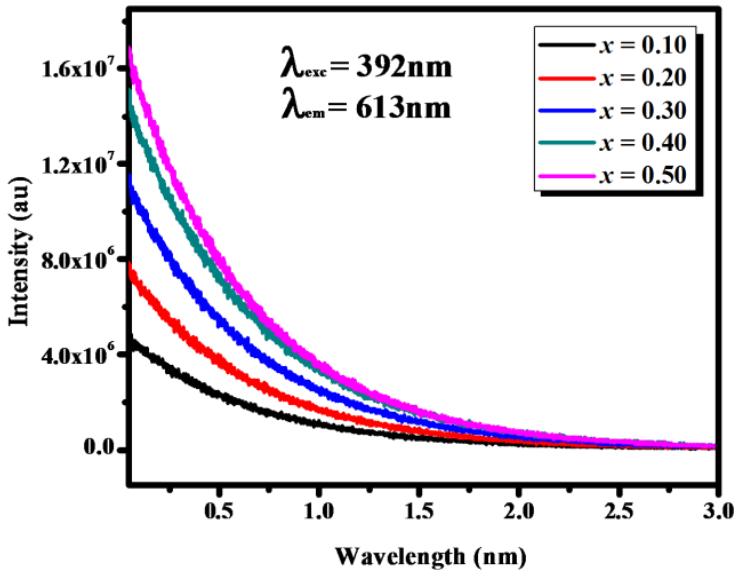

Fig. 6A.14 The fluorescence decay curves of $Gd_{3-x}Zn_2Nb_3O_{14}:xEu^{3+}$ (x = 0.10, 0.20, 0.30, 0.40 and 0.50) phosphors under 392 nm excitation.

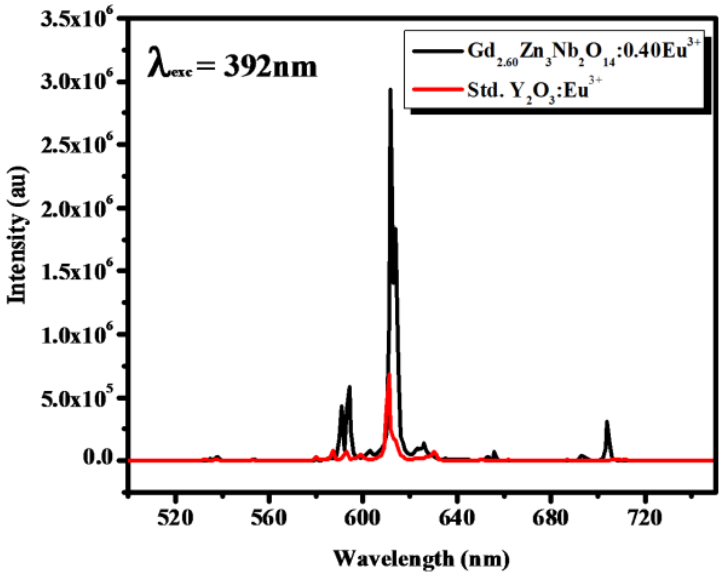

Fig. 6A.15 Comparison of emission spectra of $Gd_{2.60}Zn_2Nb_3O_{14}:\mathit{0.40}Eu^{3+}$ phosphor with the commercial red phosphor under 392nm excitation.

To demonstrate the application of red phosphor in white pc- LEDs, we have compared the emission spectra of $Gd_{2.60}Zn_2Nb_3O_{14}$:*0.40*Eu^{3+} phosphor with the commercially available red phosphor (Y_2O_3:Eu^{3+}) from Sigma Aldrich under the same experimental measurement conditions and with almost equal mole percentage of Eu^{3+} ions. From Fig. 6A.15, it is found that the relative emission intensity of $^5D_0$-$^7F_2$ transition for the $Gd_{2.60}Zn_2Nb_3O_{14}$:*0.40*Eu^{3+} phosphor is 3.9 times higher than that of commercial one under the 392 nm excitation (Hao *et al*. 2009; Dhanaraj *et al*. 2001; Liu *et al*. 2011). All of these results demonstrate the developed phosphor is a good red supplement for pc-LED applications.

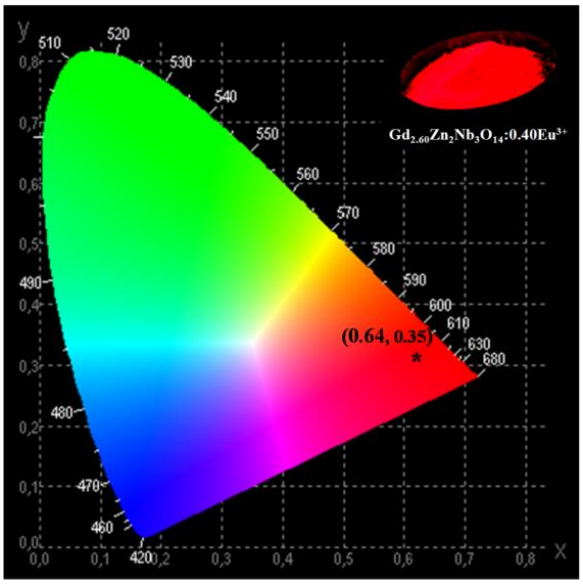

Fig. 6A.16 The CIE chromaticity coordinate diagram of the $Gd_{2.60}Zn_2Nb_3O_{14}$:*0.40*Eu^{3+} red phosphor. The inset shows the digital photograph of the $Gd_{2.60}Zn_2Nb_3O_{14}$:*0.40*Eu^{3+} phosphor under the 392 nm excitation**.**

The color of light can be described by chromaticity coordinates on a Commission International d'Eclairage (CIE) chromaticity diagram. The CIE chromaticity coordinates were calculated using the CIE color calculator software to understand the actual emission color of the developed phosphor. Fig. 6A.16 exhibits the CIE chromaticity coordinates and the luminescence digital photograph of the $Gd_{2.60}Zn_2Nb_3O_{14}$:*0.40*Eu^{3+} phosphor under the excitation of 392 nm. The color coordinates calculated on the basis of the corresponding emission spectrum is (0.64, 0.35), which is very close to the

standard coordinates (0.67, 0.33) form National Television Standard Committee (NTSC), signifying the high color purity of the as prepared phosphors. Thus, the tuning of red emission color is achievable by the change of Eu^{3+} ions concentration in the $Gd_3Zn_2Nb_3O_{14}$ host lattice.

The correlated color temperature (CCT), a characteristic property of visible light was calculated using the McCamy empirical formula (McCamy *et al*. 1992):

$$CCT\ (x, y) = -449n^3 + 3525n^2 - 6823.3n + 5520.33 \quad (6A.1)$$

where $n = (x - x_e)/(y - y_e)$. In this (x, y) represents the CIE color coordinates, and (x_e, y_e) = (0.3320, 0.1858), is the epicenter of convergence of isotemperature lines in the 1931 CIE chromaticity diagram and n is the reciprocal of slope of the line connecting (x, y) and (x_e, y_e). The calculated CCT values were found to vary from 2064 to 2566 K. Generally, CCT values less than 5000 K indicate the warm white light used for home appliances. Since the obtained CCT values are below 3000 K, the current phosphor may be suitable for use in warm white light emitting diodes and solid state lighting applications.

Table 6A.2 Optical properties of the Eu^{3+} doped narrow red phosphors $Gd_3Zn_2Nb_3O_{14}$ for pc-WLEDs

x	**Asymmetric Ratio**	***fwhm* (nm)**	**Life time (ms)**	**Efficiency (%)**	**Color Coordinates (*x*, *y*)**	**CCT (K)**	**Color Purity (%)**
0.10	5.19	3.43	0.63	20.17	(0.59, 0.34)	2064	76.3
0.20	5.17	3.43	0.64	20.41	(0.62, 0.34)	2419	85.2
0.30	4.85	3.45	0.64	20.82	(0.63, 0.35)	2302	88.3
0.40	4.66	3.50	0.65	21.07	(0.64, 0.35)	2439	91.2
0.50	4.96	3.49	0.62	20.24	(0.65, 0.35)	2566	94.2

The evaluation of color purity for the emitting color is important for the narrow banded light sources to study the effect of Eu^{3+} incorporation. The color purity of phosphors was calculated using the equation (Wu *et al.* 2012):

$$\text{Color purity} = \sqrt{\frac{(x-x_i)^2 + (y-y_i)^2}{(x_d-x_i)^2 + (y_d-y_i)^2}} \times 100 \qquad (6A.2)$$

where (x, y) are the color coordinates of the sample, (x_i, y_i) are the chromaticity coordinates of white illuminant (0.333, 0.333), and (x_d, y_d) are the coordinates of the dominant wavelength in the emission. Here, the wavelength corresponding to $^5D_0$ - $^7F_2$ transition is taken as the dominant one and hence in the present study (x_d, y_d) = (0.67, 0.33). As Eu^{3+} concentration increased from x = 0.10 to x = 0.50, the color purity was observed to increase from 76.3 to 94.2% which indicate the enhanced color purity of red emission. All these results show that the developed red phosphors with high color purity have promising application in solid-state lighting for general illumination.

6A. 4 Conclusions

In summary, a series of Eu^{3+} ions activated narrow band red emitting phosphors $Gd_{3-x}Zn_2Nb_3O_{14}$:xEu^{3+} were prepared via conventional solid state reaction method and investigated the influence of partial occupation of Zn^{2+} ions on both A and B site of the fergusonite type structure on the photoluminescence properties. The structural analysis establishes that these oxides belong to monoclinic phase with space group C2/c and exhibits similar phase as that of pure $GdNbO_4$. From the XRD, XPS and luminescence property analysis, we can conclude that the doped Eu^{3+} ions occupy the Gd^{3+}/Zn^{2+} ions site (A site). The incorporation of Eu^{3+} ions induces structural disorder in the lattice reducing the symmetry and enhanced the electric dipole transition intensity. The more severe distortion ensures stronger photoluminescence emission, which may result in high color purity. The full width half maximum (*fwhm*) of the red emission was ~3.50 nm. Such narrow band emission enables the high color purity of $Gd_3Zn_2Nb_3O_{14}$:Eu^{3+} phosphor and helps to improve the luminous efficiency of the radiation since the emitted light is concentrated mainly in the visible spectral region to

which the human eye is sensitive. The rigid and ordered network of this structure decreases the nonradiative relaxation and will finally lead to a sufficiently narrow band red emitting phosphors. Thus, the developed narrow-band red phosphor with high color qualities and warm white CCT of 2600 K is a good candidate for fabricating highly reddish pc-LEDs.

Chapter 6B

INTENSE NARROW-BAND RED EMITTING PHOSPHORS IN Eu^{3+}- ACTIVATED NIOBATE SYSTEM FOR NEXT GENERATION WHITE LEDs

A highly efficient narrow-band red emitting Eu^{3+} activated $Y_3Mg_2Nb_3O_{14}$ phosphor with high color purity were prepared via the traditional high-temperature solid state reaction route. They exhibit intense narrow-band red emission peaking at 613 nm under near-UV excitation. The color purity of the phosphor could achieve 92.4% ascribing to the narrow full width half maximum (fwhm ~ 4 nm). The emission intensity of as-prepared phosphor was found to be 9.4 times higher than the commercial red phosphor under the 392 nm excitation. Because of the intriguing red luminescence, phosphors exhibit remarkable CIE chromaticity coordinates (0.63, 0.35), good CCT values and high color purity (92.4%) makes them a promising prospect for use in the fabrication of high power WLEDs.

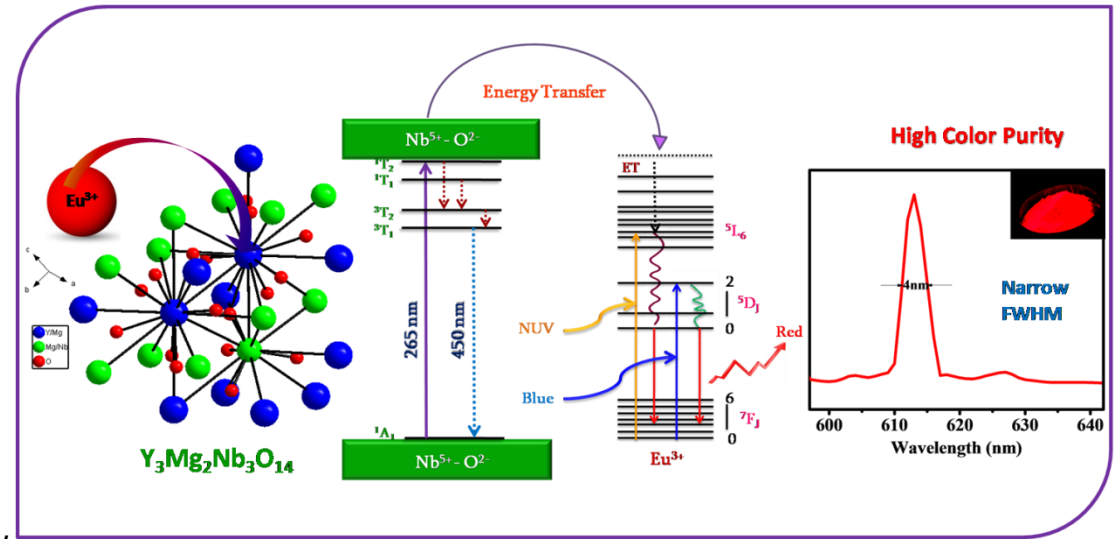

Sreena *et al.* (Communicated)

6B. 1 Introduction

A narrow-band red emitting phosphors with high optical properties such as high quantum yield, appropriate peak wavelength, narrow full width half maximum (*fwhm*) and high color purity are to be explored to meet the next generation high power white light emitting diodes. The peak position and *fwhm* of the red emission spectrum critically depends on the crystal structure, crystal rigidity, local symmetry and available number of sites for activator ions (Huang *et al*. 2014, Pust *et al*. 2014, and Takeda *et al*. 2015). Therefore, to design a narrow-band red phosphor, a rigid and ordered network is very important which can significantly decrease the non-radiative relaxation process and reduce the bandwidth. In this scenario, a series of Eu^{3+} doped narrow-emitting red phosphors were developed since its luminescence is very sensitive to the local environment and the crystal symmetry. Moreover, since the band gap between the $^5D_0$ level and the peak ground state multiplets (^7F_J) level is very high, they can give intense narrow red emission (Katelnikovas *et al*. 2012, Tanner *et al*. 2013 and Blasse *et al*. 1969). Nevertheless the Eu^{3+} activated phosphors show low absorption in blue or near-UV light due to their parity-forbidden 4f-4f transitions. The absorption of Eu^{3+} ions can be increased by selecting a suitable host lattice that has broad and intense charge transfer band and is therefore capable of efficiently absorbing the emission from InGaN-based LEDs.

Lanthanide niobates, particularly $YNbO_4$ with fergusonite structure have been widely investigated by many researchers due to their interesting physical properties such as high dielectric constant, photocatalytic behavior and photoluminescence and excellent thermal and chemical stability (Choi *et al*. 2012). $YNbO_4$, a well-known self-activated phosphor shows an efficient blue emission under excitation with UV light which is associated with the NbO_4^{3-} groups in the host crystalline lattice (Blasse *et al*. 1970, Blasse *et al*. 1976). Such luminescent emissions could be shifted towards longer wavelength when rare-earth ions replace partially Y^{3+} ions in the host crystalline lattice. When rare-earth ions are doped into the $YNbO_4$ host, there is some degree of coupling between the NbO_4^{3-} groups and the rare-earth ions. Eu^{3+} ions exhibit strong coupling with NbO_4^{3-} groups and show bright red emission. There are many research works

related to the Eu^{3+} emission in $YNbO_4$ (Liu *et al*. 2014, Hirano *et al*. 2014, Nazarov *et al*. 2010, Lu *et al*. 2015 and Lee *et al*. 2010). To improve the luminescent properties of Eu^{3+} in $YNbO_4$ host lattice, we attempted to incorporate some aliovalent cation without altering the monoclinic fergusonite crystal structure. As discussed in chapter 6A, luminescence properties of $GdNbO_4$ can be improved the by substituting Zn^{2+} ions on the part of Gd^{3+} ions. In the present study, an attempt has been made to enhance the luminescence properties of $YNbO_4$ by incorporating Mg^{2+} ions to obtain the host lattice of the general formula $Y_3Mg_2Nb_3O_{14}$. These phosphors exhibit intense narrow-band red emission peaking at 613 nm. Furthermore, the color purity of the $Y_{3-x}Mg_2Nb_3O_{14}$:$x$$Eu^{3+}$ phosphor could achieve 92.4% ascribing narrow *fwhm* (~ 4 nm). The distortion of the A site symmetry caused by the incorporation of Mg^{2+} ions in $YNbO_4$ and the red shift of the charge transfer band leads to intense narrow red emission.

6B. 2 Experimental Section

6B. 2.1 Synthesis

$Y_{3-x}Mg_2Nb_3O_{14}$:$x$$Eu^{3+}$ (x = 0, 0.10, 0.20, 0.30, 0.40 and 0.50) phosphors were prepared via conventional solid-state method using Y_2O_3, MgO, Nb_2O_5, and Eu_2O_3 (99.99% purity; Sigma-Aldrich, Germany) as the starting materials. The chemicals taken in the required stoichiometric ratios were mixed thoroughly in an agate mortar using acetone as the wetting reagent. These products were calcined at 1500°C for 6 h with intermittent grinding until a phase pure compound was obtained. The calcined product was then ground into a fine powder for carrying out further characterizations.

6B. 2.2 Characterization

The powder X-ray diffraction (XRD) analysis was carried out using a PANalytical X'pert Pro diffractometer. The particle size and morphology analysis of the samples were performed on a scanning electron microscope (JEOL, JSM-5600LV) with an acceleration voltage of 15kV. Energy dispersive analysis was carried out using a Silicon Drift Detector–X-Max^N attached with a Carl Zeiss EVO SEM. EDS elemental mapping was conducted using the Aztec Energy EDS Microanalysis Software. The absorbance study of

the samples was carried out using a Shimadzu, UV-3600 UV-Visible spectrophotometer using barium sulfate as a reference. The luminescence spectra of the prepared samples were obtained using a Fluorolog HORIBA fluorescence spectrophotometer with a Xenon lamp (450W) as the excitation source. The luminescence lifetime of the phosphors was recorded using the phosphorimeter attached to a Fluorolog®3 spectrofluorimeter.

6B. 3 Results and discussion

6B. 3.1 Structural Analysis

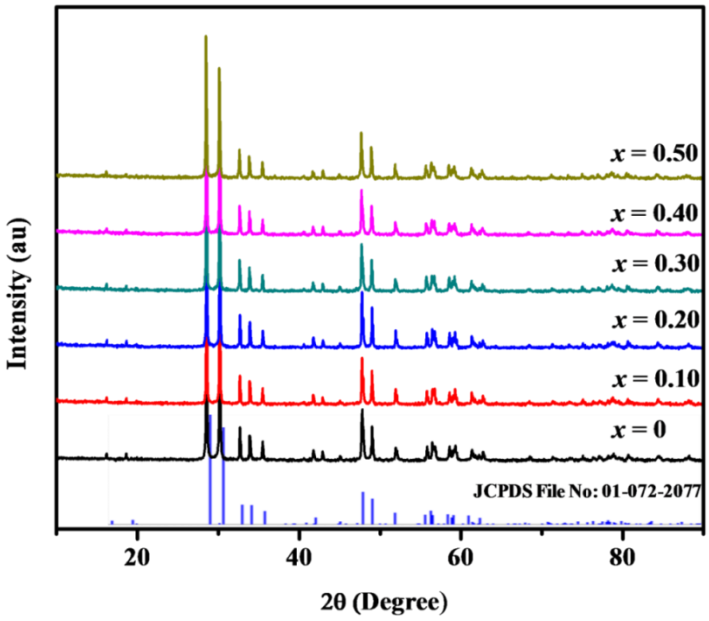

Fig. 6B.1 Powder XRD patterns of $Y_{3-x}Mg_2Nb_3O_{14}$:xEu^{3+} (x = 0, 0.10, 0.20, 0.30, 0.40 and 0.50) and the reference pattern of $YNbO_4$ (JCPDS File No. 01-072-2077).

Powder XRD patterns of $Y_{3-x}Mg_2Nb_3O_{14}$:xEu^{3+} (x = 0, 0.10, 0.20, 0.30, 0.40 and 0.50) phosphors are shown in Fig. 6B.1. It is evident from the figure that all the samples exhibit highly crystalline behavior with monoclinic fergusonite type structure. The entire diffraction peaks match well with the pure phase of $YNbO_4$ (JCPDS File No. 01-072-2077) with a space group C2/c. It is worth noting that no impurity peaks were detected even when x reaches up to 50mol% suggesting that the doping of Eu^{3+} ions into the $Y_3Mg_2Nb_3O_{14}$ system does not induce any significant changes in the crystal structure. This indicates that Eu^{3+} ion is completely dissolved in the $Y_3Mg_2Nb_3O_{14}$ host

lattice. In the $Y_3Mg_2Nb_3O_{14}$ system, one is an eight coordinated site, which is occupied by Y^{3+}/Mg^{2+} and another is a six-coordinated site, which is occupied by Nb^{5+}/Mg^{2+} ions. It means that Mg^{2+} ion is a random distribution in these two sites as shown in Fig. 6B.2. According to crystal chemistry principle, the site neutrality can be achieved by the distribution of Mg^{2+} cations over these two sites, allowing some excitability into this geometrically rigid structure. The disordered cation distribution provides local electrical neutrality in the structure and stabilization. The partial occupation of the Mg^{2+} ion on both A and B sites induce significant local lattice distortion makes the system in a disordered state reducing the symmetry which is reflected in the emission spectra. To investigate the evolution of emission spectra with the partial occupation of the Mg^{2+} ion on both A and B sites on the photoluminescence properties, Eu^{3+} ions were doped into system. Based on the similar effective ionic radius and valence state, Eu^{3+} ions are expected to substitute the Y^{3+} lattice positions (A site) in the $Y_3Mg_2Nb_3O_{14}$ system. However, since the A site is occupied by Y^{3+} and Mg^{2+} ions, from the structural analysis it is difficult to make an assumption about the site of occupation of Eu^{3+} ions. From the luminescence studies discussed in later part, we conjecture that the doped Eu^{3+} ions will occupy the Y^{3+} site upto 40mol% and on further substitution it prefers to occupy the Mg^{2+} ion site to keep up the charge neutrality. Nevertheless, substitution of Eu^{3+} ions in Y^{3+}/Mg^{2+} sites results in the increase of cell volume as the ionic radius of Eu^{3+} ion is greater than that of Y^{3+} or Mg^{2+} ions and the values are given in Table 6B.1. This is reflected in the shift of diffraction peaks to the lower angles with increasing the doping concentration of Eu^{3+} ion. On comparing the lattice parameter and cell volume of $Y_3Mg_2Nb_3O_{14}$ with that of parent compound $YNbO_4$, we can see that the cell volume decreases with the introduction of Mg^{2+} ion due to the lower ionic radius of Mg^{2+} than Y^{3+} ion. Moreover, the average crystallite size of the samples calculated from Debye-Scherrer equation (Langford *et al*. 1978) shows a sudden decrease after 40mol% of Eu^{3+} doping which may be due to the variation in the site of occupation of the Eu^{3+} ion. To confirm the structure, we performed Rietveld structure refinement of all the samples using powder X-ray diffraction data through the X'pert Highscore Plus software. A pseudo-Voigt profile function was used to fit the XRD pattern. The observed, calculated and difference Rietveld refinement XRD pattern of $Y_{2.90}Mg_2Nb_3O_{14}$:*0.10*Eu^{3+} phosphor is

shown in Fig. 6B.3, and the main parameters from the processing and refinement of data are presented in Table 6B.1. The measured positions are in good agreement with Rietveld fitting, and the data given in the JCPDS file and the final results display a good quality of refinement.

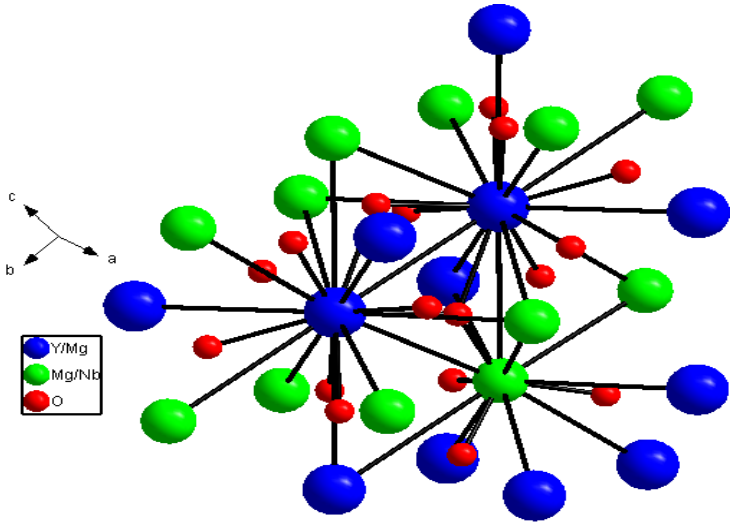

Fig. 6B.2 Schematic illustration of the monoclinic fergusonite type structure and the coordination environment of $Y_3Mg_2Nb_3O_{14}$ host lattice.

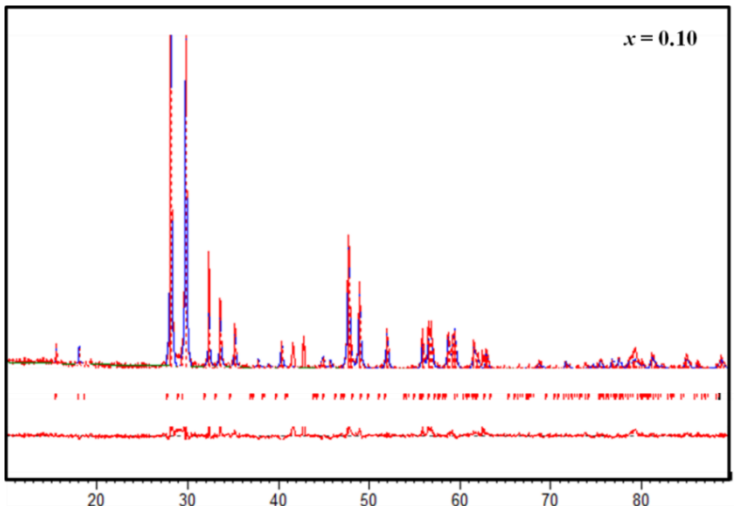

Fig. 6B.3 The observed, calculated and difference Rietveld refinement XRD pattern of $Y_{2.90}Mg_2Nb_3O_{14}$:*0.10*Eu^{3+} phosphor

Table 6B.1 Refined parameters obtained from the Rietveld analysis of $YNbO_4$ and $Y_{3-x}Mg_2Nb_3O_{14}$:xEu^{3+} (x = 0, 0.10, 0.20, 0.30, 0.40 and 0.50) phosphors.

Sample	**$YNbO_4$**	***x* = 0**	***x* = 0.10**	***x* = 0.20**	***x* = 0.30**	***x* = 0.40**	***x* = 0.50**
Crystal System	Monoclinic	Monoclinic	Monoclinic	Monoclinic	Monoclinic	Monoclinic	Monoclinic
Space group	C2/c (15)	C2/c (15)	C2/c (15)	C2/c (15)	C2/c (15)	C2/c (15)	C2/c (15)
Cell parameters							
a (Å)	7.0370(4)	7.0239(5)	7.0445(7)	7.0474(7)	7.0495(8)	7.0519(8)	7.0554(9)
b (Å)	10.9450(8)	10.9305(1)	10.959(1)	10.964(1)	10.971(2)	10.976(2)	10.980(2)
c (Å)	5.2980(3)	5.2871(5)	5.3021(6)	5.3051(6)	5.3062(7)	5.3097(7)	5.3129(8)
β (°)	134.083(3)	134.091(4)	134.108(5)	134.123(5)	134.124(6)	134.134(6)	134.149(7)
Cell Volume (Å³)	293.1800	292.1800	293.90590	294.25800	294.58910	294.96320	295.32770
Crystallite size, (nm)	42.57	42.57	51.06	51.06	51.06	63.85	42.56
Flat background	70.7356	68.2543	67.1886	67.5063	67.9100	67.1161	67.5097
Coefficient 1	-21.6684	-20.2977	-20.6865	-21.1324	-22.0082	-21.3333	-22.0328
Coefficient 2	21.5658	19.6900	20.8473	23.6397	23.1438	24.1227	24.4889
Scale factor	0.000095	0.000147	0.000139	0.000132	0.000126	0.000114	0.000104
R-Parameters							
Rexp(%)	9.20	9.31	9.362	9.39	9.42	9.54	9.569
Rp(%)	12.12	12.86	12.82	11.99	11.53	11.29	11.45
Rwp(%)	16.32	17.97	17.42	16.89	15.70	15.54	15.25
GOF	3.15	3.73	3.46	3.23	2.78	2.65	2.54

6B. 3.2 Morphological Analysis

It is well-known that luminescence intensity is closely related to the morphology of phosphor particles. The SEM images of $Y_{3-x}Mg_2Nb_3O_{14}$:xEu^{3+} (x = 0, 0.10, 0.20, 0.30, 0.40 and 0.50) phosphors shown in Fig. 6B.4, clearly presents an irregular morphology with a size range of 1-3μm. A slight agglomeration of these phosphor particles could also be observed. Moreover, the SEM-EDS analysis of $Y_{2.60}Mg_2Nb_3O_{14}$:*0.40*Eu^{3+} phosphor shown in Fig. 6B.5 makes evident that the sample contains Y, Mg, Nb, O and Eu elements and the average chemical composition is very close to the theoretical one. X-ray dot mapping images of typical $Y_{2.60}Mg_2Nb_3O_{14}$:*0.40*Eu^{3+} phosphor shown in Fig. 6B.6 demonstrates that all the elements are evenly distributed in the whole sample. These results are consistent with the XRD results which further confirm the formation of pure $Y_3Mg_2Nb_3O_{14}$ phase.

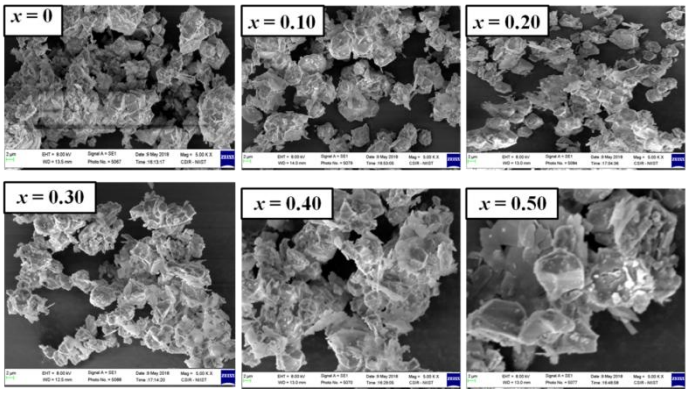

Fig. 6B.4 SEM images of $Y_{3-x}Mg_2Nb_3O_{14}$:xEu^{3+} (x = 0, 0.10, 0.20, 0.30, 0.40 and 0.50) red phosphors.

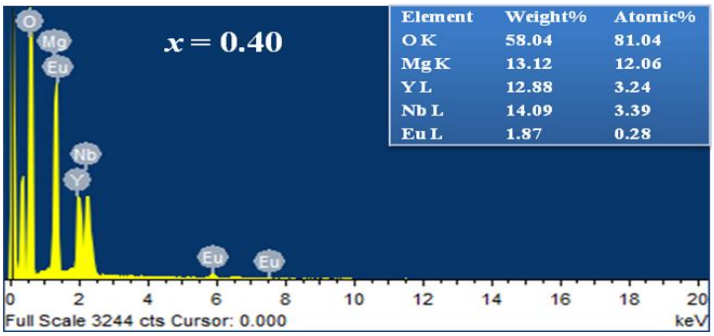

Fig. 6B.5 SEM EDS spectra of typical $Y_{2.60}Mg_2Nb_3O_{14}$:*0.40*Eu^{3+} red phosphor.

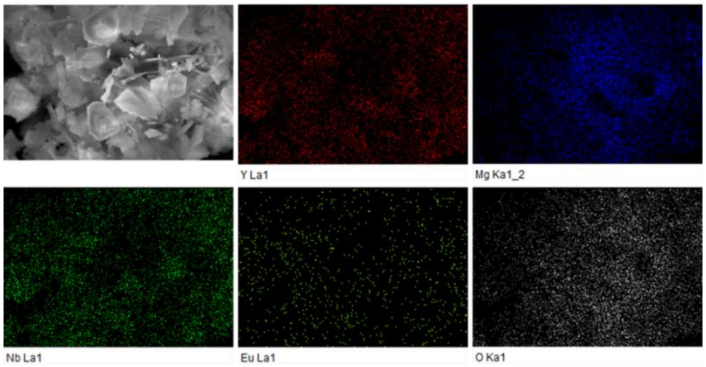

Fig. 6B.6 Elemental X-ray dot mapping of the typical $Y_{2.60}Mg_2Nb_3O_{14}$:*0.40*Eu^{3+} red phosphor calcined at 1500°C.

6B. 3.3 Optical studies

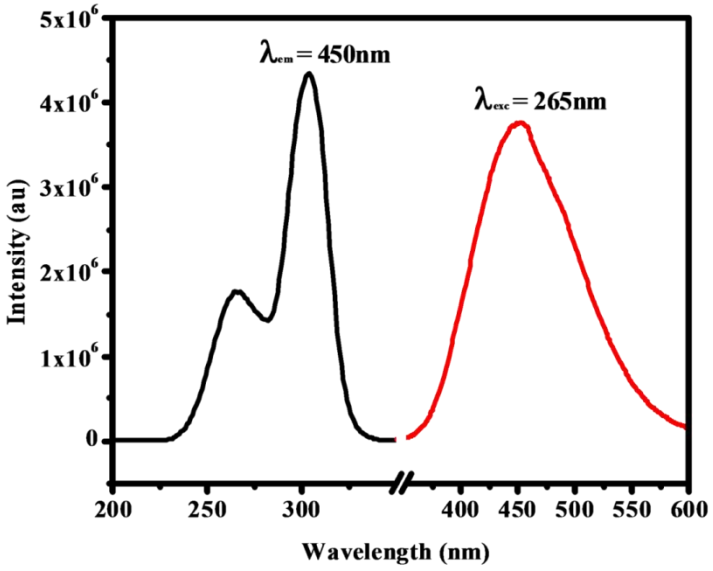

Fig. 6B.7 Photoluminescence excitation and emission spectra of parent compound $YNbO_4$ under the 265 nm excitation monitoring at 450 nm emission.

$YNbO_4$ itself is a self-activated phosphor which exhibits blue emission upon UV or X-ray excitation. Fig. 6B.7 shows the excitation and emission spectra of $YNbO_4$ sample for emission at 450 nm. The excitation spectra include a broad band from 200 to 350 nm with maxima at 265 and 300 nm. These two bands are attributed to the charge transfer from O^{2-} ligands to empty 4d orbital of Nb^{5+} ions and the splitting of the charge transfer bands is due to the two-fold symmetry in the Nb octahedra. The excitation band corresponding to the $O^{2-} \rightarrow Nb^{5+}$ charge transfer transition is weak compared to that of Y^{3+} ion transition, which implies that considerable amount of energy absorbed by the NbO_4^{3-} group, is transferred to the Y^{3+} ions in the lattice. A strong blue emission is observed under the 265 nm excitation due to the transition from metal-ligand charge transfer state to the ground state of NbO_4^{3-} groups. The luminescence color of $YNbO_4$ can be tuned from blue to red by the substitution of Eu^{3+} ions in the Y^{3+} ion site. There are a few research works related to the photoluminescence and cathodoluminescence studies of RE ion doped $YNbO_4$ host lattice. In the present work, we tried to enhance the luminescence properties of Eu^{3+} ion doped $YNbO_4$ host lattice by introducing Mg^{2+} ions in the lattice to obtain the host lattice of the general formula $Y_3Mg_2Nb_3O_{14}$ and

investigate the influence of partial occupation of Mg^{2+} ions on A and B sites on the photoluminescence properties.

Fig. 6B.8 shows the excitation spectra of $Y_{3-x}Mg_2Nb_3O_{14}:xEu^{3+}$ (x = 0.10, 0.20, 0.30, 0.40 and 0.50) phosphors when monitoring the emission at 613 nm. The excitation spectra reveal two regions: a broad absorption band ranging from 220 to 350 nm with maxima at 263 and 318 nm and several narrow excitation peaks above 350 nm. The excitation band peaking at 263 nm is ascribed to the charge transfer from the $O^{2-} \rightarrow Nb^{5+}$ ions in the NbO_4^{3-} group, while the less intense peak at 318 nm is assigned to the charge transfer of $O^{2-} \rightarrow Eu^{3+}$ ions. The presence of the excitation peak of NbO_4^{3-} groups in the excitation spectra of Eu^{3+} implies the existence of effective energy transfer from the NbO_4^{3-} groups of the host to Eu^{3+} ions. The NbO_4^{3-} group can absorb the excitation energy through $O^{2-} \rightarrow Nb^{5+}$ charge transfer transition and transfer the excitation energy to Eu^{3+} ions which give characteristic red emission.

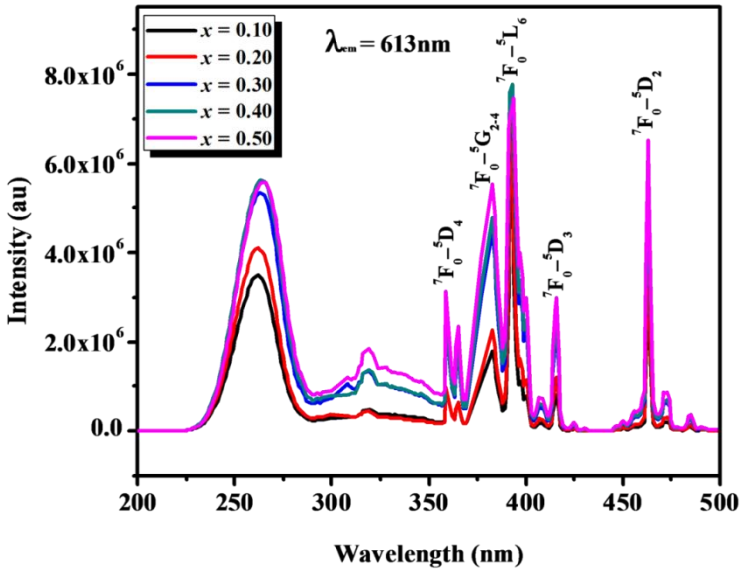

Fig. 6B.8 Photoluminescence excitation spectra of $Y_{3-x}Mg_2Nb_3O_{14}:xEu^{3+}$ (x = 0.10, 0.20, 0.30, 0.40 and 0.50) red phosphors.

It is worth noting that the CT band is red shifted with increasing the concentration of Eu^{3+} ions. This shift can be ascribed to the increase in covalency of Eu-O bond and the coordination environment of Eu^{3+} ions, which reduces the CT band

energy. In fact, the CT band position is closely associated with the coordination state of Eu^{3+} ions in the host lattice and the bond length of Eu^{3+} and anions (Hoefdraad *et al*. 1975). The energy of the lowest charge transfer absorption depends on the electronegativity difference between the $Eu^{3+} \rightarrow O^{2-}$ ligand and the $Eu^{3+} \rightarrow O^{2-}$ CT, with the lower absorption edge causing a small electronegativity difference between Eu^{3+} - O^{2-} ions. The red shift of the CT band might have contributed highly to the luminescence properties of the samples. The parity forbidden intraconfigurational f–f transitions of Eu^{3+} is also strengthened by borrowing intensity from the lowest strong absorption band (CT) by nonradiative energy transfer process. From the excitation spectra, we can see two intense peaks located at 392 and 463 nm which is the emission wavelength of near UV and blue LED chip respectively. This implies that the samples can effectively absorb UV and blue light. Furthermore, the UV visible absorption spectra of non-doped and Eu^{3+} doped phosphors were investigated by UV-visible absorption spectroscopy and illustrated in Fig. 6B.9.

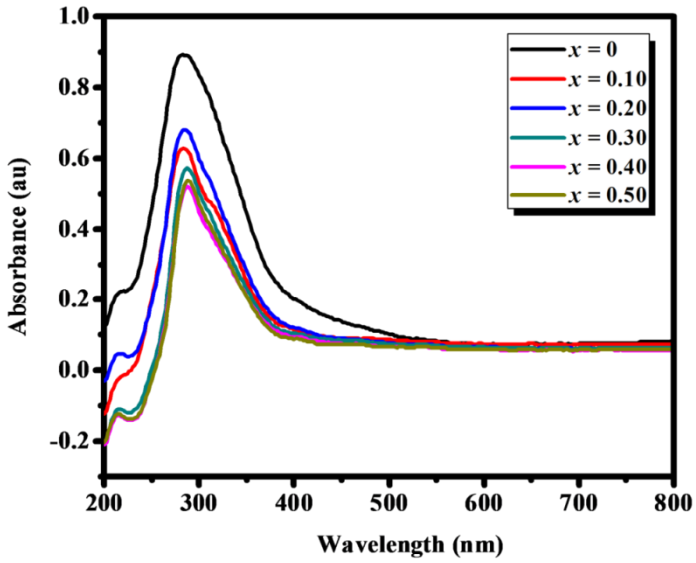

Fig. 6B.9 UV-visible absorption spectra of $Y_{3-x}Mg_2Nb_3O_{14}:xEu^{3+}$ (x = 0, 0.10, 0.20, 0.30, 0.40 and 0.50) red phosphors.

The absorption band at 280 nm can be assigned to the charge transfer transition from the oxygen ligand to the central niobate group in the host lattice, and this peak shifted towards lower wavelength side with increase in the concentration of Eu^{3+} ions,

which increases in the optical band gap of the material. It has been reported that the Y^{3+} ions will have some impact on the position of $O^{2-} \rightarrow Nb^{5+}$ CT band in $YNbO_4$ (Lee *et al*. 2001, Wiegel *et al*. 1995). The different electronic configuration and ionic radii will perturb the crystal structure, crystal field and CT band position of $Y_3Mg_2Nb_3O_{14}$ to some extent, which might lead to the blue shift of the absorption band. It can be seen that the intensity of absorbance for $Y_3Mg_2Nb_3O_{14}$ is greater than that of Eu^{3+} doped samples indicating the efficient energy transfer from the CT states to the Eu^{3+} ions.

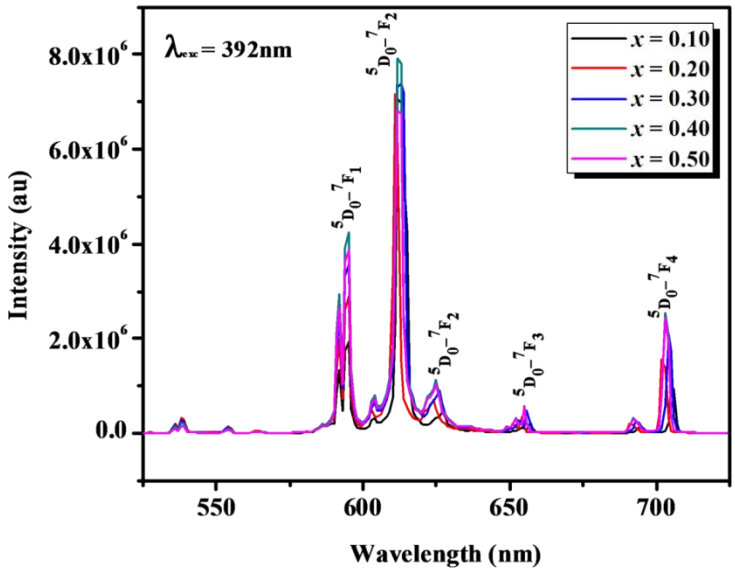

Fig. 6B.10 Photoluminescence emission spectra of $Y_{3-x}Mg_2Nb_3O_{14}$:xEu^{3+} (x = 0.10, 0.20, 0.30, 0.40 and 0.50) red phosphors under 392 nm excitation.

The emission spectra of $Y_{3-x}Mg_2Nb_3O_{14}$:xEu^{3+} (x = 0.10, 0.20, 0.30, 0.40 and 0.50) phosphors excited by 392 nm is shown in Fig. 6B.10. Typical emission lines of Eu^{3+} ions can be assigned to the optical transitions from the excited state $^5D_0$ to the ^7F_J levels (J = 0 - 4) of the $4f^6$ configurations of Eu^{3+} ions (Hsu *et al*. 1975). According to Judd-Ofelt theory, transitions to the even J-numbers have much higher intensity than those corresponding to the neighboring uneven J-numbers (Yan *et al*. 2009, Liu *et al*. 2006)). Also, $^5D_0 \rightarrow ^7F_J$ transition is very sensitive to the chemical environment around Eu^{3+} ions. When Eu^{3+} ion occupies a site with inversion symmetry in the crystal lattice, electric dipole transitions are strictly forbidden and allow only magnetic dipole transitions. If there is no inversion symmetry at the site of Eu^{3+} ion, the uneven crystal field

component can mix opposite parity states into the $4f^6$ configuration, and then electric dipole transition dominates. In the emission spectra, the intensity of the $^5D_0 \rightarrow ^7F_2$ transition is much higher than that of $^5D_0 \rightarrow ^7F_1$ transition which results in the high color purity of the as-prepared phosphors. This indicates that Eu^{3+} ions are situated on the noncentral symmetric site, which is in accordance with the crystal structure of the $Y_3Mg_2Nb_3O_{14}$ system. As mentioned in the structural analysis, the space group of the monoclinic fergusonite-type crystal structure is C2/c, which has no symmetric center. So, all the Eu^{3+} ions will occupy the noncentral symmetric C_2 site of Y^{3+} ion in the fergusonite crystal structure resulting in the intense red emission. It is observed that the luminescence intensity of red phosphors increased with increasing concentration of Eu^{3+} ions and saturated at 40 mol% doping. The enhanced electric dipole transition intensity arises from symmetry distortion caused by the incorporation of aliovalent cation like Mg^{2+} in the $YNbO_4$ lattice. The incorporation of cations with different valency and electronegativity in the crystal lattice can cause local structural distortion and modify the chemical environment around the Eu^{3+} ions, which can lead to the change in luminescence properties. As Eu^{3+} ion replaces Y^{3+} ion site for low concentrations, which has low inversion symmetry the intensity of forbidden electric dipole transition increases resulting in high color purity. However, at higher doping level the local environment around Eu^{3+} ion changes and it prefers to replace the Mg^{2+} ion in the A site for maintaining the charge neutrality and adversely affects the luminescence properties. Even though, to explore the influence of Mg^{2+} ion incorporation in the $YNbO_4$ lattice on the luminescence properties, we have compared the emission spectra of $Y_{0.80}NbO_4$:*0.20*Eu^{3+} and $Y_{2.60}Mg_2Nb_3O_{14}$:*0.40*Eu^{3+} red phosphor under 392 nm excitation (Fig. 6B.11). It is worth noting that the emission intensity gets improved by the introduction of the Mg^{2+} ion. This implies that the Mg^{2+} ion addition will perturb the symmetry of the matrix and enhance the f-f transition. Also, Mg^{2+} ions will increase the energy transfer from NbO_4 group to Eu^{3+} ions resulting in narrow red emission.

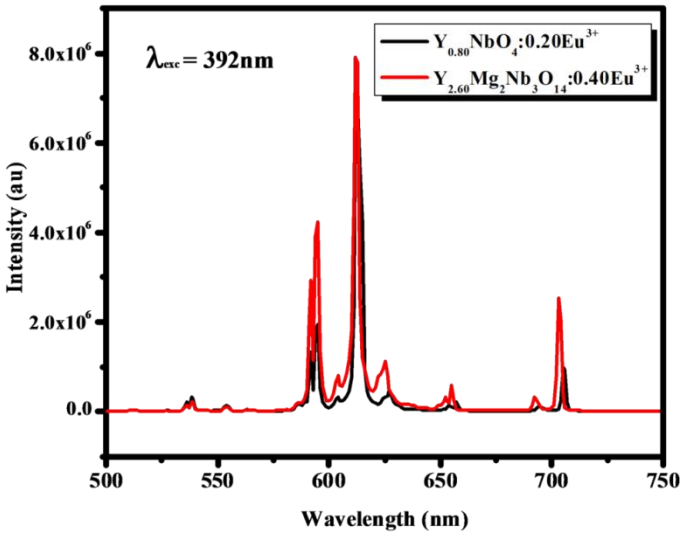

Fig. 6B.11 Comparison of the emission spectra of $Y_{0.80}NbO_4$:*0.20*Eu^{3+} and $Y_{2.60}Mg_2Nb_3O_{14}$:*0.40*Eu^{3+} red phosphor under 392 nm excitation.

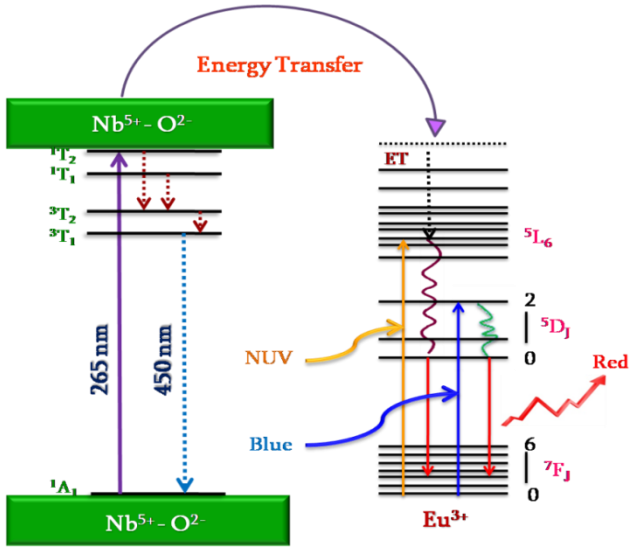

Fig. 6B.12 Schematic illustration of the energy transfer from NbO_4 group (O^{2-} - Nb^{5+} charge transfer band) to Eu^{3+} ions and the characteristic emission of Eu^{3+} ion in $Y_3Mg_2Nb_3O_{14}$ host lattice.

Schematic illustration of the energy transfer from NbO_4 group (O^{2-} - Nb^{5+} charge transfer band) to Eu^{3+} ions and the characteristic emission of Eu^{3+} ion in $Y_3Mg_2Nb_3O_{14}$ host lattice are shown in Fig. 6B.12. $YNbO_4$ exhibits self-activating luminescence under the 265 nm UV excitation due to the charge transfer transition from the O^{2-} ligand to

Nb^{5+} metal ion. The feasible excited states of Nb^{5+} are $^1T_1$, $^1T_2$, $^3T_1$ and $^3T_2$ and the ground state is $^1A_1$ (Jing *et al*. 1999). After excitation, transition from the excited state $^3T_1$ to the ground state $^1A_1$ occur and give its characteristic blue emission at around 450 nm. As Eu^{3+} ions are substituted in the $Y_3Mg_2Nb_3O_{14}$ host lattice, after excitation, the excitation energy can be nonradiatively transferred from the excited state of NbO_4 group ($O^{2-} \rightarrow Nb^{5+}$ charge transfer band) to the excited states of Eu^{3+} ions, resulting in their characteristic emission. The presence of absorption due to NbO_4^{3-} ions in the excitation spectra indicates the effective energy transfer from NbO_4 group to Eu^{3+} ions. This is also reflected in the emission spectra where no emission from NbO_4^{3-} ions could be detected which further confirm the efficient non-radiative energy transfer from NbO_4^{3-} ions to Eu^{3+} ions.

Magnetic dipole transition is relatively insensitive to the local environment around Eu^{3+} ions. However, it can be used as a standard to account for the ligand differences. The intensity ratio of the electric dipole transition to the magnetic dipole transition, called asymmetric ratio measures the symmetry of the Eu^{3+} surrounding (Kirby *et al*. 1983). Subsequently; we calculated the intensity ratio of the $^5D_0 \rightarrow ^7F_2$ transition (613 nm) to the $^5D_0 \rightarrow ^7F_1$ transition (595 nm) to study the symmetry of Eu^{3+} surroundings. The variation of asymmetric ratio with Eu^{3+} ion concentration is presented in Table 6B.2, which decreases with increasing Eu^{3+} doping. Also, the asymmetric ratio of $Y_{3-x}Mg_2Nb_3O_{14}$:$x$$Eu^{3+}$ red phosphor is more than that of $Y_{0.80}NbO_4$:*0.20*Eu^{3+} (Intensity ratio = 1.60), which is another indication for the symmetry distortion caused by the introduction of Mg^{2+} ions in the lattice. The severe distortion ensures stronger photoluminescence emission.

The full-width half maximum of the red emission peak (613 nm) calculated from the emission spectra were merely around 4 nm, which enables the high color purity of the developed phosphors. The remarkably narrow emission observed for $Y_3Mg_2Nb_3O_{14}$:Eu^{3+} may be mainly attributed to the rigid and ordered network of the fergusonite structure which decreases the non-radiative relaxation and leads to sufficiently narrow band emission. Such a rigid structure can induce weak electron-phonon interaction for the Eu^{3+} activator, which can significantly reduce the probability

of unwanted non-radiative relaxation processes in the excited Eu^{3+} ions and can also reduce the bandwidth. A small Stokes shift is necessary to reduce the *fwhm* of Eu^{3+} doped phosphors. It is reported that the differences in local coordination result in differences in peak wavelength and *fwhm* in luminescence. This implies that one type of cation crystallographic site is required to reduce the inhomogeneous line broadening effects caused by several different local crystal field environments (Hoppe *et al*. 2004, Oeckler *et al*. 2007, Kechele *et al*. 2009). In our system, the narrow emission peak is mainly attributed to the uniquely symmetric and ordered Eu^{3+} ion coordination environment.

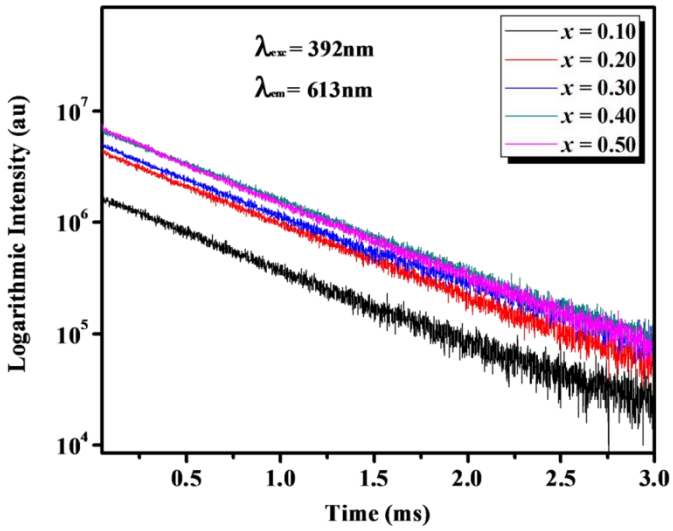

Fig. 6B.13 Decay curves of $Y_{3-x}Mg_2Nb_3O_{14}:xEu^{3+}$ (x = 0.10, 0.20, 0.30, 0.40 and 0.50) red phosphors upon monitoring at 613 nm under 392 nm excitation.

Although this phosphor exhibits narrow emission, to be useful, they must have high quantum efficiency. Hence, photoluminescence decay times were measured to assess the phosphor's quantum efficiency. Fig. 6B.13 shows the luminescence decay curves of all the samples obtained by monitoring the $^5D_0 \rightarrow {}^7F_2$ transition of Eu^{3+} at 613 nm. As shown, the decay curves can be well fitted to the single exponential function: $I = I_0 \exp(-t/\tau)$, where τ is the decay time. The decay lifetime corresponding to Eu^{3+} in $Y_3Mg_2Nb_3O_{14}$ host lattice was determined to be 0.67 ms and the single lifetime indicate that only one de-excitation process is present in this system. The lifetime of the $YNbO_4$

host emission was estimated to be 3.13μs. By comparing the decay lifetime of $YNbO_4$ host emission and the Eu^{3+} in the $Y_3Mg_2Nb_3O_{14}$ host, it is clear that lifetime of Eu^{3+} ions is much longer than that of $YNbO_4$ host emission. This result suggests that characteristic emission spectra of Eu^{3+} ion can appear in the host lattice independently. Moreover, the lifetime values of Eu^{3+} doped samples increases with Eu^{3+} concentration up to x = 0.40 and then decreases rapidly. The decrease in lifetime value at higher concentration indicates the occupation of Eu^{3+} ion in a more distorted environment in the A site (Mg^{2+} site) of the fergusonite structure. Normally, lifetime value decrease when site distortion occurs and the decay time is proportional to the transition probability. As mentioned in the structural analysis, Eu^{3+} ion probably prefers to replace Mg instead of Y at the A site for maintaining charge neutrality for higher substitution. The quantum efficiency calculated from the lifetime values (Table 6B.2) also follows the same trend as decay time i.e., quantum efficiency of Eu^{3+} ion excited state increases with Eu^{3+} doping and become maximum (37.22%) for 40 mol% Eu^{3+} doping. The obtained quantum efficiency value is comparable with the commercial $Y_3Al_5O_{12}:Ce^{3+}$ phosphor (Hou *et al*. 2012).

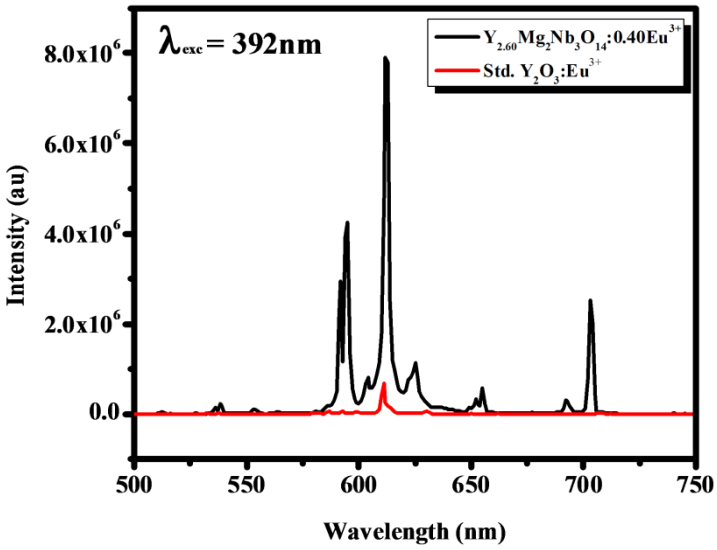

Fig. 6B.14 Comparison of the emission spectra of $Y_{2.60}Mg_2Nb_3O_{14}$:*0.40*Eu^{3+} phosphor with the commercial red phosphor under 392 nm excitation.

For the application in high powered WLEDs, we have compared the emission spectrum of $Y_{2.60}Mg_2Nb_3O_{14}$:*0.40*Eu^{3+} phosphor with the commercial red-emitter

Y_2O_3:Eu^{3+} (Sigma Aldrich) under the same experimental measurement conditions (Fig. 6B.14). The relative emission intensity of $Y_{2.60}Mg_2Nb_3O_{14}$:*0.40*Eu^{3+} phosphor was found to be 9.4 times higher than that of commercial one under the 392 nm excitation. These results demonstrate that the developed phosphor is a good candidate as a red phosphor for pc-LED applications.

The developed narrow-red emitting phosphor has another advantage that color can be best understood by analyzing the room temperature emission spectrum using the tristimulus function. The color purity of the phosphors was gauged using CIE chromaticity coordinates by CIE color calculator software. Strong, red color with CIE chromaticity coordinates (0.63, 0.35) was obtained for $Y_{2.60}Mg_2Nb_3O_{14}$:*0.40*Eu^{3+} phosphor. Plotting the color coordinates of $Y_{2.60}Mg_2Nb_3O_{14}$:*0.40*Eu^{3+} phosphor on a 1931 CIE diagram illustrated in Fig. 6B.15, display its red emission and the digital photograph of the $Y_{2.60}Mg_2Nb_3O_{14}$:*0.40*Eu^{3+} phosphor under the 392 nm excitation is shown in the inset of the Fig. 6B.15. The obtained color coordinated were very close to the standard coordinates (0.67, 0.33) from NTSC (National Television Standard Committee), indicating the high color purity of the as-prepared phosphors.

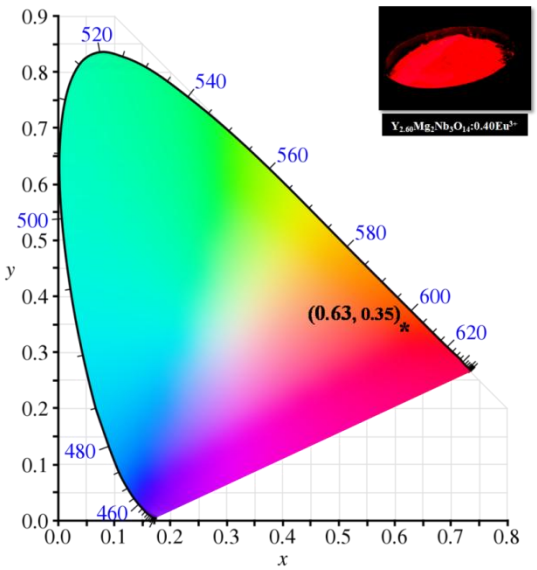

Fig. 6B.15 CIE chromaticity diagram of the $Y_{2.60}Mg_2Nb_3O_{14}$:*0.40*Eu^{3+} phosphor and the digital photograph of the $Y_{2.60}Mg_2Nb_3O_{14}$:*0.40*Eu^{3+} phosphor under the 392 nm excitation is shown in the inset of the figure.

The color purity and correlated color temperature (CCT) were calculated to characterize the color emission. The CCT parameter represents the color temperature of the light source. The correlated color temperature was estimated using the McCamy empirical formula (McCamy *et al*. 1992):

$$CCT\ (x, y) = -449n^3 + 3525n^2 - 6823.3n + 5520.33 \quad (6B.1)$$

where $n = (x - x_e)/(y - y_e)$. In this (x, y) denotes the CIE color coordinates, and $(x_e, y_e) = (0.3320, 0.1858)$, is the epicenter of convergence of isotemperature lines in the 1931 CIE chromaticity diagram and n is the reciprocal of slope of the line connecting (x, y) and (x_e, y_e). The obtained CCT values were found to vary from 2034 to 2302K. Usually, CCT values less than 5000K indicate the warm white light used for home appliances. As the obtained CCT values are below 3000K, the developed phosphor may be suitable for use in warm white light emitting diodes and solid-state lighting applications.

Table 6B.2 Optical properties of $Y_{3-x}Mg_2Nb_3O_{14}:xEu^{3+}$ (x = 0.10, 0.20, 0.30, 0.40 and 0.50) narrow red phosphors for pc-WLEDs.

x	**Asymmetric Ratio**	***fwhm* (nm)**	**Life time (ms)**	**Efficiency η (%)**	**Color coordinates (*x, y*)**	**CCT (K)**	**Color purity (%)**
0.10	3.67	3.64	0.62	26.41	(0.62, 0.36)	2034	86.55
0.20	2.45	4.02	0.63	31.44	(0.62, 0.35)	2194	86.87
0.30	2.04	4.44	0.63	34.05	(0.62, 0.35)	2194	87.00
0.40	1.85	4.94	0.67	37.22	(0.63, 0.35)	2302	89.32
0.50	1.77	4.67	0.60	31.33	(0.63, 0.36)	2127	92.40

To characterize the effect of Eu^{3+} ion incorporation on the narrow band emission of the developed phosphors, the color purity was calculated. The color purity of a dominant color is the weighted-average of the emission color coordinate relative to the coordinate of the dominant wavelength and CIE white illumination coordinate, which is calculated using the equation (Wu *et al*. 2012, Lian *et al*. 2016):

$$\text{Color purity} = \sqrt{\frac{(x-x_i)^2 + (y-y_i)^2}{(x_d-x_i)^2 + (y_d-y_i)^2}} \times 100 \quad (6B.2)$$

where (x, y) are the chromaticity coordinates of the sample, (x_i, y_i) are the coordinates of standard illuminant (0.333, 0.333), and (x_d, y_d) are the coordinates of the dominant wavelength. In this system, red emission is the dominant one and hence (x_d, y_d) = (0.67, 0.33). The color purity was found to increase from 86.55 to 92.4% with Eu^{3+} concentration which implies the improved color purity of red emission. Hence, Eu^{3+} doped $Y_3Mg_2Nb_3O_{14}$ may be a potential narrow-band red emitting phosphor for application in UV-pumped WLEDs.

6B.4 Conclusions

In this contribution, the crystal structure and luminescence properties of Eu^{3+}-activated narrow-band red emitting phosphor, $Y_{3-x}Mg_2Nb_3O_{14}$:$x$$Eu^{3+}$ prepared via conventional solid state reaction method were reported. Also investigate the influence of partial occupation of Mg^{2+} ions on both A and B site of the fergusonite type structure on the photoluminescence properties in detail. As per the powder XRD, the structure is homeotypic to that of pure $YNbO_4$ having monoclinic fergusonite structure with a space group C2/c. The luminescence property analysis corroborates the site of occupation of Eu^{3+} ions in the host lattice which can replace either Y^{3+}/Mg^{2+} ions in the A site. The Eu^{3+} doped phosphor shows intense red emission peaking at 613 nm with a narrow *fwhm* of 4 nm under the 392 nm excitation. The luminescence intensity gets enhanced by the addition of Mg^{2+} ions into the pure $YNbO_4$ host lattice. Hence, we can conclude that the enhanced electric dipole transition intensity arises from the symmetry distortion of Eu^{3+} ions in the lattice. The distortion of the A site symmetry caused by the introduction of Mg^{2+} ions and the red shift of the charge transfer energy leads to an intense $^5D_0$ – $^7F_2$ hypersensitive electric dipole transition under 392 nm excitation. Moreover, these phosphors exhibit high color purity (92.4%) with remarkable CIE chromaticity coordinates (0.63, 0.35) along with good CCT values, which can act as a potential narrow-remitting red phosphor for applications in near-UV based white LEDs lighting and display areas.

Chapter 7

CONCLUSIONS AND FUTURE SCOPE

This chapter summarizes the major conclusions derived from the work based on development of novel Eu^{3+} based red phosphors for phosphor-converted white light emitting diode applications. The conclusions drawn from the studies can serve as a guideline for the designing of new phosphor materials with improved properties. The future scope of the present work is also mentioned.

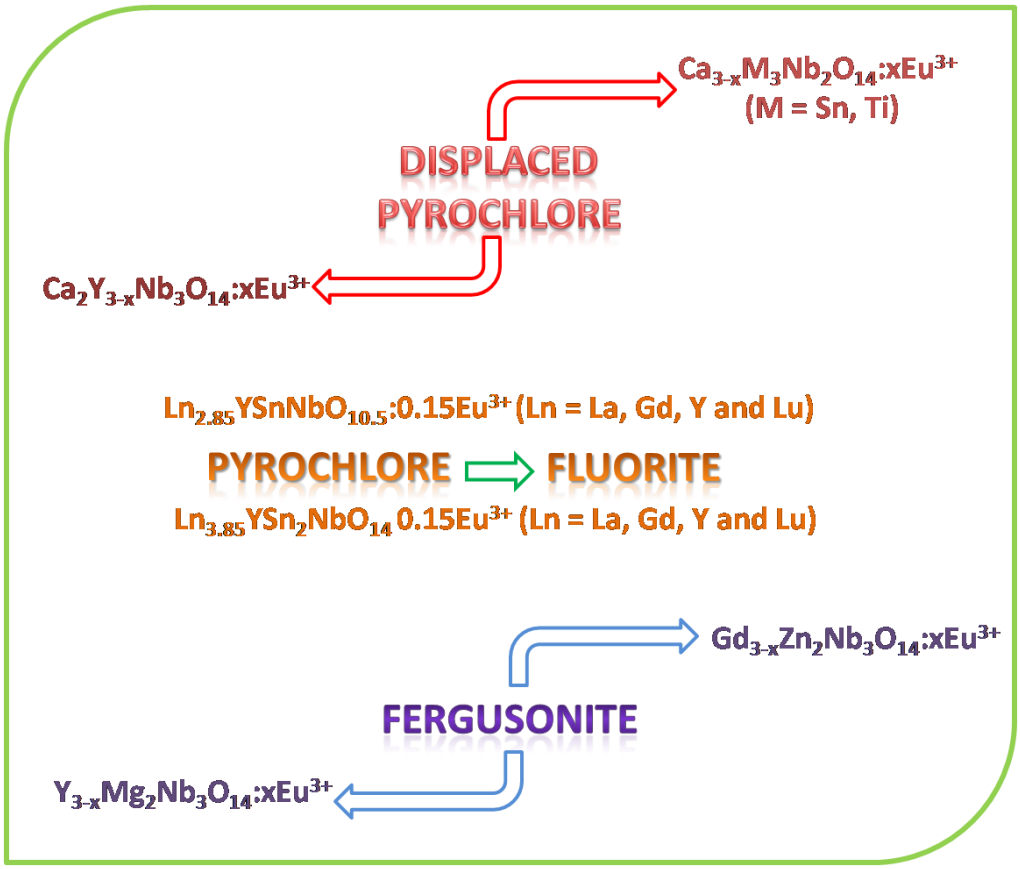

7.1 Conclusions

The development of stable and efficient red phosphors for white light emitting diodes has become a prime focus of interest in the solid state lighting industry. In this scenario, several series of Eu^{3+} based red phosphors were synthesized using solid state reaction route and their properties were optimized using various advanced techniques. The main spectral tuning strategies like modification of the host lattice, cation or anion substitution and phase transitions are discussed in detail in the previous chapters. The relevant conclusions derived from the current work are discussed here.

- Influence of partial occupancy of Sn in both A and B sites of the pyrochlore-type oxides on the photoluminescence properties was studied in $Ca_{3-x}Sn_3Nb_2O_{14}$:xEu^{3+} system
- Intense multiband emissions due to Eu^{3+} $^5D_0$–$^7F_{0,\,1,\,2}$ transitions was observed in this system
- The absence of characteristic MD transition splitting points out the local cation disorder exists in this displaced pyrochlores
- The unusual forbidden intense sharp $^5D_0$–$^7F_0$ transition indicates single site occupancy of Eu^{3+} with a narrower range of bonding environment, preventing the cluster formation
- Influence of partial substitution of less electronegative Ti^{4+} ion on both A and B sites of the $Ca_{3-x}Ti_3Nb_2O_{14}$:xEu^{3+} on the photoluminescence properties was studied
- The as-prepared phosphors exhibit intense sharp narrow red emissions due to Eu^{3+} $^5D_0$–$^7F_2$ transitions
- A cross-cutting comparative study between titanate and stannate systems convince the role of electronegativity of B-site cation on the crystal field splitting of Eu^{3+} ions
- The splitting of characteristic Eu^{3+} manifold is smaller in titanate compared to stannate phosphors

- *fwhm* of $^5D_0$-$^7F_2$ electric dipole transition were observed to be low for titanium substituted ones due to the difference in bonding environment of Ti and Sn in the host lattice.
- Evolution of emission spectra with partial occupation of medium size cation like Y on both A and B site of the pyrochlore oxides was studied in $Ca_2Y_3Nb_3O_{14}$ system
- Eu^{3+} incorporation induces structural disorder in the lattice reducing the pyrochlore D_{3d} symmetry
- The preferential occupation of Eu^{3+} ions on the B site conduces a higher coordination more than VI with disordered environment allowing forced electric dipole transitions
- These phosphors emit intense red light due to forbidden electric dipole transition with more Stark splitting indicating the low symmetry of Eu^{3+} ions in the host.
- The disordered environment with special coordination of Eu^{3+} ions allows improved quantum efficiency (η = 34%) and CIE color coordinates (0.61, 0.38).
- Photoluminescence properties were further improved in $Ca_2Y_3Nb_3O_{14}$:Eu^{3+} phosphors by the incorporation of Sr^{2+} ions in Ca^{2+} site
- Influence of phase evolution on the luminescence properties were explored in $Ln_3YSnNbO_{10.5}$ and $Ln_4YSn_2NbO_{14}$ (Ln = La, Gd, Y and Lu) systems
- Substitution of Ln^{3+} ions in the A site of the pyrochlore induces a structural transition from an ordered pyrochlore to a disordered fluorite structure with decreasing ionic radius
- Luminescence properties got enhanced with increased ordering of cations from Lu to La
- Long range ordering, ligand polarizability and covalent nature of Eu^{3+} bonding influence the emission probability and improves the quantum efficiency of the La host
- A new series of narrow band red emitting $Gd_3Zn_2Nb_3O_{14}$:Eu^{3+} phosphor was synthesized

- The developed phosphor exhibits a strong red emission peaking at 613 nm with a *fwhm* of merely ~ 3.50 nm under the 392 nm excitation.
- The relative emission intensity was found to be 3.9 times higher than that of the commercial red phosphor
- Highly efficient narrow-band red emitting Eu^{3+} activated $Y_3Mg_2Nb_3O_{14}$ phosphor were prepared
- The color purity of the phosphor could achieve 92.4% ascribing to the narrow full width half maximum (fwhm ~ 4 nm).
- The emission intensity of as-prepared phosphor was found to be 9.4 times higher than the commercial red phosphor
- Phosphors exhibit remarkable CIE chromaticity coordinates (0.63, 0.35), good CCT values and high color purity (92.4%)

Thus, the developed red phosphors are found to be suitable candidate for fabricating highly reddish pc-LEDs.

7.2 Future scope

- Thermal stability of luminescence behavior of developed red phosphors and its optimization.
- Synthesis of phosphors via different methods to achieve a more spherical morphology to improve its absorption strength.
- Enhancement in the emission intensity and efficiency by different cationic modifications, different codoping techniques etc.
- Incorporation of developed red phosphors on suitable near UV/Blue LED chips.
- The output characteristics of aforesaid LED chip - Phosphor combination

REFERENCES

Allred A. L., "Electronegativity values from thermochemical data", *J. Inorg. Nucl. Chem.*, 17 (**1961**) 215-221.

Arenas D. J., Gasparov L. V., Qui W., Nino J. C., Patterson H. C., Tanner D. B., "Raman study of phonon modes in bismuth pyrochlores", *Phys. Rev. B*, 82 (**2010)** 214302-8.

Avdeev M., Haas M. K., Jorgensen J. D., Cava R. J., "Static disorder from lone-pair electrons in $Bi_{2-x}M_xRu_2O_{7-y}$ (M= Cu, Co; x = 0, 0.4) pyrochlores*", J. Solid State Chem*., 169 (**2002**) 24-34.

Babu G. S., Valant M., Page K., Llobet A., Kolodiazhnyi T., Axelsson A. K., "New $(Bi_{1.88}Fe_{0.12})(Fe_{1.42}Te_{0.58})O_{6.87}$ pyrochlore with spin-glass transition", *Chem. Mater.*, 23 (**2011**) 2619-2625.

Balmer M. L., Su Y. L., Xu H. W., Bitten E., McCready D., Navrotsky A., "Synthesis, structure determination, and aqueous durability of $Cs_2ZrSi_3O_9$", *J. Am. Ceram. Soc.* 84 (**2001**) 153-160.

Baryshnikov G., Minaev B., Ågren H., "Theory and calculation of the phosphorescence phenomenon", *Chem. Rev*., 117 (**2017**) 6500-6537

Begg B. D., Hess N. J., McCready D. E., Thevuthasan S., Weber W. J., "Heavy-ion irradiation effects in $Gd_2(Ti_{2-x}Zr_x)O_7$ pyrochlores", *J. Nucl. Mater*., 289 (**2001**) 188-193.

Binnemans K., Gorller Walrand C., "Application of the Eu^{3+} ion for the site symmetry determination", *J. Rare Earths*, 14 (**1996**) 173-180.

Blasse G., "Energy transfer in oxidic phosphors", *Phys. Lett. A*, 28 (**1968**) 444-445.

Blasse G., "Luminescence process in niobates with fergusonite structure", *J. Lumin*., 14 (**1976**) 231-233.

Blasse G., "Handbook on the Physics and Chemistry of rare-earths", *North Holland Publishing Company*, Netherlands, (**1979**).

Blasse G., Bril A., "Luminescence phenomena in compounds with Fergusonite structure", *J. Lumin*. 3 (**1970**) 109-131.

Blasse G., Grabmair B. C., "Luminescent Materials", *Springer*, Berlin, (**1994**).

Brown S., Gupta H. C., Alonso J. A., Martinez-Lope M. J., "Lattice dynamical study of optical modes in $Tl_2Mn_2O_7$ and $In_2Mn_2O_7$ pyrochlores", *Phys. Rev. B*, 69 (**2004**) 054434-6.

Bünzli J. C. G., Choppin G. R., "Lanthanide probes in life, chemical and earth sciences: Theory and practice", *Elsevier*, New York, (**1989**).

Bunzli J. C. G., Piguet C., "Taking advantage of luminescent lanthanide Ions", *Chem. Soc. Rev*., 34 (**2005**) 1048-1077.

Capobianco J. A., Proulx P. P., Bettinelli M., Negrisolo F., "Absorption and emission spectroscopy of Eu^{3+} in metaphosphate glasses", *Phys. Rev. B: Condens. Matter*, 42 (**1990**) 5936–5944.

Chen D., Wan Z., Zhou Y., Chen Y., Yu H., Lu H., Huang P., "Lanthanide-activated $Na_5Gd_9F_{32}$ nanocrystals precipitated from a borosilicate glass: phase-separation-controlled crystallization and optical property", *J. Alloys Compd*., 625 (**2015**)149-157.

Chen M., Tanner D. B., Nino J. C., "Infrared study of the phonon modes in bismuth pyrochlores", *Phys. Rev. B*, 72 (**2005)** 054303-8

Chen X. Y., Liu G. K., "The standard and anomalous crystal-field spectra of Eu^{3+}", *J. Solid State Chem.,* 178 (**2005**) 419-428

Chen X. Y., Zhao W., Cook R. E., Liu G. K., "Anomalous luminescence dynamics of Eu^{3+} in BaFCl microcrystals" *Phys. Rev. B: Condens. Matter*, 70 (**2004**) 205122–205130.

Cheng H., Wang L., Lu Z., "A general aqueous sol-gel route to $Ln_2Sn_2O_7$ nanocrystals", *Nanotechnol.*, 19 (**2008**) 025706-12.

Choi S. H., Anoop G., Suh D. W., Kim K. P., Lee H. J., Yoo J. S., "Effect of gadolinium incorporation on optical characteristics of $YNbO_4:Eu^{3+}$ phosphors for lamp applications", J. Rare Earths, 30 (**2012**) 205-209.

Choi Y. I., Sohn Y., "Correction: photoluminescence profile mapping of Eu (III) and Tb (III/IV)-embedded in quantum size SnO_2 nanoparticles", *RSC Adv*., 4, (**2014**) 31155-31161.

Cockroft N. J., Lee S. H., Wright J. C., "Site-selective spectroscopy of defect chemistry in $SrTiO_3$, Sr_2TiO_4, and $Sr_3Ti_2O_7$", *Phys. Rev. B: Condens. Matter*, 44 (**1991**) 4117-4126.

De Dood M. J. A., Knoester J., Tip A., Polman A., "Forster transfer and the local optical density of states in erbium-doped silica", *Phys. Rev. B*, 71 (**2005**) 115102-5.

Deepa M., Prabhakar Rao P., Radhakrishnan A. N., Sibi K. S., Koshy P., "Pyrochlore type semiconducting ceramic oxides in Ca-Ce-Ti-M-O system (M = Nb or Ta)-Structure, microstructure and electrical properties, *Mater. Res. Bull*., 44 (**2009**) 1481-1488.

Dexpert-Ghys J., Faucher M., Caro P., "Site-selective excitation, crystal-field analysis, and energy transfer in europium-doped monoclinic gadolinium sesquioxide. A test of the electrostatic model", *Phys. Rev. B,* 23 (**1981**) 607-617.

Dhanaraj J., Jagannathan R., Kutty T. R. N., Chung-Hsin Lu, "Photoluminescence characteristics of $Y_2O_3:Eu^{3+}$ nanophosphors prepared using sol-gel thermolysis", *J. Phys. Chem. B,* 105 (**2001**) 11098-11105.

Dickson F. J., Hawkins K. D., White T. J., "Calcium uranium titanate-A new pyrochlore", *J. Solid State Chem*., 82 (**1989**) 146-150

Đorđević V., Antić Z., Lojpur V., Dramićanin M. D., "Europium-doped nanocrystalline Y_2O_3-La_2O_3 solid solutions with bixbyite structure", *J. Phys. Chem. Solids*, 75 (**2014**) 1152–1159.

Dorenbos P., "Relating the energy of the [Xe]$5d^1$ configuration of Ce^{3+} in inorganic compounds with anion polarizability and cation electronegativity"**,** *Phys. Rev. B*, 65 (**2002**) 235110-6.

Dorenbos P., "The Eu^{3+} charge transfer energy and the relation with the band gap of compounds", *J. Lumin*., 111 (**2005**) 89-104

Downer M. C., Burdick G. W., Sardar D. K., "A new contribution to spin-forbidden rare earth optical transition intensities: Gd^{3+} and Eu^{3+}", *J. Chem. Phys.*, 89 (**1988**) 1787–1797.

Du F., Zhu R., Huang Y., Tao Y., Jin Seo H., "Luminescence and microstructures of Eu^{3+}-doped $Ca_9LiGd_{2/3}(PO_4)_7$", *Dalton Trans*., 40 (**2011**) 11433-11440.

Du H., Yao X., Zhang L., "Structure, IR spectra and dielectric properties of Bi_2O_3-ZnO-SnO_2-Nb_2O_5 quarternary pyrochlore", *Ceram. Int.,* 28 (**2002)**231-234.

Dutta P. S., Khanna A., "Eu^{3+} activated molybdate and tungstate based red phosphors with charge transfer band in blue region", *ECS J. Solid State Sci. Technol*., 2 (**2013**) R3153-R3167

Dwivedi A., Mishra K., Rai S. B., "Multi-modal luminescence properties of RE^{3+} (Tm^{3+}, Yb^{3+}) and Bi^{3+} activated $GdNbO_4$ phosphors-upconversion, downshifting and quantum cutting for spectral conversion", *J. Phys. D: Appl. Phys.,* 48 (**2015**) 435103-435116.

Ege A., Ayvacikli M., Dinçer O., Satılmış S. U., "Spectral emission of rare earth (Tb, Eu, Dy) doped $Y_2Sn_2O_7$phosphors" *J. Lumin.,* 143 (**2013**) 653-656.

Enhai S., Weiren Z., Guoxiong Z., Xihua D., Chunyu Y., Minkang Z., "Luminescence properties of red phosphors $Ca_{10}Li(PO_4)_7:Eu^{3+}$", *J. Rare Earths*, 29 (**2011**) 440–443.

Errandonea D., Manjon F. J., "On the ferroelastic nature of the scheelite-to fergusonite phase transition in orthotungstates and orthomolybdates", *Mater. Res. Bull.,* 44 (**2009**) 807-811.

Feldmann C., Justel T., Ronda C. R., Schmidt P. J., "Inorganic luminescent materials: 100 years of research and application"**,** *Adv. Funct. Mater*., 13 (**2003**) 511-516.

Francis T. L., Rao P. P., Thomas M., Mahesh S. K., Reshmi V. R., "Effect of Zr^{4+} and Si^{4+} substitution on the luminescence properties of $CaMoO_4$: Eu^{3+} red phosphors", *J. Mater. Sci.: Mater. Electron*., 25 (**2014**) 2387-2393.

Fu, Z., Gong W., Li H., Wu Q., Li W., Yang H. K., Jeong J. H., "Synthesis and spectral properties of nanocrystalline Eu^{3+}-doped pyrochlore oxide $M_2Sn_2O_7$ (M = Gd and Y)", Curr. Appl. Phys., 11 (**2011**) 933-938.

Fu Z., Yang H. K.,, Moonn B. K., Choi B. C., Jeong J. H., "$La_2Sn_2O_7:Eu^{3+}$ micronanospheres: hydrothermal synthesis and luminescent properties", *Cryst. Growth Des.*, 9 (**2009**) 616-621.

Fujihara S., Tokumo K., "Multiband orange-red luminescence of Eu^{3+} ions based on the pyrochlore-structured host crystal", *Chem. Mater.*, 17 (**2005**), 5587-5593

Fujishiro F., Murakami M., Hashimoto T., Takahashi M., "Orange luminescence of Eu^{3+} doped $CuLaO_2$ delafossite oxide", *J. Ceram. Soc. Jpn*., 118 (**2010**) 1217-1220.

Fujishiro F., Sekimoto R., Hashimoto T., "Photoluminescence properties of $CuLa_{1-x}Ln_xO_2$ (Ln: lanthanide)-intense and peculiar luminescence from Ln^{3+} at the site with inversion symmetry", *J. Lumin*., 133 (**2013**) 217-221.

Gaon L., Jiang S., Li R., Li B., Li Y., "Effect of magnesium content on structure and dielectric properties of cubic bismuth magnesium niobate pyrochlores", *Ceram. Int*., 40(**2014**)4225-4229.

Glerup M., Nielsen O. F., Poulsen F. W., "The structural transformation from the pyrochlore structure, $A_2B_2O_7$ to the fluorite structure, AO_2, studied by Raman spectroscopy and defect chemistry modeling", *J. Solid State Chem.,* 160 (**2001**) 25-32.

Gupta H. C., Ashdhir P., Rawat C. S., "A lattice dynamical investigation for the zone-centre phonon frequencies of the $NaMnF_3$ perovskite", *J. Phys. Chem. Solids*, 57 (**1996**) 1857-1859

Gupta S. K., Mohapatra M., Natarajan V., Godbole S. V., "Site-specific luminescence of Eu^{3+} in gel-combustion-derived strontium zirconate perovskite nanophosphors", *J. Mater. Sci*., 47 (**2012**) 504-3515.

Gupta S. K., Mohapatra M., Godbole S. V. and Natarajan V., "On the unusual photoluminescence of Eu^{3+} in α-$Zn_2P_2O_7$: a time resolved emission spectrometric and Judd–Ofelt study", *RSC Adv*., 3 (**2013**) 20046-20053.

Hao B. V., Huy P. T., Khiem T. N., Thanh Ngan N. T., Duong P. H., "Synthesis of Y_2O_3:Eu^{3+} micro- and nanophosphors by sol-gel process", *J. Phys.: Conf. Ser.,* 187(**2009**) 012074-012081.

Heremans C., Wuensch B. J., Stalick J. K., Prince E., "Fast-ion conducting $Y_2(Zr_yTi_{1-y})_2O_7$ pyrochlores: neutron rietveld analysis of disorder induced by Zr Substitution", *J. Solid State Chem*., 117 (**1995**) 108-121.

Hirano M., Dozono H., "Hydrothermal formation and characteristics of rare-earth niobate phosphors and solid solutions between $YNbO_4$ and $TbNbO_4$", *Mater. Chem. Phys*., 143 (**2014**) 860-866.

Hirayama M., Sonoyama N., Yamada A., Kanno R., "Relationship between structural characteristics and photoluminescent properties of $(La_{1-x}Eu_x)_2M_2O_7$ (M=Zr, Hf, Sn) pyrochlores", *J. Lumin*., 128 (**2008**) 1819-1825.

Hoefdraad H. E., "The charge-transfer absorption band of Eu^{3+} in oxides", *J. Solid State Chem.,* 15 (**1975**) 175-177

Hölsä J., Porcher P., "Free ion and crystal field parameters for REOCI: $Eu^{3+"}$, *J. Chem. Phys*., 75 (**1981**) 2108-2117.

Hong Y. P., Ha S, Lee H .Y., Lee Y. C., Ko K. H., Kim D. W., Hong H. B., Hong K. S., "Voltage tunable dielectric properties of rf sputtered Bi_2O_3-ZnO-Nb_2O_5 pyrochlore thin films", *Thin Solid Films*, 419 (**2002**) 183-188.

Hong W., Huiling D., Xi Y., "Structural study of Bi_2O_3-ZnO-Nb_2O_5 based pyrochlores", *Mater. Sci. Eng. B*, 99 (**2003**) 20-24.

Hoppe H. A., Stadler F., Oeckler O., Schnick W., "$Ca[Si_2O_2N_2]$-A novel layer silicate", *Angew. Chem., Int. Ed*., 43 (**2004**) 5540-5542.

Hou J., Yin X., Fang Y., Huang F., Jiang W., "Novel red-emitting perovskite-type phosphor $CaLa_{1-x}MgM'O_6$:xEu^{3+} (M' = Nb, Ta) for white LED application", *Opt. Mater*., 34 (**2012**) 1394-1397.

Hsu C., Powell R. C., "Energy transfer in europium doped yttrium vanadate crystals", *J. Lumin*., 10 (**1975**) 273-293.

Huang X., "Solid-state lighting: Red phosphor converts white LEDs", *Nature Photon*., 8 (**2014)** 748-749.

Ishihara S., Tachiki M., Egami T., "Enhancement of the electron-lattice interaction due to strong electron correlation", *Phys. Rev. B,* 49 (**1994**) 8944-8954.

Islam M. N., Ghosh T. B., Chopra K. L., Acharya H. N., "XPS and X-ray diffraction studies of aluminum-doped zinc oxide transparent conducting films", *Thin Solid Films*, 280 (**1996**) 20-25.

Ji H. P., Huang Z. H., Xia Z. G., Molokeev M. S., Atuchin V. V., Fang M. H., Liu Y. G., "Discovery of new solid solution phosphors via cation substitution-dependent phase transition in $M_3(PO_4)_2$:Eu^{2+} (M = Ca/Sr/Ba) quasi-binary sets", *J Phys Chem C*, 119 (**2015**) 2038-2045.

Jia H., Cao L., Wei Y., Wang H., Xiao H., Li G., Lin J., "A narrow-band red emitting K_2LiGaF_6:Mn^{4+} phosphor with octahedral morphology: luminescent properties, growth mechanisms, and applications", *J. Alloys Compd.*, 738 (**2018**) 307-316.

Jiang X., Chen Z., Huang S., Wang J., Pan Y., "A red phosphor $BaTiF_6$:Mn^{4+}: reaction mechanism, microstructures, optical properties, and applications for white LEDs", *Dalton Trans*. 43 (**2014**) 9414-9418.

Jiao M., Guo N., Lu W., Jia Y., Lv W., Zhao Q., Shao B., You H., "Tunable blue-green-emitting $Ba_3LaNa(PO_4)_3F$:Eu^{2+},Tb^{3+} phosphor with energy transfer for near-UV white LEDs", *Inorg. Chem*., 52 (**2013**) 10340-10346.

Jin X., Götz M., Wille S., Mishra Y. K., Adelung R., Zollfrank C., **"**A novel concept for self-reporting materials: stress sensitive photoluminescence in ZnO tetrapod filled elastomers", *Adv. Mater*., 25 (**2013**) 1342-1347.

Jing X., Gibbons C., Nicholas D., Silver J., Zhang X., Vecht A., Frampton C. S., "Blue luminescence in yttrium and gadolinium niobates caused by bismuth. The importance of non-bonding ns^2 valence orbital electrons", *J. Mater. Chem.*, 9 (**1999**) 2913-2918

Jones E. D., "Light emitting diodes for general illumination", *OIDA report*, 2001

Jorgensen C. K., "Modern aspects of ligand-field theory", *North Holland*, Amsterdam, (**1971**).

Justel T., Nikol H., Ronda C., "New developments in the field of luminescent materials for lighting and displays", *Angew. Chem.,* 37 (**1998**) 3084-3103.

Judd B. R., "Optical absorption intensities of rare-earth ions", *Phys. Rev*., 127 (**1962**) 750-761.

Kamba S., Porokhonskyy V., Pashkin A., Bovtun V., Petzelt J., Nino J. C., Trolier-McKinstry S., Lanagan M. T., Randall C. A., "Anomalous broad dielectric relaxation in $Bi_{1.5}Zn_{1.0}Nb_{1.5}O_7$ pyrochlore", *Phys. Rev. B*, 66 (**2002**) 054106-7.

Katelnikovas A., Plewa J., Sakirzanovas S., Dutczak D., Enseling D., Baur F., Winkler H., Kareiva A., Thomas Jüstel, "Synthesis and optical properties of $Li_3Ba_2La_3(MoO_4)_8:Eu^{3+}$ powders and ceramics for pc LEDs", *J. Mater. Chem*., 22 (**2012**) 22126-22134.

Kaufman J. E., Christensen J. F., "Lighting Handbook", *Waverly Press*, Maryland, (**1972**).

Kechele J. A., Oeckler O., Stadler F., Schnick W., "Structure elucidation of $BaSi_2O_2N_2$–A host lattice for rare-earth doped luminescent materials in phosphor-converted (pc)-LEDs", *Solid State Sci*., 11 (**2009**) 537-543.

Kennedy B. J., Hunter B. A., Howard C. J., "Structural and bonding trends in tin pyrochlore oxides", *J. Solid State Chem*., 130 (**1997**) 58-65

Khan N., Abas N., "Comparative study of energy saving light sources", *Renewable Sustainable Energy Rev.*, 15 (**2011**) 296-309

Khanna A., Dutta P. S., "Narrow spectral emission $CaMoO_4:Eu^{3+}$, Dy^{3+}, Tb^{3+} phosphor crystals for white light emitting diodes", *J. Solid State Chem*., 198 (**2013**) 93-100.

Kirby A. F., Foster D., Richardson F. S., "Comparison of $^7F_J \leftarrow {}^5D_0$ emission spectra for Eu(III) in crystalline environments of octahedral, near-octahedral, and trigonal symmetry", *Chem. Phys. Lett*., 95 (**1983**) 507-512.

Kong L., Karatchevtseva. I., Blackford. M. G., Scales. N., Triani, G., "Aqueous chemical synthesis of $Ln_2Sn_2O_7$ pyrochlore-structured ceramics", *J. Am. Ceram. Soc.*, 96 (**2013**) 2994-3000.

Kovac J., Peternai L., Lengyel O., "Advanced light emitting diodes structures for optoelectronic applications", *Thin Solid Films,* 433 (**2003)** 22-26.

Krayzman V., Levin I., and Woicik, J. C., "Local structure of displacively disordered pyrochlore dielectrics", *Chem. Mater*, 19 (**2007**) 932-936.

Kumar V., Kumar V., Som S., Duvenhage M., Ntwaeaborwa O. M., Swart H. C., "Effect of Eu doping on the photoluminescence properties of ZnO nanophosphors for red emission applications", *Appl. Surf. Sci*., 308 **(2014**) 419-430.

Lakshminarasimhan N., Varadaraju U. V., "Eu^{3+} luminescence-a structural probe in $BiCa_4(PO_4)_3O$, an apatite related phosphate", *J. Solid State Chem*., 177 (**2004**) 3536-3544.

Langford J. I., Wilson A. J. C., "Scherrer after sixty years: a survey and some new results in the determination of crystallite size", *J. Appl. Crystallogr*., 11 (**1978**) 102-113.

Levin I., Amos T. G., Nino J. C., Vanderah T. A., Randall C. A., Lanagan M. T., "Structural study of an unusual cubic pyrochlore $Bi_{1.5}Zn_{0.92}Nb_{1.5}O_{6.92}$", *J. Solid State Chem*., 168 (**2002**) 69-75.

Lee E. Y., Kim Y. J., "Synthesis and luminescence of $YNbO_4$:Eu^{3+}, Tb^{3+} by a flux method", *Thin Solid Films*, 518 (**2010**) e72-e74.

Lee M. J., Song Y. H., Song Y. L., Han G. S., Jung H. S., Yoon D. H., "Enhanced luminous efficiency of deep red emitting $K_2SiF_6:Mn^{4+}$ phosphor dependent on KF ratio for warm-white LED", *Mater. Lett.*, 141 (**2015**) 27-30.

Lee S. K., Chang H., Han C. H., Kim H. J., Jang H. G., Park H. D., "Electronic structures and luminescence properties of $YNbO_4$ and $YNbO_4$:Bi", *J. Solid State Chem.*, 156 (**2001**) 267-273.

Lei F., Yan B., "Hydrothermal synthesis and luminescence of $CaMO_4:RE^{3+}$ (M = W, Mo; RE = Eu, Tb) submicron-phosphors", *J Solid State Chem.*, 181 (**2008**) 855-862.

Li G., Zhao Y., Xu J., Mao Z., Chen J., Wang D., "Effective suppression of AlN impurity in synthesis of $CaAlSiN_3:Eu^{2+}$ phosphors under condition of atmospheric pressure", *Mater. Chem. Phys.*, 20 (**2017**) 1-6.

Li K., Liu X., Zhang Y., Li X., Lian H., Lin J., "Host-sensitized luminescence properties in $CaNb_2O_6:Ln^{3+}$ (Ln^{3+} = Eu^{3+}/Tb^{3+}/Dy^{3+}/Sm^{3+}) phosphors with abundant colors", *Inorg. Chem.*, 54 (**2015**) 323-333.

Li K., Shang M., Lian H., Lin J., "Recent development in phosphors with different emitting colors via energy transfer for FEDs and UV/n-UV w-LEDs", *J. Mater. Chem. C*, 4 (**2016**) 5507-5630.

Li K., Zhang Y., Li X. J., Shang M. M., Lian H. Z., Lin J., "Host-sensitized luminescence in $LaNbO_4:Ln^{3+}$ (Ln^{3+} = Eu^{3+}/Tb^{3+}/Dy^{3+}) with different emission colors", *Phys. Chem. Chem. Phys.,* 17 (**2015**) 4283-4292.

Li Y., Qi S., Li P., Wang Z., "Research progress of Mn doped phosphors", *RSC Adv.*, 7 (**2017**) 38318-38334.

Lian Z. P., Yan Q. F., "Eu^{2+}-doped $NaBa_4(AlB_4O_9)_2X_3$ (X = Cl, Br) phosphors with intense two-center blue emission and high color purity for n-UV pumped white light-emitting diodes", *J. Mater Chem. C*, 4 (**2016**) 7959-7965.

Liao J., Nie L., Wang Q., Liu S., Fu J., Wen H. R., "Microwave hydrothermal method and photoluminescence properties of $Gd_2Sn_2O_7$: Eu^{3+} reddish orange phosphors", *J. Lumin.,* 183 (**2017**) 377-382.

Lin C. C., Tsai Y. T., Johnston H. E., Fang M. H., Yu F., Zhou W., Whitfield P., Li Y., Wang J., Liu R S., Attfield J. P., "Enhanced photoluminescence emission and thermal stability from introduced cation disorder in phosphors", *J Am. Chem. Soc.*, 139 (**2017**) 11766-11770.

Lin J., Zhou Z., Wang Q., "Molten salt synthesis, characterization, and luminescence properties of $GdNbO_4$/$LuTaO_4$:Eu^{3+} phosphors", *Mater. Res. Bull.,* 48 (**2013**) 2771-2775

Lin J. H., You Y. P., Lu G. X., Yang L. Q., Su M. Z., "Structural and luminescent properties of Eu^{3+} doped $Gd_{17.33}(BO_3)_4(B_2O_5)_2O_{16}$", *J. Mater. Chem*., 8 (**1998**) 1051-1054.

Lin H. Y., Fang Y. C., Huang X. R., Chu S. Y., "Luminescence and site symmetry studies of new red phosphors (Ca, Ba)$_3$(VO_4)$_2$:Eu^{3+} under blue excitation", *J. Am. Ceram. Soc*., 93 (**2010**) 138-141.

Liu C., Liu, J., Dou, K., "Judd-Ofelt intensity parameters and spectral properties of Gd_2O_3:Eu^{3+} nanocrystals", *J. Phys. Chem. B*, 110 (**2006**) 20277-20281.

Liu G., Liu S., Dong X., Wang J., "Y_2O_3:Eu^{3+} core-in-multi-hollow microspheres: facile synthesis and luminescence properties", *J. Nanosci. Nanotechnol*., 11 (**2011**) 9757-9760.

Liu G. K., Jacquier B., "Spectroscopic properties of rare earths in optical materials", *Springer*, (**2005**).

Liu X., Chen C., Li S., Dai Y., Guo H., Tang X., Xie Y., Yan L., "Host-sensitized and tunable luminescence of $GdNbO_4$:Ln^{3+} (Ln^{3+} = Eu^{3+}/Tb^{3+}/Tm^{3+}) nanocrystalline phosphors with abundant color", *Inorg. Chem*., 55 (**2016**) 10383-10396.

Liu X., Han K., Gu M., Xiao L., Ni C., Huang S., Liu B., "Effect of codopants on enhanced luminescence of $GdTaO_4:Eu^{3+}$ phosphors", *Solid State Commun*., 142 (**2007**) 680-684.

Liu X., Lu Y., Chen C., Luo S., Zeng Y., Zhang X., Shang M., Li C., Lin J., "Synthesis and luminescence properties of $YNbO_4$:A (A = Eu^{3+} and/or Tb^{3+}) nanocrystalline phosphors via a sol-gel process", *J. Phys. Chem. C*, 118 (**2014**) 27516-27524.

Liu X. M., Lin J., "Enhanced luminescence of gadolinium niobates by Bi^{3+} doping for field emission displays", *J. Lumin*., 122 (**2007**) 700-703.

Liu Y., Withers R. L., Nguyen H. B., Elliott K., Ren Q. and Chen Z., "Displacive disorder and dielectric relaxation in the stoichiometric bismuth-containing pyrochlores, $Bi_2M^{III}NbO_7$ (M = In and Sc)", *J. Solid State Chem*., 182 (**2009**) 2748-2755.

Lu Y., Chen C., Li S., Liu X., Yan L., Dai Y., Zhang A., Xie Y., Tang X., "Color-tunable luminescence of $YNbO_4:Ln^{3+}$ (Ln^{3+} = Dy^{3+} and/or Eu^{3+}) nanocrystalline phosphors prepared by a sol–gel process", *Eur. J. Inorg. Chem*., 31 (**2015**) 5262-5271.

Lü Y., Tang X., Yan L., Li K., Liu X., Shang M., Li C., Lin J., "Synthesis and luminescent properties of $GdNbO_4:RE^{3+}$ (RE = Tm, Dy) nanocrystalline phosphors via the sol-gel process", *J. Phys. Chem. C*, 117 (**2013**) 21972-21980

Lu Z., Wang J., Tang Y., Li Y., "Synthesis and photoluminescence of Eu^{3+}-doped $Y_2Sn_2O_7$ nanocrystals", *J. Solid State Chem.*, 177 (**2004**) 3075-3079.

Lufaso M. W., Vanderah T. A., Pazos I. M., Levin I., Roth R. S., Nino J. C., Provenzano V., Schenck P. K. "Phase formation, crystal chemistry, and properties in the system Bi_2O_3–Fe_2O_3–Nb_2O_5", *J. Solid State Chem*., 179 (**2006**) 3900-3910.

Lumpkin G. R., Pruneda M., Rios S., Smith K. L., Trachenko K., Whittle K. R., Zaluzec N. J., "Nature of the chemical bond and prediction of radiation tolerance in pyrochlore and defect fluorite compounds", *J. Solid State Chem*., 180 (**2007**) 1512-1518.

Maczka M., Knyazev A. V., Kuznetsova N. Y., Ptak M., Macalik L., "Raman and IR studies of $TaWO_{5.5}$, $ASbWO_6$ (A = K, Rb, Cs, Tl), and $ASbWO_6{\cdot}H_2O$ (A = H, NH_4, Li, Na) pyrochlore oxides", *J. Raman Spectrosc*., 42 (**2011**) 529-533.

Mahesh S. K., Prabhakar Rao P., Thomas M., Linda Francis T., Koshy P., "Influence of cation substitution and activator site exchange on the photoluminescence properties of Eu^{3+}-doped quaternary pyrochlore oxides", *Inorg. Chem*., 52 (**2013**) 13304-13313.

Mandal B. P., Banerji A., Sathe V., Deb S. K., Tyagi A. K., "Order disorder transition in $Nd_{2-y}Gd_yZr_2O_7$ pyrochlore solid solution: An X-ray diffraction and Raman spectroscopic study", *J. Solid State Chem*., 180 (**2007**) 2643-2648.

Mandal B. P., Garg N., Sharma S. M., Tyagi A. K., "Preparation, XRD and Raman spectroscopic studies on new compounds $RE_2Hf_2O_7$ (RE = Dy, Ho, Er, Tm, Lu, Y): Pyrochlores or defect-fluorite?", *J. Solid State Chem*., 179 (**2006**) 1990-1994.

Martínez- Martínez R., Rivera S., Yescas-Mendoza E., Alvarez E., Falcony C., Caldiño U., "Luminescence properties of Ce^{3+}-Dy^{3+} codoped aluminium oxide films", *Opt. Mater*., 33 (**2011**)1320-1324.

McCamy C. S., "Correlated color temperature as an explicit function of chromaticity coordinates", *Color Res. Appl*., 17 (**1992**) 142-144.

McCauley R. A., "Infrared absorption characteristics of the pyrochlore structure", *J. Opt. Soc. Am.*, 63 (**1973**) 721-725.

McCauley R. A**., "**Structural characteristics of pyrochlore formation", *J. Appl. Phys.*, 51 (**1980**) 290-294.

Michel D., Perezy Jorba M., Collongues R., "Study by Raman spectroscopy of order-disorder phenomena occurring in some binary oxides with fluorite-related structures", *J. Raman Spectrosc.*, 5 (**1976**) 163-180.

Minervini L., Grimes R. W., "Disorder in pyrochlore oxides", *J. Am. Ceram. Soc.*, 83 (**2000**) 1873-1878.

Moreno I., Contreras U., "Color distribution from multicolor LED arrays", *Opt. Express*, 15 (**2007**) 3607-3618.

Moulder J. F., Stickle W. F., Sobol P. E., Bomben K. D., Chastain J., Kings R. C., Jr.(Eds.), "Handbook of X-ray Photoelectron Spectroscopy", *Physics Electronics Inc.,* Eden Prairie, MN, (**1995**).

Nakamura S., Pearton S., Fasol G., "The blue laser diode: the complete story", *Springer-Verlag*, Berlin Heidelberg New York, (**2001)**.

Nakamura S., Senoh M., Mukai T., "P-GaN/N-InGaN/N-GaN double-heterostructure blue-lightemitting diodes", *J. App. Phys.,* 32 (**1993)** L8-L11.

Nalwa H. S., Rohwer L. S., "Handbook of luminescence, display materials and display devices", *American Scientific Publishers*, California (**2003**).

Nazarov M., Kim Y. J., Lee E. Y., Min K. I., Jeong M. S., Lee S. W., Noh D. Y., "Luminescence and Raman studies of $YNbO_4$ phosphors doped by Eu^{3+}, Ga^{3+}, and $Al^{3+"}$, *J. Appl. Phys.*, 107 (**2010**) 103104-6.

Nguyen H. B., Nore´n L., Liu Y., Withers R. L., Wei X., Elcombe M. M., "The disordered structures and low temperature dielectric relaxation properties of two misplaced-displacive cubic pyrochlores found in the Bi_2O_3-$M^{II}O$-Nb_2O_5 (M = Mg, Ni) systems", *J. Solid State Chem.*, 180 (**2007**) 2558-2565

Nguyen H. B., Liu Y., Withers R. L., "Relaxor dielectric properties of a $(Ca_{1.5}Ti_{0.5})(NbTi)O_7$ 'misplaced-displacive' cubic pyrochlore synthesized via metallorganic decomposition", *Solid State Commun*., 145 (**2008**) 72 -76.

Nigam S., Sudarsan V., Majumder C., Vatsa R., "Structural differences existing in bulk and nanoparticles of $Y_2Sn_2O_7$: Investigated by experimental and theoretical methods", *J. Solid State Chem*., 200 (**2013**) 202-208.

Nigam S., Sudarsan S., Vatsa R. K., "Effect of annealing temperature on the structural and photoluminescence properties of $Y_2Sn_2O_7$: Eu nanoparticles", *Eur. J. Inorg. Chem.,* 2013 (**2013**) 357-363.

Oeckler O., Stadler F., Rosenthal T., Schnick W., "Real structure of $SrSi_2O_2N_2$", *Solid State Sci*., 9 (**2007**) 205-212.

Ofelt G. S., "Intensities of crystal spectra of rare-earth ions." *J. Chem. Phys*., 37 (**1962**) 511-520

Panero W. R., Stixrude L., Ewing R. C., "First-principles calculation of defect-formation energies in the $Y_2(Ti,Sn,Zr)_2O_7$ pyrochlore", *Phys. Rev.* B, 70 (**2004**) 054110-11

Parchur A. K., Ningthoujam R. S., "Behaviour of electric and magnetic dipole transitions of Eu^{3+}, $^5D_0 \rightarrow {}^7F_0$ and Eu-O charge transfer band in Li^+ co-doped $YPO_4:Eu^{3+}$", *RSC Adv*., 2 (**2012**) 10859-10868.

Parchur A. K., Ningthoujam R. S., Rai B. S., Okram G. S., Singh R. A., Tyagi M., Gadkari S. C., Tewari R., Vatsa R. K., "Luminescence properties of Eu^{3+} doped $CaMoO_4$ nanoparticles", *Dalton Trans*., 40 (**2011**) 7595-7601.

Pawade V. B., Swart H. C., Dhoble S. J., "Review of rare earth activated blue emission phosphors prepared by combustion synthesis", *Renewable Sustainable Energy Rev.*, 52 (**2015**) 596-612.

Peacock R. D., "The intensities of lanthanide f-f transitions", *Struct. Bond*., 22 (**1975**) 83-122.

Pei Z. W., Su Q., Li S. H., "Investigation on the luminescence properties of Dy^{3+} and Eu^{3+} in alkaline-earth borates", *J. Lumin*., 50 (**1991**) 123-126.

Peng C., Zhang H., Yu J., Meng Q., Fu L., Li H., Guo X., "Synthesis, characterization, and luminescence properties of the ternary europium complex covalently bonded to mesoporous SBA-15", *J. Phys. Chem. B*, 109 (**2005**) 15278-15287.

Peng L., Wang Y., Wang Z., Dong Q., "Multiplesite structure and photoluminescence properties of Eu^{3+} doped MgO nanocrystals", *Appl. Phys. A,* 102 (**2011**) 387-392.

Phillips J. M., Coltrin M. E., Crawford M. H., Fischer A. J., Krames M. R., Mach R. M., Mueller G. O., Ohno Y., Rohwer L. E. S., Simmons J. A., Tsao J. Y., "Research challenges to ultra-efficient inorganic solid-state lighting", *Laser Photonics. Rev*., 1 (**2007**) 307-333.

Pires A. M., Davolos M. R., Malta O. L., "Eu^{3+}-O^{2-} associates luminescence in Ba_2SiO_4", *J. Lumin*., 72 (**1997**) 244-246.

Piriou B., Richard-Plouet M., Parmentier J., Ferey F., Vilminot S., "Evidence of Eu^{3+}-O^{2-} associates by luminescence study of some silicates and aluminosilicates", *J. Alloys Compd*., 262 (**1997**) 450-453.

Pokhrel M., Brik M. G., Mao Y., "Particle size and crystal phase dependent photoluminescence of $La_2Zr_2O_7$:Eu^{3+} nanoparticles", *J. Am. Ceram. Soc.*, 98 (**2015**) 3192-3201.

Pust P., Schmidt P. J., Schnick W., "A revolution in lighting", *Nat. Mater*., 14 (**2015**) 454-458.

Pust P., Weiler V., Hecht C., Tucks A., Wochnik A. S., Hen A. K., Wiechert D., Scheu C., Schmidt P. J., Schnick W., "Narrow-band red-emitting $Sr[LiAl_3N_4]: Eu^{2+}$ as a next-generation LED phosphor material", *Nat. Mater.*, 13 (**2014**) 891-896.

Qin X., Liu X., Huang W., Bettinelli M., Liu X., "Lanthanide-activated phosphors based on 4f-5d optical transitions: theoretical and experimental aspects", *Chem. Rev.*, 117 (**2017**) 4488-4527.

Radhakrishnan A. N., Prabhakar Rao P., Sibi K. S., Deepa M., Peter Koshy., "Order-disorder phase transformations in quaternary pyrochlore oxide system: Investigated by X-ray diffraction, transmission electron microscopy and Raman spectroscopic techniques", *J. Solid State Chem.*, 182 (**2009**) 2312-2318

Radhakrishnan A. N., Rao P. P., Sibi K., Linsa M., Deepa M., Koshy P., **"**Influence of disorder-to-order transition on lattice thermal expansion and oxide ion conductivity in $(Ca_xGd_{1-x})_2(Zr_{1-x}M_x)_2O_7$ pyrochlore solid solutions", *Dalton Trans.*, 40 (**2011**) 3839-3848.

Raj A. K., Rao P. P., Sreena T. S., Sameera S., James V., Renju U. A., "Remarkable changes in the photoluminescent properties of $Y_2Ce_2O_7:Eu^{3+}$ red phosphors through modification of the cerium oxidation states and oxygen vacancy ordering", *Phys. Chem. Chem. Phys.*, 16 (**2014**) 23699-23710.

Randall C. A., Nino J. C., Baker A., Youn H. J., Hitomi A., Thayer R., Edge L. F., Sogabe T., Anderson D., Shrout T. R., Trolier-McKinstry S., Lanagan M. T., "Bi-pyrochlore and Zirconolite dielectrics", *Am. Ceram. Soc. Bull.*, 82 (**2003**) 9101-9108.

Ren W., Trolier-McKinstry S., Randall C. A., Shrout T. R., "Bismuth zinc niobate pyrochlore dielectric thin films for capacitive applications", *J. Appl. Phys.*, 89 (**2001**) 767-774.

Roth R. S., Vanderah T. A., Bordet P., Grey I. E., Mumme W. G., Cai L., Nino J. C., "Pyrochlore formation, phase relations, and properties in the CaO-TiO_2-$(Nb,Ta)_2O_5$ systems", *J. Solid State Chem*., 181 (**2008**) 406-414.

Saha S., Singh S., Dkhil B., Suryanarayanan R., Dhalenne G., Revcolevschi A., Sood A. K., "Temperature-dependent Raman and X-ray studies of the spin-ice pyrochlore $Dy_2Ti_2O_7$ and nonmagnetic pyrochlore $Lu_2Ti_2O_7$", *Phys. Rev. B*, 78 (**2008**) 214102-10.

Scheetz B. E., White W. B., "Characterization of anion disorder in zirconate $A_2B_2O_7$ compounds by Raman spectroscopy", *J. Am. Ceam. Soc.*, 62 (**1979**) 468-470.

Shannon R. D., "Revised effective ionic radii and schematic studies of interatomic distances in halides and chalcogenides" *Acta Crystallogr., Sect. A: Cryst. Phys., Diffr., Theor. Gen. Cryst.,* 32 (**1976**) 751-767.

Shao Q., Wang L., Song L., Dong Y., Liang C., He J., Jiang J., "Temperature dependence of photoluminescence spectra and dynamics of the red-emitting K_2SiF_6:Mn^{4+} phosphor", *J. Alloys Compd*., 695 (**2017**) 221-226.

Sharma V., Nigam S., Sudarsan V., Vatsa R. K., "High temperature stabilization of $Y_2Sn_2O_7$:Eu luminescent nanoparticles-A facile synthesis", J. Lumin., 179 (**2016**) 248-253.

Shionoya S., Yen W. M., Yamamoto H., (Eds.), "Phosphor Handbook", *CRC press* (**2006**).

Shoemaker D. P., Seshadri R., Hector A. L., Llobet A., Proffen T., Fennie C. J., "Atomic displacements in the charge ice pyrochlore $Bi_2Ti_2O_6O'$ studied by neutron total scattering", *J. Phys. Rev. B*, 81 (**2010**) 144113-9.

Shoemaker D. P., Seshadri R., Tachibana M., Hector A. L., "Incoherent Bi off-centering in $Bi_2Ti_2O_6O'$ and $Bi_2Ru_2O_6O'$: Insulator versus metal", *Phys. Rev. B*, 84 (**2011**) 064117-6.

Sickafus K. E., Grimes R. W., Valdez J. A., Ishimaru M., Li F., McClellan K. J., Hartman T., "Radiation tolerance of complex oxides", *Science,* 289 (**2000**) 748-751.

Singh B. P., Parchur A. K., Ningthoujam R. S., Ansari A. A., Singh P., Rai S. B., "Influence of Gd^{3+} co-doping on structural property of $CaMoO_4$:Eu nanoparticles", *Dalton Trans.*, 43 (**2014**) 4770-4778.

Singh J., Krupanidhi S. B., "Probing disorder in cubic pyrochlore $Bi_{1.5}Zn_{1.0}Nb_{1.5}O_7$ (BZN) thin films", Solid State Commun., 150 (**2010**) 2257-2261.

Smentek L., Kedziorski A., "f ↔ f electric dipole transitions; old problems in a new light", *J. Alloys Compd*., 488 (**2009**) 586-590.

Smet P. F., Parmentier A. B., Poelman D., "Selecting conversion phosphors for white light-emitting diodes", *J. Electrochem. Soc.*, 158 (**2011**) R37-R54.

Smith T., Guild J., "The C.I.E. colorimetric standards and their use**",** *Trans. Opt. Soc.,* 33 (**1931**) 73-134.

Soares Santos P. C. R., Nogueira H. I. S., Felix V.; Drew M. G. B., Sa Ferreira R. A., Carlos L. D., Trindade T., "Novel lanthanide luminescent materials based on complexes of 3-Hydroxypicolinic acid and silica nanoparticles"**,** *Chem. Mater*., 15 (**2003**) 100-108.

Som S., Mitra P., Kumar V., Kumar V., Terblans J. J., Swart H. C., Sharma S. K., "The energy transfer phenomena and colour tunability in $Y_2O_2S:Eu^{3+}/Dy^{3+}$ micro-fibers for white emission in solid state lighting applications", *Dalton Trans.*, 43 (**2014**) 9860-9871.

Souza A. S., Oliveira Y. A. R. and Couto dos Santos M. A., "Enhanced approach to the Eu^{3+} ion $^5D_0$ - $^7F_0$ transition intensity", *Opt. Mater*., 35 (**2013**) 1633-1635.

Srivastava A. M., "Chemical bonding and crystal field splitting of the Eu^{3+} $^7F_1$ level in the pyrochlores $Ln_2B_2O_7$ (Ln = La^{3+}, Gd^{3+}, Y^{3+}, Lu^{3+}; B = Sn^{4+}, Ti^{4+})", *Opt. Mater*., 31 (**2009**) 881-885.

Stevens W. R., "Building Physics: Lighting", *Pergamon Press*, London, (**1969**).

Su Y., Li L., Li G., "Synthesis and optimum luminescence of $CaWO_4$-based red phosphors with codoping of Eu^{3+} and $Na^{+"}$, *Chem. Mater*., 20 (**2008**) 6060-6067.

Subramanian M. A., Aravamudan G., Rao G. V. S., "Oxide pyrochlores-A review" *Prog. Solid State Chem*., 15 (**1983**) 55-143.

Tabira Y., Withers R. L., Yamada T., Ishizawa N. Z., "Annular dynamical disorder of the rare earth ions in a $La_2Zr_2O_7$ pyrochlore via single crystal synchrotron X-ray diffraction", *Z Kristallogr*., 216 (**2001**) 92-98.

Takeda T., Hirosaki N., Funahashi S., Xie R. J., "New phosphor discovery by the single particle diagnosis approach", *Materials Discovery*, 1 (**2015**) 29-37.

Tan K. B., Khaw C. C., Lee C. K., .Zainal Z, Miles G. C., "Structures and solid solution mechanisms of pyrochlore phases in the systems Bi_2O_3-ZnO-$(Nb, Ta)_2O_5$", *J. Alloys Compd*., 508 (**2010**) 457-462.

Tang J., Gao J., Chen J., Hao L., Xu X., Lee M., "Contribution of cations to the photoluminescence properties of Eu-doped barium oxonitridosilicates phosphors", *Comp. Mater. Sci*., 79 (**2013**) 478-484.

Tanner P. A., "Some misconceptions concerning the electronic spectra of tri-positive europium and cerium", *Chem. Soc. Rev*., 42 (**2013**) 5090-5101.

Tay Y. Y., Li S., Sun C. Q., Chen P., "Size dependence of $Zn2p_{3/2}$ binding energy in nanocrystalline ZnO", *Appl. Phys. Lett*., 88 (**2006**) 173118-3.

Thomas M., Prabhakar Rao P., Reshmi V. R., Linda Francis T., Koshy P., "Improvement of Morphology and Luminescence Properties of Powellite Type Red Phosphors $CaGd_{1-x}NbMoO_8:xEu^{3+}$ Synthesized via Citrate Gel Route", *J. Am. Ceram. Soc*., 95 (**2012**) 2260-2265.

Tsai Y. T., Chiang C. Y., Zhou W., Lee J. F., Sheu H. S., Liu R. S., "Structural ordering and charge variation induced by cation substitution in $(Sr,Ca)AlSiN_3$:Eu phosphor", *J. Am. Chem. Soc*., 137 (**2015**) 8936-8939.

Valant M., Davies P. K., "Crystal chemistry and dielectric properties of chemically substituted $(Bi_{1.5}Zn_{1.0}Nb_{1.5})O_7$ and $Bi_2(Zn_{2/3}Nb_{4/3})O_7$ pyrochlores", *J. Am. Ceram. Soc.,* 83 (**2000**) 147-53

Vanderah T. A., Levin I., Lufaso M. W., "An unexpected crystal-chemical principle for the pyrochlore structure", *Eur. J. Inorg. Chem*., 14 (**2005**) 2895-2901.

Vanderah T. A., Siegrist T., Lufaso M. W., Yeager M. C., Roth R. S., Nino J. C., Yates S., "Phase formation and properties in the system $B_{i2}O_3$:$2CoO_{1+x}$:Nb_2O_5", *Eur. J. Inorg. Chem.*, 23 (**2006**) 4908-4914.

Vandenborre M. T., Husson E., Chatry J. P., Michel D., "Rare-earth titanates and stannates of pyrochlore structure; vibrational spectra and force fields", *J. Raman Spectrosc*., 14 (**1983**) 63-71.

Vegard L., "Die Konstitution der Mischkristalle und die Raumfüllung der Atome", *Z. Phys*. 5 (**1921**) 17-26.

Wan C., Qu Z., Du A., Pan W., "Influence of B site substituent Ti on the structure and thermophysical properties of $A_2B_2O_7$-type pyrochlore $Gd_2Zr_2O_7$", *Acta Mater.*, 57 (**2009**) 4782-4789.

Wan J., Liu Q., Liu G., Zhou Z., Xie R. J., "$Y_2Si_4N_6C:Ce^{3+}$ carbide nitride green yellow phosphors: novel synthesis, photoluminescence properties, and applications", *J. Mater. Chem. C*, 5 (**2017**) 6061-6070.

Wang H., Kamba S., Du H., Zhang M., Chia C. T., Veljko S., Denisov S., Kadlec F., Petzelt J., Yao X., "Microwave dielectric relaxation in cubic bismuth based pyrochlores containing titanium", *J. Appl. Phys*., 100 (**2006**) 014105–7.

Wang J., Cheng Y., Huang Y., Cai P., Kim S. I. and Seo H. J., "Structural and luminescent properties of red-emitting Eu^{3+}-doped ternary rare earth antimonates R_3SbO_7 (R = La, Gd, Y)", *J. Mater. Chem. C*, 2 (**2014**) 5559–5569.

Wang S. M., Lu M. K., Zhou G. J., Zhou Y. Y., Zhang H. P., Wang S. F., Yang Z. S., "Synthesis and luminescence properties of $La_{2-x}RE_xSn_2O_7$(RE = Eu and Dy) phosphor nanoparticles", *Mater. Sci. Eng., B*, 133 (**2006**) 231-234.

Wang S. S., Chen W. T., Li Y., Wang J., Sheu H. S., Liu R. S., "Neighboring-cation substitution tuning of photoluminescence by remote-controlled activator in phosphor lattice", *J A.m. Chem. Soc.,* 135 (**2013**) 12504-12507.

Wang W. N., Widiyastuti W., Ogi T., Lenggoro I. W., Okuyama K., "Correlations between Crystallite/Particle Size and Photoluminescence Properties of Submicrometer Phosphors", *Chem. Mater*., 19 (**2007**) 1723-1730.

Wen D., Feng J., Li J., Shi J., Wu M., Su Q., "$K_2Ln(PO_4)(WO_4):Tb^{3+}$, Eu^{3+} (Ln = Y, Gd and Lu) phosphors: highly efficient pure red and tuneable emission for white light-emitting diodes", *J. Mater. Chem. C,* 3 (**2015**) 2107-2114.

Wiegel M., Middel W., Blasse G., **"**Influence of ns^2 ions on the luminescence of niobates and tantalates"*, J. Mater. Chem*., 5 **(1995**) 981-983.

Wu Y. F., Nien Y. T., Wang Y. J., Chen I. G., "Enhancement of photoluminescence and color purity of $CaTiO_3$:Eu phosphor by Li doping", *J. Am. Ceram. Soc*., 95 (**2012**) 1360-1366.

Wybourne B. G., "The fascination of the rare earths-then, now and in the future", *J. Alloys Compd*., 380 (**2004**) 96-100.

Xie F., Li J., Dong Z., Wen D., Shi J., Yan J., Wu M., "Energy transfer and luminescent properties of $Ca_8MgLu(PO_4)_7:Tb^{3+}/Eu^{3+}$ as a green-to-red color tunable phosphor under NUV excitation", *RSC Adv*., 5 (**2015**) 59830-59836.

Xie R. J., Hirosaki N., "Silicon-based oxynitride and nitride phosphors for white LEDs-A review", *Sci. Technol. Adv. Mater*., 8 (**2007**) 588-600

Xie R. J., Hirosaki N., Takeda T., Suehiro T., "On the performance enhancement of nitride phosphors as spectral conversion materials in solid state lighting", *ECS J. Solid State Sci. Technol*., 2 (**2013**) R3031-R3040.

Xie R. J., Li Y. Q., Yamamoto H., Hirosaki N., "Nitride phosphors and solid state lighting", *CRC Press*, (**2011**).

Yan B., Wu J. H., "$NaY(MoO_4)_2:Eu^{3+}$ and $NaY_{0.9}Bi_{0.1}(MoO_4)_2:Eu^{3+}$ submicrometer phosphors: Hydrothermal synthesis assisted by room temperature-solid state reaction, microstructure and photoluminescence", *Mater. Chem. Phys*., 116 (**2009**) 67-71.

Yang M., Zhao X. D., Ji Y., Liu F. Y., Liu W., Sun J. Y., Liu X. Y., "Hydrothermal approach and luminescent properties for the synthesis of orthoniobates $GdNbO_4:Ln^{3+}$ (Ln = Dy, Eu) single crystals under high-temperature high pressure conditions", *New J. Chem*., 38 (**2014**) 4249-4257.

Ye S., Xiao F., Pan Y. X., Ma Y. Y., Zhang Q. Y., "Phosphors in phosphor-converted white light-emitting diodes: Recent advances in materials, techniques and properties", *Mater. Sci. Eng. R,* 71 (**2010**) 1-34.

Yiyao G. E., Zhaobo T., Ying C., Siyuan S., Jie Z., Zhipeng X., "Effect of comburent ratios on combustion synthesis of Eu-doped β-SiAlON green phosphors", *J. Rare Earths,* 35 (**2017**) 775-782.

Yogamalar R., Mahendran V., Srinivasan R., Beitollahi A., Kumar R. P., Bose A. C., Vinu A., "Gas-sensing properties of needle-shaped Ni-doped SnO_2 nanocrystals prepared by a simple sol–gel chemical precipitation method", *Chem. Asian J*., 5 (**2010**) 2379-2385.

Yuan H., Huang Z., Chen F., Shen Q., Zhang L., "Plasma activated synthesis and photoluminescence of red phosphor $Sr_2Si_5N_8:Eu^{2+}$", *J. Alloys Compd*., 720 (**2017**) 521-528.

Zhao M., Xia Z. G., Molokeev M. S., Ning L. X., Liu Q. L., "Temperature and Eu^{2+}-doping induced phase selection in $NaAlSiO_4$ polymorphs and the controlled yellow/blue emission", *Chem Mater*., 29 (**2017**) 6552-6559.

Zhang A., Lü M., Yang Z., Zhou G., Zhou Y., "Systematic research on $RE_2Zr_2O_7$ (RE = La, Nd, Eu and Y) nanocrystals: Preparation, structure and photoluminescence characterization", *Solid State Sci.*, 10, (**2008**), 74-81

Zhang F. X., Manoun B., Saxena S. K., Zha C. S., "Structure change of pyrochlore $Sm_2Ti_2O_7$ at high pressures", *Appl. Phys. Lett.*, 86 (**2005**) 181906-3.

Zhang F. X., Wang J. W., Lian J., Lang M. K., Becker U., Ewing R. C., **"**Phase stability and pressure dependence of defect formation in $Gd_2Ti_2O_7$ and $Gd_2Zr_2O_7$ pyrochlores", *Phys. Rev. Lett*., 100 (**2008**) 045503-4

Zhang X., Zhou L., Pang Q., Shi J., Gong M., "Tunable luminescence and $Ce^{3+} \rightarrow Tb^{3+} \rightarrow Eu^{3+}$ energy transfer of broadband-excited and narrow line red emitting $Y_2SiO_5:Ce^{3+}, Tb^{3+}, Eu^{3+}$ Phosphor", *J. Phys. Chem. C*, 118 (**2014**) 7591-7598

Zhang Y., Zhang Z., Zhu X., Liu Z., Li Y., Al-Kassab T., "Dielectric properties and microstructural characterization of cubic pyrochlore bismuth magnesium niobates", *Appl. Phys. A,* 115 (**2014**) 661-666.

Zhou Q., Zhou Y., Liu Y., Luo L., Wang Z., Peng J., Yan J., Wu M., "A new red phosphor $BaGeF_6:Mn^{4+}$:hydrothermal synthesis, photoluminescence properties, and its application in warm white LED devices", *J. Mater. Chem. C*, 3 (**2015**) 3055-3059.

LIST OF PUBLICATIONS

1. **T S Sreena**, P. Prabhakar Rao, Linda Francis, Athira K V Raj, Parvathi S Babu, "Structural and Photoluminescence Properties of Stannate based Displaced Pyrochlore type Red Phosphors:$Ca_{3-x}Sn_3Nb_2O_{14}$:$x$$Eu^{3+}$", ***Dalton Transactions,*** **(2015)** 44, 8718-8728.

2. **T. S. Sreena**, P. Prabhakar Rao, Athira K. V. Raj, Parvathi S Babu, "Influence of Structural Disorder on the Photoluminescence Properties of Eu^{3+} Doped Red Phosphors:$Ca_2Y_{3-x}Nb_3O_{14}$:$x$$Eu^{3+}$", ***Chemistry Select,*** **(2016)** 1, 3413-3422.

3. **T. S. Sreena**, P. Prabhakar Rao, K. N. Ajmal, Athira K. V. Raj, "Influence of morphology on luminescence properties of xenotime-type red phosphors $NaYP_2O_7$:Eu^{3+} synthesized via solid state and citrate-gel routes", ***Journal of Materials Science: Materials in Electronics***, **(2018)** 29, 7458-7467.

4. **T. S. Sreena**, P. Prabhakar Rao, Athira K. V. Raj, Aju Thara T. R, "Narrow-band red-emitting phosphor, $Gd_3Zn_2Nb_3O_{14}$:Eu^{3+} with high color purity for phosphor-converted white light emitting diodes", ***Journal of Alloys and Compounds***, **(2018)** 751, 148-158.

5. **T. S. Sreena**, P. Prabhakar Rao, Athira K. V. Raj, T. R Aju Thara, "Exploitation of Eu^{3+} Red Luminescence through Order-Disorder Structural Transition in Lanthanide Stannate Pyrochlore for Warm White LED Applications", ***Physical Chemistry Chemical Physics,*** **(2018)** 20, 24287-24299.

6. **T. S. Sreena**, P. Prabhakar Rao, Athira K. V. Raj, T. R Aju Thara, "Intense Narrow-band Red Emitting Phosphors in Eu^{3+}-activated Niobate System for Next Generation White LEDs" (*Communicated*).

7. Athira K. V. Raj, P. Prabhakar Rao, **Sreena T. S**, Aju Thara T. R, "Broad greenish yellow luminescence in $CaMoO_4$ by Si^{4+} acceptor doping as potential phosphors for white light emitting diode applications", ***Journal of Materials Science: Materials in Electronics***, (**2018**) (https://doi.org/10.1007/s10854-018-9757-x)

8. Athira K. V. Raj, P. Prabhakar Rao, **Sreena T. S**, Aju Thara T. R, "Pigmentary Colors from yellow to red in $Bi_2Ce_2O_7$ by rare earth ion substitutions as possible high NIR reflecting pigments", ***Dyes and Pigments***, (**2019**) 160, 177-187.

9. Athira K. V. Raj, P. Prabhakar Rao, **Sreena T. S,** Ajuthara T. R., "Influence of local structure on photoluminescence properties of Eu^{3+} doped CeO_2 red phosphors through induced oxygen vacancies by contrasting rare earth substitutions", ***Physical Chemistry Chemical Physics,*** **(2017)** 19, 20110-20120.

10. V. R. Reshmi, P. Prabhakar Rao, Athira K. V. Raj, **T. S. Sreena**, "Novel molybdenum based pyrochlore type red phosphors, $NaGd_{1-x}SnMoO_7$:$x$$Eu^{3+}$ under near UV and blue excitation", ***Journal of Luminescence,*** **(2017)** 190, 6-9.

11. Aju Thara T. R., P. Prabhakar Rao, Saraswathy Divya, Athira K.V Raj, and **Sreena Thankom Sreedharan**, "Enhanced NIR Reflectance with Brilliant Yellow Hues in Scheelite type Solid Solutions, $(LiLaZn)_{1/3}MoO_4$-$BiVO_4$ for Energy Saving Products", ***ACS Sustainable Chemistry and Engineering,*** **(2017)** 5, 5118-5126.

12. Athira K. V. Raj, P. Prabhakar Rao, S. Sameera, S. Divya, T. R. Ajuthara, **T. S. Sreena**, "High IR Reflecting Yellow Colorants in Yttrium-doped $MgBi_{2-x}O_4$ Solid Solutions", ***Chemistry Letters,*** **(2016)** 45, 928-930.

13. Parvathi S. Babu, P. Prabhakar Rao**,** S.K. Mahesh, T. Linda Francis, **T. S. Sreena**, "Studies on the photoluminescent properties of a single phase white light emitting phosphor $CaLa_{1-x}NbMoO_8$: x Dy^{3+} for pc-white LED applications", ***Materials Letters,*** **(2016)** 170, 196-198.

14. T. Linda Francis, P. Prabhakar Rao, Mahesh S. K, **Sreena T S**, Parvathi S Babu, "Effect of host structure on the photoluminescence properties of $Ln_3TaO7:Eu^{3+}$ red phosphors", ***Optical Materials***, **(2016)** 52, 134-143.

15. T. Linda Francis, P. Prabhakar Rao, Mahesh S. K, **Sreena T S,** Parvathi S Babu, "Novel red phosphors $Gd_2GaTaO_7:Eu^{3+}$, Bi^{3+} for white LED applications", ***Journal of Material Science: Materials in Electronics,*** **(2015)** 26, 5743-5747.

16. Athira K. V. Raj, P. Prabhakar Rao, **T. S. Sreena,** S. Sameera, Vineetha James, U. A. Renju, "Remarkable changes in the photoluminescent properties of $Y_2Ce_2O_7$:Eu^{3+} red phosphors through modification of the cerium oxidation states and oxygen vacancy ordering", ***Physical Chemistry Chemical Physics,*** **(2014)** 16, 23699-23710.

17. T. Linda Francis, P. Prabhakar Rao, Mariyam Thomas, S.K. Mahesh, V. R. Reshmi and **Sreena T S**, Structural influence on the photoluminescence properties of Eu^{3+} doped Gd_3MO_7 (M = Nb, Sb, and Ta) red phosphors, ***Physical Chemistry Chemical Physics,*** **(2014)** 6, 17108-15.

LIST OF CONFERENCE PAPERS

1. **Sreena T S**, P. Prabhakar Rao*, Athira K.V. Raj and Aju Thara T R, Development of Eu^{3+} doped Narrow-Band Red-Emitting Phosphor for Phosphor-Converted White Light Emitting Diodes, *National Conference on Luminescence and its Applications (NCLA) 2018*

2. **Sreena T S,** P. Prabhakar Rao* and Athira K.V. Raj, Structural and Photoluminescence Properties of Eu^{3+} Doped Pyrochlore-Type Red Phosphors $Ca_3Ti_3Nb_2O_{14}$ for WLED Applications, *National Conference on Luminescence and its Applications (NCLA) 2016.* **Best Poster Award.**

3. **Sreena T S,** P. Prabhakar Rao*, Linda Francis, Athira K. V. Raj and Parvathy S. Babu, Synthesis and characterization of Eu^{3+} doped pyrochlore-type red phosphors $Ca_3Sn_3M_2O_{14}$(M = Nb, Sb and Ta) for white light emitting diode applications, *International Conference on science, Technology and Applications of Rare Earths (ICSTAR) 2015*.

4. **Sreena T S,** P. Prabhakar Rao*, Mahesh S K, Linda Francis, Athira K. V. Raj and Parvathy S. Babu, Studies on the photoluminescence properties of $CaMoO_4$: 0.2 Eu^{3+} red phosphors by the addition of $SmPO_4$, *International Conference on Luminescence and its Applications (ICLA) 2015.*

5. **Sreena T S**, P. Prabhakar Rao*, T Linda Francis, Athira K.V. Raj and Parvathi S. Babu, Synthesis and Characterization of Eu^{3+} doped Pyrochlore-type Red

Phosphors $Ca_3Sn_3M_2O_{14}$ (M = Nb, Sb, Ta) for White Light Emitting Diode Applications, *NSPA, 2015.*

6. **Sreena T S,** P. Prabhakar Rao*, Athira K. V. Raj, Mahesh S K, Linda Francis, Reshmi V R and Parvathy S. Babu, Photoluminescence of pyrochlore type red emitting phosphors, *National Conference on Advanced Technologies for Materials Processing and Diagnostics,* (*ISAS) 2014*

7. **Sreena T S,** P. Prabhakar Rao*, Mahesh S K, Linda Francis, Reshmi V R and Athira K. V. Raj, Synthesis and characterization of stannate based pyrochlore red emitting phosphors for white light emitting diodes, *International Conference on Advanced Functional Materials (ICAFM) 2014*.